SIMULATION AND OPTIMIZATION OF FOAM EOR PROCESSES

Proefschrift

ter verkrijging van de graad van doctor
aan de Technische Universiteit Delft,
op gezag van de Rector Magnificus prof. ir. K.C.A.M. Luyben,
voorzitter van het College voor Promoties,
in het openbaar te verdedigen op
dinsdag 5 juli 2011 om 10:00 uur

door

Maryam NAMDAR ZANGANEH

Master of Science in Petroleum Engineering

geboren te Teheran, Iran.

Dit proefschrift is goedgekeurd door de promotoren:
Prof. dr. W.R. Rossen
Prof. dr. ir. J.D. Jansen

Samenstelling promotiecommissie:

Rector Magnificus,	voorzitter
Prof. dr. W.R. Rossen,	Technische Universiteit Delft, promotor
Prof. dr. ir. J.D. Jansen,	Technische Universiteit Delft, promotor
Prof. dr. J. Bruining,	Technische Universiteit Delft
Prof. dr. ir. A.W. Heemink,	Technische Universiteit Delft
Prof. dr. D. Marchesin,	Instituto Nacional de Matemática Pura e Aplicada, Rio de Janeiro, Brazil
Prof. dr. P.L.J. Zitha,	Technische Universiteit Delft
Dr. J.F.B.M. Kraaijevanger,	Shell Global Solutions International

This research was carried out within the context of the Integrated Systems Approach to Petroleum Production (ISAPP) Knowledge Centre. ISAPP is a joint project between Delft University of Technology (TU Delft), Shell International Exploration and Production (SIEP), and the Dutch Organization for Applied Scientific Research (TNO).

ISBN: 978-90-8891-299-3

Cover design by Maryam Namdar Zanganeh (Saturation profile plotted on an *x*-*t* diagram)

Printed by Proefschriftmaken.nl || Printyourthesis.com.

To Hamidreza and my parents

Contents

Chapter 1

Introduction

1.1. World Energy Demand

In 2009, the first decline in energy consumption occurred since 1982 due to the recent global economic recession (BP Statistical Review of World Energy 2010). Nevertheless, the recession is over now and there is again a growing demand for energy worldwide. The world's primary energy resources include oil, natural gas, coal, nuclear, and hydroelectric power. **Fig. 1** illustrates the annual worldwide consumption of the primary energy resources in the year 2009.

Fig. 1: Annual consumption of the primary energy resources per capita in the year 2009. The consumption is in tons oil equivalent (BP Statistical Review of World Energy 2010).

Although coal is the world's most abundant fossil fuel, oil maintains its position as the world's principal fuel. Looking at the regional markets in **Fig. 2**, the highest consumption of the fossil fuels per region is as follows: oil and natural gas in the Middle East, coal in Asia Pacific, nuclear in Europe and Eurasia, and hydroelectric in South and Central America (BP Statistical Review of World Energy 2010).

Wind and solar energy are also rapidly growing. Their energy generation capacity has risen by 31% and 47% respectively in 2009. China and the US are the leading countries in applying wind energy (BP Statistical Review of World Energy 2010).

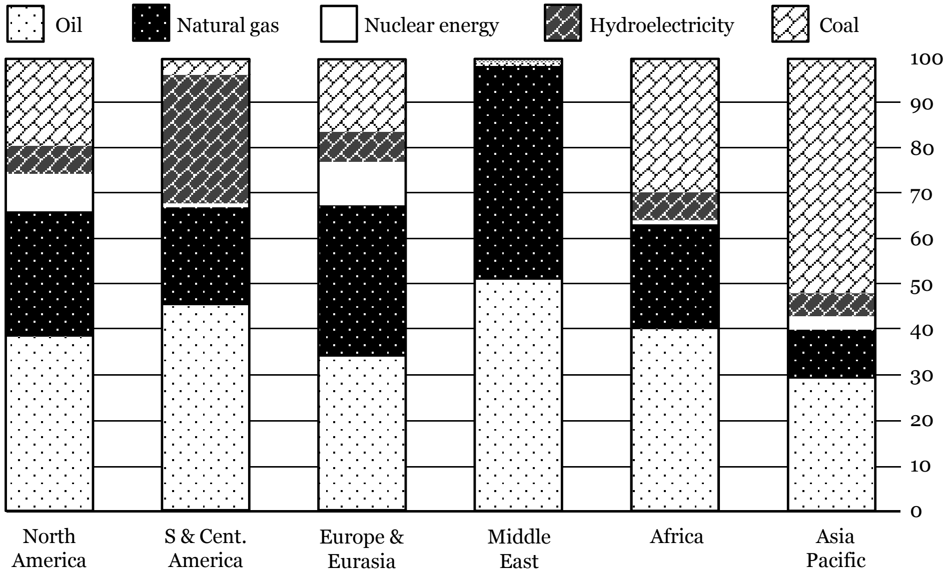

Fig. 2: Regional consumption pattern of the primary energy resources in percentage at the end of 2009. (BP Statistical Review of World Energy 2010).

The future availability of fossil fuels is expressed by R/P ratio, which is the remaining amount of these fuels *in years*. This ratio is computed by dividing the remaining reserves at the end of a year by the production in that year; assuming that the production will remain constant in the years ahead. At the end of 2009, this ratio was equal to 45.7 years for oil, 62.8 years for natural gas, and 119 years for coal (BP Statistical Review of World Energy 2010). Therefore, as will be discussed later, it is important to efficiently produce the remaining oil and gas reserves to improve the hydrocarbon recovery from hydrocarbon reservoirs.

1.2. Hydrocarbon Reservoirs

Hydrocarbon reservoirs are subsurface bodies of rock containing hydrocarbons. Reservoir rocks must have sufficient porosity (fraction of void volume in the rock) and permeability (ability to transport fluids) to accumulate and conduct the fluids. Reservoir-rock types are generally sandstone and limestone. Hydrocarbon reservoirs are generally located at a depth of 1-5 km and their thickness varies from a few meters to hundreds of meters. The areal scale of reservoirs ranges from a few square kilometers to a few hundred square kilometers.

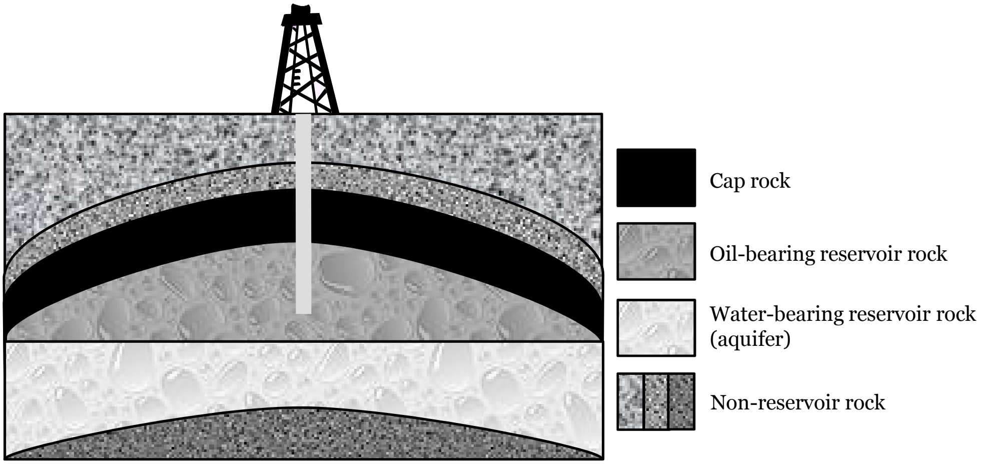

Fig. 3: Schematic vertical cross-section of an oil reservoir. The reservoir is confined by an impermeable cap rock at the top and an aquifer at the bottom. The oil/water interface is called oil-water contact.

A schematic vertical cross-section of an oil reservoir is illustrated in **Fig. 3**. Oil is trapped beneath an impermeable rock (usually a shale layer) called cap rock. From below, oil is usually in contact with an aquifer that is a water-bearing reservoir rock. Oil production wells are completed in the oil-bearing section of the reservoir. The reservoir is initially in a static condition at high pressure. Once production begins, oil flows to surface via the well(s) and the pressure starts to decline. Various oil-recovery mechanisms exist to maintain the reservoir pressure and boost oil production. They are discussed below.

1.3. Recovery Mechanisms for Hydrocarbon Reservoirs

When a virgin reservoir comes into production, the initial reservoir pressure is usually high enough to make the hydrocarbons flow to the surface through the well(s) with the *natural* reservoir energy corresponding to water-drive (aquifer), gas-drive (gas cap or solution gas), or gravity drainage. However, if the initial reservoir pressure is not adequate or the reservoir pressure declines due to production, artificial lift techniques (e.g., down-hole pumps, gas lift) are required to reduce the bottomhole pressure and assist the production. The period of application of these two methods (i.e., natural flow and artificial lift) is considered as the *primary* recovery stage of the reservoir. On average, about 10% of the initial hydrocarbons in place is produced during the primary recovery (**Fig. 4**).

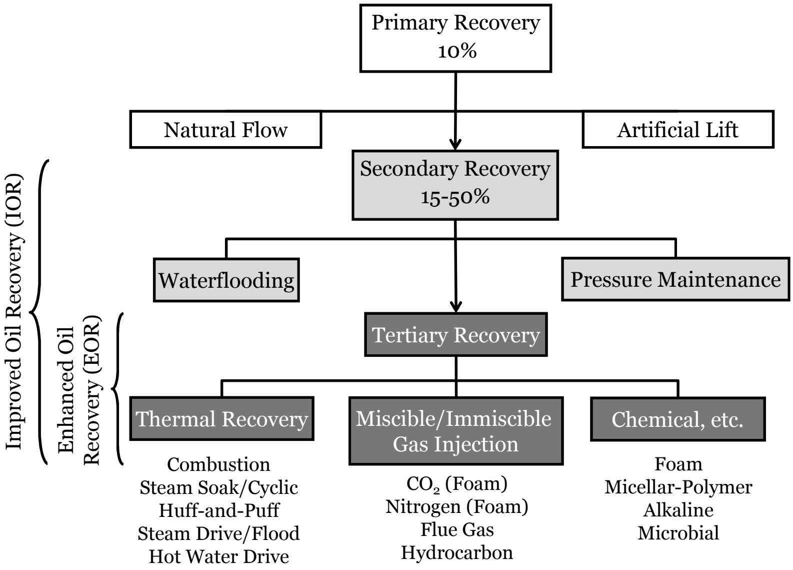

Fig. 4: Oil-recovery mechanisms. Modified from Stosur et al. (2003). Original source of the figure is Moritis (2000).

When the reservoir pressure is so depleted that oil production is not economical any more, the *secondary* recovery stage starts with the main purpose of *pressure maintenance* in the reservoir to displace the hydrocarbons. During this stage, fluid(s) (water, gas) is/are injected through injection wells to mimic the *natural* drives that were initially in place. Waterflooding and gas injection are the most common techniques in secondary recovery. Water is injected into the aquifer or production zone and/or gas is injected into the gas cap to push the hydrocarbons to the production wells. Secondary recovery stops when oil production declines, considerable amounts of the injected fluid are produced, and further production is no longer economical. At the end of the secondary recovery, the oil-recovery factor is typically between 15 and 50%.

To further increase oil recovery, *tertiary* recovery techniques are employed to improve both the sweep and displacement efficiencies. These techniques alter fluid and/or rock-fluid interaction properties. Some of them (e.g., thermal recovery, miscible gas injection, microbial EOR) mainly modify the oil properties. Polymers increase water viscosity, while surfactants have different applications. In surfactant flooding, surfactants lower the interfacial tension between oil and water, increasing capillary number and reducing residual oil saturation. In foam flooding, a mixture of surfactant, water, and gas can turn into foam and gas-phase mobility is reduced by making a stable foam. Surfactants also alter the rock wettability. Although these techniques are called *tertiary*, they can be initiated throughout the entire productive life of the reservoir. The three major categories are thermal recovery, miscible/immiscible gas injection, and chemical flooding (see Fig. 4 for details). Each of these methods performs at its best if it is applied at the reservoir conditions that are favorable for that method. These conditions involve the oil and water saturation at the beginning of the tertiary recovery, oil properties (composition, API gravity, and viscosity), reservoir temperature, pressure, thickness, depth, porosity, permeability, reservoir type, and rock type. For instance, foam may collapse at high oil saturation, low water saturation, and in the presence of light oils (high API gravity). As a result, it is not recommended to apply foam at early stages of the reservoir life due to high oil saturation. These tertiary recovery methods are also called *enhanced oil recovery* (EOR) methods.

EOR techniques are relatively expensive; hence, it is extremely important to optimize them to have an economically feasible process (Jansen 2011). Otherwise, the cost of the injected fluid itself (such as surfactant) can simply exceed the revenue of the remaining oil to be produced.

1.4. Foam EOR

Foam has a variety of applications in oil extraction ranging from drilling (to transport cuttings to the surface), to near-wellbore well-stimulation treatments (to divert acids to improve the acid-injection profile) (Gdanski 1993; Zhou and Rossen 1994), and gas mobility control in EOR (Schramm 1994; Rossen 1996). Foam is also used in shallow subsurface application to improve the sweep of surfactant solutions in aquifer remediation (Hirasaki et al. 2000). In this work, foam is specifically used for controlling the mobility of injected gas to improve sweep and displacement efficiencies in EOR.

Foam is generally divided into two wide categories: *foam in bulk* and *foam in porous media* (see **Fig. 5**). In *foam in bulk*, the size of a container is *much larger* than individual bubbles, whereas in *foam in porous media*, the diameter of bubbles is *comparable* to or *larger* than the pore size (Rossen 1992). Foam in porous media is defined as “a dispersion of gas in a liquid such that the liquid phase is continuous, and at least some part of the gas is made discontinuous by thin liquid films called *lamellae*” according to Hirasaki (1989). The lamellae (of the order of 10-100 nm thick) are stabilized by surfactants adsorbed at the gas/liquid interface.

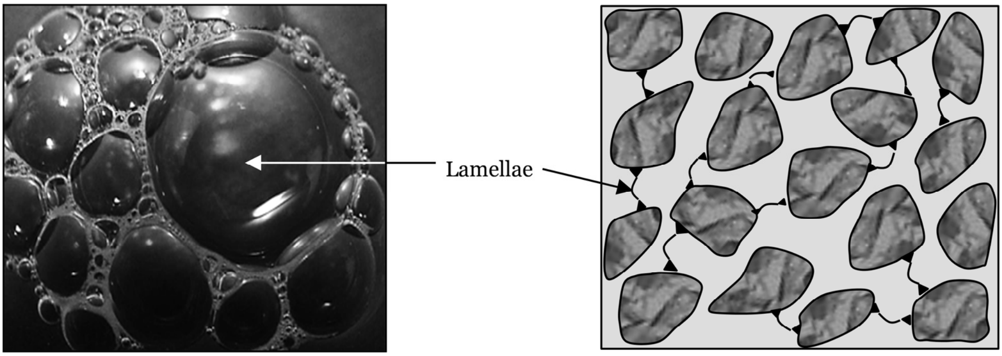

(a) (b)

Fig 5: (a) Foam in bulk that is encountered in everyday life. (b) Foam in porous media. Lamellae are thin liquid films with a thickness of the order of 10-100 nm sketched between grains of rock in Fig. 5b.

In the presence of foam, gas mobility in porous media is drastically reduced through trapping a large fraction of gas in place and increasing the effective gas viscosity. Forward movement of gas trapped inside foam bubbles must first overcome capillary resistance to movement of the lamellae. If the bubbles do flow, drag between the foam bubbles and pore walls/constrictions further hinders gas movement. Nevertheless, to a good approximation foam does not alter the relative-permeability functions or viscosities of water and oil phases (Bernard and Jacobs 1965; Huh and Handy 1989; Vassenden and Holt 2000; Chou 1990).

1.4.1. History and Field Tests

The application of foam to mobility control goes back to 1958 when it was first proposed by Bond and Holbrook (1958). Fried (1961) conducted the first research on the mechanisms of the foam-drive processes. Further research was performed by Bernard and Holm (1964) and Marsden and his colleagues in 1960's (Marsden et al. 1967; Raza and Marsden 1965). Later, foam was suggested for mobility control in various processes (Reisberg 1972; Kamal and Marsden 1973; Bernard et al. 1980). Lawson and Reisberg (1980) conducted experiments in cores to study the performance of foam for mobility control in surfactant-alternating-gas (SAG) flooding. Due to lack of understanding of the mechanisms of mobility control by foam at that time, this concept was not adopted immediately (Li et al. 2008).

Many advances have been made in understanding this concept since then and many field tests on foam EOR have been carried out (Hanssen 1994). Turta and Singhal (1998) investigated more than 40 foam EOR projects. Shan (2001) lists 11 foam field trials (see **Table 1**) with CO_2, N_2, air or hydrocarbon-gas (HC) foam. They include different injection strategies at a fixed pressure (*P*) or injection rate (*Q*): SAG and/or continuous foam injection (i.e., coinjection of surfactant solution and gas at a fixed water fractional flow or foam quality). While Shan has excluded steam-foam trials, Hirasaki (1989) and Eson (1989) have reviewed various steam-foam-drive field projects. One of the most successful field tests of foam for mobility control is the foam-assisted water-alternating-gas (FAWAG) trial performed in the Snorre field in the North Sea (Blaker et al. 2002). Prior to this, foam application in the North Sea had been mainly limited to production-well treatments (Aarra et al. 1996; Svorstøl et al. 1997).

Table 1: Summary of foam field trials excluding steam foam (from Shan 2001).

Field Trial	Gas	SAG	Continuous
Rangely Weber Sand Unit (Jonas et al. 1990)	CO_2	-	Const. *P*
North Ward-Estes (Chou et al. 1992)	CO_2	Const. *P*	-
San Andres & S.E. Utah (Hoefner et al. 1995)	CO_2	Const. *Q*	Const. *Q*
EVGSAU (Stevens et al. 1992; Stevens and Martin et al. 1995)	CO_2	Const. *Q*	-
Siggins Field (Holm 1970)	Air	Const. *Q*	Const. *Q*
Painter Reservoir (Kuehne et al. 1998)	N_2	-	Const. *Q*
Prudhoe Bay (Krause et al. 1992)	N_2	Const. *Q*	Const. *Q*
Triassic Field (Liu et al. 1988)	HC	Const. *Q*	-
Oseberg Field (Aarra et al. 1995)	HC	Const. *Q*	-
Pembina/Ostracod ‘G’ Pool (Chad et al. 1988)	N_2+HC	-	Const. *Q*
Snorre Field in North Sea (Svorstøl et al. 1997; Blaker et al. 2002)	N_2+HC	Const. *Q*	Const. *Q*

1.4.2. Physics

Foam EOR processes must be applied under favorable reservoir conditions for foam (lamella) stability to achieve a successful displacement. Foam is sensitive to several parameters including oil saturation, water saturation through its effect on capillary pressure, surfactant concentration and chemical formulation, salinity, oil composition, heterogeneity, and capillary number which reflects flow rate. Among these parameters, we confine our investigations to the effect of oil and water saturations and surfactant concentration on foam stability.

Specifically, foam may be weakened or destroyed at high oil saturations and/or low water saturations (high capillary pressures). The presence of enough surfactant in the reservoir is also a key parameter for foam formation. If any of the above conditions is violated (too much oil for instance), foam may collapse completely and injected gas almost immediately breaks through to the production well, leaving much of the oil behind. In order to prevent this, it is of extreme importance to intelligently design a foam process. This comprises the selection of a suitable surfactant that fits both the economics and the above criteria.

Surfactant must be able to produce strong lamellae that survive the reservoir conditions. Thus, very careful surfactant selection is required. First, the approximate distribution of oil and water saturations in the reservoir before starting foam EOR must be identified. Next, extensive experiments must be conducted with the real reservoir oil to screen surfactant chemical formulations and discover the exact effects (weakening/killing) of the factors endangering the foam stability. Lastly, the surfactant that can produce a foam stable at the reservoir conditions is selected.

Surfactants can be very expensive if they are designed for specialized purposes. Moreover, surfactant loss due to adsorption on the rock surface can seriously damage the economics of the projects, such that the cost of the surfactant lost to the rock by itself can exceed the revenue of the remaining oil to be produced (see §4.4 for more detail).

1.4.3. Models Describing Foam Behavior in Porous Media

In the presence of foam, the gas-phase mobility is significantly reduced (Bernard and Holm 1964; Huh and Handy 1989). However, the water relative-permeability function remains unchanged (Bernard and Jacobs 1965; Huh and Handy 1989; Vassenden and Holt 2000). We like-wise assume that foam does not alter the oil relative permeability. Experiments clearly show that the gas mobility in the presence of foam (hereafter referred to as *foam mobility*) is dependent on foam texture (i.e., bubble size) inside the rock, which is difficult to measure in situ. Based on this, models are developed to describe the complex mechanisms governing foam *texture* and foam *mobility*:

- Fully mechanistic models
    - Population-balance models
    - Network models
- Local-steady-state models

1.4.3.1. Fully Mechanistic Models

Fully mechanistic models aim at completely describing the central role of foam texture and all the factors influencing it, in a *dynamic* way.

1.4.3.1.1. Population-Balance Models

Population-balance models strive to fully describe foam *dynamics* by incorporating all the mechanisms controlling and influencing foam texture, which dominates foam mobility. These models analytically describe the dynamics of foam generation, trapping, and coalescence on the pore scale. A conservation equation is introduced in this model in which the rate of change of foam texture depends on the rate of inflow, outflow, generation, trapping, and coalescence of lamellae (Patzek 1988; Falls et al. 1988; Friedmann et al. 1991; Kovscek 1995, 1997; Nguyen et al. 2000; Zitha et al. 2006; Kam et al. 2007). This type of model has been successfully applied to describe laboratory experiments (Falls et al. 1988; Friedmann et al. 1991; Chen et al. 2010). Variations of the population balance differ primarily in their assumptions about foam generation. Chen et al. (2010) has developed a simplified population-balance model based on the local-steady-state assumption (§1.4.3.2), in which the rates of foam generation and coalescence are taken to be equal.

Pros: This type of model fully describes foam dynamics to the extent that it is complete and that all its mathematical expressions for describing foam behavior are accurate. Only this type of model could represent foam dynamics where local steady-state does not apply, for instance near the injection face, where foam generation occurs, and within shock fronts.

Cons: It is complex. Numerous parameters are required to be determined from experiments due to the lack of comprehensive understanding of the foam mechanisms inside a rock. These parameters are essentially difficult to measure. Moreover, there is ambiguity in understanding the correct mechanisms from coreflood experiments. For instance, it is generally impossible to differentiate between a low lamellae destruction rate and high lamellae generation rate (Zeilinger 1996).

1.4.3.1.2. Network Models

Percolation or statistical network models represent a disordered medium (the pore space of rock) by a random spatial distribution of interconnected flow paths (a network) representative of the topology of the porous medium, with bond conductivities reflecting pore size. This concept is applied to describe *generation* and *displacement* of foam in porous media. Gas mobility is reduced by blockage of the network (Chou 1990; Rossen and Gauglitz 1990; Rossen et al. 1994, 1995; Kharabaf and Yortsos 1998; Chen et al. 2005) and is reduced to zero by foam at the percolation threshold. Gas flows only if the fraction of throats not blocked by lamellae exceeds the percolation threshold (Rossen et al. 1994).

Of the works cited above, only Chou (1990) attempted to build a complete model for foam. A key assumption of this theory is that lamellae are continuously regenerated by snap-off mechanisms in pore throats with an aspect ratio greater than some critical value, blocking gas flow. Chou's model assumes local steady-state; lamellae are quickly regenerated at the throats if ruptured. The balance between characteristic times for lamella destruction and regeneration leads to a probability that a throat is blocked at any time; gas mobility is reduced according to the fraction of throats blocked.

Pros: The models of Rossen and Gauglitz (1990), Kharabaf and Yortsos (1998) and Chen et al. (2005) provide insights into mechanisms of foam generation and mobility, but not complete foam models.

Cons: Fully dynamic network models (Chen et al. 2005) are computationally expensive. No one has yet attempted to define a complete model for foam based on dynamic computations on a pore network. Chou's local-steady-state model is based on the problematic assumption that lamellae break (requiring high capillary pressure) and then regenerate by snap-off (requiring low capillary pressure), with no explanation offered for why this would occur (cf. Rossen 2003). Moreover, gas is assumed to be incompressible (Chou 1990).

1.4.3.2. Local-Steady-State Models

Local-steady-state models preserve the central role of foam texture in gas mobility while being simple. The local-steady-state assumption implies that foam reaches the steady state corresponding to the local saturation of the regime in which it resides relatively fast (Rossen and Bruining 2007). This model also assumes that gas mobility is fully determined by the local conditions (i.e., saturations, surfactant concentration, velocities, etc.). Population-balance models employ an extra differential equation to describe bubble texture as a function of local conditions, whereas local-steady-state models make use of an algebraic relation to describe foam rheology.

A typical approach for describing foam rheology in local-steady-state models is through the models based on *mobility-reduction factor*. These models were first proposed by Marfoe et al. (1987) and improved by Islam and Farouq Ali (1990). In these models, a mobility-reduction factor obtained from steady-state laboratory experiments is applied to modify gas mobility in the presence of foam. These models are based on the *local-steady-state* assumption and *implicitly* reflect the effect of foam texture on gas mobility reduction through the variation of the pressure gradient as a function of parameters influencing the gas mobility (i.e., absolute rock permeability, surfactant concentration, superficial velocities, water and oil saturations, pressure drop, etc.). Foam mobility is eventually obtained by multiplying either gas relative permeability or gas viscosity, or both, by these correlations.

Different ranges of complexity can be accounted for in describing the effect of various features on foam and the effect of foam on gas mobility in local-steady-state models. Complexity ranges from simply assuming a fixed reduction in gas mobility (Mayberry et al. 2008) to more complicated models (Namdar Zanganeh et al. 2011; Chapter 3).

Most local-steady-state models incorporate the existence of a *limiting capillary pressure*. Lamellae are extremely sensitive to capillary pressure (P_c); these thin liquid films are drained and foam collapses at high P_c. Khatib et al. (1988) discovered through experiments that foam collapses rather abruptly at/above a certain value of P_c and they called it the *limiting capillary pressure* (P_c^*). Since capillary pressure depends on water saturation (S_w) in rock, this suggests that for a given surfactant formulation foam collapses at a fixed value of $S_w = S_w^*$; foam reduces mobility greatly for $S_w > S_w^*$, but little or not at all for $S_w \leq S_w^*$ in water-wet reservoirs. Models with this mechanism represent a local-steady-state form of the population-balance model for strong foams where the capillary pressure controls foam texture.

Pros:

- Local-steady-state models can be implemented very easily. They implicitly account for the central role of foam texture in gas mobility. Although they do not individually account for mechanisms of foam generation and collapse (as in population-balance models), recently there is agreement that local steady-state applies to foam displacements at field scale and even at laboratory scale (Chen et al. 2010), unless the pressure gradient in the field is less than that required for foam generation, where the local-steady-state assumption may not apply (Mamun et al. 2002).
- The numerical solution of foam models under the local-steady-state assumption is much less complex and numerically more stable than population-balance models (Kam et al. 2007).
- Various studies reveal that population-balance models and local-steady-state models produce comparable results when modeling foam at the field scale and even at the laboratory scale; assuming local steady-state (Rossen et al. 1999; Kam et al. 2007; Chen et al. 2010). Thus, it is crucial to clearly find the conditions for which the added complexity (i.e., modeling with population-balance model) is indeed necessary.

Cons:

- The effect of foam texture inside the rock is, in general, not explicitly accounted for (Bertin et al. 1998). Moreover, these models are case-specific and they lack generality (Nguyen et al. 2000).
- Applicability of this type of model might be impaired if there is hysteresis in gas trapping due to the complex relation between capillary pressure and liquid saturation (Chen et al. 1990).

1.4.4. Method of Characteristics

The method of characteristics (MOC) is useful for solving the equations for foam flow (Zhou and Rossen 1995; Rossen et al. 1999; Namdar Zanganeh et al. 2011) and other EOR processes (Lake 1989; Marchesin and Plohr 2001; Orr 2005). The MOC is an *analytical* technique for solving a system of first-order quasi-linear partial-differential equations (PDEs). One of the two essential principles of the MOC is solving the PDEs by converting them into systems of ordinary-differential equations and then integrating them simultaneously to find the solution.

With additional simplifying assumptions, the transport equations can be solved by the MOC. The assumptions we make include one-dimensional (1D), immiscible displacement; incompressible phases; Newtonian mobilities; absence of gravity, dispersion, gradients of capillary pressure, and viscous fingering (which are 2D effects); and immediate attainment of local steady-state. (See Chapter 2 for the complete list of assumptions.) Some of these assumptions have been relaxed in the literature[*]. In spite of these simplifying assumptions, the MOC is found to be accurate and useful in foam field tests at the Snorre field (Martinsen and Vassenden 1999).

The MOC applied to injection processes involving two-phase flow gives rise to *fractional-flow theory* in the petroleum engineering community. Fractional-flow theory was first applied to foam displacements by Zhou and Rossen (1995) following the same principles as were first introduced by Buckley and Leverett (1942) for two phase water/oil flow. In the MOC, fixed-saturation waves propagate through the porous medium. The wave velocities are derived from fractional-flow functions that are dependent on phase mobilities. Gas mobility in the presence of foam is modified by a mobility-reduction factor (§1.4.3.2) in the MOC; hence, the MOC incorporates the local-steady-state assumption.

Pros:

- The MOC provides exact solutions for benchmarking the accuracy and numerical artifacts of numerical simulators.
- The MOC solutions have proved useful in highlighting key mechanisms and strategies for improving foam performance (Zhou and Rossen 1994, 1995; Rossen et al. 1999; Shan and Rossen 2004; Mayberry et al. 2008), and in better understanding foam simulation models (Rossen et al. 1999; Dong and Rossen 2007).

---

[*] e.g., non-Newtonian mobilities: Rossen et al. (2008, 2010); non-steady-state assumption (assuming local-steady-state except at specific locations): Ashoori et al. (2011a, 2011b); miscible phases: Orr (2005); 1D in the presence of gravity: Rodrigues (2010).

- Rossen et al. (1999) showed that a population-balance model that required 10 parameters for defining foam behavior in radial flow can be represented by only 1 parameter using fractional-flow theory. These insights can lead to an improved EOR process design. Also, one can identify the most important conditions for conducting experiments.
- The use of an empirical mobility-reduction factor greatly simplifies foam modeling in porous media, although it cannot capture transient foam behavior.
- Incorporating the limiting capillary pressure concept into the MOC simplifies the modeling task greatly without loss of generality (Hill and Rossen 1994; Zeilinger 1996).

Cons:

- The MOC solutions are valid only in one-dimension.
- If the solution is very complex, it is usually hard to find, using the MOC; a numerical solution may help in finding it.
- Because of its simplifying assumptions, the MOC cannot be used in complex real-world applications where many of its assumptions are violated. Its usefulness is in the insights it offers, not as a quantitative, predictive tool for real reservoirs.

1.5. Oil-Production Optimization

Chemical EOR is relatively expensive due to the high cost of the injected chemicals such as surfactants. Their excessive use leads to processes that are not economically feasible. Thus, optimizing the injected amount of these chemicals is of extreme importance (Jansen 2011). There are two optimization modes: short-term (daily, weekly) and long-term (years to decades). We address the long-term optimization of foam EOR processes in Chapter 5.

Any optimization problem consists of two main parts: the objective function that must be minimized or maximized (optimized) and one or more controllable parameters that should be adjusted to arrive at the optimum control settings, leading to the optimized objective function. We intend to find the optimum amount of the injected surfactant that maximizes the long-term cumulative oil production. Thus, our objective function is the cumulative oil production, and the control settings in our case could in principle be one or more of the following variables: composition of the injected surfactant solution (in simultaneous injection of gas and surfactant solution, the switching time between surfactant solution and gas injection (in surfactant alternating gas injection), and various control settings such as flow rate, bottomhole pressure and valve settings. As an initial case study, we optimize the duration of surfactant injection in a SAG process to maximize total oil production.

1.5.1. Optimization Methods

There exist various optimization methods. Some of them are gradient-based, and some are derivative-free methods. Gradient-based methods in general can very efficiently find an optimum with few forward model evaluations, and they assure that the objective function grows at each iteration (in the maximization problem). However, they only provide local information about the objective function in the neighborhood of certain values of the controllable parameters. Therefore, if the objective function has multiple local optima, it is highly probable to find a local optimum instead of a global optimum (Sarma et al. 2005), because gradient-based methods tend to find the optimum closest to the initial guess. Since the results obtained by these methods are generally dependent on the initial guess of the controllable parameter, it is beneficial to try different choices as an initial guess. The ensemble Kalman filter (EnKF) and optimal control theory (OCT) are gradient-based.

In OCT, gradients are computed analytically by an adjoint equation (Oliver et al. 2008). We note that sometimes a wider class of methods is used in OCT for gradient calculation, but in this thesis we do not consider those other methods. OCT is particularly useful in optimization problems where a large number of controllable parameters must be optimized. However, implementation of the adjoint routine is complex and time-consuming and requires considerable code development. The adjoint routine depends on the forward model (system equations). Thus, every time that the forward model is modified, the adjoint code must be updated and one needs access to the simulator's source code to do so (Sarma et al. 2005; Chen et al. 2009; Jansen 2011).

EnKF is an adjoint-free method and is the extension of Kalman filter to nonlinear problems. It has been mainly used for history-matching problems, but it is applied in optimization as well (Oliver et al. 2008; Chen et al. 2009). In this method, stochastic gradients are calculated that are *approximations* of the analytical gradients. EnKF is easy to implement and computes the gradients via the sensitivities provided by the ensembles, while the simulator acts as a black box. The computational cost of EnKF is claimed to be nearly independent of the number of unknown parameters (Chen et al. 2009). However, the quality of the approximated gradients is affected by the ensemble size and level of nonlinearity of the system.

Global optimization methods such as simulated annealing (Yang et al. 2003) are in principle capable of finding the global optimum, provided that a sufficient number (usually large) of forward model evaluations is performed. However, they do not ensure monotonic optimization of the objective function. Therefore, these methods are computationally expensive and are not favored if the number of controllable parameters is large and the individual function evaluations take a long time (Brouwer 2004).

We use OCT in this thesis, in which gradients are computed analytically and backward in time by an adjoint equation. We apply OCT because of its efficiency and because the simulator MoReS, that was available for this study, is already equipped to compute the required gradients.

1.6. Research Objectives

The specific objectives of this research are stated as follows:

- To evaluate the success of 1D foam EOR processes in the presence of mobile oil by means of an analytical technique and assert the operating conditions leading to successful processes.
- To investigate the performance of the numerical simulator in matching the 1D analytical solutions of foam EOR processes and gain insights to ensure finding correct solutions in 3D simulations.
- To find the physics underlying a 3D oil displacement process by foam, comprehend the physical conditions leading to the optimum switching time between surfactant and gas injection cycles in SAG EOR processes, and suggest favorable conditions for maximizing the oil recovery.
- To assess the usefulness and performance of a gradient-based optimization routine in optimizing the switching time to maximize the oil-recovery factor from petroleum reservoirs both in 1D and 3D simulations.

1.7. Outline

This thesis consists of 6 chapters, starting with Chapter 1 as the introduction.

Chapter 2 discusses the mathematics of the MOC applied to three-phase flow. We describe an efficient technique for constructing the saturation paths. Moreover, we explain the procedure for finding the displacement route.

In Chapter 3, the MOC is applied to foam EOR processes in 1D in the presence of mobile oil and we present the analytical solutions for various cases. We examine the sensitivity of the displacement to initial oil and water saturations in the reservoir, foam quality, the functional forms used to express foam sensitivity to oil and water saturations, and linear and nonlinear relative-permeability models. Chapter 3 and a part of Chapter 2 are published in Namdar Zanganeh et al. (2011).

In Chapter 4, the performance of the numerical simulator is validated against the MOC solutions in 1D obtained in Chapter 3. This chapter introduces the three-phase relative-permeability model used in Chapter 5. Next, different options in the simulator for incorporating foam and modeling surfactant transport are introduced and their limitations are discussed. Finally, the performance of the simulator in modeling foam displacement is validated against the available MOC analytical solutions in Chapter 3. The insights gained from this validation help defining the 3D model in Chapter 5 and validating the results to ensure finding correct solutions in 3D simulations.

In Chapter 5, the simulation model is introduced first. Then, the effect of the switching time on the objective function is investigated in three different scenarios in which different injection-well constraints and end-time constraints are applied. It continues with a brief overview on the history and application of optimal control theory in petroleum engineering. After that, three methods of gradient calculation are discussed and the adjoint method that is used in this chapter is explained. The application of the adjoint method for calculating the gradient with respect to switching time is discussed in detail afterwards. Finally, the capability of a gradient-based optimization routine is investigated in finding the switching time that maximizes the cumulative oil production. The performance of the optimization routine is examined for four cases varying in the simulation mode (i.e., 1D or 3D) and the foam model (i.e., linear or nonlinear).

Finally, the main conclusions of the thesis are summarized in Chapter 6.

Chapter 2

Solution Paths in Three-Phase Flow

2.1. Introduction

Riemann (1860) gave an analytical solution to a system of first-order partial-differential equations (Eq. 1) in the context of Euler's equation for gas dynamics. There he also described the fundamentals of the method of characteristics (MOC). Fractional-flow theory for two mobile phases (water/oil) was first developed by Buckley and Leverett (1942). Certain aspects of this theory were extended to multicomponent, two-phase systems by Helfferich (1981) under the name coherence theory (Pope 1980; Lake 1989; Falls and Schulte 1992a, 1992b). Rarefaction-wave theory, also known as coherence theory, is a subset of the MOC; more mathematical details can be found in Helfferich and Klein (1970), Lake (1989), Rhee et al. (2001), Juanes and Patzek (2004b), and Dafermos (2005) for general systems. Marchesin and Plohr (2001) reviewed the recent progress on mathematical theory of immiscible three-phase flow in the appendix of their paper for models with nonlinear relative-permeability functions.

One of the two major principles in the MOC is converting the partial-differential equations (PDEs) into a system of ordinary-differential equations (ODEs). For the special types of initial-boundary data appearing in injection problems, this system of ODEs is then integrated simultaneously to give the smooth solution to the original PDEs. The other principle is the relationship between left and right states of a discontinuity propagating with a fixed speed, discovered independently by two engineers, Rankine and Hugoniot (Smoller 1983).

In this chapter, smooth solutions of the classical three-phase conservation law are reformulated as an eigenvalue problem that has two eigenvalues and is solved by the MOC. In three-phase flow, the larger eigenvalue is the fast characteristic speed (σ^{fast}). The eigenvector corresponding to σ^{fast} points in the direction of fast characteristics. Fast saturation paths are constructed by numerical integration in the direction of the fast eigenvector. The same story holds for the slow characteristic speed (σ^{slow}) that is the smaller eigenvalue. Saturation paths are the only possible directions on the so-called ternary diagram (i.e., saturation space) along which the saturations can vary continuously during the displacement for the injection problem, without contradicting the three-phase mass-conservation law. We describe an efficient technique for constructing these saturation paths. We also describe the procedure for finding the displacement route. A displacement route is the particular path representing a given displacement that passes from the injection to the initial condition. In Chapter 3, this method is applied to three-phase foam EOR processes in one-dimension (1D).

2.2. Assumptions

We make the following assumptions and restrictions, to simplify the description of the three-phase flow process:

- Flow is rectilinear and 1D in a horizontal porous medium, and gravity is neglected.
- Up to three mobile phases are present: oil, water, and gas. We have an immiscible displacement; i.e., each phase is assumed to consist of only its own pseudo-component.
- Properties (e.g., mobilities) are independent of pressure and depend only on phase saturations.
- Fluids are injected at fixed fractional flows[*].
- Flow is isothermal and all phases are incompressible.
- The porous medium is assumed to be homogeneous.
- Dispersive processes (e.g., fingering, capillary diffusion, and dispersion) can be neglected.
- There is instantaneous attainment of local steady-state saturations.
- Mobilities are Newtonian; i.e., they do not depend on total superficial velocity.
- The injection rate of each of the injected fluids (gas/water) is constant; the initial conditions are homogenous in the reservoir.
- For simplicity, adsorption of surfactant on rock is neglected.

Many of these assumptions have been relaxed in the literature.

2.3. Theory

Riemann (1860) gave an analytical solution for a system of first-order partial-differential equations such as the one in Eq. 1, describing the fundamentals of the MOC, in the context of Euler's equation for gas dynamics; see Dafermos (2005) for a modern review. The solution of injection problems for conservation laws consists of a sequence of constant-state regions, rarefaction waves (which become more spread out on propagation), and propagating

---

[*] This implies injecting fluids at a fixed volumetric ratio since phases are incompressible.

discontinuities (either shock waves or indifferent waves).

One of the two essential principles of the MOC is solving the PDEs (i.e., Eq. 1) by converting them into ODEs and then integrating them simultaneously to find the solution.

$$\frac{\partial S_\alpha}{\partial t_D}+\frac{\partial f_\alpha}{\partial x_D}=0 \qquad \alpha=w,o, \tag{1}$$

where S_α and f_α are the saturation and fractional-flow function of phase α (water or oil), respectively[*]. Eq. 1 is the dimensionless representation of the 1D, immiscible, incompressible three-phase-flow equation in porous media in the absence of dispersive processes and gravity.

In rectilinear flow, the dimensionless position is defined as $x_D=x/L$ where L is the length of the medium. The dimensionless time t_D is defined as the total volume of fluid injected until time t divided by the total pore volume (PV) of the medium [see Lake (1989) for more details]. The fractional-flow function f_α in a horizontal system, ignoring the capillary pressure gradient, is defined as the mobility of phase α (i.e., $kk_{r\alpha}/\mu_\alpha$) divided by the summation of the mobilities of all the phases, where k is the rock absolute permeability and $k_{r\alpha}$ and μ_α are, respectively, the relative permeability and viscosity of phase α.

Coherent waves were found in Riemann's work and were given that name by Helfferich and Klein (1970) in the context of flow in porous media [also see Rhee et al. (1971) and Rhee et al. (2001)]. For smooth waves[†], the solution procedure results in a set of saturation paths on the phase diagram that satisfy the PDE in Eq. 1, from which we find the solution by specifying the initial and injection conditions. Saturation paths for rarefaction waves are the same as those in coherence theory; for shock waves, they have different properties.

The rarefaction-wave characteristic speed (σ) is a function of the dependent variables (i.e., S_w, S_o) given by

$$\sigma=\frac{\mathrm{d}x_D}{\mathrm{d}t_D}, \quad \text{where} \quad \begin{pmatrix} f_{ww} & f_{wo} \\ f_{ow} & f_{oo} \end{pmatrix}\begin{pmatrix} \mathrm{d}S_w \\ \mathrm{d}S_o \end{pmatrix}=\sigma\begin{pmatrix} \mathrm{d}S_w \\ \mathrm{d}S_o \end{pmatrix}, \tag{2}$$

where $f_{wo}\equiv\left(\partial f_w/\partial S_o\right)_{S_w}$ and so on.

---

[*] Eq. 1 is the mass-conservation equation and is valid for all three phases. However, the fact that the three phases jointly fill the void space ($S_w + S_o + S_g = 1$) results in eliminating one of the three mass-conservation equations leading to a *complete* system of *two* equations for solving two of the three main unknowns (i.e., S_w, S_o, and S_g). The third unknown (S_g here) is evaluated accordingly.

[†] Smooth means that a certain number of derivatives exist and are continuous. The number of continuous derivatives necessary for a wave to be considered smooth is problem dependent and may vary from one to infinity. In the case of our problem, having two continuous derivatives is sufficient.

The two allowed characteristic velocities are the two eigenvalues of Eq. 2, which are given by

$$\begin{aligned} \sigma^{slow} &= \frac{1}{2}\left[(f_{ww}+f_{oo}) - \sqrt{(f_{ww}-f_{oo})^2 + 4 f_{wo} f_{ow}} \right], \\ \sigma^{fast} &= \frac{1}{2}\left[(f_{ww}+f_{oo}) + \sqrt{(f_{ww}-f_{oo})^2 + 4 f_{wo} f_{ow}} \right], \end{aligned} \tag{3}$$

where, by definition $\sigma^{fast} \geq \sigma^{slow}$ if the roots are real. The eigenvalues in Eq. 3 can be real or complex, depending on the relative-permeability model used and the state at which they are evaluated. Marchesin and Medeiros (1989) and Falls and Schulte (1992a) described a sufficiency condition to ensure real characteristic velocities. Their sufficiency condition states that, if the relative permeability of each phase during three-phase flow is a unique function of only its own saturation, the characteristic velocities are real everywhere in the three-phase flow region. Isaacson et al. (1992) and Guzmán (1995) have examined some common relative-permeability models. If the relative-permeability model is such that the resulting system has everywhere two real, distinct eigenvalues, then it is called strictly hyperbolic. An *umbilic* point is an isolated point where the eigenvalues are real but coincident (equal) which contradicts the assumption of *distinct eigenvalues* of strictly hyperbolic systems. The existence of umbilic points causes our system to be nonstrictly hyperbolic for each of the cases we will consider.

Rarefaction waves are paths along which the characteristic speed is non-decreasing in the downstream direction and must be obtained by integrating Eq. 4 resulting in coherent waves (Courant and Friedrichs 1948; Smoller 1983). Solving for $\mathrm{d}S_w$ and $\mathrm{d}S_o$ in Eq. 2 gives:

$$\left(\frac{\mathrm{d}S_o}{\mathrm{d}S_w}\right)^{slow} = \frac{\sigma^{slow} - f_{ww}}{f_{wo}}, \qquad \text{or equivalently} \qquad \left(\frac{\mathrm{d}S_w}{\mathrm{d}S_o}\right)^{slow} = \frac{\sigma^{slow} - f_{oo}}{f_{ow}}, \tag{4}$$

with similar equations for fast paths. Falls and Schulte (1992a) observed that it is convenient to use the first equation when $|\mathrm{d}S_o/\mathrm{d}S_w| \leq 1$ and switch to the second one when $|\mathrm{d}S_o/\mathrm{d}S_w| > 1$ (this ensures finding the solution whenever either $\mathrm{d}S_w$ or $\mathrm{d}S_o$ is close to zero). The locus of the integral of Eq. 4 corresponding to σ^{slow} and σ^{fast} are called a *slow* and a *fast* rarefaction path, respectively. These derivations and their theoretical background are discussed in more detail elsewhere (Helfferich 1981; Lake 1989; Falls and Schulte 1992a).

At this stage, we can map out the solution of Eq. 4 as saturation paths on the ternary diagram based on Eq. 4 (**Fig. 1**); see Appendix A in Namdar Zanganeh et al. (2009) for this procedure. There is another procedure for mapping out the saturation paths [described e.g., by Courant and Friedrichs (1948) in the context of shocks in gas dynamics and recently by Azevedo et al. (2010) in the context of three-phase flow in porous media], that is more robust than the above mentioned procedure and is explained below in §2.4.2.

The ternary diagram with the saturation paths acts as a map for finding the displacement route (i.e., the particular path that passes from the injection to the initial condition for a given displacement) for any arbitrary pair of injection and initial reservoir conditions for that specific system. The procedure of finding the displacement route is discussed below in §2.5.

2.4. Plotting the Saturation Paths

To map out the saturation paths, we follow two major steps. First, we identify the wave family (i.e., fast or slow) to which the lines defining residual-saturations belong and then, starting from these lines we map out the saturation paths inside the three-phase-flow region of the ternary diagram. Mapping out the saturation paths can be performed in several ways. The method explained here for mapping out the saturation paths follows from that in the Azevedo et al. (2010) and is very efficient. Moreover, its performance is not affected if the path is not monotone with respect to any of the saturations.

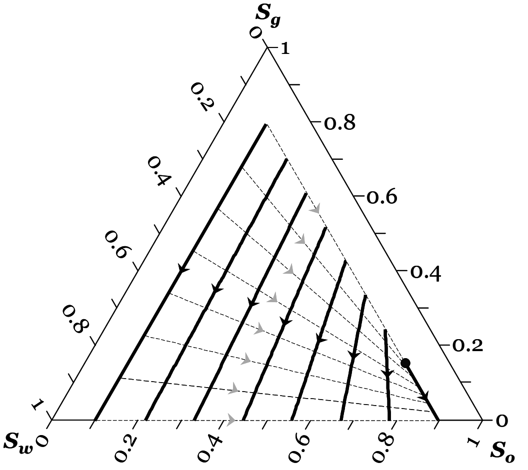

Fig. 1: Ternary diagram for the linear relative-permeability model in Chapter 3 in the absence of foam. The ternary diagram illustrates solutions to Eq. 1 before applying initial and injection conditions. Heavy lines are the fast paths, and thin dashed lines are the slow paths. Arrows are in the direction of increasing σ. The only umbilic point is located along the S_{wr} line and is indicated by a solid black circle.

2.4.1. Identifying the Wave Family (Slow/Fast) of the Residual-Saturations Lines

In all the cases that we study in Chapter 3, the residual-saturation lines are saturation paths. We discover this by verifying if a certain property is valid along them. For the $S_w = S_{wr}$ line to be a saturation path, dS_w/dS_o must be equal to zero for the points along this line (see Eq. 4), since S_w is constant there. For the $S_o = S_{or}$ line to be a saturation path, dS_o/dS_w must be zero because S_o is constant. Lastly, in order for the $S_g = S_{gr}$ line to be a path, dS_o/dS_w and dS_w/dS_o

must be equal to (-1) along the S_{gr} line. We also calculate (dS_o/dS_w) or (dS_w/dS_o) for both σ^{fast} and σ^{slow} from Eq. 4. Based on whether or not the fast or slow solution is in agreement with the above-mentioned criteria, the family to which the residual-saturation line belongs is then determined. In Fig. 1, $(dS_o/dS_w)^{fast} = 0$ on the S_{or} line and $(dS_o/dS_w)^{slow} = -1$ on the S_{gr} line. Thus, the lines at $S_o = S_{or}$ and $S_g = S_{gr}$ are saturation paths and belong to the fast and slow saturation-wave families, respectively. However, the path along $S_w = S_{wr}$ line switches from slow to fast at the umbilic point. The umbilic point is a point at which the eigenvalues are equal ($\sigma^{fast} = \sigma^{slow}$), the eigenvectors coincide, and the path changes from fast to slow (Falls and Schulte 1992a). We show examples with foam in Chapter 3 where an umbilic point may also occur on $S_o = S_{or}$ or on $S_g = S_{gr}$ lines. It is very important to identify and calculate the location of these umbilic points accurately, because they are used in identifying the wave family (slow/fast) to which each segment of the boundary of the three-phase region belongs.

2.4.2. Mapping Out the Saturation Paths Inside the Three-Phase Region

Once the type of the saturation path (fast/slow) on the residual-saturation lines is determined, one can map out the rest of the paths inside the ternary diagram. Imagine that we want to plot the paths originating from $S_o = S_{or}$. Following the criterion[*] that no two slow or fast paths cross one another [for more details see Helfferich and Klein (1970)], all the paths originating from $S_o = S_{or}$ must be slow paths, because the line $S_o = S_{or}$ is a fast path. Accordingly, these slow paths should terminate on a fast path as well to satisfy the above-mentioned criterion. They can terminate on the $S_o = S_{or}$ or the fast-path portion of $S_w = S_{wr}$; however, as the paths in Fig. 1 are straight lines, they should land on the fast-path portion of $S_w = S_{wr}$.

For the MOC applied to injection problems [see Azevedo et al. (2010) for more details], the mass-conservation Eq. 1 is reformulated in terms of the self-similarity variable $\xi = x_D/t_D$, where $\boldsymbol{s} = \boldsymbol{s}(\xi)$, by using the chain rule and multiplying the equation by t_D

$$-\xi\frac{d\boldsymbol{s}}{d\xi}+\mathbf{J}(\boldsymbol{s})\frac{d\boldsymbol{s}}{d\xi}=\mathbf{0} \qquad \text{where} \qquad \mathbf{J}(S):=\frac{\partial f(\boldsymbol{s})}{\partial \boldsymbol{s}}=\begin{pmatrix} f_{ww} & f_{wo} \\ f_{ow} & f_{oo}\end{pmatrix}, \tag{5}$$

where $\boldsymbol{s} = (S_w, S_o)^T$ and $\boldsymbol{f}(\mathbf{s})=(f_w, f_o)^T$ and $\mathbf{J}$ is the 2×2 Jacobian matrix in Eq. 2. If we introduce a 2×2 identity matrix $\mathbf{I}$ into Eq. 5, it can be rewritten as

$$\left(\mathbf{J}(\boldsymbol{s})-\xi\mathbf{I}\right)\boldsymbol{r}(\boldsymbol{s})=\mathbf{0} \qquad \text{where} \qquad \boldsymbol{r}(\boldsymbol{s})=(r_w,r_o)^T=\frac{d\boldsymbol{s}}{d\xi}=\begin{pmatrix} dS_w/d\xi \\ dS_o/d\xi\end{pmatrix}. \tag{6}$$

---

[*] This criterion holds only for strictly hyperbolic systems.

The saturation paths are constructed in three steps:

(1) The eigenvalues (i.e., ξ^{fast} and ξ^{slow}) must be calculated. Thus, the determinant of the term **($\mathbf{J}(\boldsymbol{s})$- $\xi\mathbf{I}$)** in Eq. 6 must be equal to zero.

$$\left|\mathbf{J}(\boldsymbol{s})-\xi\mathbf{I}\right|=\begin{vmatrix} f_{ww}-\xi & f_{wo} \\ f_{ow} & f_{oo}-\xi \end{vmatrix}=\left(f_{ww}-\xi\right)\left(f_{oo}-\xi\right)-f_{wo}f_{ow}=0. \tag{7}$$

Solving this equation returns the expressions for ξ^{fast} and ξ^{slow} in Eq. 3.

(2) The eigenvector (i.e., r_w and r_o) must be computed after substituting either value of ξ determined in step 1 in Eq. 6:

$$\begin{pmatrix} f_{ww}-\xi & f_{wo} \\ f_{ow} & f_{oo}-\xi \end{pmatrix}\begin{pmatrix} \mathrm{d}S_w/\mathrm{d}\xi \\ \mathrm{d}S_o/\mathrm{d}\xi \end{pmatrix}=0, \qquad \text{or equivalently,} \tag{8}$$

$$\begin{cases} \left(f_{ww}-\xi\right)\dfrac{\mathrm{d}S_w}{\mathrm{d}\xi}+f_{wo}\dfrac{\mathrm{d}S_o}{\mathrm{d}\xi}=0, \\ \left(f_{oo}-\xi\right)\dfrac{\mathrm{d}S_o}{\mathrm{d}\xi}+f_{ow}\dfrac{\mathrm{d}S_w}{\mathrm{d}\xi}=0. \end{cases} \tag{9}$$

Here we choose to calculate r_o = dS_o/dξ from the first equation in Eq. 9 for the slow paths:

$$\frac{\mathrm{d}S_o}{\mathrm{d}\xi^{slow}}=\frac{\xi^{slow}-f_{ww}}{f_{wo}}\frac{\mathrm{d}S_w}{\mathrm{d}\xi^{slow}}, \tag{10}$$

with similar equation for the fast paths. The value of r_w = dS_w/dξ^{slow} in Eq. 10 is arbitrary in this formulation. If one reformulates the above and writes r_w in terms of r_o, then the choice of r_o is arbitrary. For Eq. 10, we choose $r_w = f_{wo}$[*]. Thus, we obtain $r_o = (\xi^{slow} - f_{ww})$ from Eq. 10.

(3) The saturation paths are constructed by integrating the following ODE:

$$\frac{\mathrm{d}\boldsymbol{s}}{\mathrm{d}\eta}=\frac{\boldsymbol{r}(\boldsymbol{s})}{\left|\boldsymbol{r}(\boldsymbol{s})\right|}=\frac{\left(f_{wo}\,,\,\xi^{slow}-f_{ww}\right)^{\mathrm{T}}}{\sqrt{f_{wo}^2+\left(\xi^{slow}-f_{ww}\right)^2}}, \tag{11}$$

where $|\boldsymbol{r}(\boldsymbol{s})|$ is the magnitude of $\boldsymbol{r}(\boldsymbol{s})$ and η is an arc length and accepts any arbitrary value.

---

[*] The eigenvector $\boldsymbol{r}(\boldsymbol{s})$ is a vector with two components (i.e., r_w and r_o). Multiplying *both* components by the same nonzero constant results in another vector that is also an eigenvector. If the constant is negative, it points to the opposite direction, but, as an eigenvector, it is equivalent to the original one. In addition, the formula for the eigenvector is not unique, but all formulae are equivalent. Therefore, the choice of r_w in Eq. 10 is arbitrary. In Eq. 10, for convenience we choose r_w as the denominator of the $(\xi^{slow} - f_{ww})/f_{wo}$ ratio to avoid division to zero if f_{wo} becomes zero. Moreover, the two components of an eigenvector are not important in our approach, but the slope of the eigenvector is important (i.e., dS_o/dS_w or dS_w/dS_o).

Equivalently, Eq. 11 can be written as

$$\frac{\mathrm{d}S_w}{\mathrm{d}\eta}=\frac{f_{wo}}{\sqrt{f_{wo}^2+\left(\xi^{slow}-f_{ww}\right)^2}} \quad \text{and} \quad \frac{\mathrm{d}S_o}{\mathrm{d}\eta}=\frac{\xi^{slow}-f_{ww}}{\sqrt{f_{wo}^2+\left(\xi^{slow}-f_{ww}\right)^2}}. \tag{12}$$

Solving this equation provides the vector $\boldsymbol{s} = (S_w, S_o)$ and constructs the entire saturation path or part of it, based on the range of η that we choose. In fact, η defines the range in which Eq. 12 is solved. As a result, the length of the saturation path obtained from Eq. 12 is proportional to the range defined for η. In our calculations, we never needed to choose η larger than one. (It is important to emphasize that only the *length* of η is important, i.e., there is no difference between [0, 1] and [200, 201] for instance.) Starting from the initial point, if we choose η = [0, 1], the path is plotted in one direction and if we choose η = [1, 0], the path is plotted in the direction opposite to the previous one. This is important to note, because for instance if we start from the residual-saturation lines, the path is plotted only if it points towards the inside of the ternary diagram. If we choose a wrong direction, the path will point to direction outside the ternary diagram and is not plotted because it is unphysical. If we shrink the range, only part of the path is plotted, so we should integrate between [0,1]. By enlarging the range we can ensure that the entire saturation path is plotted in one go. We can choose the initial point to start the path from any point inside the ternary diagram or on the sides (residual-saturation lines).

It is possible to solve Eq. 12 by one of the available ODE solvers in MATLAB. The ode45 routine (Runge-Kutta method) is the first choice but does not always find the correct solution. In this case, it is recommended to use ode15s (Gear's method). To improve the performance of these methods, one can also provide the following Jacobian matrix analytically into the routine (we were able to find the solution with the ode15s without providing this matrix):

$$\begin{pmatrix} \partial A_w/\partial S_w & \partial A_w/\partial S_o \\ \partial A_o/\partial S_w & \partial A_o/\partial S_o \end{pmatrix}, \tag{13}$$

where A_w and A_o are the right-hand sides of the differential equations in Eq. 12, respectively. In the above formulations, we chose the first ODE in Eq. 9 to find the eigenvectors. However, sometimes integrating Eq. 12 with those eigenvectors does not result in finding the $\boldsymbol{s}$. In that case, we have to switch to the second ODE and repeat the procedure.

In some cases, if there is a region with complex eigenvalues in the course of the saturation path, the ODE solver stops once it reaches this region. In this case, we need to make the range of η shorter such that the path ends before entering this region.

To assure that the path is correctly calculated, the eigenvector at the next calculated point [i.e., $\boldsymbol{r}_{n+1}(\boldsymbol{s})$] must be in the same direction as the eigenvector of the previous calculated point [i.e., $\boldsymbol{r}_n(\boldsymbol{s})$] along the saturation path. In other words, $(r_w,r_o)_n \cdot (r_w,r_o)_{n+1} > 0$, where "·" is the inner vector product. Every time that this condition is violated, the entire $\boldsymbol{r}(\boldsymbol{s})$ vector must be multiplied by (-1).

If one uses MATLAB for the calculations, it is important to note that this software is prone to finding complex saturations due to round-off errors. In other words, zeroes are sometimes represented by extremely small values[*]. If these values are negative and are raised to a power smaller than one or a non-integer power, they may result in complex saturations and the procedure fails. Therefore, it is necessary to make use of the procedure in the footnote to avoid complex saturations.

2.5. Finding the Displacement Route

Once the saturation paths are mapped out on the ternary diagram by numerically integrating either of Eq. 4 or Eq. 12 (e.g., through using one of the MATLAB ODE solvers), we specify the direction of increasing σ (characteristic speed given by Eq. 3) on every path by arrows (see Fig. 1). At this stage, the ternary diagram with the saturation paths acts as a map for finding the displacement route (i.e., the particular path that passes from the injection to the initial condition) for any arbitrary pair of injection and initial reservoir condition for that specific system. We state the admissibility conditions for the displacement route in §2.5.1, and in §2.5.2 we discuss the procedure that we applied for finding them.

2.5.1. Admissibility Conditions for the Displacement Route

The fundamental waves encountered in this work include rarefaction waves and shock waves. For the displacement route to be admissible, it is required that characteristic velocities along the rarefaction waves and shock velocities be non-decreasing in the downstream direction [i.e., from the injection condition (J) to the initial condition (I)].

In order for a shock to be admissible, it must satisfy two conditions: (1) the *Rankine-Hugoniot jump condition* and (2) the *Lax condition*:

---

[*] This problem in our case raises from the way of representing S_g in terms of S_w and S_o. (In our formulations, S_w and S_o are the primary variables.) If one puts S_g equal to $(1 - S_w - S_o)$, then for instance for $S_w = 0.8$ and $S_o = 0.2$, this expression returns a negative nonzero value for S_g (i.e., -5.55e-017). However, if one substitutes S_g by $(-S_w - S_o + 1)$ this expression returns zero.

(1) Any discontinuity in a system governed by Eq. 1 must satisfy the *Rankine-Hugoniot jump condition* (Riemann 1860; Courant and Friedrichs 1948), which is the representation of conservation of mass for propagating discontinuities:

$$\begin{cases} v_{shock}\left(S_w^u - S_w^d\right) = f_w^u - f_w^d \\ v_{shock}\left(S_o^u - S_o^d\right) = f_o^u - f_o^d \end{cases}, \tag{14}$$

where v_{shock} is the shock velocity and superscripts u and d indicate the upstream and downstream sides of the shock, respectively. For a fixed upstream state, Eq. 14 determines a curve of downstream states for possible shocks.

(2) A genuine shock must also satisfy the *Lax condition* (Lax 1957). For a single scalar equation (such as Buckley-Leverett for oil-water flow without gas), the Lax condition requires that the characteristic lines impinge on the shock; i.e., $\sigma_d < v_{shock} < \sigma_u$, where $\sigma = (\mathrm{d}f_\alpha/\mathrm{d}S_\alpha)$. For systems of two equations, the following criteria must hold for a slow and a fast Lax shock, respectively (They are inspired in isothermal gas dynamics and must be true for many systems of two conservation laws.):

$$\text{Slow:}\begin{cases} \sigma_d^{slow} < v_{shock}^{slow} < \sigma_u^{slow} \\ \sigma_u^{fast} > v_{shock}^{slow};\, v_{shock}^{slow} < \sigma_d^{fast} \end{cases}, \qquad \text{Fast:}\begin{cases} \sigma_d^{fast} < v_{shock}^{fast} < \sigma_u^{fast} \\ \sigma_u^{slow} < v_{shock}^{fast};\, v_{shock}^{fast} > \sigma_d^{slow} \end{cases}, \tag{15}$$

where σ_d^{slow} is the slow characteristic speed of the point just downstream of the shock, and so on. Other discontinuities are not allowed by Lax in systems of two equations. Nevertheless, limits of Lax shocks, when one of the inequalities become an equality, occur in multiphase flow, even in the Buckley-Leverett case. By allowing Lax limits, *wave groups* form. In our examples, each wave group is a consecutive sequence of a rarefaction wave and a shock wave or vice versa (wave groups consist of many shocks and rarefaction waves, in general). Consecutive waves in wave groups are not separated by a region of constant state in physical space. The displacement routes in this work consist of two or three wave groups (see Fig. A-1 for various combinations of wave groups encountered in Chapter 3), but this is not a general result for non-strictly hyperbolic models; see Schecter et al. (1996) for a complete discussion of all possible types of wave groups in non-strictly hyperbolic models.

2.5.2. Procedure of Finding the Displacement Route

As mentioned in §2.5.1, we must take a sequence of wave groups in increasing velocity from *J* to *I* (Isaacson et al. 1992). Thus, it is not possible to switch from a fast path to a slow path meeting at a point in the course of moving from *J* to *I* (because $\sigma^{fast} > \sigma^{slow}$ at any point).

In general when there are two wave groups consisting solely of rarefaction waves (i.e., in the absence of shocks), a displacement route starts from the injection condition along a slow path. Then, it changes at some point (*IJ*) to a fast path starting from this point and then follows this path to the initial condition (e.g., see Fig. 1a and Fig. 6a in Chapter 3). *IJ* is a constant-state region because the slow and fast characteristic velocities on both sides of *IJ* are different and the formation of constant-state regions is inevitable in this case. If *J* and *I* lie on a single slow or fast path, the other path is unnecessary. The displacement route in these two cases can be easily found by looking at the ternary diagram. Fig. 1a in Chapter 3 is an example of this case: A slow path is followed by a fast path from *J* to *I*, on which characteristic velocities are non-decreasing in the downstream direction. Therefore, these two rarefaction waves construct the displacement route with a constant-state *IJ* in between.

Unless characteristic velocities are non-decreasing from *J* to *I*, there *must* be shocks from one point to another in the saturation space, otherwise the problem has no solution. We encountered the following situations in Chapter 3[*]:

(1) The slow path from *J* intersects a fast path from *I*, but the characteristic velocities are *not* increasing along the *entire* path from *J* to *I*. Two situations happen in this case:

(1a) The shock is to a path originating from *J* or *I* (e.g., see Figs. 3a, 6b, and 7).

(1b) The shock is to a path *not* originating from *J* or *I* (e.g., see Figs. 3b and 4b).

(2) The slow path from *J* *does not* intersect a fast path from *I* (e.g., see Figs. 4a and 8).

In situation (1a), it is relatively easy to find the displacement route. For instance in Fig. 7, σ is not increasing along only the first portion of the slow path. Therefore, there is a shock from *J* to a point with increasing σ along the remainder of the path. Thus, *J* is the upstream state of the shock and we require to find the downstream state[†]. For this purpose, we check the validity of the Rankine-Hugoniot jump condition (Eq. 14) along the portion of the path from *J* to *I* with increasing σ. Equalities in Eq. 14 must hold for the upstream and downstream states of a shock. In other words, we set the properties (S_α and f_α) along this part as the *possible* downstream state of the shock: the *acceptable* downstream state is the one at which $\left(f_\alpha^u - f_\alpha^d\right)/\left(S_\alpha^u - S_\alpha^d\right)$ ratio is equal for all the phases[‡] and the value of this ratio at the *acceptable* downstream state [i.e., (0.35, 0.43, 0.22) in Fig. 7] gives the shock velocity (υ_{shock}).

---

[*] The figures referred to in this section belong to Chapter 3.

[†] In case of Fig. 6b, *I* is the downstream state of the shock that is known and we require to find the upstream state. This is also the case for the second shocks in Figs. 4a and 8 from *J* to *I* (situation 2).

[‡] If one of the phase saturations is invariant along the shock, then the $\left(f_\alpha^u - f_\alpha^d\right)/\left(S_\alpha^u - S_\alpha^d\right)$ ratio corresponding to that phase is not defined and the ratios must be identical for the other two phases (e.g., S_w is constant along the shock in Fig. 3a). If this is not the case, then it suffices to check the intersection of two curves and the third curve will intersect at the same point (the sum of the three saturations and the sum of the three fractional-flow functions are equal to unity).

If the Rankine-Hugoniot jump condition does not hold anywhere along the path, then situation (1b) might be the case. Further, we examine the Lax condition in Eq. 15: for this shock, the limit of the slow Lax shock is satisfied (i.e., $\sigma_d^{slow} = \upsilon_{shock}$) and the shock velocity is identical to the characteristic speed of the rarefaction wave downstream of the shock.

In situations (1b) and (2), the solution is more complex and is hard to find using the procedure discussed in situation (1a). In such circumstances, we used a fine-grid numerical simulator to help in finding the solution. The numerical simulation provided us with the following information: type of the fundamental waves in the displacement route (i.e., rarefaction wave or shock wave), sequence of the waves, and an approximate location(s) of the constant-state region(s). The admissibility of the shock(s) was then verified by checking the Rankine-Hugoniot jump condition (Eq. 14) and the Lax condition (Eq. 15).

2.5.3. The Wave-Curve Method

We applied the procedure discussed in §2.5.2 in Chapter 3 for finding the displacement route. However, there is an alternative procedure called the *wave-curve method* developed by Lax (1973) and Liu (1974). Prior to that, it was outlined briefly by Courant and Friedrichs (1948) in the context of shocks in gas dynamics. In this method, the displacement route (which is a sequence of rarefaction waves, shock waves, and constant-state regions) is constructed by following a sequence of curves in the saturation space. This method is capable of finding the displacement route even in the presence of shock waves in which the route is constructed in an essentially analytic approach. In the context of petroleum engineering, Marchesin and Plohr (2001) applied this method to water-alternating-gas (WAG) recovery. They also provided a review of the mathematical, as well as engineering, literature regarding the wave-curve method. Azevedo et al. (2010) briefly discussed this method and applied it to solve a certain class of injection problems (co-injecting a mixture of water and gas) for immiscible three-phase flow.

Chapter 3

The Method of Characteristics Applied to Oil Displacement by Foam

Abstract[*]

Solutions obtained by the method of characteristics (MOC) provide key insights into complex foam enhanced-oil-recovery (EOR) displacements and the simulators that represent them. Most applications of the MOC to foam have excluded oil. We extend the MOC to foam flow with oil, where foam is weakened or destroyed by oil saturations above a critical oil saturation and/or weakened or destroyed at low water saturations, as seen in experiments and represented in foam simulators. Simulators account for the effects of oil and capillary pressure on foam using algorithms that bring foam strength to zero as a function of oil or water saturation, respectively. Different simulators use different algorithms to accomplish this.

We examine SAG (surfactant-alternating-gas) and continuous foam-flood (coinjection of gas and surfactant solution) processes in one dimension (1D), using both the MOC and numerical simulation. We find that the way simulators express the negative effect of oil or water saturation on foam can have a large effect on the calculated nature of the displacement. For instance, for gas injection in a SAG process, if foam collapses at the injection point because of very high capillary pressure, foam has almost no effect on the displacement in the cases examined in this chapter. On the other hand, if foam maintains finite strength at the injection point in the gas-injection cycle of a SAG process, displacement leads to success in several cases. However, successful mobility control is always possible with continuous foam flood if the initial oil saturation in the reservoir is below the critical oil saturation above which foam collapses.

---

[*] Published in SPE Journal (M. Namdar Zanganeh et al. 2011).

The resulting displacements can be complex. One may observe, for instance, foam propagation predicted at residual water saturation, with zero flow of water. In other cases, the displacement jumps in a shock past the entire range of conditions in which foam forms. We examine the sensitivity of the displacement to initial oil and water saturations in the reservoir, foam quality, the functional forms used to express foam sensitivity to oil and water saturations, and linear and nonlinear relative-permeability models.

3.1. Introduction

Foam is a means of improving sweep efficiency in gas and surfactant EOR (Schramm 1994; Rossen 1996; Li et al. 2008). Foam also is used routinely for improving the acid-injection profile in well-stimulation treatments (Gdanski 1993; Zhou and Rossen 1994) and on a pilot basis to improve the sweep of surfactant solutions in aquifer remediation (Hirasaki et al. 2000).

MOC solutions have proved useful in highlighting key mechanisms and strategies for improving foam performance (Zhou and Rossen 1994, 1995; Rossen et al. 1999; Shan and Rossen 2004; Mayberry et al. 2008) and in better understanding foam simulation models (Rossen et al. 1999; Dong and Rossen 2007). It must be noted, however, that because of its simplifying assumptions, the MOC cannot be used in complex real-world applications where many of its assumptions are violated. Its usefulness is in the insights it offers, not as a quantitative, predictive tool for real reservoirs.

Previous application of the MOC to foam has been mostly limited to two-phase flow; oil, if present, has been assumed to be immobile at its residual saturation. Mayberry et al. (2008) applied the three-phase MOC to foam, where foam strength does not depend on oil or water saturation and gas is completely immiscible with water and oil. They examined three cases, in which foam reduces gas mobility greatly, moderately, and not at all; the reduction in initial oil saturation to its residual saturation is much more rapid when gas mobility is reduced greatly by foam. Rosman and Kam (2009) extended this model to layered formations. Ashoori et al. (2010) examined first-contact-miscible gas floods with foam, where there is only one non-aqueous phase present at any location.

The ability of foam to reduce gas mobility is affected both by the presence of many crude oils and by water saturation. The effect of crude oils on foam is complex and only partially understood (Law et al. 1992; Schramm 1994; Hatziavramidis et al. 1995; Rossen 1996; Svorstøl et al. 1996; Mannhardt and Svorstøl 1999). Experimental evidence shows that apparent foam viscosity is strongly reduced at oil saturations greater than some critical saturation, below which foam is weakened proportionately to oil saturation (Law et al. 1992;

Svorstøl et al. 1996; Mannhardt and Svorstøl 1999). Moreover, foam dries out and at least partially collapses abruptly at a water saturation corresponding to the *limiting capillary pressure* (Khatib et al. 1988; Zhou and Rossen 1995). The foam model we use partially follows that in the STARS™ simulator of the Computer Modeling Group (Shrivastava et al. 1999; Vassenden et al. 1999; Cheng et al. 2000; Computer Modeling Group 1998, 2009).

In this chapter, we investigate the sensitivity of three-phase 1D displacements to initial phase saturations in the reservoir and the foam quality (i.e., fraction of gas in the injected fluid). We test two injection schemes and several functional forms used to express the effect of low water saturation and high oil saturation on foam. We also examine the effect of linear and nonlinear relative-permeability models.

3.2. Relative-Permeability Model

Most relative-permeability models give rise to elliptic regions (Bell et al. 1986). A short review on loss of hyperbolicity (appearance of elliptic regions and umbilic points) in three-phase flow models is given in Marchesin and Plohr (2001). We examine a linear and a nonlinear relative-permeability model (in the absence of foam) that does not suffer from this problem, even after incorporating our foam model.

3.2.1. Linear Model

We applied a linear Corey-type relative-permeability model (Lake 1989) for the MOC analysis in this chapter:

$$k_{r\alpha} = K_{r\alpha} \frac{S_\alpha - S_{\alpha r}}{1 - S_{wr} - S_{or} - S_{gr}} \qquad \alpha = w, o, g, \tag{1}$$

where $S_{\alpha r}$ is the residual saturation and $K_{r\alpha}$ is the end-point relative permeability of phase α. See Table B-1 for parameters used in Eq. 1. Although this model is not a realistic one (Lake 1989), it obeys the sufficiency condition of Falls and Schulte (1992a) and does not produce any elliptic regions. **Fig. 1a** illustrates the saturation paths for this relative-permeability model in the absence of foam. This model is strictly hyperbolic inside the ternary diagram and has a single umbilic point along the residual-water-saturation line. Moreover, it has the advantage of having saturation paths that are easy to describe and use in the absence of foam, just straight lines. Thus, it makes it easier to see the effect of foam on saturation paths. This model is the basis of the three-phase foam MOC modeling of Mayberry et al. 2008. In all the models in this chapter, we looked for the elliptic regions and umbilic points both analytically and numerically, and we found umbilic points only along residual-saturation lines.

3.2.2. Nonlinear Model

We implemented the relative-permeability model proposed by Juanes and Patzek (2004a, 2004b). This model is strictly hyperbolic everywhere inside the ternary diagram and presents a single umbilic point at the corner of 100% gas saturation. This model assumes that the water and gas relative permeabilities each depends only on its own saturation, whereas the oil relative permeability depends on all saturations. The residual saturations in this model are taken equal to zero:

$$k_{rw} = S_w^2, \qquad k_{ro} = S_o(1-S_w)(1-S_g), \qquad k_{rg} = 0.1S_g + 0.9S_g^2. \tag{2}$$

3.3. Foam Model

Foam is not a phase but a phenomenon that greatly alters the gas mobility, depending on water and oil saturations and other factors. In the absence of foam, we assume water, oil, and gas viscosities are 1, 5, and 0.02 cp, respectively. The presence of foam reduces gas-phase mobility dramatically (Bernard and Holm 1964; Huh and Handy 1989). In reality, the relative permeability and viscosity effects of foam are inextricable, and only mobility is directly observable in an experiment (Rossen 1992). It is computationally equivalent to alter gas mobility for foam by modifying gas viscosity or gas relative permeability or both (Shan and Rossen 2004). In the foam models applied here, the gas relative-permeability function alone is altered to account for all effects of foam on gas mobility. The water relative-permeability function (k_{rw}) is assumed to remain unaltered in the presence of foam (Bernard and Jacobs 1965; Huh and Handy 1989; Vassenden and Holt 2000). We likewise assume that the oil relative-permeability function (k_{ro}) remains unchanged in the presence of foam.

Our models are partially based on the foam model of the STARS™ simulator (Surguchev et al. 1995; Vassenden et al. 1999; Martinsen and Vassenden 1999; Cheng et al. 2000; Chalbaud et al. 2002; Renkema and Rossen 2007; Computer Modeling Group 1998, 2009). Gas relative permeability in the absence of foam (k_{rg}^{nf}) is rescaled to gas relative permeability in the presence of foam (k_{rg}^{f}) by multiplying k_{rg}^{nf} by a dimensionless interpolation factor (f_{mr})*:

$$k_{rg}^{f} = k_{rg}^{nf} \times f_{mr}, \qquad \text{where} \quad f_{mr} = \frac{1}{1 + fmmob \times F_w \times F_o \times \ldots}, \tag{3}$$

where *fmmob* corresponds to the normalized resistance to flow of a foam of minimum-size bubbles, in the absence of factors increasing bubble size (Surguchev et al. 1995) and F_w and F_o

---

* f_{mr} is referred to as MRF or FM elsewhere.

are the functions describing the stability of lamellae in the presence of water and oil, respectively. The complications caused by the implementation of the foam model on the ternary diagram are discussed in Appendix C. If the stability of lamellae is not reduced under any circumstances, gas mobility is reduced by the greatest possible factor, (1+*fmmob*). We call this full-strength foam. f_{mr} also accounts for the effects of surfactant concentration, oil composition, capillary number (flow rate), and effect of salt on foam mobility (Computer Modeling Group 2009), in ways that are not addressed here.

3.3.1. Effect of Low Water Saturation on Foam

Foam dries out and collapses in the absence of enough water, specifically at the limiting capillary pressure (P_c^*). Khatib et al. (1988) conducted multiphase-flow experiments in beadpacks and found an abrupt transition from strong foam to much weaker foam at P_c^*; this value of capillary pressure corresponds to a limiting water saturation (S_w^*). They also found that P_c^* varies with oil saturation, superficial velocity, and absolute permeability. A large body of evidence supports lamella rupture near the limiting capillary pressure (Jiménez and Radke 1989; Aronson et al. 1994; Rossen et al. 1995). However, it is not yet clear whether foam collapses completely at S_w^* (Shan and Rossen 2004); relevant data are few (Kibodeaux and Rossen 1997; Wassmuth et al. 2001; Xu and Rossen 2004). Therefore, we applied three different models for F_w to represent the weakening and killing effect of low water saturations on oil recovery. These functions are discussed in Appendix C.

3.3.2. Effect of High Oil Saturation on Foam

The presence of oil has a significant effect on the formation and breakdown of foam. The interactions between oil phase and foam lamellae are extremely complex (Nikolov et al. 1986). Koczo et al. (1992) performed an extended experimental study and showed that solubilized oil destabilizes foam. Foam destabilization may often involve the migration of emulsified oil droplets from the foam film lamellae into the Plateau borders (Nikolov et al. 1986). Schramm and Novosad (1992) found that more-viscous oils would be expected to emulsify more slowly than the others, and this would be expected to retard the rate of foam-lamella breakage. They found that foam was less stable in the presence of lighter crude oils.

Law et al. (1992) stated that, in general, foam degrades as oil saturation increases. They also stated that, if S_o were above a so-called critical foaming saturation (S_o^*), foam would collapse. Mannhardt and Svorstøl (1999) referred to this saturation as the critical oil saturation (S_o^*). Svorstøl et al. (1996) and Mannhardt and Svorstøl (1999) have shown that apparent foam viscosity is strongly reduced at high S_o at Snorre reservoir conditions. However, foam was still present for oil saturations above the critical oil saturation in their experiments (see Appendix

C for more details). As a result, we use two different sensitivity functions for F_o to investigate how these two types of behavior (killing and weakening) would influence the oil recovery in a foam-flood process. We discuss these functions and their parameters in Appendix C.

3.4. Results and Discussion for Linear Relative-Permeability Model

We examine the sensitivity of the displacement to the initial reservoir condition, the foam quality, and the functional forms used to express the sensitivity of foam to oil and water saturations. In all our examples where foam is sensitive to low water saturations, foam weakens slightly below and greatly above $S_w^* = 0.316$ or breaks at water saturations less than or equal to $S_w^* = 0.316$. In the examples where foam is sensitive to oil, foam weakens or breaks at oil saturations of $S_o^* = 0.2$ or larger. In all the examples, $S_g(I) = 0$. We examine two different initial conditions (I):

- $S_o(I) < S_o^*$ and $S_w(I) > S_w^*$, specifically $(S_w, S_o)_I = (0.83, 0.17)$, where foam at I is relatively unaffected by S_w and S_o.
- $S_o(I) > S_o^*$ and $S_w(I) < S_w^*$, specifically $(S_w, S_o)_I = (0.27, 0.73)$, where foam at I is affected by both S_w and S_o.

We select these two specific initial conditions as typical samples from the two important zones on the ternary diagram [i.e., $S_o(I) < S_o^*$ and $S_w(I) < S_w^*$]. Displacement routes for other initial conditions are similar to the routes of one of these two initial conditions.

We investigate two different injection conditions (J): the gas-injection cycle ($f_g = 1$) of a SAG flood (hereafter referred to as *gas-injection cycle of SAG* or *gas/SAG*) and coinjection of surfactant solution and gas ($f_g \approx 2/3$, $f_w \approx 1/3$), hereafter referred to as *foam flood.* The significance of studying the gas-injection cycle of SAG is that, if gas mobility is not reduced during gas injection, the entire SAG process is likely to fail; gas may disappear to the override zone, for instance, before the next liquid slug is introduced. In both cases, we assume that enough surfactant is injected to the reservoir before gas or foam injection, such that surfactant stays ahead of the gas front. In other words, surfactant propagation does not limit the rate of foam advance. If it does, there is a jump at the surfactant front to another three-phase diagram with saturation paths reflecting flow without foam (Zeilinger 1996). This jump is governed by material balances on surfactant, water, and oil. We wish to avoid that complication here.

We analyze the effect of applying different functions F_w and F_o (see Eq. 3 and Appendix C) to represent the effects of water and oil saturation, respectively, on foam. We categorize our results on the basis of the nature of the functions F_w and F_o.

In some complex cases where the displacement route cannot be determined easily from the saturation paths, numerical simulations suggest where to search for shocks that satisfy Eqs. 14 and 15 in Chapter 2. The 1D simulator used here is quite similar to that used in the simulations in Kam et al. (2007) and Kam (2008) except for the substitution of the local-steady-state foam models in Appendix C to replace a population-balance calculation in the mechanistic foam simulation. The simulator is fully implicit in time and uses upstream weighting in space. All simulations are conducted with 200 gridblocks. However, in some cases, numerical simulations have difficulty finding the correct solution (i.e., cases where only the MOC gave a reliable solution) (see Fig. C-5). In some instances, we refer to the *displacement route* by the *solution* of a given case.

We establish three base-case scenarios as a basis of comparison. (See Table B-1 for model parameters.) To do so, we require a criterion to distinguish a successful foam EOR process. Mobility control is the primary goal of a foam process. A successful foam process, therefore, is a process that can reduce the gas mobility efficiently. In our model, however, mobility control in the process as a whole, and especially in the foam bank, is reflected in the time to produce all mobile oil (oil in excess of residual saturation), which we call final recovery time ($t_{D,final}$). Processes without effective mobility control for the gas take long times to reduce oil to residual saturation. We take $t_{D,final}$ for the waterflood as one basis of comparison. We encountered some foam processes with $t_{D,final}$ shorter than waterflood that are paradoxically less efficient than waterflood during the first pore-volume injection (PVI), however. Therefore, we report both $t_{D,final}$ and RF_{1PVI} (fraction of mobile oil recovered after 1 PVI) in tables. RF_{1PVI} values are given as a percentage next to $t_{D,final}$ values, and successful cases (relative to waterflood) are shown in boldface. Our model of completely immiscible phases does not represent the additional advantages of gas in terms of miscibility and reduction in residual oil saturation.

In Figs. 1 through 6, fast and slow paths are shown as solid, heavy, black lines and thin, black, dashed lines, respectively. The rarefaction segment of the displacement route is depicted as a thick, light gray line, and the shock is shown by a thick, light gray dashed line. Constant-state regions are called *IJ* and are denoted by light-gray-filled circles along the displacement route. Arrows along saturation paths are in the direction of increasing σ. This direction may reverse along a given path once or several times. These points of reversal are called *inflection* points and are marked with small circles along the saturation paths: small solid and unfilled circles along fast and slow paths, respectively. Umbilic points are marked by solid circles along the residual-saturation lines. All the figures are produced with the linear relative-permeability model, and the weakening effect of water is represented by Eq. C-1.

3.4.1. Base-Case Scenarios

Our base-case scenarios are as follows (see Table B-1 for model parameters):

- Waterflooding with no gas present.
- Gas-injection cycle of WAG and continuous coinjection of gas and water, both in the absence of foam.
- Gas-injection cycle of SAG and continuous coinjection of gas and surfactant, both in the ideal case of full-strength foam.

We solved the two-phase (water/oil) Buckley-Leverett displacement in order to evaluate the waterflood performance. We use this case as the basis with which we compare the results of the foam processes because the rate of oil recovery is a reflection of the mobility of the displacing banks. A successful foam process in this context is a process that can reduce gas mobility efficiently and perform better than waterflood. Although the values of $t_{D,final}$ are similar for the two waterflood cases (see **Table 1**), oil is produced more rapidly at the start for the case with higher $S_o(I)$. Water mobility is lower at higher initial oil saturations (if $k_{r\alpha}$ is a monotonically increasing function of S_α), and, hence, the initial rate of oil recovery is greater with the greater value of $S_o(I)$ (Lake 1989). For instance, the case with higher $S_o(I)$ reaches 50% recovery almost 2.5 times faster than the case with lower $S_o(I)$. It is 1.7 times faster to reach 80% recovery.

Injecting only gas into the reservoir in the absence of foam (reflecting the gas-injection cycle of WAG; **Fig. 1a**), results in early gas breakthrough because of very high gas mobility. The performance of such a displacement for $S_o(I) = 0.73$ is shown in Fig. 1b. This figure shows that gas almost immediately (right side of the figure shows early stage) breaks through at the outlet ($x_D = 1$); the displacing bank has high mobility, and, as a result, it takes 200 PVI (see Table 1) until all the recoverable oil is produced. Only 9.8% of the oil is recovered after 1 PVI, and another 40% is recovered after 28 PVI. The presence of very-slow-moving rarefaction waves in the solution is the reason for such a poor performance of the displacement.

Continuous coinjection of water and gas in the absence of foam with $f_w = 1/3$ improves this situation by reducing the gas fractional flow at the outlet. As a result, oil is recovered almost 17 times faster compared to the earlier gas-injection case. However, this case is still less efficient than waterflooding. Increasing the water fraction in the injection stream improves the final recovery time; the best performance has zero injected-gas fraction ($f_w = 1$). Table 1 indicates that, in this case and in the gas-injection case, final recovery times depend only on the injection condition and are independent of the initial condition. We discuss the reason later.

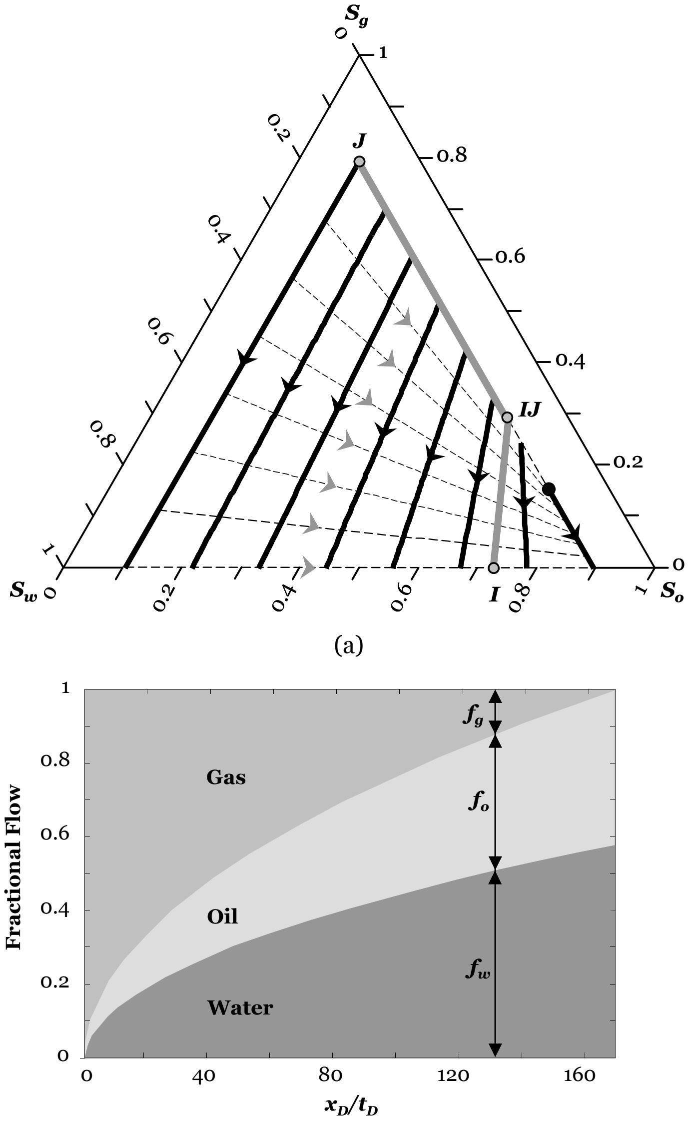

(a)

(b)

Fig. 1: Results for gas-injection cycle of WAG in the absence of foam in a reservoir initially at (S_w, S_o, S_g) = (0.27, 0.73, 0). (a) Ternary diagram and displacement route. Heavy black lines are the fast paths, and thin dashed black lines are the slow paths. Arrows along the paths are in the direction of increasing σ. The thick, light-gray lines are rarefaction waves. The only umbilic point is located along the S_{wr} line and is indicated by a solid black circle. (b) Fractional flows plotted against the self-similarity variable x_D/t_D. On the horizontal axis, time moves leftward. Gas breaks through at the outlet (x_D = 1) at about 0.006-PV injection ($x_D/t_D \approx 168$), and gas fractional flow increases rapidly. Oil fractional flow at the outlet is initially 0.42 and decreases with time.

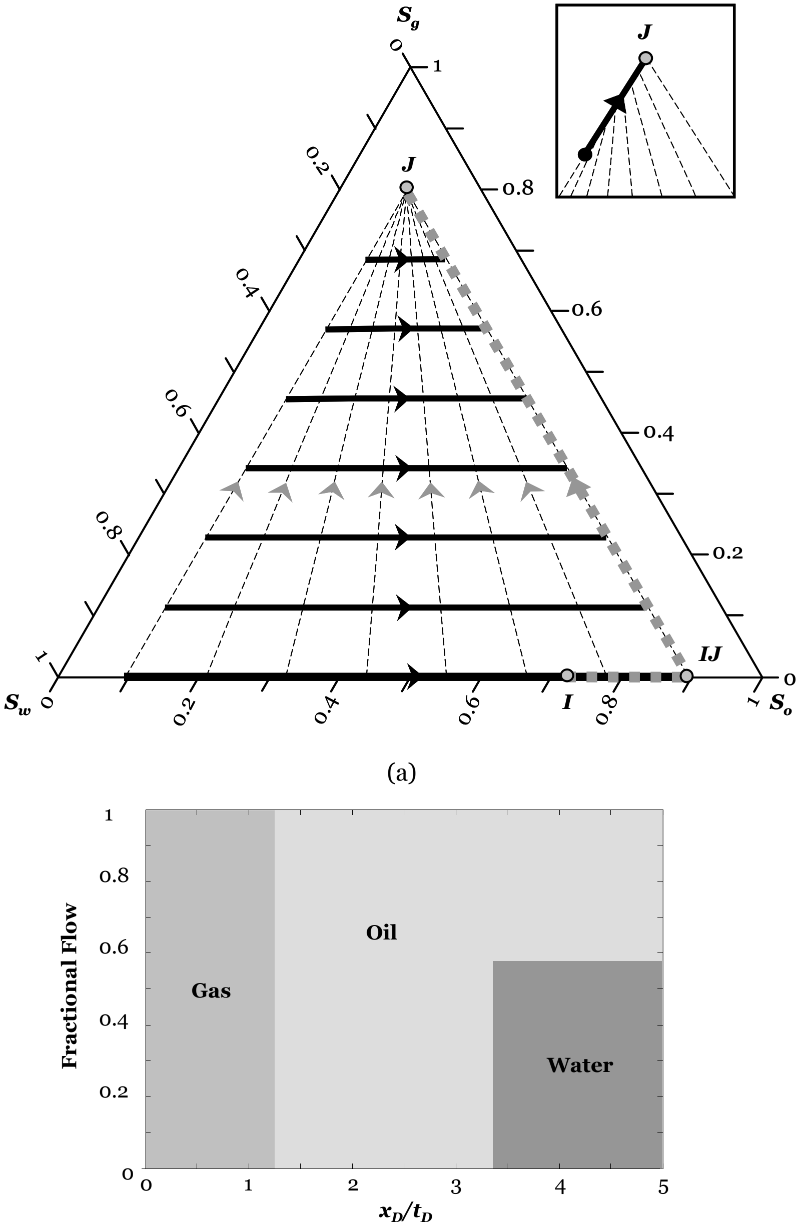

(a)

(b)

Fig. 2: Results for gas-injection cycle of SAG with full-strength foam present everywhere in the reservoir, with *I* at (S_w, S_o) = (0.27, 0.73). (a) Ternary diagram and displacement route. The thick, light-gray dashed lines are shock waves. The inset shows the small segment of the fast path along the S_{or} line close to *J*. (b) Fractional flow plotted against the self-similarity variable x_D/t_D. As in Fig. 1b, time increases to the left.

In the ideal case of full-strength foam (**Fig. 2a**), gas mobility is reduced everywhere to the greatest extent possible (i.e., by a factor of 55,001). Therefore, the best performance of foam is achieved in this case. Fig. 2b shows that, in the gas-injection cycle of SAG, no gas reaches the outlet until all the recoverable oil is produced, after only 0.8 PVI (x_D/t_D = 1.25). The improved displacement efficiency in this case reflects the occurrence of the constant-state *IJ* with both water and gas at their residual saturations (Fig. 2a), leading to the formation of an oil bank ahead of the gas front.

We see again from Table 1 that the final recovery times for the ideal case of full-strength foam are independent of the initial condition. This behavior can be explained by the fact that $t_{D,final}$ is the inverse of the wave velocity at point *J*. If Injection point *J* is on a rarefaction wave, $t_{D,final}$ is the inverse of the characteristic speed σ at *J*, and, if it terminates a shock, $t_{D,final}$ is the inverse of the shock velocity starting from *J*. Consequently, $t_{D,final}$ values are identical for any number of displacements sharing the same rarefaction-wave or shock-wave velocity at *J*, regardless of the initial condition. However, sharing identical *J* and $t_{D,final}$ does not result in identical displacement efficiencies at shorter times. As can be seen from Table 1, higher $S_o(I)$ corresponds to greater oil-recovery factor after 1 PVI because the shock from *I* to *IJ* is much faster for higher $S_o(I)$. As a result, more oil is produced during the early stage (during the shock from *I* to *IJ*) rather than the late stage (during the shock from *IJ* to *J*); see Fig. 2a. Also, note that although RF_{1PVI} for a foam flood with $S_o(I)$ = 0.17 (i.e., 27%) is marginally larger than RF_{1PVI} for waterflood (26%), the foam-flood recovery curve is well above the waterflood recovery curve for the rest of the process.

Table 1: $t_{D,final}$ and RF_{1PVI} for base-case scenarios.

$S_o(I)$	Full-Strength Foam $^*RF$ after 0.7 PVI		Waterflood	No Foam	
	Gas/SAG	Foam Flood, $f_w(J)$= ⅓	$f_w(J)$ = 1	Coinjection, $f_w(J)$= ⅓	Gas/WAG
0.17	0.8 (19%*)	1.2 (27%)	4.61 (26%)	11.4 (10%)	200 (6%)
0.73	0.8 (84%*)	1.2 (81%)	4.45 (59%)	11.4 (24%)	200 (9.7%)

3.4.2. Scenario 1—Oil Kills Foam

In this scenario, foam does not survive at $S_o(I) \geq S_o^*$ [e.g., $S_o(I)$ = 0.73]. **Table 2** summarizes the displacement performance of this scenario.

3.4.2.1. Case 1—Oil Kills Foam and Water Has No Effect

The ternary diagram for this case is shown in **Fig. 3a**. Full-strength foam forms at *J* for both gas/SAG and foam flood because oil saturation is too low at S_{or} to affect foam and water has no effect. However, as foam collapses at I [$S_o(I) > S_o^*$], there is an extremely slow-moving shock from J to the point of complete foam collapse for both injection schemes. Ironically, injection of strong foam does not give successful displacement for $S_o(I) > S_o^*$ because of a shock over the strong-foam region to the region of foam collapse, and oil is recovered very slowly (Table 2). (See Fig. 3a for a plot of the fractional-flow function emphasizing this shock.) For the gas-injection cycle of SAG (Fig. 3a), the point of complete foam collapse upstream of the shock is at (0.1, 0.2, 0.7). For the foam flood, the solution resembles the one in **Fig. 4b** and the oil-recovery curve is slightly above the no-foam curve. For $S_o(I) < S_o^*$, both initial and injection conditions are in the region of strong foam ($S_o < S_o^*$). Existence of strong foam in this region results in the formation of two fast-moving shocks, leading to efficient displacement in both injection schemes [(S)(S) solution type in Appendix A].

Assuming that water has no effect on foam implies that foam survives at S_{wr}, whereas foam bubbles would collapse at this saturation from very high capillary pressure (Khatib et al. 1988). Foam collapse at S_{wr} alters the analysis (see Case 8).

3.4.2.2. Case 2—Oil Kills Foam and Water Weakens Foam

For both the gas-injection cycle of SAG (Fig. 4a) and foam flood (Fig. 4b), foam at J is merely weakened, not killed, by low S_w. (k_{rg} is reduced by a factor of 82 and 164 at J for the gas-injection cycle of SAG and the foam flood, respectively.) For $S_o(I) > S_o^*$, the same displacement behavior as in Case 1 exists for both injection schemes: oil is displaced to its residual saturation extremely slowly, and the process is nearly as inefficient as if no foam were present at all. (See Fig. 4b for foam flood; for the gas-injection cycle of SAG, the route resembles that in Fig. 3a.)

For $S_o(I) < S_o^*$, the foam-flood behavior is similar to Case 1 and, hence, efficient. However, for the gas-injection cycle of SAG, the solution type [i.e., (S)(RS); see Appendix A] and performance differs from Case 1 (see Fig. 4a). In this case, displacement efficiency is as good as it is for the waterflood until 0.7 PVI because both processes have identical initial conditions and produce for some time at the initial condition [i.e., at $S_o = S_o(I)$]. For the gas-injection cycle of SAG, at 0.7 PVI, production at the initial condition ends and, as the displacement mechanism changes, the oil-recovery curve deviates from the waterflood curve and oil production deteriorates afterwards. Nevertheless, the gas-injection cycle of SAG still performs significantly better than the no-foam case shown in **Fig. 5a**.

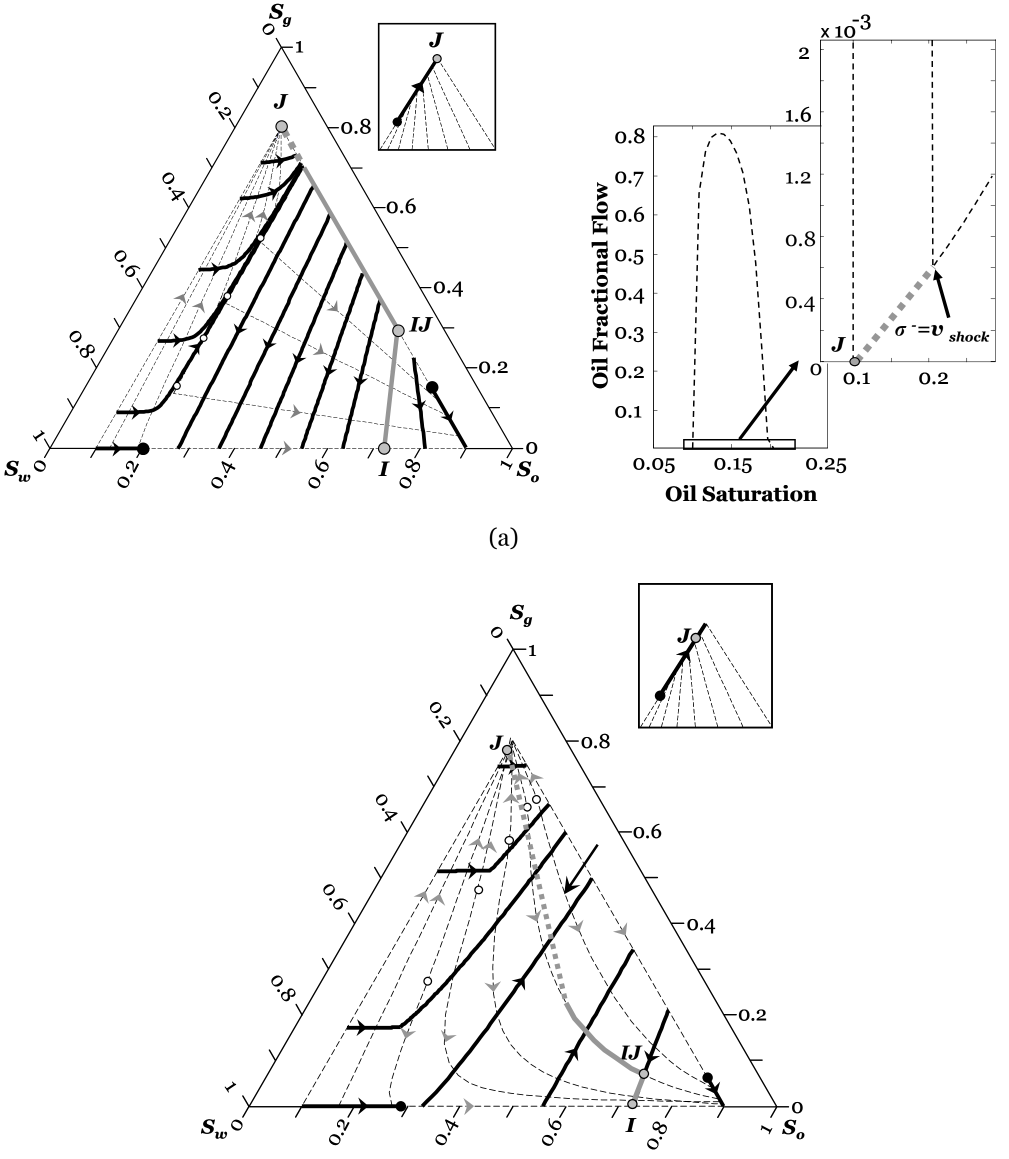

(a)

(b)

Fig. 3: Ternary diagrams and displacement routes for a reservoir initially at (0.27, 0.73, 0). (a) Foam is killed at $S_o(I) \geq S_o^*$ ($S_o^* = 0.2$) and water has no effect; the displacement route shown is for gas-injection cycle of SAG with IJ at (0.1, 0.6049, 0.2951). The fractional-flow curve on the right corresponds to the slow-path segment of the S_{wr} line. The shock passes over the entire foam region and lands in the no-foam region. (b) Foam is merely weakened by high S_o and water has no effect; the displacement route shown is for foam flood with IJ at (0.2177, 0.7149, 0.0674). The single arrow on the right shows the slow path originating from J. The shock from J is to a point on a different slow path.

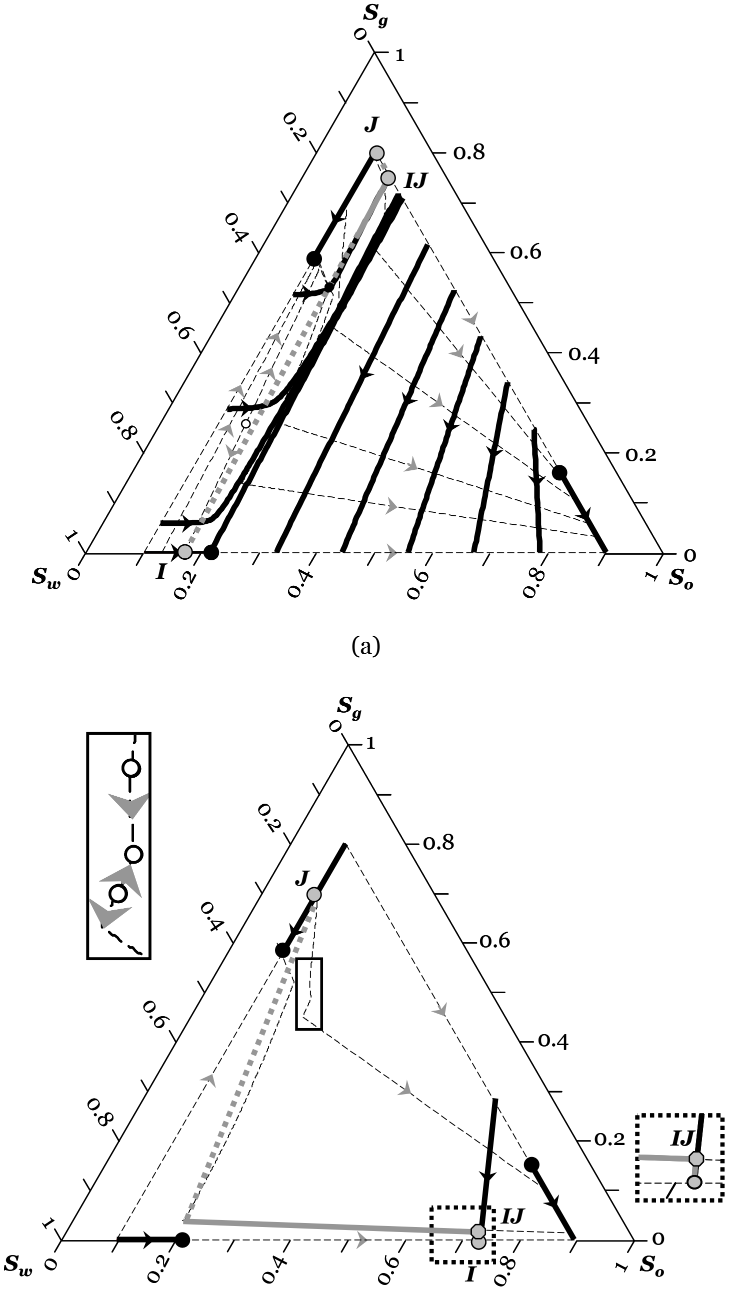

(a)

(b)

Fig. 4: Ternary diagrams and displacement routes when foam is killed at $S_o \geq S_o^*$ ($S_o^* = 0.2$) and weakened at low S_w ($S_w^* = 0.316$). (a) Gas-injection cycle of SAG with *I* at (0.83,0.17,0). (b) Foam flood with *I* at (0.27,0.73,0). Only the paths involved in the displacement are shown here, to avoid clutter.

The model applied here for the weakening effect of water [Eq. C-1, taken from the STARS™ simulator (Computer Modeling Group 1998)] suffers from a significant shortcoming. This model implies finite foam strength at $S_w = S_{wr}$ (k_{rg} is reduced 82-fold), where capillary pressure is very high. In nature, foam bubbles cannot survive at very high capillary pressure (Khatib et al. 1988). This unrealistic assumption is key to the implied success for the cases of gas-injection cycle of SAG, for which the injection condition during gas injection is at S_{wr}. Two models that account for foam collapse at S_{wr} are discussed later (Scenarios 2 and 4).

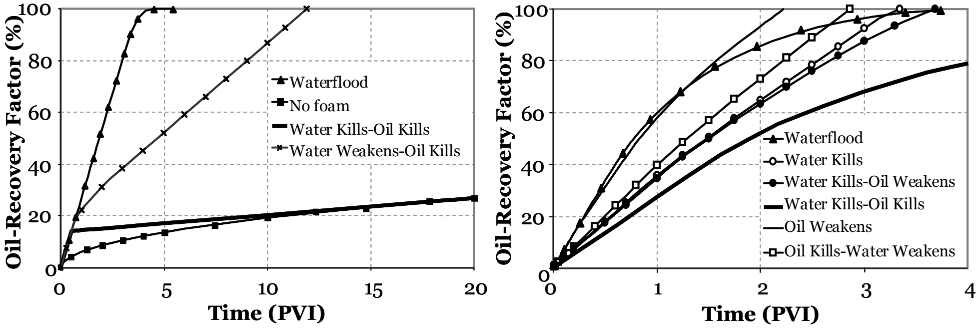

(a) (b)

Fig. 5: Oil-recovery factor versus time. (a) Gas-injection cycle of SAG with $S_o(I) = 0.17$. (b) Foam flood with $S_o(I) = 0.73$.

3.4.2.3. Case 3—Both Oil and Water Kill Foam

The region in which foam survives here is restricted to the zone confined by $S_{or} \leq S_o < S_o^*$ and $S_w \leq S_w^*$. If both J and I are located in this region, the displacement is efficient because of the formation of two fast-moving shocks. However, if foam is killed at both J and I [e.g., at J in the gas-injection cycle of SAG, with $S_o(I) > S_o^*$], the displacement is identical to the no-foam case because the entire displacement is in the no-foam region. In the case of the gas-injection cycle of SAG with $S_o(I) < S_o^*$, where foam is killed at J, oil recovery is as efficient as waterflood (Fig. 5a) until 0.53 PVI. Thereafter, production at the initial-state condition I terminates and, as the displacement mechanism changes, the oil-recovery curve strongly deviates from the waterflood curve and approaches the no-foam curve. These two curves are coincident from approximately 19 PVI (the solution upstream of the shock is identical to the no-foam case). In total, this displacement is nearly as inefficient as if no foam were present at all. The foam flood is successful only if foam survives at I (see Fig. 5b for the unsuccessful case).

Our findings for the processes in which foam collapses at S_{wr} may not apply to real-field applications with a complete SAG process (i.e., combination of both surfactant-injection and gas-injection cycles) and other relative-permeability and foam models.

3.4.2.4. Summary of Scenario 1

Regardless of whether foam is sensitive to water saturation, if foam is destroyed by oil at the initial condition, the displacement is nearly as inefficient as if no foam were present at all for both injection schemes. In these cases, the slight improvement in oil recovery and $t_{D,final}$ over that with no foam is caused by the formation of foam at point *J*, which gives a shock rather than a rarefaction wave to the state upstream of *J*.

Regardless of whether foam is sensitive to water saturation, if it is not destroyed by oil at the initial condition, the foam flood is successful and more efficient than a waterflood. Note that, although RF_{1PVI} values for foam floods with $S_o(I) = 0.17$ are marginally above RF_{1PVI} for waterflood (26%), the foam-flood recovery curves are well above the waterflood curve for the rest of the displacement. However, even if foam is not destroyed at *I* but is sensitive to S_w, the gas-injection cycle of SAG results in an unsuccessful gas mobility control (Fig. 5a). If foam does not survive at S_{wr}, then the gas-injection cycle of SAG is considered unsuccessful relative to waterflood in all cases we examined.

Table 2: $t_{D,final}$ and RF_{1PVI} when oil kills foam.

Injection	Oil	Kills		
	Water	No Effect	Weakens	Kills
Gas/SAG	$S_o(I) = 0.17$	**1.8 (40%)**	11.9 (22.3%)	200 (14.5%)
Foam Flood $f_w(J) = 1/3$		**2.1 (27.5%)**	**2.76 (28.6%)**	**3.5 (27.4%)**
	$S_o(I) = 0.73$	8.1 (30%)	8.4 (29.2%)	8.7 (28.1%)
Gas/SAG		175.1 (15.2%)	175.1 (9.7%)	200 (9.7%)

3.4.3. Scenario 2—Water Kills Foam

Table 3 summarizes the displacement performance of this scenario. In Scenario 2, foam does not survive at $S_w \le S_w^*$ [e.g., at *J* in the gas-injection cycle of SAG and at *I* for $S_o(I) = 0.73$]. The performance of this combination of *J* and *I* where foam is destroyed at both *J* and *I* has already been discussed in Case 3 and was marked a failure. However, in the gas-injection cycle of SAG with $S_w(I) > S_w^*$ [i.e., $S_o(I) = 0.17$], the slight improvement in *RF* over that with no foam at early stages (see Fig. 5a for water kills-oil kills curve) is caused by the formation of foam at point *I*, which gives a shock rather than a rarefaction wave to *I* (regardless of the foam sensitivity to S_o). The solution upstream of the shock is identical to that in the no-foam case.

The following Cases 4 and 5 focus on foam-flood performance when oil does not kill foam (the foam-flood case in which both oil and water kill foam has already been discussed in Case 3).

3.4.3.1. Case 4—Foam Flood When Water Kills Foam and Oil Has No Effect

Fig. 6a shows the solution of this case. If foam survives at *I* [$S_w(I) > S_w^*$ or $S_o(I) = 0.17$], the displacement is more efficient than waterflood and the oil-recovery curve stays above the waterflood curve. However, if foam is destroyed at *I* [$S_w(I) < S_w^*$ or $S_o(I) = 0.73$; see Fig. 6a], displacement is less efficient at 1 PVI than waterflood, despite the fact that $t_{D,final}$ is shorter than the waterflood case (see Fig. 5b). As we discussed earlier in connection with §3.4.1, waterflood is more efficient for the case with $S_o(I) = 0.73$ than for $S_o(I) = 0.17$ because of lower water mobility at higher oil saturations. Therefore, the waterflood acts more efficiently and is preferred over foam flood in this case until the very last stage of the displacement, where foam-flood recovery exceeds the waterflood recovery.

3.4.3.2. Case 5—Foam Flood When Water Kills and Oil Weakens Foam

Fig. 7 shows the ternary diagram of this case. The same story applies as in Case 4 for both *I*, except that the solution types are different (Fig. 5b and Table A-1).

3.4.3.3. Summary of Scenario 2

The gas-injection cycle of SAG is nearly as inefficient as if no foam were present at all, at any *I*. In the case of foam flood, $t_{D,final}$ is not a reliable measure for distinguishing the success or failure of the process, and oil-recovery curves should be examined. As the oil effect becomes more severe (from no effect to killing; for example, see Fig. 5b), foam-flood efficiency deteriorates and oil is recovered more slowly.

3.4.4. Scenario 3—Oil Weakens Foam

Table 4 provides the displacement performance of this scenario. The case in which high S_o weakens foam and low S_w kills foam is already discussed in Scenario 2 above.

3.4.4.1. Case 6—Oil Weakens Foam and Water Has No Effect

Fig. 3b shows the solution of this case. While $S_o(I) < S_o^*$, both injection schemes (i.e., gas/SAG and foam flood) are significantly more efficient than waterflood. However, for $S_o(I) = 0.73$ [i.e., $S_o(I) > S_o^*$] as explained in §3.4.1, the waterflood sweeps the reservoir more efficiently in this case compared to $S_o(I) = 0.17$. Therefore, the waterflood exceeds gas- and foam-flood oil recovery until a certain point. Only after 1.6 PVI for the gas-injection cycle of SAG (not shown here) and 1.3 PVI for foam flood (see Fig. 5b) these two processes start to exceed the waterflood performance; they eventually recover the last of the oil twice as fast as waterflood. The solution type affects the displacement efficiency of the process. In this case, processes sharing the same initial condition have similar solution type (see Table A-1).

As noted, real foams would be expected to collapse at S_{wr}, in contradiction to this case.

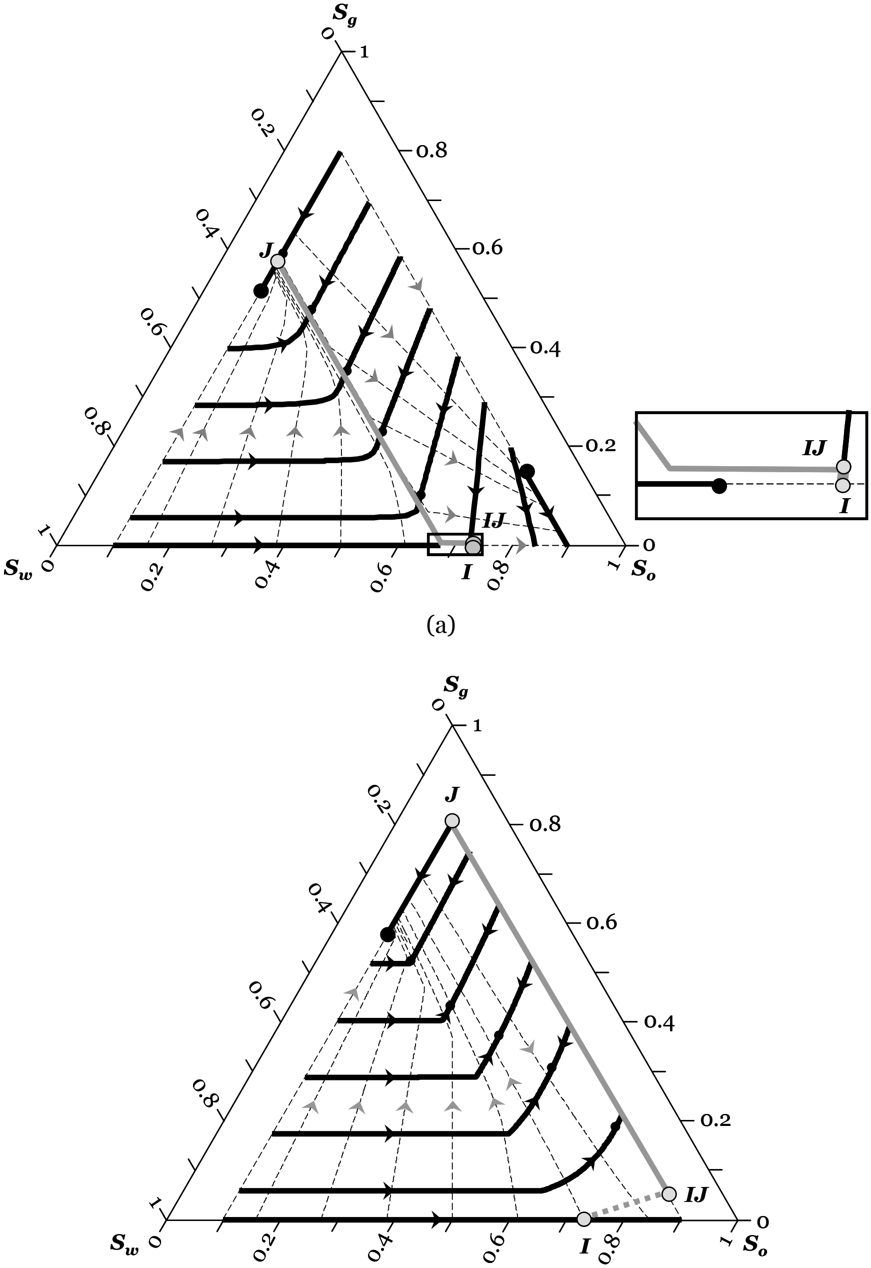

(a)

(b)

Fig. 6: Ternary diagrams and displacement routes for a reservoir initially at (0.27, 0.73, 0). (a) Foam is killed at $S_w \leq S_w^*$ ($S_w^* = 0.316$) and oil has no effect; the displacement route shown is for foam flood, with *IJ* at (0.2688, 0.7267, 0.0045). (b) Foam is only weakened by low S_w ($S_w^* = 0.316$) and oil has no effect; the displacement route is for gas-injection cycle of SAG, with *IJ* at (0.1, 0.8485, 0.0515).

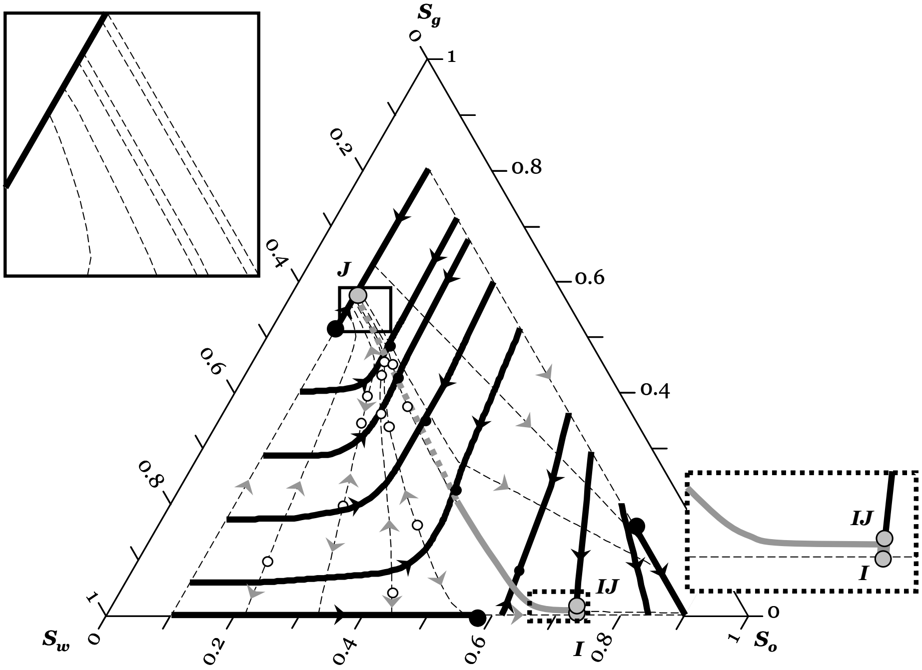

Fig. 7: Ternary diagram and displacement route for foam flood when foam is killed at $S_w \leq S_w^*$ ($S_w^* = 0.316$) and weakened at high S_o ($S_o^* = 0.2$), with IJ at (0.2680, 0.7262, 0.0058).

Table 3: $t_{D,final}$ and RF_{1PVI} when water kills foam.

$S_o(I)$	Water	Kills		
	Oil	No Effect	Weakens	Kills
0.17	Gas/SAG	200 (15%)	200 (15%)	200 (14.5%)
0.73		200 (9.7%)	200 (9.7%)	200 (9.7%)
0.17	Foam Flood $f_w(J) = ⅓$	**3.35 (27.7%)**	**3.32 (27.8%)**	**3.5 (27.4%)**
0.73		3.35 (35.8%)	3.69 (34.7%)	8.7 (28.1%)

3.4.4.2. Case 7—Both Oil and Water Weaken Foam

The ternary diagram of this case is shown in **Fig. 8**. Even though both injection schemes perform more efficiently than waterflood for $S_o(I) < S_o^*$, the gas-injection cycle of SAG fails for $S_o(I) > S_o^*$ [i.e., $S_o(I) = 0.73$] because the shock back to J is very slow moving. Besides, the foam-flood performance for this initial condition is also unsatisfactory because it lags behind waterflood recovery until 94% of the oil is recovered (see Fig. 5b).

As noted, real foams would be expected to collapse at S_{wr}, in contradiction to this case.

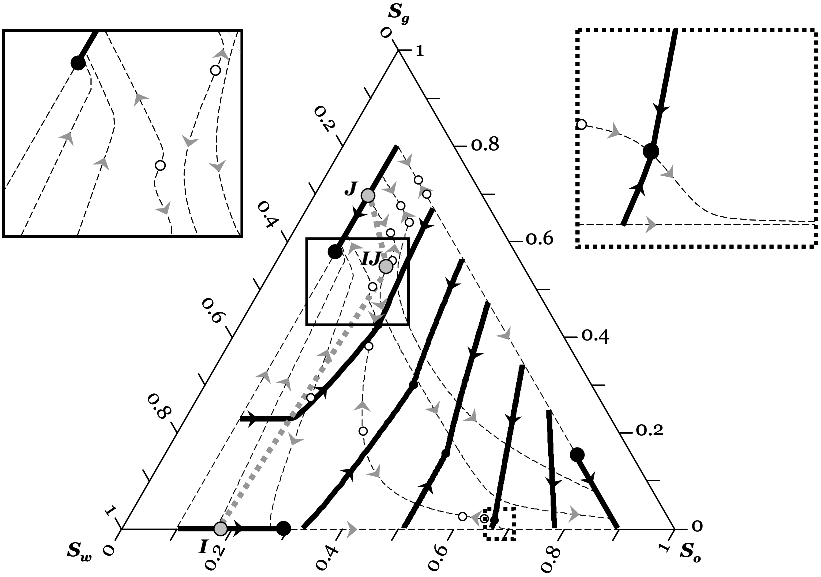

Fig. 8: Ternary diagram and displacement route for foam flood when foam is weakened by both low S_w (S_w^*= 0.316) and high S_o (S_o^* = 0.2), with *IJ* at (0.24, 0.2, 0.56).

3.4.4.3. Summary of Scenario 3

Displacement performance worsens as the effect of water saturation on foam becomes more severe (see Fig. 5b and Table 4). If foam is weakened by oil saturations above S_o^*, the displacement is more efficient than waterflood in two cases: (1) foam flood with $S_o(I) < S_o^*$, regardless of the foam sensitivity to S_w; and (2) the gas-injection cycle of SAG with $S_o(I) < S_o^*$, if foam is not killed at *J* by low S_w.

Table 4: t_{Dfinal} and RF_{1PVI} when oil weakens foam.

$S_o(I)$	Oil	Weakens		
	Water	No Effect	Weakens	Kills
0.17	Gas/SAG	**1.0 (89.9%)**	**2.45 (33.1%)**	200 (15%)
0.73		2.18 (52.6%)	119.6 (10.3%)	200 (9.7%)
0.17	Foam Flood $f_w(J)$= ⅓	**1.5 (26.9%)**	**1.97 (29.6%)**	**3.32 (27.8%)**
0.73		2.23 (57.9%)	2.86 (39.9%)	3.69 (34.7%)

3.4.5. Scenario 4—Water Weakens Foam

The two cases in which low S_w weakens foam and high S_o may kill or weaken foam have already been investigated in Cases 2 and 7. **Table 5** summarizes the displacement performance of this scenario. Our weakening model fails to kill foam even at S_{wr}.

3.4.5.1. Case 8—Water Weakens Foam and Oil Has No Effect

Fig. 6b illustrates the solution of this case. If water saturations below $S_w^* = 0.316$ weaken foam abruptly but smoothly, we find the resulting displacement successful at any I in both injection schemes. The displacement route for the gas-injection cycle of SAG with $S_w(I) < S_w^*$ is shown in Fig. 6b. The segment of the route along $S_w = S_{wr}$ corresponds to $f_w = 0$ (i.e., no net water transport even as foam advances).

However, this successful gas-injection process is obtained under the unrealistic assumption that foam survives at S_{wr} (Eq. C-1). A fairly simple modification of this equation (Eq. C-2) keeps a behavior similar to Eq. C-1 everywhere but for S_w near S_{wr}, where foam collapse is complete. We investigated this model by numerical simulation. However, this model, like the water-killing foam model used here, fails the design criterion developed from the MOC without oil (Shan and Rossen 2004) (i.e., formation of a low-mobility bank upon gas injection). With Eq. C-2, the conclusions for foam flood stay the same as with Eq. C-1, although $t_{D,final}$ values slightly increase (see Table 5); however, performance for the gas-injection cycle of SAG is affected adversely. Regardless of the initial condition, gas/SAG processes perform as well as waterflood at very early stages [until 0.85 PVI for $S_o(I) = 0.17$ and 0.25 PVI for $S_o(I) = 0.73$]. Afterward, they strongly deviate from the waterflood oil-recovery curve and their oil-recovery factors drop significantly [$RF_{1PVI} = 23.4\%$ for $S_o(I) = 0.17$ and $RF_{1PVI} = 29\%$ for $S_o(I) = 0.73$]. At the same time that the model with Eq. C-1 achieves 100% recovery (at 2.4 PVI), the model with Eq. C-2 recovers only 23.5% for $S_o(I) = 0.17$ and 36% for $S_o(I) = 0.73$.

For the cases examined, waterflood is preferred over gas/SAG if foam is killed at J. This significant difference in gas flood performance highlights the crucial role of the sensitivity functions and the importance of defining the sensitivity functions in accordance with reality to obtain reliable results.

3.4.5.2. Summary of Scenario 4

As the effect of oil on foam becomes more severe, the final recovery time and oil-recovery factor worsen for both injection schemes. Increasing the water fraction of the injected fluid to one-third results in successful mobility control except in the case where foam is sensitive to high oil saturation at the initial condition. For the gas-injection cycle of SAG, with finite foam strength at S_{wr}, successful mobility control can be achieved only if foam is insensitive to oil saturation or is weakened by oil saturation and $S_o(I) < S_o^*$. However, the gas-injection cycle of SAG leads to failure in case of complete foam collapse at S_{wr}. Table 5 represents the results reflecting the performance of both models for the effect of water.

Table 5: $t_{D,final}$ and $RF_{1\text{PVI}}$ when water weakens foam.

$S_o(I)$	Water	Weakens (Eq. C-1; $F_w \neq 0$ at S_{wr})			Weakens (Eq. C-2; $F_w = 0$ at S_{wr})		
	Oil	No Effect	Weakens	Kills	No Effect	Weakens	Kills
0.17	Gas/SAG	**2.4 (33.4%)**	**2.45 (33.1%)**	11.9 (22.3%)	200 (23.4%)	200 (23.4%)	200 (21.5%)
0.73		**2.4 (75.5%)**	119.6 (10.3%)	175.1 (9.7%)	200 (29%)	200 (11%)	200 (10.5%)
0.17	Foam Flood $f_w(J) = ⅓$	**1.6 (30.1%)**	**1.97 (29.6%)**	**2.76 (28.6%)**	**1.96 (31.5%)**	**1.99 (28.8%)**	**2.82 (28.7%)**
0.73		**1.6 (80.5%)**	2.86 (39.9%)	8.4 (29.2%)	**1.96 (67%)**	2.95 (38.6%)	8.42 (28.8%)

3.5. Effect of a Nonlinear Relative-Permeability Model

We extend our analysis to cases with the nonlinear model in Eq. 6 (with no elliptic regions), and we conduct numerical simulations for two different oil viscosities (2, 5 cp).

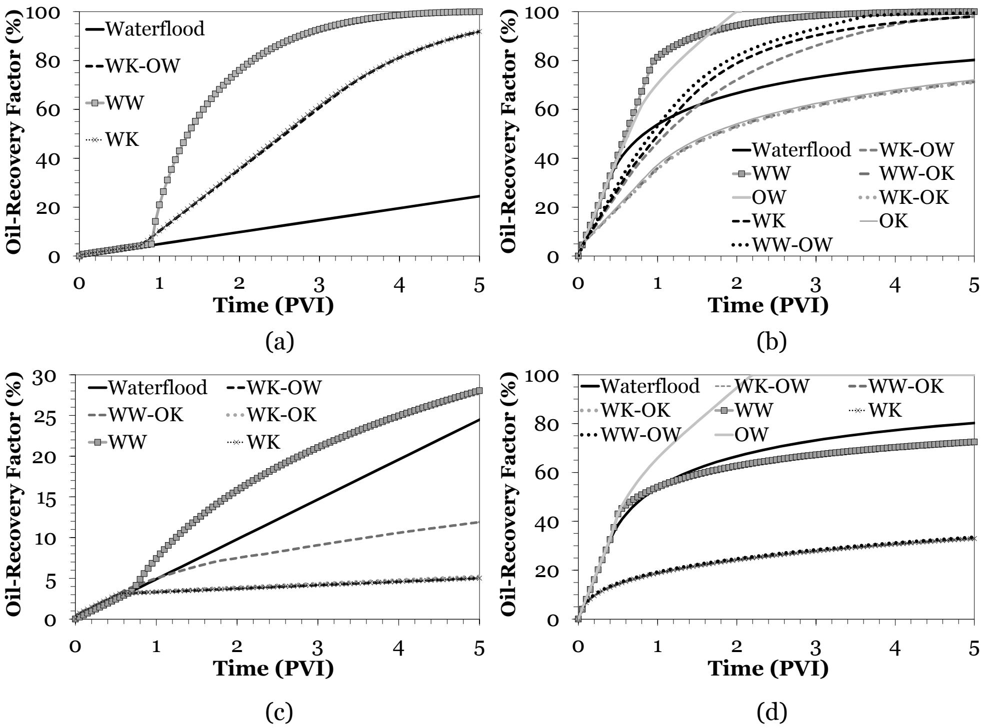

(a)

(b)

(c)

(d)

Fig. 9: Oil-recovery factor versus time for the nonlinear relative-permeability model in Eq. 6. We abbreviated the name of the cases to fit in the figures; e.g., WK-OW represents Water Kills-Oil Weakens and WK stands for Water Kills, but oil has no effect. (a) Foam flood with $S_o(I) = 0.17$. (b) Foam flood with $S_o(I) = 0.73$. (c) Gas-injection cycle of SAG with $S_o(I) = 0.17$. The curves of WK-OW, WK-OK, and WK are coincident. The WW curve drops below the waterflood curve shortly after 5.5 PVI. (d) Gas-injection cycle of SAG with $S_o(I) = 0.73$. Except for the waterflood, OW, and WW curves, the rest of the curves are coincident. The numerical simulator was exhibiting oscillations for the cases not shown in this figure.

We assume complete foam collapse at S_{wr} (Eq. C-2) for the weakening effect of water instead of Eq. C-1, all through the simulations. We applied the same criteria as earlier for distinguishing successful foam processes.

Success was always attained for a foam flood with $S_o(I) < S_o^*$ (**Fig. 9a**), as with the linear relative-permeability model with complete foam collapse at S_{wr}. Contrary to the case of the linear relative-permeability model, a foam flood with $S_o(I) > S_o^*$ also appeared to be successful if foam is weakened or not affected (i.e., not killed) at high oil saturations (Fig. 9b).

With complete foam collapse at S_{wr}, gas injection was *un*successful in most of the cases examined, similar to the conclusion in the linear case (Figs. 9c and 9d). Gas injection is successful in only two cases:

(1) $S_o(I) < S_o^*$: for times shorter than 5.5 PVI only if water weakens foam and oil has no effect.

(2) $S_o(I) > S_o^*$: only if oil weakens foam and water has no effect.

The overall conclusions for both oil viscosities are the same; although, as expected, oil is recovered much faster at the lower oil viscosity.

3.6. Conclusions

- MOC solutions have proved useful in highlighting key mechanisms and strategies for improving foam performance and in understanding foam simulation models better.
- We extend the MOC to foam flow with oil. We examine the effects of foam quality, initial oil saturation, foam sensitivity to high oil saturation and low water saturation, relative-permeability model, and oil viscosity on oil displacements with foam in one dimension using the MOC.
- The time required to produce all mobile oil ($t_{D,final}$) is not a definitive measure of mobility control in these simulations. The comparison of the oil-recovery performance with waterflood acts as a second screening criterion for a successful foam process.
- Regardless of whether foam is sensitive to water saturation, if foam is destroyed by oil at the initial condition, the displacement is nearly as inefficient as if no foam were present at all for both injection schemes and both relative-permeability models examined.
- Foam models that represent foam collapse at the limiting capillary pressure as a function of water saturation should ensure that they do not imply finite foam strength at $S_w = S_{wr}$, where capillary pressure is extremely high. In real foams, foam bubbles collapse at S_{wr} because of high capillary pressure. The failure to represent this mechanism properly in

models leads to misleading prediction of success in SAG foam processes. However, foam collapse at S_{wr} is not so crucial to modeling foam-injection processes.

- Incorporating foam collapse at S_{wr} results in the failure of a gas-injection cycle of a SAG process in cases examined in this chapter, regardless of the reservoir initial condition and foam sensitivity to S_w and S_o, for the relative-permeability models we examined. Ignoring foam collapse at S_{wr} leads to success in a gas-injection cycle of SAG in several occasions. Our findings for these processes may not apply to real-field applications with a complete SAG process (i.e., combination of surfactant-injection and gas-injection cycles) and other relative-permeability and foam models.
- If foam collapse at S_{wr} is incorporated into the linear-relative-permeability model, foam flood is always preferred over waterflood and is considered successful for $S_o(I) < S_o^*$. A foam flood is successful for any initial condition if foam is only weakened (not killed) by low S_w and not affected by S_o.
- If foam collapse at S_{wr} is incorporated into the nonlinear relative-permeability model, foam flood is always preferred over waterflooding and considered successful if foam is not killed at the initial condition because of high oil saturation.
- Based on this study, it is not recommended to start a foam EOR process at early stages of the reservoir life for a foam formulation that is sensitive to high oil saturation; specifically when $S_o(I) > S_o^*$, because high initial oil saturation causes the foam EOR process to fail.
- Therefore, the effect of low S_w and high S_o on foam must be well understood and represented accurately to avoid spurious decisions leading to failure based on unrealistic foam models and parameter values.
- Oil viscosity does not affect the overall conclusions for the nonlinear relative-permeability model tested. As expected, oil is recovered much faster with lower oil viscosity.
- It must be noted, however, that because of its simplifying assumptions, the MOC cannot be used in complex real-world applications where many of its assumptions are violated. Its usefulness is in the insights it offers, not as a quantitative, predictive tool for real reservoirs.

Chapter 4

Numerical Simulation of Foam EOR

4.1. Introduction

There are two general approaches for incorporating the effect of foam in commercial simulators. The first approach is to apply fully mechanistic models such as a population-balance model or a percolation model. This approach allows for explicit representation of foam dynamics such as generation, propagation, and coalescence in porous media as observed in core-scale experiments. The second approach is through using mobility-reduction factors (§1.4.3.2), in which the foam dynamics are implicitly incorporated in correlations that are multiplied to the gas mobility to modify it. These empirical correlations are dimensionless and determine the gas-mobility reduction in the presence of foam. A general overview of these models with their advantages and disadvantages is given in Chapter 1.

The STARS™ simulator has both the mechanistic models and models based on mobility-reduction factor implemented in it for modeling foam. As for the mobility-reduction factor models that is of our interest, a number of empirical correlations are defined in this simulator. These correlations do not include different types of sensitivities to water saturation (S_w) and oil saturation (S_o). They only include the weakening effect at low S_w (in the 1998 version) and killing effect at high S_o (modified in the 2007 version). Moreover, some of the correlations used there (e.g., killing effect of oil and sensitivity to surfactant concentration) are not differentiable at certain points. These limitations and shortcomings are discussed in detail in Appendix C. There, we have provided a new differentiable correlation for sensitivity to surfactant concentration and stated a condition for the correlation for the killing effect of oil, for which the correlation is differentiable. Further, new correlations are introduced for the sensitivity types to S_w and S_o that are not available in STARS™ (i.e., a killing effect at low S_w and a weakening effect at high S_o). Although we have adopted some of the empirical correlations from this simulator, we have not, however, used this simulator in any of our simulations. In this simulator, surfactant is treated as an extra component and an extra flow equation is employed for modeling its transport (Computer Modeling Group 2009).

The Modular Reservoir Simulator (MoReS) developed by Shell has a comprehensive simulation capability. Mobility-reduction factor for foam modeling can be easily implemented in it by the user. Therefore, it has the flexibility to accept any type of empirical correlations. These correlations can be provided in two different ways: one can implement the exact correlations in the input file, or generate a table of a mobility-reduction factor based on the correlations and use that instead. Modeling surfactant transport is also possible in two different ways: it is possible to model it as a passive tracer or as an extra component. Based on the ultimate goal of the user (simulation and/or optimization), one can choose the available option for incorporating foam and modeling surfactant transport. At this point, limited options are available for these purposes in combination with the adjoint-based optimization routine in MoReS.

All the simulations from this chapter onwards are performed with MoReS (hereafter referred to as *the simulator*). Although it has been significantly validated, some of the newer features and especially the combination of various advanced options have not yet been fully tested (Dynamo/MoReS Online User Documentation 2010). Consequently, this chapter partly focuses on validating this simulator with the analytical solutions obtained by the method of characteristics (MOC) in Chapter 3 for the one-dimensional (1D) oil displacement by foam.

In the simulator, the model equations are solved at discrete time intervals on a user-specified spatial grid, with a fully implicit Newton-Raphson scheme and one-point upstream mobility weighting (Dynamo/MoReS Online User Documentation 2010).

In this chapter, we first introduce the available three-phase relative-permeability models for this work. Next, different options in the simulator for incorporating foam (used in Chapters 4 and 5) and modeling surfactant transport (only used in Chapter 5) are introduced and their limitations are discussed. Finally, the performance of the simulator in modeling foam displacement in 1D is validated against the available MOC analytical solutions in Chapter 3 (i.e., with the linear relative-permeability model).

4.2. Three-Phase Relative-Permeability Models

The most commonly used models in commercial simulators are Stone's models (Stone 1970, 1973). The Stone I model introduced in 1970 is based on a channel-flow approach in which it is assumed that at most one mobile fluid can flow in any flow channel. The water relative-permeability function (k_{rw}) and the gas relative-permeability function (k_{rg}) are functions of their own saturations. However, the oil relative-permeability function (k_{ro}) is based on the two-phase relations for oil/water and gas/water systems and is a function of both S_w and S_g. (Since the sum of the saturations adds up to one, the dependence of S_o can be eliminated.) The Stone I model has a difficulty in estimating the three-phase residual oil saturation. A modified model, known as the Stone II model, was introduced by Aziz and Settari (1979) and is more commonly used. Later, Baker (1988) proposed a model that uses *saturation-weighted* interpolation of oil relative-permeability functions from two-phase water/oil and gas/oil relative-permeability data. The *segregated* model in ECLIPSE™ and the *saturation-weighted* model in MoReS (Masalmeh and Wei 2010) are variations on this approach. Heiba (1984) suggested a model in which a *linear* interpolation between the two-phase data is performed [see Yuen et al. (2008) and Ahmadloo et al. (2009) for the details of the models]. MoReS accommodates a similar model entitled *linear-isoperms* model, in which the isoperms lines connecting the water/oil data and gas/oil data are *straight* lines on a volume-fraction phase diagram (see **Fig. 1**) (Masalmeh and Wei 2010).

Baker's saturation-weighted model has proven useful in matching the experimental data in several studies and it is shown to be superior to the Stone's models (Baker 1988; Delshad and Pope 1989; Baker 1993; Blunt 2000; Pejic and Maini 2003; Yuen et al. 2008). In this work, the linear-isoperms model is applied (Masalmeh and Wei 2010).

Here, we confine ourselves to review those models that are available for this work. Nevertheless, there are many other relative-permeability models available in literature (Delshad and Pope 1989; Sahni et al. 1996; Helset et al. 1998; Blunt 2000).

4.2.1. Linear Model

We applied a linear Corey-type relative-permeability model for the 1D-MOC analysis in this work, in which the relative permeability of each phase is a function of its own saturation:

$$k_{r\alpha} = K_{r\alpha} \frac{S_\alpha - S_{\alpha r}}{1 - S_{wr} - S_{or} - S_{gr}} \qquad \alpha = w, o, g,$$

where $S_{\alpha r}$ is the residual saturation and $K_{r\alpha}$ is the end-point relative permeability of phase α. See Table B-1 for parameters used in the above equation. This model is used in Chapter 3 and §4.5 to validate the performance of the simulator in modeling foam displacement by comparing its results with the available 1D-MOC solutions in Chapter 3. This model is discussed in more detail in §3.2.1.

4.2.2. Two-Phase Relative-Permeability Models Used in Linear-Isoperms and Saturation-Weighted Models

In the saturation-weighted and linear-isoperms models discussed below, the relative permeabilities of the water (wetting) and gas (non-wetting) phases are a function of only their own phase saturation. The three-phase relative permeability of the intermediate phase (oil) or k_{ro} is based on the saturations of the two other phases and is constructed by a certain type of interpolation between the existing two-phase relative-permeability data (Eqs. 1 and 2). In this work, the water/oil and gas/oil functions are available. We used the MAKECOREY function in the simulator to create the two-phase relative-permeability tables (i.e., k_{rw}, k_{row}, k_{rg}, and k_{rog} tables) according to Corey's correlations.

For the two-phase water/oil system (S_g = 0) we have:

$$k_{rw} = K_{rw}\left(\frac{S_w - S_{wr}}{1 - S_{wr} - S_{orw}}\right)^{n_w},$$
$$k_{row} = K_{row}\left(\frac{1 - S_w - S_{orw}}{1 - S_{wr} - S_{orw}}\right)^{n_{ow}}, \tag{1}$$

where K_{rw} is the end-point relative permeability of water, and K_{row} is the end-point relative permeability of oil at S_{wr}. The residual oil saturation to waterflood is denoted by S_{orw}. The Corey exponents for water is represented by n_w.

For the two-phase gas/oil system ($S_w = S_{wr}$) we have:

$$k_{rg} = K_{rg}\left(\frac{S_g - S_{gr}}{1 - S_{wr} - S_{gr} - S_{org}}\right)^{n_g},$$
$$k_{rog} = K_{rog}\left(\frac{1 - S_g - S_{org} - S_{wr}}{1 - S_{wr} - S_{gr} - S_{org}}\right)^{n_{og}}, \tag{2}$$

where K_{rg} is the end-point relative permeability of gas, and K_{rog} is the end-point relative permeability of oil at S_{gr}. The residual oil saturation to gas flood is denoted by S_{org}. The Corey exponents for gas is represented by n_g. It is very important to note that the two-phase tables must be consistent: k_{row} ($S_w = S_{wr}$) = k_{rog} (S_g = 0), i.e., K_{row} must be equal to K_{rog}. Also, k_{ro} must be zero when S_o equals zero; therefore, k_{row} (S_w = 1) = k_{rog} (S_g = 1 - S_{wr}) = 0.

4.2.3. Saturation-Weighted Model

The saturation-weighted model is a variation of the model of Baker (1988). The water and gas phase relative-permeability functions (i.e., k_{rw} and k_{rg}) are the same as those in Corey's model in Eqs. 1 and 2. This model uses *saturation-weighted* interpolation for the prediction of the oil (intermediate phase) relative permeability (k_{ro}) from two-phase water/oil (k_{row}) and gas/oil (k_{rog}) relative-permeability data (Masalmeh and Wei 2010):

$$k_{ro} = \frac{\left(S_w - S_{wr}\right)k_{row} + \left(S_g - S_{gr}\right)k_{rog}}{\left(S_w - S_{wr}\right) + \left(S_g - S_{gr}\right)}, \tag{3}$$

where (S_w-S_{wr}) and (S_g-S_{gr}) are the weighting factors. The weighting factors of k_{row} and k_{rog} are zero for $S_w < S_{wr}$ and $S_g < S_{gr}$, respectively. For consistency, k_{row} ($S_w = S_{wr}$) = k_{rog} ($S_g = 0$) = k_{ro} ($S_w = S_{wr}$, $S_g = 0$).

The procedure shown here is slightly different from Baker (1988). There, he used (1-S_o) instead of S_w for determining k_{row} and (1-S_o) instead of S_g for calculating k_{rog} in Eqs. 1 and 2. Another variation from Baker's model is that normalized saturations (i.e., S_w^* and S_g^*) are used in k_{row} and k_{rog} functions in Eqs. 1 and 2 instead of S_w and S_g:

$$\begin{aligned} S_w^* &= S^*\left(1 - S_{wr} - S_{orw}\right) + S_{wr}, \\ S_g^* &= S^*\left(1 - S_{wr} - S_{gr} - S_{org}\right) + S_{gr}, \\ S^* &= \frac{S_w - S_{wr}}{1 - S_{wr} - S_{orw}} + \frac{S_g - S_{gr}}{1 - S_{wr} - S_{gr} - S_{org}}. \end{aligned} \tag{4}$$

This model can be used in combination with the adjoint method in the simulator*.

4.2.4. Linear-Isoperms Model

In the linear-isoperms model, the points with equal relative permeability in the water/oil and gas/oil tables are connected with *straight* lines. These lines are called isoperms; see Fig. 1.

The difference between saturation-weighted and linear-isoperms models for the prediction of k_{ro} is small when one uses small values for n_{og}. However, the saturation-weighted model predicts larger values of k_{ro} for larger n_{og} values at small values of oil saturation due to the weighting factors used in this model that lead to higher oil recovery. This effect may or may not be real, i.e., based on measurements. Without any experimental data, it is recommended to use the saturation-weighted model†. The saturation-weighted model is computationally more robust and efficient, because it is mathematically represented in a more straightforward way; however, we do not use it in Chapter 5, because for $n_{og} = 3$, the oil recovery is deemed too optimistic for the range of oil saturations encountered in the simulations.

---

* This requires setting a certain flag (i.e., RLPDATA.RLPCALC_BEFORE_2008_1) to ON in the 2010.1 version of the simulator. If this flag is set to OFF, the derivatives of the oil relative-permeability function (k_{ro}) are not calculated correctly for the saturation-weighted model in the 2010.1 version. This problem is entirely solved in the 2011 version and does not require the flag.

† Personal communication L. Wei, Shell Global Solutions International, Rijswijk.

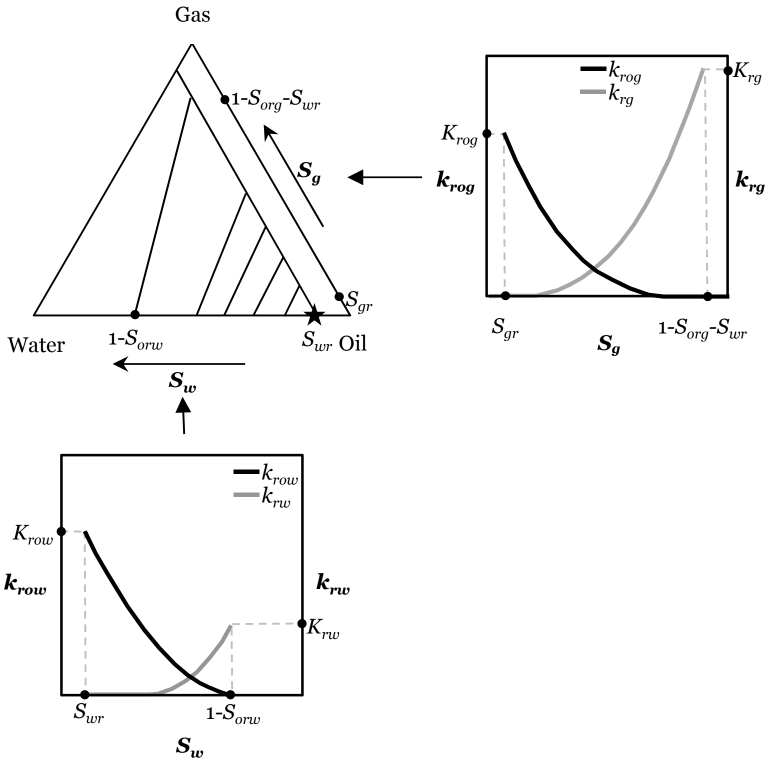

Fig. 1: Concept of the linear-isoperms model. For consistency, k_{ro} ($S_w = S_{wr}$, S_g = 0) = k_{row} ($S_w = S_{wr}$) = k_{rog} (S_g = 0). This point is represented by a star on the ternary diagram (adapted from Dynamo/MoReS Online User Documentation 2010).

4.3. Incorporating the Effect of Foam

The presence of foam reduces gas-phase mobility dramatically (Bernard and Holm 1964; Huh and Handy 1989). However, the water and oil relative-permeability functions, to a reasonable approximation, remain unaltered in the presence of foam (Bernard and Jacobs 1965; Huh and Handy 1989; Vassenden and Holt 2000). It is computationally equivalent to alter the gas mobility for foam by modifying the gas viscosity (μ_g) and/or the gas relative permeability (k_{rg}) (Shan and Rossen 2004). In the simulator, μ_g or the gas relative mobility (λ_{rg}) is altered based on the choice made for incorporating foam in the model (see §4.3.1 and §4.3.2 for details). Here, we confine ourselves to discussing the case in which the gas relative mobility in the absence of foam (λ_{rg}^{nf}) is rescaled to the gas relative mobility in the presence of foam (λ_{rg}^{f}) by multiplying λ_{rg}^{nf} by a dimensionless interpolation factor (f_{mr})*:

---

* f_{mr} is referred to as MRF or FM elsewhere.

$$\lambda_{rg}^{f} = \lambda_{rg}^{nf} \times f_{mr}, \qquad \text{where} \quad f_{mr} = \frac{1}{1 + fmmob \times F_w \times F_o \times F_s \times \ldots}, \tag{5}$$

where f_{mr} is the mobility-reduction factor and *fmmob* represents the normalized resistance to flow of a foam of minimum-size bubbles, in the absence of factors increasing bubble size (Surguchev et al. 1995) and F_w and F_o are the functions describing the stability of lamellae in the presence of water and oil, respectively. Similarly, to rescale gas viscosity in the absence of foam (μ_g^{nf}) to gas viscosity in the presence of foam (μ_g^{f}), the term μ_g^{nf} is divided by f_{mr}.

There are two approaches in the simulator for incorporating the effect of foam: by monitors and by plugging tables. Both approaches for incorporating the effect of foam are examined here and the simulator capability to match the analytical MOC solution is investigated.

4.3.1. Monitors

The simulator is equipped with a powerful input command language with the possibility to define monitors. A monitor is a piece of command language, similar to a function that is executed at predefined times or conditions (Dynamo/MoReS Online User Documentation 2010). This offers additional flexibility to customize the simulations. This approach modifies the *gas viscosity*.

f_{mr} can be defined by a monitor. f_{mr} is calculated based on F_w and F_o functions, explicitly defined by a command language in the monitors, as functions of S_w and S_o. The foam monitor solves for f_{mr} immediately before a time step (and also before the first time step). In other words, the f_{mr} applied at each time step is evaluated at the saturations in the previous time step (explicit implementation). In contrast, in the plugging table (§4.3.2), f_{mr} is extracted from the table based on the saturations at the current time step (implicit implementation).

4.3.2. Plugging Tables

f_{mr} can be defined by a plugging table generated based on F_w and F_o functions for various combinations of S_w and S_o. The plugging table *directly* modifies the *gas mobility* as a function of S_w and S_o from which the plugging table factor (f_{mr}) is applied to the gas mobility. As mentioned earlier, the f_{mr} value is implicitly extracted from the table during each time step (i.e., f_{mr} is evaluated at the saturations of the same time step).

Every plugging table is defined once for a certain set of foam parameters (see the last two rows of Table B-1 for the foam parameters). This pre-defined table is included in the input file and remains fixed unless the foam parameters are changed.

Special care must be taken in creating the plugging tables. F_w and F_o curves must be refined well enough in terms of S_w and S_o to fully capture all the sharp changes and corners in these functions. Failure to create an accurate table leads to erroneous results. However, the table generation may take excessive time if too much refinement is involved. The table-generation time grows exponentially with the table size [e.g., 4 hours for a table with 1 million rows, 8.5 hours for 1.7 million rows, 16 hours for 2.4 million rows, and 20 hours for 2.6 million rows on an Intel Core 2 Duo E8400 (6M Cache, 3.00 GHz Processor)].

When the plugging table is dependent on more than two parameters, the tradeoff between the level of refinement, accuracy, and table-generation time becomes even more important. Thus, a balance between the level of refinement and accuracy is necessary for achieving correct results. **Table 1** gives the only two formats of the plugging table that are acceptable to the simulator for a case where each of the F_w and F_o curves can be fully represented by three points, i.e., two line segments. This simplistic representation is only for illustration purposes and is unrealistic. Note that the values in the S_w and S_o vectors must be in ascending order.

Table 1: Two samples of a plugging table for the saturations shown in Fig. 2.

S_w	S_o	f_{mr}
a_w	a_o	$f_{mr}\,(a_w,a_o)$
b_w	a_o	$f_{mr}\,(b_w,a_o)$
c_w	a_o	$f_{mr}\,(c_w,a_o)$
a_w	b_o	$f_{mr}\,(a_w,b_o)$
b_w	b_o	$f_{mr}\,(b_w,b_o)$
c_w	b_o	$f_{mr}\,(c_w,b_o)$
a_w	c_o	$f_{mr}\,(a_w,c_o)$
b_w	c_o	$f_{mr}\,(b_w,c_o)$
c_w	c_o	$f_{mr}\,(c_w,c_o)$

S_o	S_w	f_{mr}
a_o	a_w	$f_{mr}\,(a_w,a_o)$
b_o	a_w	$f_{mr}\,(a_w,b_o)$
c_o	a_w	$f_{mr}\,(a_w,c_o)$
a_o	b_w	$f_{mr}\,(b_w,a_o)$
b_o	b_w	$f_{mr}\,(b_w,b_o)$
c_o	b_w	$f_{mr}\,(b_w,c_o)$
a_o	c_w	$f_{mr}\,(c_w,a_o)$
b_o	c_w	$f_{mr}\,(c_w,b_o)$
c_o	c_w	$f_{mr}\,(c_w,c_o)$

It is important to note that in the tables both S_w and S_o must range from zero to one, inclusive: although some combinations of S_w and S_o might add up to a value larger than one, they should be still included in the table. Otherwise, the simulator fills out the table for the missing points. This increases the computational time and can also introduce wrong values for f_{mr} (calculated by extrapolation) leading to incorrect results. Thus, the table must always have $\dim(S_w)\times\dim(S_o)$ rows, where $\dim(S_w)$ and $\dim(S_o)$ are the dimensions of S_w and S_o vectors.

Multi-dimensional tables are always interpolated *linearly* in the simulator. By multi-dimensional we mean that the target function (f_{mr} here) is a *multivariate* (S_w, S_o, etc.) function. Sometimes, F_w and/or F_o curve(s) might include linear segments. It is important to note that an extremely coarse representation of the linear segment(s) may introduce error into the calculation of f_{mr} by linear interpolation as shown in **Fig. 2** for a simple case. Therefore, sufficient refinement is required even in this case.

The foam models (i.e., F_w and F_o functions) and parameters used in this chapter are identical to those used in Chapter 3. (See Table B-1 for model parameters.)

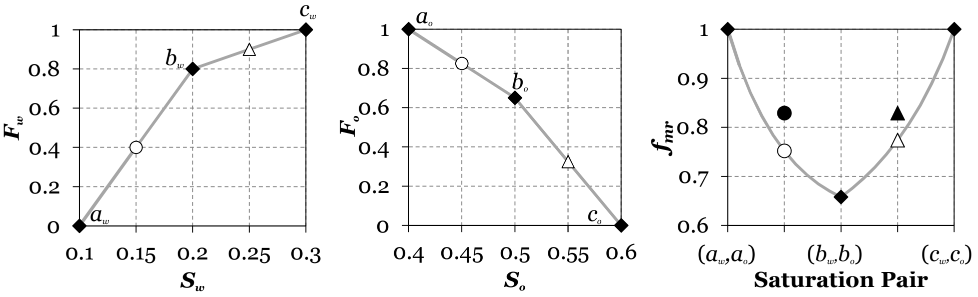

(a) (b) (c)

Fig. 2: Coarse representation of the linear segments in F_w and F_o curves has introduced an error in the f_{mr} calculation through linear interpolation, where $f_{mr} = (1+F_wF_o)^{-1}$. Each of the F_w and F_o curves are represented with only three points, called by a_α, b_α, and c_α (Figs. 2a and 2b). If we introduce two additional points on the F_w and F_o curves (i.e., the white-filled circle and triangle), the f_{mr} for the corresponding saturation pairs is calculated by linearly interpolating between the existing f_{mr} values in Fig. 2c resulting in the black-filled circle and triangle in this figure. However, the white-filled markers in Fig. 2c are the correct values of f_{mr} at those additional points. Although F_w and F_o curves are linear from a_α to b_α and from b_α to c_α, however, f_{mr} varies nonlinearly in these regions. Consequently, linear interpolation on the f_{mr} curve results in 10% and 7% error in the interpolated value of f_{mr} at the saturation pairs corresponding to the black circle and triangle in Fig. 2c, respectively.

4.3.3. Comparing the Monitor and Plugging Table

A plugging table must be refined sufficiently to be able to fully capture the behavior of the sensitivity functions. This can be investigated by comparing the results of two identical input decks one with a plugging table and another one with the corresponding monitor. The oil production profiles should coincide. An instance of this comparison is shown in **Fig. 3**. It is clear from the oil production profiles in the figure that the plugging table used is a good representation of the monitor. Therefore, in all our simulations in Chapter 5, replacing the monitor with a plugging table is of no harm to the quality of the results, due to the sufficient refinement of the table.

4.3.4. Compatibility with the Optimization Routine

The adjoint routine* in the 2010.1 version of the simulator is not capable of handling the foam monitor. We provide all the foam sensitivity functions (i.e., F_w, F_o, and F_s) in terms of exact functions in the monitor, and then all these functions are combined into the gas mobility-

---

* The adjoint routine provides analytical gradients used in the optimization routine for finding optimum control settings and is discussed in detail in Chapter 5.

reduction factor (Eq. 5). The present adjoint routine is not able to cope with monitors that cause state-dependent changes. For instance, foam monitor changes gas viscosity as a function of phase saturations. Future versions of the adjoint-based optimization routine in the simulator will be able to cope with this type of monitors and will require the user to provide the analytical derivatives of those functions. However, plugging tables are compatible with the present adjoint routine. As a result, the only option left at this point is applying plugging tables for incorporating the effect of foam in Chapter 5.

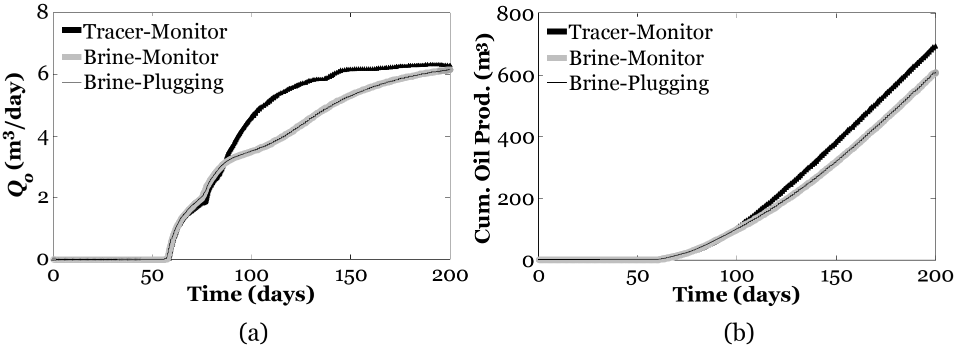

Fig. 3: Comparing different foam and surfactant models. In this figure, the switching time[*] is 30 days and the foam model is nonlinear (water weakens and oil kills foam and *epsurf* = 100; see §C.5 for the definition of *epsurf*). (a) Oil-production rate versus time. (b) Cumulative oil production versus time. Both injection and production wells are operating at constant prescribed bottomhole pressures. The foam front has not reached the production well at 200 days in any of the cases. Note that plugging tables are not compatible with passive tracers, so there is no plot corresponding to this combination.

4.4. Modeling Surfactant Transport

Surfactants serve as foaming agents for foam generation. Surfactants are generally injected into the reservoir in two different ways: injection in a SAG mode where foam is then generated as surfactant solution contacts gas inside the reservoir; and coinjection of aqueous surfactant solution and gas, i.e., foam injection. However, coinjection is operationally more challenging (Blaker et al. 2002). Blaker et al. (2002) performed a field-scale foam-assisted water-alternating-gas (FAWAG) project on the Snorre field with the purpose of gas mobility control. They list three parameters as the main factors describing the foam properties:

- surfactant molecular structure,
- surfactant concentration (C_s),
- foam quality (i.e., gas fraction of foam at reservoir conditions).

---

[*] At the switching time, surfactant solution injection is terminated and gas injection begins.

Various experimental studies (Svorstøl et al. 1996; Vassenden and Holt 1998; Mannhardt and Svorstøl 1999) revealed that foam strength was only sensitive to surfactant concentration at very low C_s. In addition, the mobility-reduction factor was invariant for foam qualities less than 95% (Cheng et al. 2000; Alvarez et al. 2001) [see also Yin et al. (2009) for an extensive study on the effect of optimum foam quality and surfactant adsorption behavior on CO_2-foam flooding]. Blaker et al. also name three additional criteria for the selection of surfactant:

- low surfactant loss,
- small minimum surfactant concentration ($C_{s,min}$) for foam generation,
- adequate mobility reduction.

Surfactant loss is mainly associated with three causes: *irreversible* adsorption to the rock surface, partitioning to the oil phase, and chemical or microbial degradation. The effect of the latter was minor. However, surfactant adsorption to the rock significantly limited the extent of foam propagation for a specific volume of injected surfactant in their case. They reported adsorption of 0.5 mg/g rock for a sandstone rock in the Snorre field. Their simulations showed that adsorption and $C_{s,min}$ have the largest impact on the foam efficiency. In their case, the critical-micelle concentration (CMC) of the surfactant was of the order of 0.01 wt.%. The CMC is the surfactant concentration above which micelles are spontaneously formed.

In our simulations in Chapter 5, we took the critical-surfactant concentration (C_s^*) for foam generation half the injected concentration; $C_{s,inj}$ = 0.24 wt.%. This choice is based on a strategy to minimize the effects of numerical dispersion; see §C-5 for more detail. Note that C_s^* is different from the CMC and CMC $\ll$ C_s^*. A 0.24 wt.% (or 2400 ppm) surfactant solution means that there is 2.4 kg of surfactant in every 1000 kg of the surfactant solution.

In the simulations performed in this work, for the sake of simplicity, we do not consider the adsorption of surfactant on the rock surface. We assume that there has been a surfactant preflush into the reservoir prior to the start of the foam flooding process to satisfy adsorption. However, from the economical point of view, the cost of this surfactant preflush might exceed the oil revenue and make the entire process uneconomical. In order to have an economically sound foam EOR process, the cost of the surfactant preflush must be much lower than the oil revenues. The procedure for calculating the surfactant preflush size is explained in Appendix A of Renkema and Rossen (2007). Based on that, the following inequality must hold:

$$\begin{gathered}\text{oil revenue} \gg \text{cost of surfactant preflush or}\\ \frac{\varphi V_{res}\left(S_{oI}-S_{org}\right)}{0.159}\times(\text{oil price/bbl})\times\frac{RF}{100}\gg \rho_{rock}V_{res}\left(1\text{-}\varphi\right)\times(\text{kg surf. ads./kg rock})\times(\text{surf. cost/kg surf.}),\end{gathered} \tag{6}$$

where S_{oI} is the initial oil saturation in the reservoir *before* the preflush, S_{org} is the residual oil saturation to gas flood, *RF* is the *percentage* of movable oil[*] produced *after* preflush, V_{res} is the reservoir volume, φ is porosity, ρ is density, and 0.159 is the conversion factor for converting m³ to barrels. Note that we used S_{org} as the lowest reachable saturation after foam EOR, because gas is the major displacing agent in foam EOR processes. We can reformulate Eq. 6 in the more clear format as follows:

$$\frac{\text{oil price/ bbl}}{\text{surf. cost/ kg surf.}} \gg \frac{100}{RF} \times \frac{0.159(1-\varphi)}{\varphi} \times \frac{\rho_{\text{rock}}}{\left(S_{oI}-S_{org}\right)} \times \left(\text{kg surf. ads./kg rock}\right). \qquad (7)$$

This inequality is independent of the reservoir volume V_{res}, which vanishes from both sides of Eq. 6. It is also independent of injected surfactant concentration, since it is based entirely on adsorption. Foam EOR processes usually start when waterflooding is no longer economical, and S_{oI} is the average water saturation at this stage. This formula is derived under two implicit assumptions: first, surfactant comes into contact with the entire rock surface in the reservoir; and secondly, it ignores the surfactant left in the fluids at the end of the process. Therefore, Eq. 7 is just a rough estimate, and over-estimates adsorption, since sweep is not complete. For a typical water-wet sandstone reservoir with S_{oI} = 0.3, S_{org} = 0, φ = 0.2, ρ_{rock} = 2650 kg/m³, and the above-mentioned adsorption value of 0.5 g surfactant per kg of rock, the right side of Eq. 7 is approximately equal to 280/*RF*. Thus, the above inequality holds if the oil price per barrel is at least (280/*RF*) times higher than the surfactant cost per kg. An average-quality surfactant (those injected with water) generally costs 3-10 $/kg. Specialized surfactants designed for specific purposes may cost up to 30 $/kg[†]. With these parameters, if surfactant costs 6 $/kg on average, the oil price must be very much higher than (1680/*RF*) $/bbl. With the current oil price of 110 $/bbl[‡], the entire oil revenue pays off for only the cost of the surfactant adsorbed to the rock surface, if *RF* = 15%. We also emphasize that there is a cost associated with the surfactant preflush as well. Thus, an economical SAG process is the one that its total oil revenue is well above the surfactant cost adsorbed to the rock surface plus the cost of the surfactant preflush (plus the cost of the injected gas, operational costs, etc.).

This brief analysis reveals the crucial role of surfactant cost on the economics of a foam EOR process and the importance of optimizing its use. We note that higher oil prices result in more expensive surfactants, as their ingredients are manufactured from oil. One way to make this process more profitable is by reducing the surfactant retention due to adsorption on the rock surface, for instance by applying alkali agents (Flaaten et al. 2009, 2010). We optimize the

---

[*] By that we mean the movable oil in place before the start of surfactant preflush, i.e., $\varphi\, V_{res}\, (S_{oI} - S_{org})$.

[†] Personal communication T. Matsuura, Shell Global Solutions International, Rijswijk.

[‡] Average OPEC basket price in May 2011.

amount of the injected surfactant in Chapter 5 to maximize the oil-recovery factor in a SAG process. However, optimizing the net-present value (by considering the surfactant cost) may result in a different optimum.

There are two approaches for modeling surfactant transport in the simulator which are applied later in Chapter 5 but not in the simulations shown later in §4.5. One is through defining the surfactant as a passive tracer and the other one is by modeling it as an active component. An active component is the normal type of component used in simulations. We specifically use the brine option in Chapter 5, that allows for the injection of saline water into the reservoir and we imagine that salt is representing the surfactant in the simulations.

4.4.1. Passive Tracer

A passive tracer can be regarded as a dye in a fluid. It does not influence the properties of the fluid that carries it, contrary to a normal component. Currently, a passive tracer must be attached to one component (H_2O, HEAVY, or LIGHT) in the simulator (Dynamo/MoReS Online User Documentation 2010). We inject surfactant together with water (H_2O component) into the reservoir and the amount of dissolved surfactant in the aqueous solution is so small that it does not change the properties of water (though it does affect the transport of gas by imposing the foam model). Thus, surfactant is well represented by a passive tracer. In order to have a proper definition of surfactant as a passive tracer, surfactant must stay in the same phase as the host fluid. This is automatically taken care of when surfactant is attached to H_2O, because H_2O is only present in the water phase. However, it is not always possible to inject surfactant with gas, since surfactant must be attached to the LIGHT component that can be present in both oil and gas phases. Injecting surfactant with gas is only possible if there is no LIGHT component in the oil phase.

Passive-tracer fluxes are computed with a dedicated solver that reduces numerical dispersion. This solver is separate from the one that solves the material balance for the normal components in water, oil, and gas phases. This dedicated solver employs a high-order-accurate discretization scheme for computing the tracer fluxes. The tracer solver is based on the fact that passive tracer is transported by the host fluid without altering its properties. At every time step, the fluxes of the normal components are calculated first and the tracer equation is solved next (Dynamo/MoReS Online User Documentation 2010).

It is also important to note that plugging tables are incompatible with passive tracers, because plugging tables do not accept passive-tracer concentration (TRC) as an input. In the F_s function defined in the monitor, TRC directly replaces the surfactant concentration.

4.4.2. Brine

The brine option in the simulator represents the surfactant as a normal active component. Therefore, it suffers from stronger numerical dispersion than when treating surfactant as a passive tracer (**Fig. 4**). Numerical dispersion results in artificial mixing of the fluids and faster propagation of the leading edge of the entire surfactant bank. As a result, surfactant breaks through faster when numerical dispersion exists. The brine option was originally designed for injecting water into the reservoir with a salinity so much different from the original water in the reservoir that it makes the property differences important. Thus, the water phase comprises two components: H_2O and INJECTED_H_2O. The H_2O component refers to the in-situ reservoir water and the INJECTED_H_2O indicates the injected water with different salinity. The density and viscosity of the water phase in each gridblock is dependent on the relative amounts of its two components. The water relative permeability is independent of the water phase composition. The INJECTED_H_2O component only exists in the water phase and is solved as a fully coupled component adding an extra equation to be solved (Dynamo/MoReS Online User Documentation 2010).

Here, we imagine that *salt* is our surfactant and we incorporate its concentration as the surfactant concentration in our foam model. We further assume that the original water in the reservoir has zero salinity (as there is no surfactant initially present in the reservoir).

The brine option is an alternative to the passive tracers but *is not equivalent*. The brine option has two main shortcomings:

- Salt is defined as a normal component in the water phase: hence, it changes the water properties (i.e., density, viscosity), contrary to the passive tracer. A simple *pressure dependent* linearization with zero reference pressure is performed in the simulator to calculate both water-phase density and viscosity. The density of the injected brine solution with 2400 ppm of salt at zero reference pressure is 985.04 kg/m^3 as opposed to the zero-salinity water density of 983.3 kg/m^3 (i.e., less than 0.18% change in density). The water viscosity in the absence of salt is 4.667E-4 Pa·s and the viscosity of the brine solution is 4.678E-4 Pa·s (i.e., less than 0.24% viscosity change). Therefore, for our case, changes in both density and viscosity are negligible and this shortcoming does not raise a concern. The difference could be made even smaller by using a lower salinity to represent the injected surfactant concentration.
- It suffers from higher numerical dispersion than the passive-tracer option: therefore, the brine front is more dispersed and travels ahead of the passive-tracer front (Fig. 4). This can greatly affect the solutions and the oil production in the ways discussed in §4.4.3.

Overall, the brine option is less accurate than the passive-tracer option in the case investigated in Chapter 5. It is preferable to incorporate the surfactant transport by a passive tracer, unless optimization by the adjoint routine is the ultimate aim (see §4.4.4 for compatibility issues).

Both monitors and plugging tables are compatible with the brine option for incorporating the effect of foam. Plugging tables directly accept the brine composition in the water phase as an input. When defining a plugging table, the brine composition must be multiplied by the concentration of the injected brine (i.e., 0.0024 here) to retrieve the value of C_s in F_s function.

4.4.3. Comparing the Passive-Tracer and Brine Option

As mentioned earlier, the brine option suffers from worse numerical dispersion than treating surfactant as a passive tracer in the case investigated in Chapter 5. Therefore, the leading edge of the *surfactant* front modeled with the brine option (surf$_{brine}$) travels *ahead* of the *surfactant* front modeled with the passive-tracer option (surf$_{tracer}$). However, Fig. 4 illustrates that the *foam* front obtained from the brine option (foam$_{brine}$) is *behind* the *foam* front obtained from the passive-tracer option (foam$_{tracer}$). (In Fig. 4, foam fronts are represented by heavy-black lines.) We discuss the cause of this paradox in the paragraph below. It should be noted that dispersion would not affect the position of the foam front (triggered at half the injected surfactant concentration) if the dispersed surfactant concentration profile were symmetric. It is not, for two reasons: radial flow, and the change in water saturation at the foam front (Cheng 2002).

In the formulation of our foam model, foam forms abruptly when C_s exceeds C_s^*. The amount of injected surfactant is identical for both the brine and passive-tracer option (0.216 PV). Thus, since the advance of the surf$_{tracer}$ front is less than the surf$_{brine}$ front, there is a chance to meet $C_s \geq C_s^*$ criterion in more gridblocks with the passive-tracer option than the brine option. This is clearly seen in Fig. 4 by comparing the location of the white and black fronts.

Since the foam$_{tracer}$ front stays ahead of the foam$_{brine}$ front, oil is swept more efficiently with the passive-tracer option resulting in higher oil recovery (Fig. 3). In addition, less gas is injected, and less gas is produced from the reservoir with the passive-tracer option. To elaborate, both wells are operating at constant prescribed bottomhole pressures; hence, the overall pressure drop in the reservoir is fixed. The overall gas mobility is lower with the tracer option (foam is present in more gridblocks with the passive-tracer option compared to the brine option). Therefore overall, less gas is injected into the reservoir with the further advance of foam to conform with the fixed overall pressure drop.

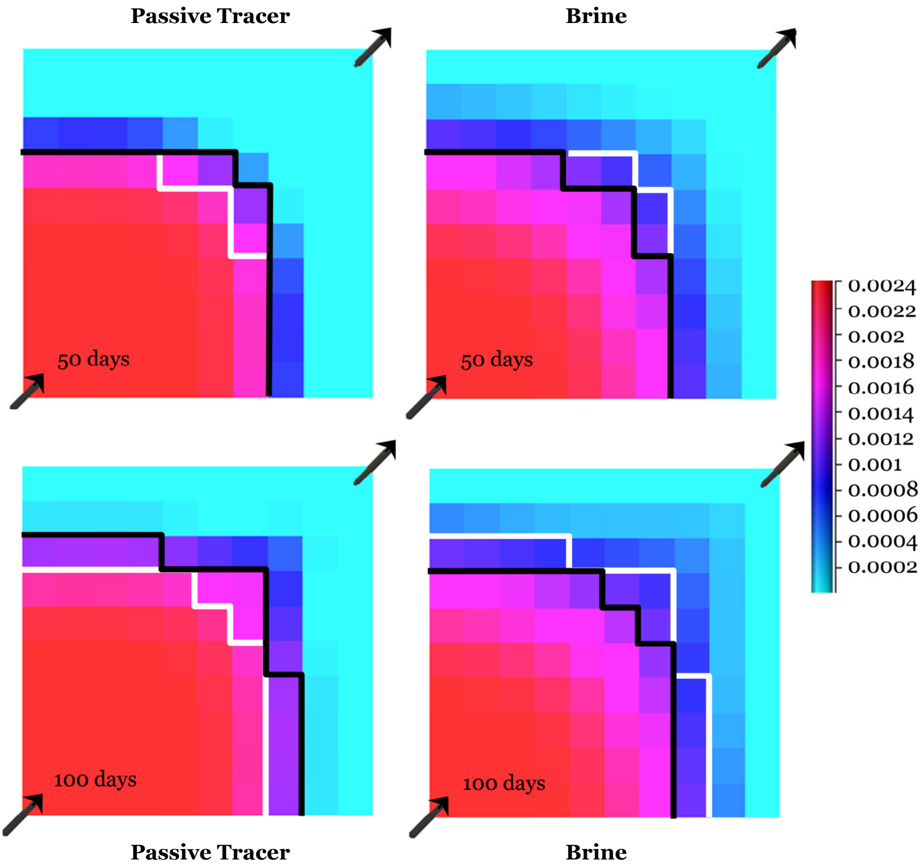

Fig. 4: Comparing the surfactant-concentration profiles for the passive-tracer and brine option (*epsurf* = 100 and $C_s^* = 0.0012$; see §C.5 for more details). The simulations are in 3D, but only the top layer is shown for the sake of clarity. The foam/no-foam boundary in each figure is shown by a heavy-black line; whereas the heavy-white line corresponds to the location of the boundary at the same time but with the other surfactant-flow modeling option. For instance in the top-left figure, the black boundary corresponds to the passive-tracer option and the white boundary corresponds to the brine option, both at 50 days. This figure shows that the foam front with the passive-tracer option is ahead of the foam front with the brine option. In both cases, foam is modeled by the monitor option. Both wells are operating at constant prescribed bottomhole pressures. The total simulation time is 200 days and we inject 0.216 PV of surfactant solution during the first 30 days, after which surfactant injection stops and gas injection starts. The foam front has not reached the production well at 200 days in any of the cases.

4.4.4. Compatibility with the Optimization Routine

The adjoint routine in the 2010.1 version of the simulator is not compatible with passive tracers (passive-tracer flux is computed by a dedicated solver and the adjoint algorithm is not yet extended to deal with that). Therefore, the only choice is applying the brine option for modeling surfactant transport in Chapter 5. Brine is considered as another component in the model and hence it does not have the same advantage as the passive tracer, that is the *limited* dispersion (i.e., numerical dispersion is higher with the brine option). We have compared these two options in detail in §4.4.3.

Application of the brine option clearly affects the results and lowers the cumulative oil production compared to the passive-tracer option (also seen in Fig. 3) in ways discussed in §4.4.3. One has to be aware of this drawback of the brine option when interpreting the results.

4.5. 1D Simulations

The reservoir (**Fig. 5**) is a 100×1×1 m horizontal, homogeneous block with one injection and one production well located at the center of the first and last gridblock, respectively. It has a porosity of 20% and a horizontal permeability of 100 mD. Flow is rectilinear and one-dimensional in the reservoir and gravity effects are disregarded.

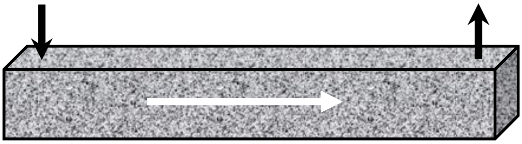

Fig. 5: 1D reservoir.

The foam model used in this chapter incorporates only the effect of water and oil saturations on foam strength and foam strength is not affected by surfactant concentration (i.e., it is assumed that there is enough surfactant everywhere in the reservoir at all times). Thus, surfactant transport is not modeled here. It is further assumed that enough surfactant is already injected into the reservoir to satisfy adsorption.

Verifying the simulator results with the 1D analytical solutions obtained by the MOC in Chapter 3 requires as close as possible the exact representation of the assumptions behind the MOC in the simulator. Here, we compare the MOC solutions obtained in Chapter 3 with the results obtained from the simulator at identical conditions. The MOC solutions in Chapter 3 are based on the linear relative-permeability model described in §3.2.1. Foam strength is sensitive only to water and oil saturations, through the F_w and F_o functions in Eq. 5. All the phases are assumed incompressible (i.e., no density change with pressure change). In the MOC solution, the phases are assumed to be completely immiscible (i.e., there is no mixing of any kind between the phases). We do not allow for any miscibility or phase behavior between the phases. All the properties are taken from Table B-1.

We investigate two different injection conditions (J): the gas-injection cycle (f_g = 1) of a SAG flood (hereafter referred to as *gas/SAG*) and continuous coinjection of surfactant solution and gas ($f_g \approx 2/3, f_w \approx 1/3$), hereafter referred to as *foam flood*.

In Chapter 3, comparisons were based on the parameter $t_{D,final}$ (final recovery time) defined as the dimensionless time to produce all the movable oil (oil in excess of residual saturation). For instance, $t_{D,final}$ = 200 means that it takes 200 PV of the injected fluid to recover all the movable oil. For the sake of comparing this dimensionless parameter with the outcome of the simulator, we need to translate $t_{D,final}$ to dimensional injection rates. For instance, it takes 200 years to produce all movable oil for a process with $t_{D,final}$ = 200 when injecting 1 PV of fluid per year. This is equivalent to injecting a total of 0.055 m^3/day of fluid (in foam flood with $f_g \approx 2/3$, this implies injecting 0.03645 m^3/day of gas and 0.01855 m^3/day of water).

For both injection conditions, a constant total injection rate must hold for the entire simulation to match the MOC solutions and maintain a fixed ratio with physical time. This condition is met only if the injection well operates at a constant injection rate as the active constraint during the entire simulation. If the maximum bottomhole pressure of the injection well ($P_{wf,max}^{inj}$) is exceeded for any reason (such as formation of strong foam near the well), the active constraint will change into $P_{wf,max}^{inj}$ and the well will no longer operate at the prescribed constant injection rate until the bottomhole pressure drops below $P_{wf,max}^{inj}$ again. To avoid this complexity, we set $P_{wf,max}^{inj}$ at a relatively high value that is never reached. The production well operates at a constant prescribed bottomhole pressure ($P_{wf,min}^{prod}$).

Moreover in foam flood, the constant volumetric gas/water ratio of (2/3)/(1/3) = 2 must be also maintained at all times to ensure matching the analytical solution. This is done by specifying the mass fractions of the injected phases, corresponding to a volumetric gas/water ratio of 2. In this case, the injected mass fraction of water is approximately 0.982 and for gas is one minus this value. Since the phases are incompressible, maintaining a constant mass ratio is equivalent to maintaining a constant volumetric ratio. As a result, the saturations corresponding to the injection state must match the saturations at J in Chapter 3 in every case. This is also a good test for examining whether the foam model defined by a plugging table is indeed a good representation of the exact functions or not.

In all the cases studied below, the total injection rate is set to 1 PV/year. This injection rate might be unrealistic in a real field application. However, the purpose of this chapter is examining whether or not the simulator is capable of accurately simulating a foam process by matching the MOC solutions in Chapter 3.

4.5.1. Choice of Time-Step and Gridblock Size

In general, the time-step (Δt) and gridblock size (Δx) cannot be chosen independently. Proper choice of Δt and Δx is of extreme importance in simulating foam processes. Numerical simulations can only capture the correct displacement behavior, if choices of Δt and Δx suit the nature of the problem of interest. The foam EOR process introduced in Chapter 3 has a complex nature due to the structure of the foam model and its effect on gas mobility in the presence of foam. Foam dries out and partially collapses abruptly in the absence of enough water. In addition, it might be also destroyed in the presence of too much oil. Both of these effects can introduce drastic changes in gas mobility (the larger is *fmmob*, the sharper the changes are) leading to complex displacements including shocks. If the MOC solution is in the proximity of the boundaries at which gas mobility changes drastically, numerical dispersion may introduce oscillations over this boundary leading to incorrect solution for an improper choice of Δt and Δx.

Apart from the accuracy of the foam plugging tables (if applied), the appropriate choice of $\Delta t/\Delta x$ (and also individual Δt and Δx) can significantly improve the match of the simulation to the analytical solution. For the sake of illustration and clarity, we elaborate on the effects of the choices of Δt, Δx, and $\Delta t/\Delta x$ ratio for a single case. In this particular case shown in **Fig. 6**, foam is killed at $S_w \leq S_w^*$ ($S_w^* = 0.316$). Thus, $S_w = S_w^*$ line is a *foam/no-foam boundary*. There is low-mobility foam on one side ($S_w > S_w^*$) and high-mobility gas or *no foam* on the other side ($S_w \leq S_w^*$). Thus, there is a drastic change in gas mobility over the *foam/no-foam* boundary. The injected foam quality is 2/3 and the initial oil saturation $S_o(I)$ is 0.73 (point *I*). According to the MOC solution, the displacement route consists of only two rarefaction waves (i.e., slow and fast) meeting at the constant-state region *IJ* in Fig. 6 (i.e., *J*-slow-*IJ*-fast-*I*). Although $S_o(I)$ is too high for the start of a foam flood, we picked this specific case because of the interesting behavior of its numerical solution. We observed that numerical simulators may have difficulty in converging to the correct solution in displacements in which part of the solution is extremely close to the *foam/no-foam* boundary (see Fig. 5a in Chapter 3 for the MOC solution of this case). This problem is more pronounced when the changes in properties (gas mobility here) over the boundary are significant.

Fig. 6 illustrates the sensitivity of the numerical solution obtained by the simulator for various choices of $\Delta t/\Delta x$ ratio while keeping $\Delta x = 1$ m. Oscillations occur for $\Delta t/\Delta x > 0.04$ day/m and the solution is scattered around the MOC solution (**Figs. 7a and 7c**). However, simulations exhibit no oscillations, and they closely follow the MOC solution, for $\Delta t/\Delta x \leq 0.04$ day/m (Figs. 6 and 7b). We see from Fig. 7b that at fixed $\Delta x = 1$ m, the saturation profiles overlay for $\Delta t/\Delta x \leq 0.04$ day/m and reducing Δt further does not make a visible improvement in the solution. The numerical dispersion caused by time discretization at $\Delta t \leq 0.04$ day is negligible compared to the numerical dispersion introduced by $\Delta x = 1$ m. This is the closest that one can get to the MOC solution with $\Delta x = 1$ m, since the remaining mismatch between the numerical and the MOC solution corresponds to the numerical dispersion due to spatial discretization.

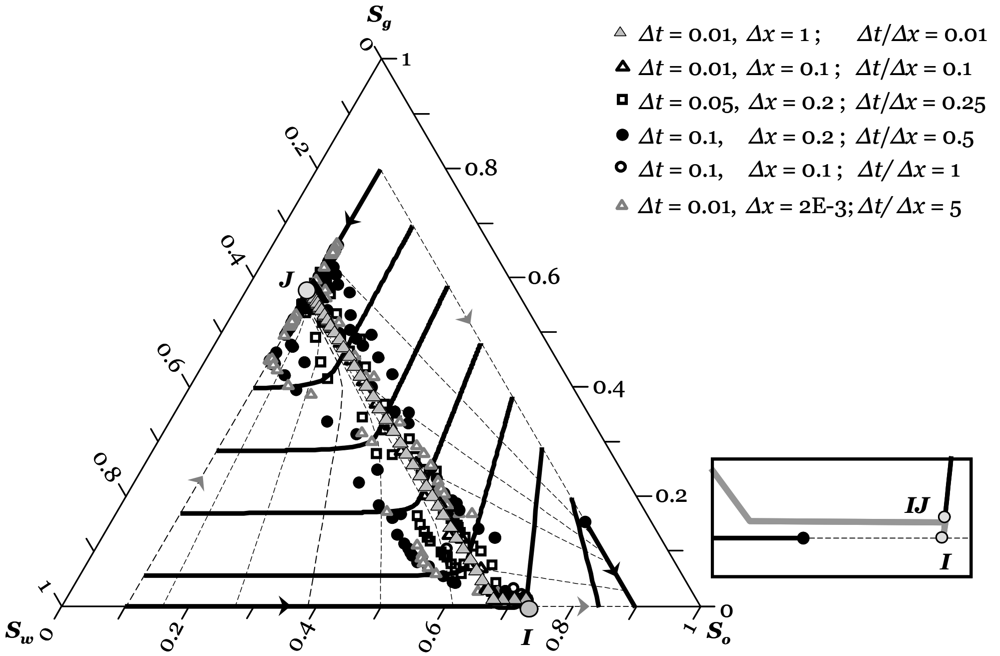

Fig. 6: Numerical simulations do not always find the correct solution and may sometimes exhibit oscillations. The reservoir is initially at (0.27, 0.73, 0) and foam is killed at $S_w \leq S_w^*$ ($S_w^* = 0.316$) and oil has no effect on foam strength, and the solutions shown are for a foam flood with an injection condition at (0.32335, 0.1, 0.57665) or foam quality of 2/3 ($f_g = 2/3$). The simulator results are shown for various $\Delta t/\Delta x$ ratios with constant Δx = 1 m (reservoir is 100 m long). For $\Delta t/\Delta x \leq 0.04$ day/m (see Table 2), simulations closely follow the MOC solution in Fig. 8a in Chapter 3. Foam is modeled with a monitor. Water-saturation profiles are shown in Fig. 7.

Table 2: Oil-recovery factors (RF_{sim}) for various choices of Δt at Δx = 1 m for the case shown in Fig. 6. RF_{sim} is obtained from the simulator at $t_{end,\mathrm{MOC}}$ that is the time at which all the mobile oil is recovered from the reservoir according to the MOC solution. Fig. 7 shows that for $\Delta t/\Delta x \leq 0.04$ day/m, the saturation profiles coincide but do not perfectly match the MOC solution. RF_{sim} exhibits the same behavior and it remains unchanged for $\Delta t/\Delta x \leq 0.04$ day/m. For ratios exceeding 0.04, the solution is no longer valid due to oscillations. Also, high RF values at $\Delta t/\Delta x > 0.04$ day/m are misleading and one should not take that as an indication of finding the match with the MOC solution by the simulator.

Δt (day)	$\Delta t / \Delta x$ (day/m)	RF_{sim}(%) (at $t_{end,\mathrm{MOC}}$)
0.001	0.001	97.2
0.01	0.01	97.2
0.04	0.04	97.2
0.1	0.1	97.9
0.5	0.5	98.3
1	1	99.2

This is also observed for oil-recovery factors for this case shown in **Table 2** in which further refinement in time does not change the recovery factor. In short, reducing Δt beyond a certain limit at a fixed Δx does not lead to any further improvement.

We also performed the same practice as in Table 2 for Δx = 0.25 m. We still found the same ratio, $\Delta t/\Delta x$ = 0.04 day/m, as the threshold between the valid and invalid numerical solution. It should be noted however that, this threshold ratio is case dependent and might be smaller or larger than 0.04 for the other cases studied in this chapter.

The source of oscillations observed in Figs. 6 and 7 is numerical dispersion. Numerical dispersion is mainly a function of Δt and Δx and is also proportional to total velocity and also the derivative of the fractional-flow function with respect to saturation $\mathrm{d}f_\alpha/\mathrm{d}S_\alpha$ (Salimi and Bruining 2011; also see Appendix D for more details). The proximity of the MOC solution to the foam/no-foam boundary at $S_w^* = 0.316$ (see Fig. 6) makes this case extremely sensitive to the magnitude of numerical dispersion. Therefore, an inappropriate choice of Δt and Δx magnifies the numerical dispersion term, leading to an inaccurate flux approximation and consequently to incorrect saturations. A small error in saturation approximation might cause the solution to fall on the wrong side of the boundary (no-foam side with $S_w \leq S_w^*$).

With Δx = 1 m (Table 2), choices of Δt > 0.04 day are inappropriate and lead to fluctuations. However, the numerical solution closely follows the MOC solution with $\Delta t \leq$ 0.04 day as seen in Figs. 7b and 7d. We illustrate the typical shape of the fluctuations in S_w over time for Δt = 1 day and Δx = 1 m in Fig. 7c. We elucidate the cause of these oscillations in the *first* gridblock. This gridblock is initially at $S_w(I) = 0.27$ and we start injecting *foam* into this gridblock with $f_g = 2/3$, which corresponds to $S_w(J) = 0.32335$ [note that $S_w(J) > S_w^*$]. According to the MOC solution in Fig. 7d, S_w must rise monotonically from $S_w(I)$ and eventually reach $S_w(J)$ without oscillations. At the injection point J, water and gas mobilities are 280 and 535 (Pa·s)$^{-1}$, respectively. Thus, gas is more mobile than water at J and moves more easily out of the first gridblock. Accordingly, S_w rises in this gridblock (not in agreement with the MOC due to numerical dispersion) until exceeding S_w^* at which foam forms for the first time in gridblock 1 (**Fig. 8**) at time step 21 or 1.05 day and λ_g drops to 3 (Pa·s)$^{-1}$ while water mobility is 290 (Pa·s)$^{-1}$. As mentioned earlier, numerical dispersion is proportional to $\mathrm{d}f_\alpha/\mathrm{d}S_\alpha$: the higher is $\mathrm{d}f_\alpha/\mathrm{d}S_\alpha$, the higher the numerical dispersion is. At this moment, $\mathrm{d}f_w/\mathrm{d}S_w > \mathrm{d}f_g/\mathrm{d}S_g$, so the numerical dispersion effect is larger for water. Thus, the *water* output flux is *overestimated* due to numerical dispersion, leading to an artificial decrease in S_w and artificial increase in S_g. This numerical artifact continues to reduce S_w until it falls below S_w^* where foam collapses and $\mathrm{d}f_g/\mathrm{d}S_g > \mathrm{d}f_w/\mathrm{d}S_w$ (time step 22). Thus, *gas* output flux is *overestimated* and S_w starts to rise until it exceeds S_w^* for the second time (time step 23).

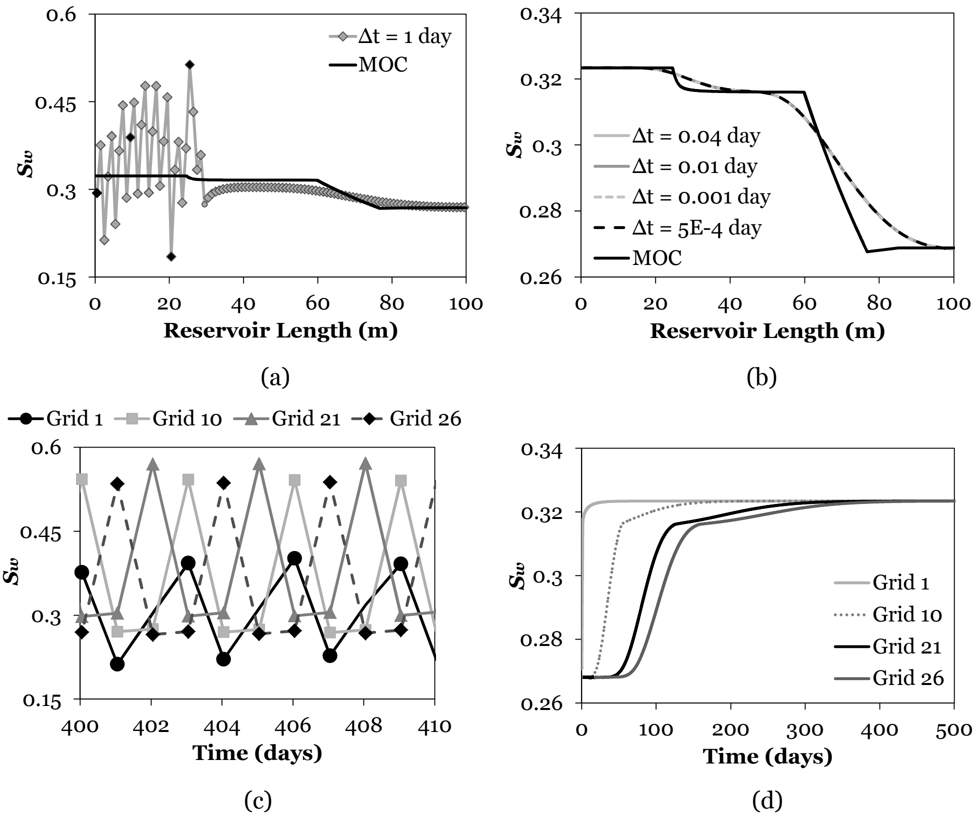

(a) (b)

(c) (d)

Fig. 7: (a) Water-saturation profiles at t = 300 days for the case shown in Fig. 6. Δt = 1 day and Δx = 1 m ($\Delta t/\Delta x$=1 day/m); the simulator is not finding the correct solution; details of the MOC solution is more visible in Fig. 7b. The black markers on the Δt = 1 curve correspond to gridblocks 1, 10, 21, and 26. (b) Water-saturation profiles at 300 days at various (small) time-step sizes (Δx = 1 m). Simulation results for $\Delta t/\Delta x \leq$ 0.04 day/m have no oscillations and are close to the MOC solution. At t = 300 days, only the *J*-slow-*IJ* segment of the entire displacement route is visible. *J* is visible from 0 to 24.5 m, slow path from 24.5 to 85.2 m, and *IJ* from 85.2 m onwards. The relatively flat part of the profile in the middle is not a constant state but corresponds to the corner in the slow path magnified in the inset of Fig. 6. (c) Fluctuations in water saturation over time in the gridblocks depicted by black markers in Fig. 7a between 400 and 410 days. The saturation in each of the gridblocks constantly fluctuates back and forth between an upper and a lower bound from one time step to the next. This behavior lasts forever and never returns to the injected value. (d) Saturation change over time in the absence of oscillations (Δt = 0.01 day and Δx = 1 m). In Fig. 7d, S_w in all gridblocks finally reverts to the injected value. Note that the vertical scales of the figures are not the same.

This oscillating behavior repeats itself forever to keep the numerical scheme mass conservative in the gridblock and water saturation in the gridblock never reverts to $S_w(J)$. In short, the inaccurate estimation of S_w is illustrated by fluctuating across the foam/no-foam boundary as observed in Fig. 7c. As the front moves, other gridblocks inherit this symptom and start to fluctuate. As mentioned earlier, this symptom is observed for $\Delta t > 0.04$ day at $\Delta x = 1$ m (see Table 2). However, the numerical solution closely follows the MOC solution with $\Delta t \leq 0.04$ day (Figs. 7b and 7d).

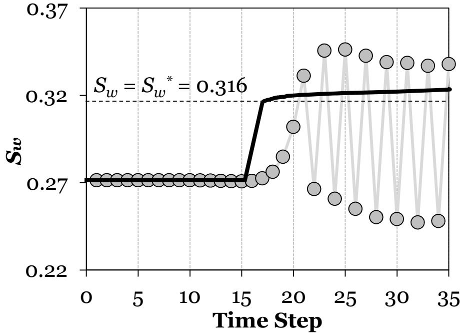

Fig. 8: S_w profile per time step in the first gridblock for the case shown in Figs. 6 and 7. The oscillating profile corresponds to $\Delta t = 1$ day and $\Delta x = 1$ m, and the solid-black line is for $\Delta t = 0.01$ day and $\Delta x = 1$ m.

As mentioned earlier, it is not possible to improve the solution beyond a certain limit at a fixed Δx by refining Δt (Fig. 7b). The solution can be improved in two ways:

(1) by fixing Δt and reducing Δx: By reducing Δx at a fixed Δt, the $\Delta t/\Delta x$ ratio increases. Consequently, Δx must stay above a certain limit (that is case dependent) in order to prevent oscillations caused by a relatively large $\Delta t/\Delta x$ ratio. With $\Delta t = 0.01$ day, oscillations are observed for $\Delta x < 0.2$ m or $\Delta t/\Delta x > 0.05$ day/m and we could not obtain a close match with $\Delta x > 0.2$ m. However, there is more stability at a smaller Δx if Δt is smaller. Results for $\Delta t = 5\text{E-}4$ day are shown in **Fig. 9**, in which we get very close to the MOC solution at $\Delta x = 0.033$ m ($\Delta t/\Delta x = 0.015$ day/m) and the solution is still free from oscillations.

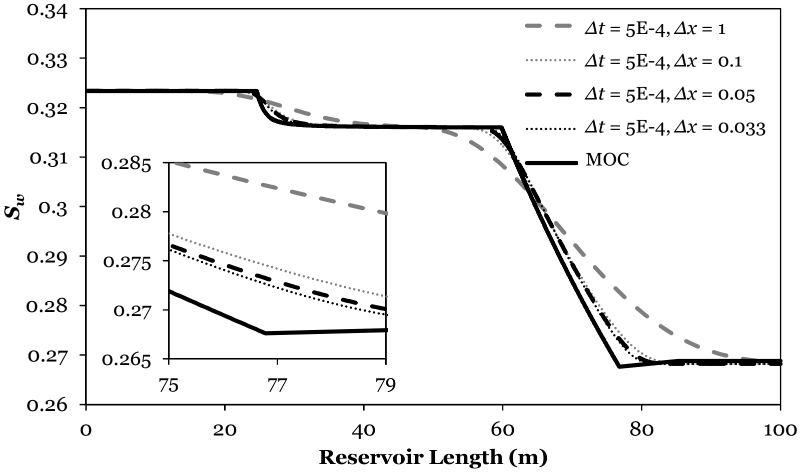

Fig. 9: S_w profiles at 300 days for various choices of Δx (m) at Δt = 5E-4 day for the case in Fig. 6.

(2) by fixing $\Delta t/\Delta x$ and reducing both Δx and Δt with the same proportions: For a fixed $\Delta t/\Delta x$ ratio of 0.01 day/m (**Fig. 10**), the solution improves significantly by refining both Δx and Δt proportionally.

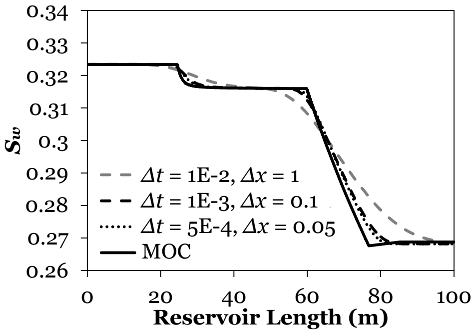

Fig. 10: Water-saturation profiles at 300 days for selected cases in Table 3 at $\Delta t/\Delta x$ =0.01 day/m.

We also investigated the effect of different choices of Δt and Δx at a fixed $\Delta t/\Delta x$ ratio of 0.01 day/m on the oil-recovery factor (see **Table 3**). For all the choices studied, the numerical solution closely follows the analytical solution without oscillations; however, the accuracy in predicting the oil-recovery factor differed. Smaller choices of Δt and Δx lead to more accurate predictions, as also shown in Fig. 10. However, the simulation time increases significantly for the smaller choices of Δt and Δx, whereas the accuracy of RF_{sim} (at $t_{end,\mathrm{MOC}}$) is not improved that much after a certain limit. Therefore, we need to preserve a balance between the runtime (i.e., choice of the Δt and Δx) and the acceptable error in RF_{sim}.

Table 3: Effect of the choice of Δt and Δx at a constant ratio of $\Delta t/\Delta x$ =0.01 day/m for the case in Fig. 6. At this ratio, the simulator results are without oscillations and the RF_{sim} estimate approaches 100% upon refining Δt and Δx. Water-saturation profiles for selected cases are shown in Fig. 10.

Δt (day)	Δx (m)	RF_{sim}(%) (at $t_{end,\mathrm{MOC}}$)
0.1	10	88.68
0.01	1	97.22
0.005	0.5	98.27
0.0025	0.25	98.98
0.001	0.1	99.55
0.0005	0.05	99.79

4.5.2. Simulation Results

The simulation results are divided into two sections based on the way that the effect of foam is incorporated in the model, i.e., monitor or plugging table. Each section has two subsections based on the two injection conditions investigated: foam flood ($f_g \approx 2/3, f_w \approx 1/3$) and gas/SAG ($f_g = 1$). In all the cases shown below, a sensitivity analysis similar to that above is performed for finding the best choice of time-step and gridblock size that matches the MOC analytical solution. However, the simulator is unable to find a match in some cases.

In all the cases, the injection rate is equal to 1 PV/year. $t_{end,\mathrm{MOC}}$ represents the time required in years to produce all the movable oil, as calculated by the MOC. RF_{sim} is the oil-recovery factor[*] obtained from the numerical simulations at $t_{end,\mathrm{MOC}}$. We terminate the simulations in the simulator at $t_{end,\mathrm{MOC}}$. The MOC solution gives 100% oil-recovery factor at this time. In some cases that will be elaborated on later in this section, the simulator gives a value of RF_{sim} at $t_{end,\mathrm{MOC}}$ very close to 100% (i.e., RF_{MOC} at $t_{end,\mathrm{MOC}}$); even though the solution shows oscillations around the MOC solution. As a result, mere closeness of RF_{sim} to 100% is not always a correct indicator that the simulator has found the correct solution (see §4.5.2.1.2).

In the tables below, only the choice of Δt and Δx leading to the match with the MOC is given. A match is indicated between the simulator result and the MOC solution if all the following conditions are met: (1) the numerical solution (saturation and pressure) is free from any oscillations, (2) saturation profile from the simulator closely follow the MOC solution (e.g., see Figs. 6 and 7), and (3) the value of RF_{sim} at $t_{end,\mathrm{MOC}}$ is close to 100% (i.e., RF_{MOC} at $t_{end,\mathrm{MOC}}$). For instance, in the case discussed in §4.5.1, the simulator had no oscillations for $\Delta t \leq 0.04$ day at $\Delta x = 1$ m. Fig. 7b and Table 2 show that the solutions found for $\Delta t \leq 0.04$ day are not exactly matching the MOC solution, but approximating it to a reasonable extent. The error in approximating RF_{sim} for the choice of $\Delta x = 1$ m and $\Delta t \leq 0.04$ day is less than 3%. This order of error is acceptable for our purpose and we claim that the match is found with the MOC solution with this choice of Δt and Δx. Of course, one can find a more accurate match if required by following either of the two strategies mentioned at the end of §4.5.1. For most of the cases examined below, we found a match with $\Delta x = 1$ m and $\Delta t = 0.01$ day.

4.5.2.1. Foam Modeled by a Monitor

4.5.2.1.1. Foam Flood

As mentioned earlier in this chapter, the functions F_w and F_o are explicitly defined by a command language in the monitors, as a function of S_w and S_o. It can be seen that except for one case where even our own fine-grid numerical simulator did not find the correct solution (similar to Fig. C-5), the simulator does an acceptable job in matching the MOC solution (**Table 4**). We see later in this chapter that using a monitor greatly improves the results without the need of exhaustive effort for refining the plugging tables to match with the MOC.

---

[*] RF_{sim} is equal to the percentage of mobile oil (oil in excess of residual saturation) produced at $t_{end,\mathrm{MOC}}$.

Table 4: The simulator's performance in matching the MOC solution for foam flood. (foam modeled by a monitor)

Water	Oil	$S_o(I)$	Δx (m)	Δt (day)	$t_{end,\mathrm{MOC}}$ (years)	$RF_{sim}(\%)$ (at $t_{end,\mathrm{MOC}}$)	Match with MOC found?
Weakens	No effect	0.17	1	0.01	1.96	95.5	Yes
		0.73			1.96	98.5	
	Weakens	0.17		0.1	1.99	89.8	
		0.73		0.01	2.95	96.2	
	Kills	0.17			2.7	98.1	
		0.73			8.4	100	
Kills	No effect	0.17			3.35	96.7	
		0.73			3.35	97.2	
	Weakens	0.17			3.32	99.4	
		0.73	0.2		3.69	99.3	
	Kills	0.17			3.5	99.4	
		0.73	1		8.7	99.9	
No effect	Weakens	0.17			1.5	100	
		0.73			2.23	100	
	Kills	0.73	0.1	1	8.1	100	
		0.17	-[*]		2.1	-[*]	No

4.5.2.1.2. *Gas/SAG*

Results from Chapter 3 clearly showed that *incorporating foam collapse at S_{wr}* (i.e., $F_w = 0$ at $S_w = S_{wr}$) results in the failure of gas/SAG in the cases examined, regardless of the reservoir initial condition, relative-permeability model, and foam sensitivity to S_w and S_o. Therefore, gas/SAG is nearly as inefficient as if no foam were present at all; if $F_w = 0$ at $S_w = S_{wr}$. In both of the cases where S_w influences foam strength in this chapter (i.e., weakening or killing effect), complete foam collapse at S_{wr} is incorporated. Thus, the performance of these unsuccessful cases is not of practical interest and we only examine the simulator's performance for the cases that are considered successful according to Chapter 3 (**Table 5**).

Table 5: The simulator's performance in matching the MOC solution for successful gas/SAG (foam modeled by a monitor).

Water	Oil	$S_o(I)$	$t_{end,\mathrm{MOC}}$ (years)	Match with MOC found?
No effect	Weakens	0.17	1	No
	Kills		1.8	No

---

[*] We couldn't find a satisfactory simulation result for this case and therefore we leave this space blank.

Despite various choices of Δt and Δx examined, the simulator was unable to find the match for the only two successful gas/SAG cases due to oscillations across the $S_o = S_o^*$ line. For the case where oil kills foam, our fine-grid simulator was also unable to find the correct solution (Fig. C-5). In both of these cases, the displacement route consists of (*S*)(*S*) wave group and the simulator was unable to find the match (see Table A-1 for information about the wave groups).

Fig. 11 is the simulator's solution for the case where oil weakens the foam for Δt = 0.01 day and Δx = 1 m. This choice of Δt and Δx is selected because it has the highest RF_{sim} among the others. At early times (Fig. 11b), the simulator finds the correct *IJ* at (0.1, 0.2982, 0.6018); however, as time proceeds, oscillations around *IJ* become the dominant feature and last to the end. Consequently, the oil-recovery prediction is significantly impaired (82.85%).

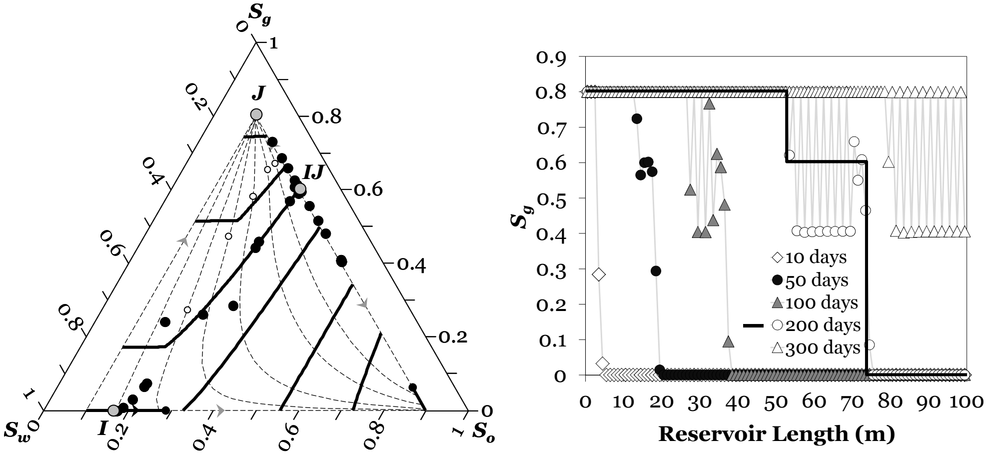

(a) (b)

Fig. 11: Numerical simulations do not always find the correct solution and may sometimes exhibit oscillations. (a) Simulator results for Δx = 1 m and Δt = 0.01 days. Reservoir is initially at (0.83, 0.17, 0) and foam is weakened at $S_o > S_o^*$ (S_o^* = 0.2) and water has no effect, and the solution shown is for gas/SAG. The small unfilled circles along the saturation paths are inflection points (see the last paragraph in §3.4 for more information). (b) S_g profile at different times; the MOC solution at t = 200 days is shown as a solid-black line. *IJ* found by the MOC is located at (0.1, 0.2982, 0.6018); however, the solution oscillates around this value and does not find a constant state (RF_{sim} = 82.85%). We could not find a match with the MOC solution with the choices of Δt and Δx examined in this case.

4.5.2.2. Foam Modeled by a Plugging Table

4.5.2.2.1. Foam Flood

As discussed earlier in §4.3.2, the plugging table must be refined enough to capture all the specifics of the original functions F_w and F_o. Otherwise, it leads to spurious results and failure to match the MOC solution. **Table 6** summarizes the simulator's performance when using the plugging tables for defining the foam model. dim(S_α) is the number of saturation points used to refine the $F_\alpha(S_\alpha)$ curve. Ideally, a larger dim(S_α) results in a solution closer to the case with monitors. However, excessive refinement takes extremely long times for the simulator to generate the tables. As a result, dim(S_α) must be chosen such that the table-generation time is affordable and the accuracy is not compromised.

Table 6: The simulator's performance in matching the MOC solution for foam flood.
(foam modeled by a plugging table)

Water	Oil	$S_o(I)$	dim(S_w)	dim(S_o)	Δx (m)	Δt (day)	$t_{end,\mathrm{MOC}}$ (years)	RF_{sim}(%) (at $t_{end,\mathrm{MOC}}$)	Match with MOC found?
Weakens	No effect	0.17	1,064	-	1	0.01	1.96	95.4	Yes
		0.73					1.96	98.5	
	Weakens	0.17	1,064	1,580		0.1	1.99	99.72	
		0.73				0.01	2.95	96.2	
	Kills	0.17	1,064	1,013			2.7	95.9	
		0.73					8.4	100	
Kills	No effect	0.17	151	-	0.1	0.1	3.35	98.9	
		0.73					3.35	99.3	
	Weakens	0.17	225	113	1	0.01	3.32	99.4	
		0.73			0.1	0.1	3.69	99.6	
	Kills	0.17	978	1,013	0.2	0.01	3.5	99.4	
		0.73			1		8.7	99.9	
No effect	Weakens	0.17	-	15,752			1.5	100	
		0.73					2.23	98.8	
	Kills	0.73	-	10,013	0.1	0.1	8.1	100	
		0.17			-		2.1	-	No

In the case where foam is weakened by oil [$S_o(I)$ = 0.17, Δx = 0.1 m, and Δt = 0.01 day], a very high oil-recovery factor (RF_{sim} = 99.96%) is achieved for dim(S_o)=14,262. However, this high RF value is misleading and does not indicate that the simulator has found the match with the MOC. This is due to a similar behavior observed in Fig. 11 (oscillations around IJ is dominant here as well). Even refining the gridblock and time-step size to 5E-3 m and 5E-5 day does not result in an accurate match. However, further refinement of the plugging table by increasing the dim(S_o) to 15,572 resolved this problem and led to RF_{sim} = 100% without oscillations.

4.5.2.2.2. Gas/SAG

The performance of the simulator in this case is similar to the case with monitors, hence it is not repeated here. In all the cases examined, it is not possible to match the MOC with plugging tables if the match is not found with the monitors. If the match is found by monitors, it is still possible not to find a match with plugging tables, if inaccurate tables are used.

In Chapter 5, we model a complete SAG displacement process (including both surfactant-injection and gas-injection cycles) in 3D with a *nonlinear* relative-permeability model, in which foam is weakened at low S_w (F_w = 0 at S_{wr}), killed at high S_o, and is *sensitive* to surfactant concentration. We did not validate the performance of the 1D simulation in the similar case here (water weakens, oil kills, *without* sensitivity to surfactant concentration, and with *linear* relative-permeability model), because it was not *successful* under our definition. However, the simulator is able to find the match with the MOC solution in that case. In Chapter 5, we have validated the 3D simulation results in §5.2.1 in ways discussed in §4.6.

4.6. Validating the Simulations in the Absence of an Analytical Solution

So far, we validated the 1D simulations of the simulator with the analytical solution obtained by the MOC. In some cases such as 3D simulations with gravity (Chapter 5), the MOC solution is not available and we require to validate the results. Although there is no MOC solution in these circumstances, the insights obtained from the 1D analysis can provide valuable measures for detecting wrong simulations. In the 1D simulations in this chapter, the major symptom of wrong simulations was wild, spurious fluctuations in saturations. Therefore, in the absence of the MOC solution, one way of identifying wrong results is to look for similar symptoms in the saturation (**Fig. 12**) and/or pressure profiles. If these symptoms disappear after sufficient refinement in space or time or both, then the results exhibiting the symptoms are obviously wrong. This is comparable but not equivalent to detecting the oscillations in 1D.

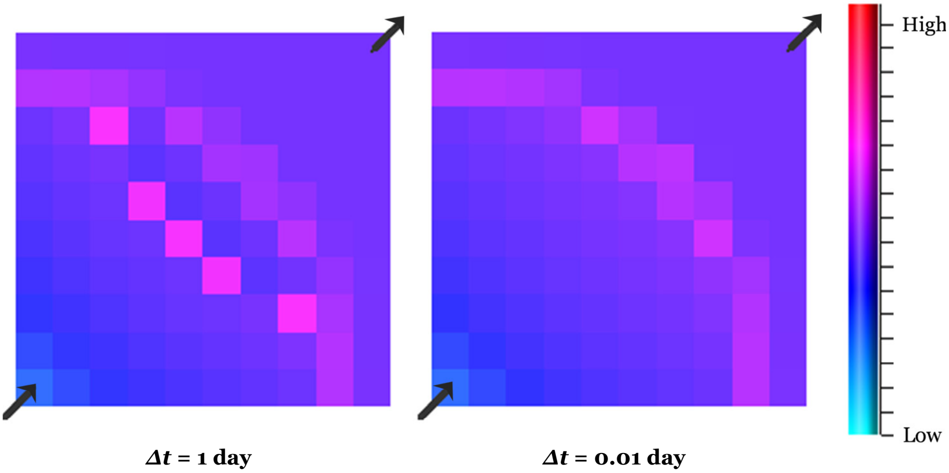

Δt = 1 day

Δt = 0.01 day

Fig. 12: Oil-saturation profiles for identical cases with different Δt. High-saturation gridblocks in the profile with Δt = 1 day vanish by using the smaller Δt = 0.01 day. Therefore, the solution with Δt = 1 day is obviously wrong and those high-saturation gridblocks are symptoms of an improper choice of Δt.

Fig. 12 also suggests that proper choices of Δt and Δx must be found by performing sensitivity analysis on these parameters. In our case, we define the *proper choice* as a choice with which symptoms as in Fig. 12 do not occur, and for which further refinement of time and spatial grids would not significantly influence the results (e.g., cumulative oil production). This procedure gives some assurance (if not perfect assurance) in the absence of the MOC solution.

4.7. Conclusions

All hydrocarbon reservoirs are in 3D. However, there is no analytical solution for a real 3D displacement (with gravity) to evaluate the correctness and accuracy of the numerical simulations. The MOC provides exact solutions for benchmarking the accuracy and numerical artifacts of numerical simulators. Therefore, it is essential to evaluate the performance of the numerical simulator in 1D with the available analytical solutions from the MOC, prior to performing simulations in higher dimensions (i.e., 2D and 3D). This analysis elucidates many important aspects:

Appropriate choice of Δt *and* Δx*:*

- In finding an accurate numerical solution that matches the MOC solution, some displacements are more sensitive to the choice of Δt and Δx than others. If a part of the solution (e.g., rarefaction wave and/or constant-state region) is in the proximity of the foam/no-foam boundary at which drastic changes in gas mobility occur, the simulator may exhibit oscillations across the boundary with an improper choice of Δt and Δx and fail to find the correct solution. In some cases, we were unable to obtain a correct numerical solution with the choices of Δt and Δx examined.

- At fixed Δx, once the numerical dispersion due to time discretization becomes negligible compared to the numerical dispersion introduced by spatial discretization, it is impossible to improve the solution by refining Δt. At this stage, the remaining mismatch between the numerical and the MOC solution corresponds to numerical dispersion caused by Δx.

- An inappropriate choice of Δt and Δx leads to erroneous results that might be hard to identify in 3D simulations in the absence of the MOC solution. One needs to look for symptoms to identify them and find the proper choices of Δt and Δx by performing sensitivity analysis on these parameters. In our case, we define the *proper choice* as a choice with which symptoms as in Fig. 12 do not occur, and for which further refinement of time and spatial grids would not significantly influence the results. This procedure gives some assurance (if not perfect assurance) in the absence of the MOC solution.

Verifying the accuracy of the plugging table:

- Prior to moving to simulations in higher dimensions, it is crucial to validate the accuracy of the plugging table by comparing the simulation results with the MOC. A plugging table is the backbone of the foam model and inaccurate representation of the foam model in it leads to erroneous results.

- In the absence of an analytical solution, it is possible to verify the accuracy of a plugging table by comparing the simulation results (e.g., flow rates) to the results obtained by monitors for the same case. They must match if the plugging table is accurate.

- It is always advised to use monitors instead of plugging tables when possible. This prevents the possible introduction of errors in the model by inaccurately defining the tables. It also eliminates the exhaustive task of trading off between the table accuracy and table-generation time.

Range of validity of the simulator:

- If a part of the solution (rarefaction wave, constant-state region) is located very close to the foam/no-foam boundary over which the gas mobility changes drastically, the simulator might be unable to find the correct solution.

- In all the cases examined, it is not possible to find a match with the MOC using plugging tables, if the match is not found by the monitors.

- For foam flood, the simulator matches the MOC solution well with both approaches for incorporating the effect of foam (monitors and plugging tables). It fails to find the correct solution in only one case (similar to Fig. C-5) where even our fine-grid simulator used in Chapter 3 is unable to find the solution.

- For gas/SAG, only the *successful* cases in Chapter 3 are examined and the simulator was unable to match the MOC with the choices of Δt and Δx examined. We did not examine the case similar to the one investigated in Chapter 5 here (water weakens, oil kills), because it was considered *unsuccessful* under our definition; however, the simulator is able to find the match with the MOC solution in that case.

- With the insight that we gained through the validation of the simulator's performance against the MOC solution, we concluded to apply simpler physics for the foam model in the 3D simulations in Chapter 5 to ensure finding the correct solution.

Chapter 5

Optimization of Foam EOR

5.1. Introduction

Once a hydrocarbon reservoir comes into production, we deal with a dynamic system that needs to be produced in an economically feasible manner. This requires an optimal control strategy dictating the injection and production policy that results in minimizing or maximizing a specific objective function. The optimal control strategy is designed to result in the best displacement efficiency or best economic performance, which is reflected in the chosen objective function. The objective function in the former case is the ultimate oil recovery and in the latter case is the net present value.

Our objective is maximizing the cumulative oil production by finding the optimum switching time between the surfactant and gas injection cycles in surfactant-alternating-gas (SAG) processes. In these EOR processes, foam is a means of improving sweep efficiency that reduces the gas mobility by capturing gas in foam bubbles and hindering its movement. We also investigate the capability of a gradient-based optimization routine applied to these EOR processes. The simulations are carried out by the Shell in-house reservoir simulator MoReS (hereafter referred to as *the simulator*). This work is a first attempt to apply optimal control theory to foam EOR processes.

In this work, we restrict ourselves to optimal control theory (OCT) where we calculate the gradients using adjoint equations. (Sometimes a wider class of methods is used in OCT, but in this thesis we do not consider those other methods.) Adjoint-based schemes are very efficient for gradient calculations and are particularly useful in optimization problems where a large number of controllable parameters must be optimized. However, their implementation is complex and time-consuming and requires considerable code development. The adjoint code depends on the forward model. Therefore, every time that the forward model is modified, the adjoint code must be updated and one needs access to the simulator's source code to do it

(Sarma et al. 2005; Chen et al. 2009; Jansen 2011). The adjoint routine in the simulator has been extensively validated for waterflooding (Kraaijevanger 2007; van Essen 2010) and also recently for polymer flooding (Van Doren et al. 2011). In principle, it could be applied to many other oil-recovery mechanisms and optimization problems after being validated first for the new applications.

In this chapter, we first introduce the simulation model. Then, we investigate the effect of the switching time[*] on our objective function in three different scenarios in which different injection-well constraints and end-time constraints are applied. We continue with a brief overview of the history and application of optimal control theory in petroleum engineering. We discuss three methods of gradient calculation and we elaborate on the adjoint method which is used in this chapter. The application of the adjoint method for calculating the gradient with respect to switching time is discussed in detail afterwards. Finally, we investigate the capability of a gradient-based optimization routine applied to foam EOR processes in finding the switching time that maximizes the cumulative oil production. We examine the optimization routine in four cases varying in the simulation mode (i.e., 1D or 3D) and the foam model (i.e., linear or nonlinear). We end this chapter with concluding remarks.

5.2. Problem Statement

We model a foam-displacement process in 1D and 3D. In particular, we optimize the duration of the surfactant slug injection in SAG flooding, that maximizes the cumulative oil production. We represent the duration of the surfactant slug by the *switching time* (t_s). Initially, surfactant solution (surfactant dissolved in water) is injected into the reservoir for t_s days. At t_s, surfactant injection is terminated and gas injection starts.

The 3D reservoir is rectangular, 100×100×30 m, with one injection and one production well, located on the opposite sides of the reservoir (see **Fig. 1b**). Both wells are vertical, located in the middle of the corner gridblocks, and are perforated in the entire interval. Both wells operate at constant prescribed bottomhole pressures [i.e., maximum-bottomhole-pressure constraint for the injection well ($P_{wf,max}^{inj}$) and minimum bottomhole pressure constraint for the production well ($P_{wf,min}^{prod}$)], unless otherwise is stated. In the 3D simulations, we have used 1000 gridblocks (i.e., 10×10×10), unless otherwise is stated.

Some of the simulations are in 1D. In the 1D simulations (Fig. 1a), the reservoir is 100×1×1 m

---

[*] The switching time is our control variable and is defined as the time at which surfactant injection is terminated and gas injection begins.

and we have used 100×1×1 gridblocks, unless otherwise is stated. In the 1D simulations, wells are positioned in the middle of the first and last gridblocks.

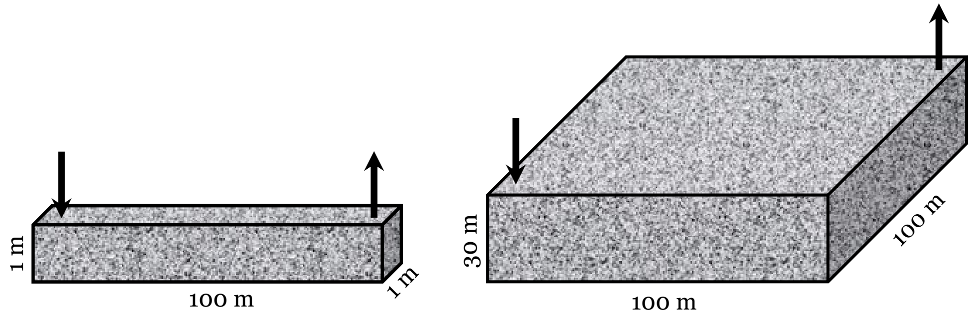

(a) (b)

Fig. 1: Reservoir geometry in (a) 1D and (b) 3D simulations.

We aim at investigating the gas performance in sweeping oil. Thus, we would like to minimize the effect of water in displacing oil. In addition, EOR processes usually come after a period of waterflooding. Therefore, we set the initial oil saturation in the reservoir before starting the foam EOR (prior to surfactant injection, to be precise) at the residual oil saturation to waterflood (S_{orw}). This way, water is unable to displace oil unless the oil saturation exceeds S_{orw}. Therefore, oil is not displaced nor produced before the switching time. After the switching time, gas injection begins. We further assume that gas, though immiscible, is capable of displacing oil leading to oil production; specifically, we set the residual oil saturation to gas flood (S_{org}) lower than S_{orw}. Setting S_{org} equal to zero implies that gas is able to displace all the oil in the reservoir, not by miscibly displacing oil, but by immiscibly displacing oil to a low residual saturation.

The two-phase relative-permeability curves are shown in **Fig. 2**. We use the linear-isoperms model (§4.2.4) as the three-phase relative-permeability model in this chapter.

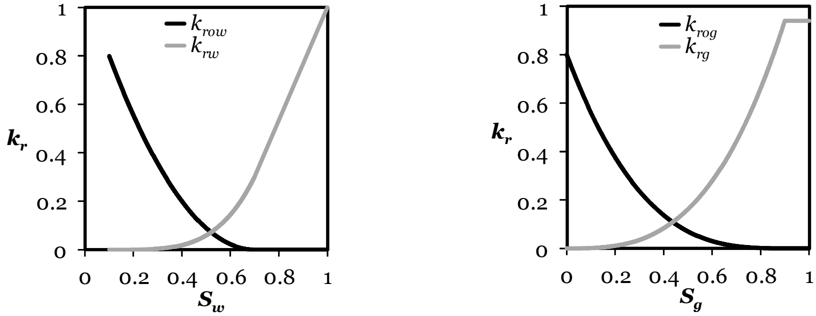

Fig. 2: Two-phase relative-permeability curves used in Chapter 5 with parameters in Table B-2. The three-phase relative permeabilities are obtained from the linear-isoperms model (§4.2.4).

Simulation parameters are summarized in Tables B-2 and B-3. There is initially no gas present in the reservoir. Initial oil and water saturations are equal to 0.3 and 0.7, respectively. The injected surfactant concentration is 0.24 wt.%. In other words, there is 2.4 kg of surfactant in every 1000 kg of the surfactant solution. The gas phase is slightly compressible in the simulations (i.e., c_g = 1.68E-8 Pa^{-1}).

Our foam model incorporates the effects of water saturation, oil saturations, and surfactant concentration on foam strength according to **Fig. 3**. In the nonlinear foam model shown in Fig. 3, foam is weakened at low water saturations according to Eq. C-2. Note that foam strength is equal to zero at the connate water saturation according to this equation. In addition, foam is killed at high oil saturations as in Eq. C-4. The foam sensitivity to surfactant concentration is defined by Eq. C-8 (see Appendix C for more details). According to the nonlinear foam model, foam strength changes abruptly with small changes in water saturation, in agreement with laboratory data. It also changes abruptly with changes in surfactant concentration, for reasons discussed in Appendix C. In fact, laboratory data suggest an even sharper change in foam strength with water saturation (Cheng et al. 2000), but as shown below, the function we use here already causes problems for a gradient-based optimization routine.

These types of functions can lead to drastic changes in gas mobility in individual gridblocks as fronts pass, in the ways discussed in §5.3.1. These abrupt changes in properties may challenge a gradient-based optimization routine as discussed in detail in §5.9.

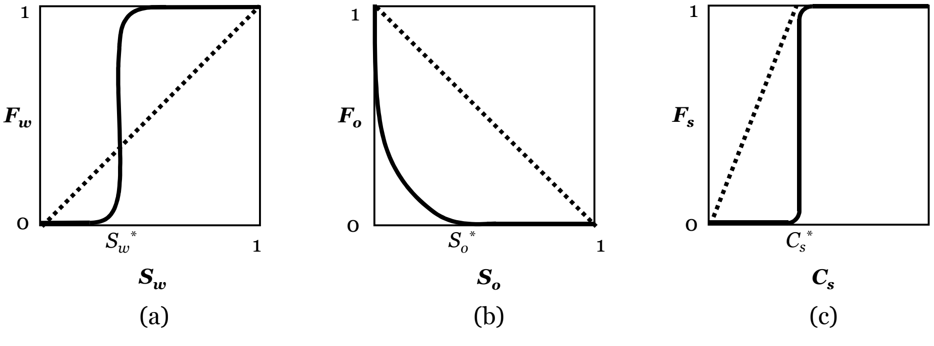

Fig. 3: Foam models: The *linear* foam model is illustrated by dashed lines and the *nonlinear* foam model by solid lines. (a) Foam sensitivity to water saturation; nonlinear model: foam is weakened at $S_w \leq S_w^*$ (Eq. C-2: S_w^* = *fmdry* = 0.316, *epdry* = 1000). (b) Foam sensitivity to oil saturation; nonlinear model: foam is killed at $S_o \geq S_o^*$ (Eq. C-4: S_o^* = *fmoil* = 0.4, *epoil* = 1.5, *floil* = 0). (c) Foam sensitivity to surfactant concentration; nonlinear model: $F_s = 1$ for $C_s \geq C_s^*$ (Eq. C-8: C_s^* = 1.2E-3, *epsurf* = 100). Note that all these *nonlinear* functions are differentiable. The nonlinear foam model is discussed in detail in Appendix C.

Since this model will be also used with the adjoint routine, the effect of foam is incorporated by plugging tables, and surfactant transport is modeled by the brine option, because the combination of other options introduced in §4.3 and §4.4 is not compatible with the adjoint routine in the 2010.1 version of the simulator. (See §4.3.4 and §4.4.4 for more detail about the compatibility issues with the adjoint routine).

In general, optimization of an objective function is carried out by combining the adjoint routine and an optimization routine for finding the optimum. The adjoint routine is employed for efficiently calculating the *analytical* gradient of the objective function with respect to various static and dynamic parameters. Gradients always point to the direction of the maximum growth of the objective function and a gradient-based optimization routine utilizes the gradients to search for the optimum. Some of the static variables are the permeability and porosity. The dynamic control variables include:

- well-control variables such as active constraints (e.g., bottomhole pressure, surface and reservoir volume rates of the phases, and mass rates of the components),
- downhole valve settings,
- the injection composition,
- the switching time.

We aim at investigating the capability of a gradient-based optimization routine applied to foam EOR processes. Our objective is finding the switching time ($t_{s,opt}$) that maximizes the cumulative oil production. We choose a simple case with only one control variable (i.e., the switching time between the surfactant and gas injection cycles) for this investigation. Having only one control variable, the global trend of the objective function $\mathcal{J}$ (i.e., the cumulative oil production) can be easily constructed by a reasonable number of perturbation runs. Once the global trend of $\mathcal{J}$ is available, $t_{s,opt}$ can be easily identified. This way, we have a solid reference case against which to evaluate the performance of the optimization routine.

5.2.1. Validating the 3D Simulations

We validated the performance of the simulator for 1D simulations against the MOC solution in Chapter 4 for several cases. Since there exists no MOC solution for the 3D case (including gravity) studied in this chapter, we require to take additional measures to ensure the correctness of the 3D-simulation results. In addition to the procedure described in §4.6, we also simplified the physics of the problem as follows.

We observed in the 1D numerical simulations in Chapter 4 that having sharp changes in properties over the foam/no-foam boundary challenges the simulator's performance. Since it is not possible to validate the 3D-simulation results against an analytical solution, at least one can use a *weaker* foam with a much lower value of *fmmob* than the one used in Chapters 3 and 4[*] (i.e., 55,000). Setting a smaller value of *fmmob* smoothens the sharp changes in properties to a large extent. In addition, it minimizes the effect of abrupt changes in the gas mobility, to ensure finding the correct solution in the forward run with a reasonable time-step and gridblock size for a 3D simulation. This is of special importance for 3D simulations in which one cannot afford a large number of gridblocks and extremely small Δt. Because of this reason, we use *fmmob* = 1,000 in this chapter for both 1D and 3D simulations.

Furthermore, if a foam represented by a high value of *fmmob* (e.g., 55,000) were to form near the injection well, it would cause a significant drop in the injection rate in an injection well operating at a constant prescribed bottomhole pressure. In the case of injecting at a fixed rate, the presence of a very-low-mobility foam near the injection well leads to extremely high bottomhole pressure values that may lead to fracturing the formation around the wellbore.

Moreover, it is important to note that we are not claiming that the solutions obtained from 3D simulations with 10×10×10 gridblocks in this chapter are an accurate description of a real foam process, only that they provide a case study for testing a gradient-based optimization routine. We neither claim that it falls under the *successful* category, according to the definition in Chapter 3.

5.3. Switching Time

The switching time (t_s) is the time at which surfactant solution injection is terminated and gas injection begins. In other words, t_s is the duration of the surfactant injection. Prior to t_s, there is no foam in the reservoir due to the absence of gas. However, once gas injection begins, foam formation and coalescence are initiated in the reservoir. In the simulations, this sudden change in the injection composition from 100% surfactant solution to 100% gas at the switching time produces a period of wild fluctuations in the gas-injection rate (Q_g) or the bottomhole pressure (P_{wf}) of the injection well (based on the active well constraint) right after the switch. These fluctuations do not vanish if we take (much) smaller time steps, so are due to the spatial discretization scheme used in the simulator. The nonlinear foam model in Fig. 3 is applied all through §5.3. Nevertheless, there is no fluctuation in the gas-injection rate when applying the linear foam model.

---

[*] We note that the gas mobility-reduction factor is inversely related to *fmmob*. However, gas mobility is reduced by a factor of $1/(1+fmmob)$ only if other factors such as water saturation, oil saturation, and surfactant concentration are not influencing the foam strength. If foam strength is sensitive to these parameters, gas mobility is reduced to a lesser extent; nevertheless, the reduction in gas mobility in a SAG process can still be significant (Shan and Rossen 2004).

5.3.1. Effects of Switch on Injection Well Performance

In this section, we first discuss the behavior of the Q_g profile in a *foam-free* case (i.e., without switch: $t_s = 0$). This means that only gas is injected throughout the simulation. Then, we elaborate on a case in the *presence* of foam with the switching time (i.e., with surfactant injection prior to gas injection). Both the injection and production wells operate at a constant prescribed bottomhole pressures ($P_{wf,max}^{inj}$ and $P_{wf,min}^{prod}$), unless otherwise is stated.

5.3.1.1. Without Switch (Foam-Free Case)

Fig. 4a illustrates the Q_g profile in a 3D reservoir for the *foam-free* case and Fig. 4b magnifies the Q_g trend at early times. The general shape of the curve shrinks and expands both vertically and horizontally by varying $P_{wf,max}^{inj}$ and $P_{wf,min}^{prod}$ while keeping the initial reservoir pressure constant. In these variations, the location of points *A*, *B*, *C*, and *D* in Fig. 4b (i.e., maximum, minimum, maximum, and minimum in Q_g) may change but they do not vanish from the profile. The existence of the two declining segments of the profile (i.e., *AB* and *CD*) depends on the relative-permeability model (see Fig. 2 and §4.2.4), initial phase saturations, and on the injected fluid (water/gas). The behavior seen in Fig. 4 can be explained by the variations in the total mobility (i.e., $\lambda_{tot} = \lambda_w + \lambda_o + \lambda_g$) in the gridblocks containing the injection and production wells, and the competition between λ_w and λ_g in those gridblocks* (see the footnote for the discussion about the treatment of phase mobilities in the well model). We base our discussion on the *fixed* pressure drop between the injection and production wells, i.e., $P_{wf,max}^{inj} - P_{wf,min}^{prod}$ and we emphasize that the injection rate is sensitive to both wells, in the ways that will be discussed below. We elaborate on the behavior of each segment by first stating the observed trend and then explaining its cause.

- *AB* segment:
  - *Observations*: There is a very sharp decline in Q_g from *A* to *B*. In this time interval (about 4 hours), $\lambda_g < \lambda_w$ in the injection-well gridblocks. Moreover, λ_{tot} in the injection-well gridblocks (λ_{tot}^{inj}) is dropping, while λ_{tot} in the production-well gridblocks (λ_{tot}^{prod}) is almost constant (0.005% change).

---

* In the *well model* used in the simulator, the well *inflow* (*outflow*) model is based on the Peaceman (1983) model, and the injection (production) rate depends on the mobility of the flowing phase:

- For gridblocks containing the *injection* well, the phase mobility depends on both *wellbore* and *gridblock* conditions: It is a product of the phase saturations of the fluid present in the *wellbore* and the total mobility of the fluids in the *gridblock* (this term incorporates the resistance applied by the fluids displaced from the gridblocks containing the injection well).
- For gridblocks containing the *production* well, viscosity and relative permeability are evaluated at gridblock conditions (Dynamo/MoReS Online User Documentation 2010).

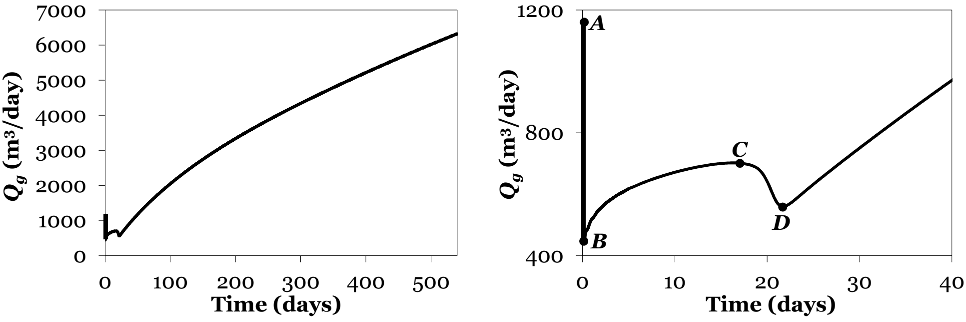

(a) (b)

Fig. 4: (a) Gas-injection-rate profile versus time in the absence of the switching time (t_s = 0). Simulation lasts for 540 days. The 3D reservoir consists of 1000 (10×10×10) gridblocks. (b) Magnification of Fig. 4a at early times. The injection well operates at a constant prescribed bottomhole pressure ($P_{wf,max}^{inj}$).

- *Cause*: There is a fixed pressure drop between the wells; hence, reduction in λ_{tot}^{inj} results in a declining Q_g. The cause of decline in λ_{tot}^{inj} can be explained by looking at k_{rw} and k_{rg} curves in Fig. 2. Initially, S_w = 0.7 and S_g = 0 in the reservoir. With the start of gas injection in this time interval, S_w begins to drop from 0.7 and S_g starts to rise from zero, while S_o remains relatively unchanged at 0.3 (for absolute values of ΔS_w and ΔS_g we have $\Delta S_w \approx \Delta S_g \approx 0.125$). However, Fig. 2 reveals that the change in k_{rw} is much larger than the change in k_{rg} in the range of saturation changes in this time interval (i.e., S_w = [0.7: 0.575] and S_g = [0: 0.125]), even though μ_g is 50 times less than μ_w and one would expect to have λ_g larger than λ_w. However, since S_g is not high enough in this time interval, λ_w stays larger than λ_g in the *AB* segment and k_{rw} is *at least* 50 times larger than k_{rg} ($k_{rw}/k_{rg} \geq 50$). Water and gas mobilities become equal at point *B* in the injection-well gridblocks; i.e., $\lambda_w = \lambda_g$ at *B* (k_{rw} = 50 k_{rg}). Moreover, the rise in k_{rg} cannot compensate the drop in k_{rw} and consequently λ_{tot}^{inj} declines in this segment as S_g rises in the injection-well gridblocks. In this segment, λ_{tot}^{inj} is dominated by λ_w.

- *BC* segment:

  - *Observations*: Q_g rises from *B* to *C*. $\lambda_g > \lambda_w$ in the injection-well gridblocks and λ_{tot}^{inj} is rising, while λ_{tot}^{prod} remains relatively unchanged (0.04% change).

  - *Cause*: As mentioned in the *AB* segment, λ_w becomes equal to λ_g at *B*. From point *B* onwards, S_g is sufficiently high that $k_{rw}/k_{rg} < 50$. Therefore, λ_g is always larger than λ_w in the injection-well gridblocks after point *B*. Consequently, the growth in λ_g caused by increase in S_g is significantly larger than the decline in λ_w caused by declining S_w. Therefore, λ_{tot}^{inj} and consequently Q_g rise from point *B* forwards.

- *CD* segment:
  - *Observations*: Q_g declines from *C* to *D* and $\lambda_g < \lambda_w$ in the production-well gridblocks. λ_{tot}^{prod} starts to decline, while λ_{tot}^{inj} is still rising.
  - *Cause*: Until point *C*, the trend in Q_g was under the influence of the injection well, because λ_{tot}^{prod} was relatively constant. However, after point *C*, λ_{tot}^{prod} starts to decline considerably and from this moment on, the trend in Q_g is under the influence of the production well, because there has been no change in the increasing trend of λ_{tot}^{inj}. This segment includes two sub-segments. One with a moderate slope and the other one with a steep slope. In the segment with the moderate slope, decline in λ_{tot}^{prod} is not significant (0.2%), therefore, the decline in Q_g is moderate as well. However, once gas reaches the production well, λ_{tot}^{prod} declines significantly (35%). This behavior is explained by the same reason discussed in the *AB* segment: Although S_g increases in the production-well gridblocks once gas breaks through to the production well; however, the corresponding rise in λ_g cannot compensate for the steep decline in λ_w, because S_g is not yet sufficiently high to have $k_{rw}/k_{rg} < 50$ (i.e., λ_g is lower than λ_w in this segment). Therefore, the ability of the production well to produce fluids is reduced and since the overall pressure drop is fixed, the injection well must regulate (reduce) Q_g to accommodate this change. This decline continues until S_g becomes sufficiently high (i.e., $k_{rw}/k_{rg} < 50$) in the highest gridblock of the production well such that λ_g overcomes λ_w. The water and gas mobilities become equal at *D*. The gas cut is around 1% at this point. Moreover, λ_{tot}^{prod} is controlled by λ_w in this segment.
  - *D* onwards: In this segment, λ_g is larger than λ_w in the production-well gridblocks and gas has found a continuous path between the wells. Since it has gained a very high mobility in the production well, gas is easily produced from this end. Again, having a fixed overall pressure drop enables the injection well to inject more gas into the reservoir, hence, Q_g rises continuously afterwards and λ_{tot}^{prod} is dominated by λ_g in this segment.

In short, one might expect an increasing trend of Q_g in the absence of foam. However, we have two separate declining segments in the Q_g profile. In the *AB* segment, λ_w is larger than λ_g in the injection-well gridblocks, and in the *CD* segment, the same behavior is observed in the production-well gridblocks. This behavior is caused by the fact that there is not yet enough gas in the corresponding well gridblocks to dominate λ_w. S_g continues to rise in those gridblocks until it reaches a point at which the two mobilities become equal in each of the wells (*B, D*). Point *B* corresponds to this competition in the injection-well gridblocks and point *D* to the same phenomenon in the production-well gridblocks. Once λ_g exceeds λ_w in the corresponding well gridblocks, we observe the increasing trend of Q_g as expected. Therefore, the two minima in Q_g at *B* and *D* originate from the competition between λ_w and λ_g in the wells.

5.3.1.2. With Switch (Foam Case)

Operating at a constant prescribed bottomhole pressure in the injection well ($P_{wf,max}^{inj}$) implies injecting with the maximum possible flow rate at the prescribed $P_{wf,max}^{inj}$. If foam (low-mobility fluid) forms in the gridblocks *around the wellbore*[*], the gas flow rate must be regulated (lowered) to conform with this constraint. In contrast, when foam is weakened substantially in those gridblocks, the flow rate is increased. Therefore, fluctuations in Q_g are caused by drastic changes in gas mobility as a result of foam formation and coalescence in the gridblocks adjacent to the well. **Fig. 5** illustrates the Q_g profile for a 3D reservoir in this case and the fluctuations caused by the presence of foam (t_s = 66 days). One observes that the general shape of the profile is similar to the *foam-free* case in Fig. 4 discussed in §5.3.1.1, but the fluctuations are new. The tip of the first spike (see the inset in Fig. 5) corresponds to the initial gas-injection rate at $P_{wf,max}^{inj}$. At this moment, favorable conditions for foam generation are present in the reservoir [i.e., S_w (= 0.7) > S_w^*, S_o (= 0.3) < S_o^*, and $C_s > C_s^*$]. Thus, as soon as the smallest amount of gas enters the reservoir, foam is created around the wellbore, and Q_g drops immediately as a result. Gas injection causes water saturation to drop around the wellbore and once the first gridblock around the wellbore dries out sufficiently (i.e., $S_w \leq S_w^*$, according to the nonlinear foam model in Fig. 3a), foam strength drops drastically in this gridblock and provides an escape path for the gas to the adjacent gridblocks, causing a jump in the injection rate. This produces the second spike in the gas-injection profile in Fig. 5. This phenomenon repeatedly occurs in the rest of the gridblocks *around the wellbore* causing further spikes, but with smaller amplitude. Once S_w drops below S_w^* in all those gridblocks, no further spikes are observed. It is easier to observe and investigate the details of this phenomenon in 1D.

The relationship between the spikes in the Q_g and water-saturation drop in the gridblocks is more obvious in 1D simulations. In a 1D reservoir, there is merely one flow path between the injection and production wells, as opposed to 3D with numerous flow paths. Gas can flow into the next gridblock only if S_w drops below S_w^* in that gridblock. Gas breakthrough occurs after 0.42 PV of gas injection, shortly before S_w drops below S_w^* in the last gridblock. Consequently, we observe as many spikes as the number of gridblocks in the gas-injection rate profile in 1D (**Fig. 6**). The first 5 spikes of the profile with 100 gridblocks in Fig. 6 are magnified in **Fig. 7**. We have also plotted the saturation profiles in the first 5 gridblocks. The moment at which the n^{th} spike in Q_g occurs corresponds to the moment at which water saturation in the n^{th} gridblock drops below S_w^* = 0.316.

---

[*] The gridblocks in the vertical column containing the well and a few gridblocks adjacent to that column.

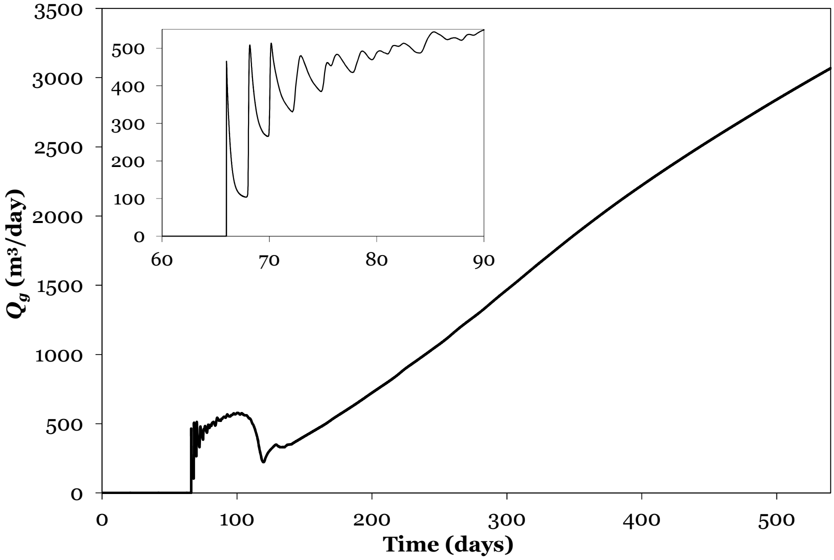

Fig. 5: Gas-injection-rate profile versus time for a 3D displacement. Simulation ends after 540 days and t_s = 66 days. The inset magnifies the fluctuations right after the switching time. The reservoir consists of 1000 (10×10×10) gridblocks.

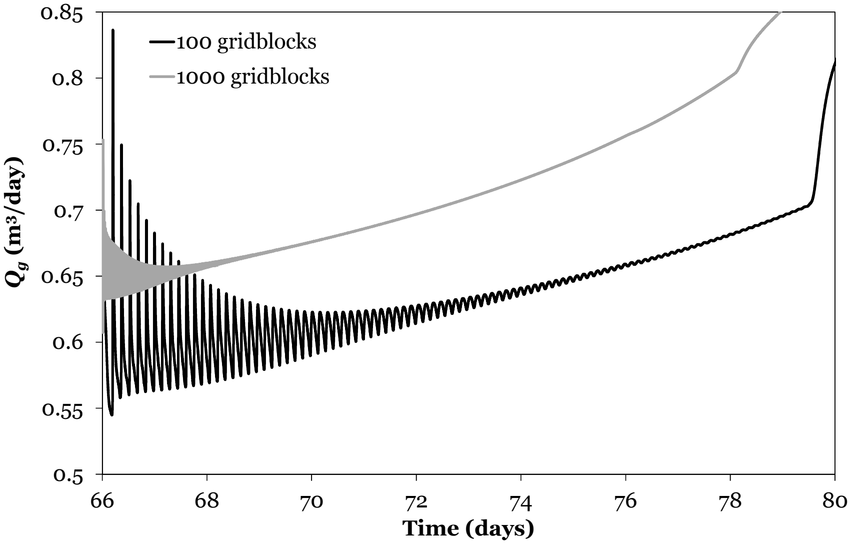

Fig. 6: Period of fluctuating gas-injection rate in a 1D displacement with t_s = 66 days. The reservoir is 100x1x1 m. All the simulation parameters are similar to the 3D simulations above. The injection well is operating at a constant prescribed bottomhole pressure. The number of spikes is equal to the number of gridblocks in the 1D case. This figure also illustrates the effect of spatial discretization on the fluctuations. Finer grids lower the amplitude of the spikes and shrinks the fluctuation interval to a region very close to the switching time at t_s = 66 days.

Figs. 6 and 7a clearly show that Q_g is affected as S_w drops below S_w^* in each successive gridblock in a 1D reservoir. Such a drop in S_w in a gridblock results in a sudden increase in λ_g in that gridblock, producing a sudden change in the pressure of every gridblock including the well gridblock. Here, we first explain that how the fluctuations in gridblock pressure are introduced in a 1D reservoir, then we discuss how this mechanism affects the well-gridblock pressure (P_1), and we finally relate the fluctuations in P_1 to the fluctuations in Q_g.

We consider the well gridblock (i.e., $n = 1$) in a 1D reservoir. Initially, conditions are favorable for foam formation in this gridblock [i.e., S_w (= 0.7) > S_w^*, S_o (= 0.3) < S_o^*, and $C_s > C_s^*$]. Once gas injection is initiated, S_w drops and foam formation lowers the total mobility in this gridblock and Q_g and P_1 decline accordingly (Fig. 7b). This decline continues until S_w drops below S_w^* in this gridblock, causing a significant reduction in foam strength and a substantial increase in gas mobility of gridblock 1. The simulator uses the *upwind*[*] finite-difference scheme for inter-grid spatial discretization. As a result, the pressure drop between gridblock n and n+1 must diminish to avoid excessive outflow from gridblock n. Consequently, the pressure of all the gridblocks downstream of gridblock 1 (i.e., $n > 1$) suddenly increases significantly. This behavior repeats itself in the remaining gridblocks until S_w drops below S_w^* in the last gridblock and gas breaks through to the production well. The reason that P_n ($n > 1$) does not rise as a result of S_w dropping below S_w^* in gridblock n is that P_n is dependent on phase mobilities in gridblock n-1 that has not changed significantly.

We notice small pressure drop in gridblocks at the upstream side of gridblock n (the gridblock that S_w has dropped below S_w^* in it). These are attributed to the fact that the scheme is mass conservative. The increase in total flux flowing out of gridblock n is compensated by an increase in total flux flowing into gridblock n. This increase subsequently results in an increase in Q_g (the most upstream point) and a minor decline in P_1. (This is because the bottomhole pressure in the injection well is constant; therefore, P_1 is the only parameter in the injection-rate equation that can be adjusted to accommodate this increase in Q_g.) These minor declines in P_1 (not visible at the scale of the figure, but similar to those in the pressure profile of e.g., gridblock 2) happen every time that S_w drops below S_w^* in any gridblock.

Q_g is *proportional* to the pressure difference between the wellbore and P_1. Since $P_{wf,max}^{inj}$ is constant, this pressure difference reflects the fluctuations in P_1. Consequently, Q_g exhibits fluctuations as in Fig. 7 as a result of water-saturation drop below S_w^* in every gridblock.

---

[*] In the upwind scheme, the flux of phase α in gridblock n+1 is dependent on the mobility of phase α in gridblock n, located upstream of gridblock n+1.

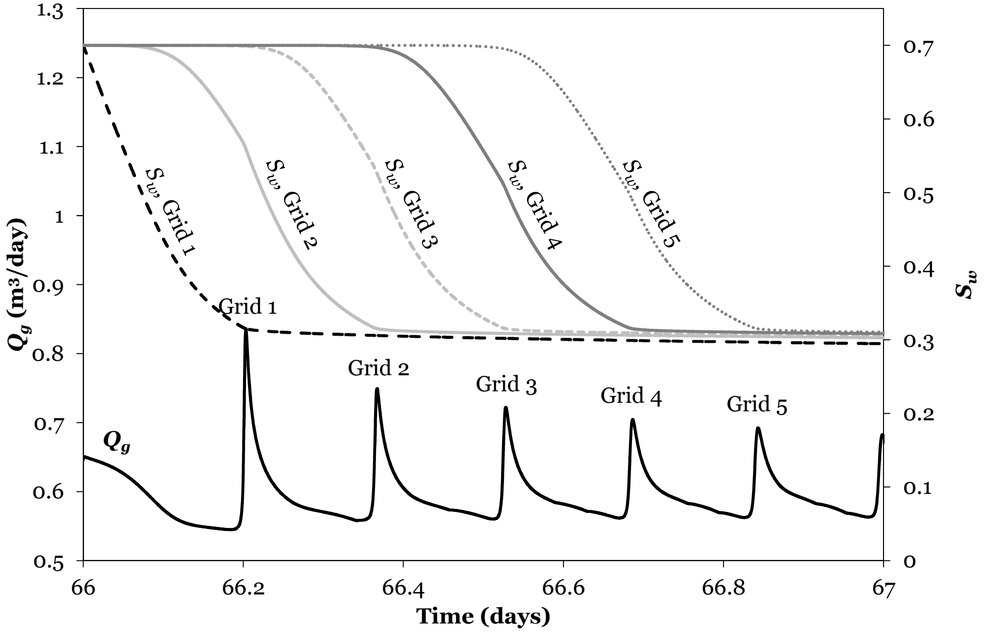

(a)

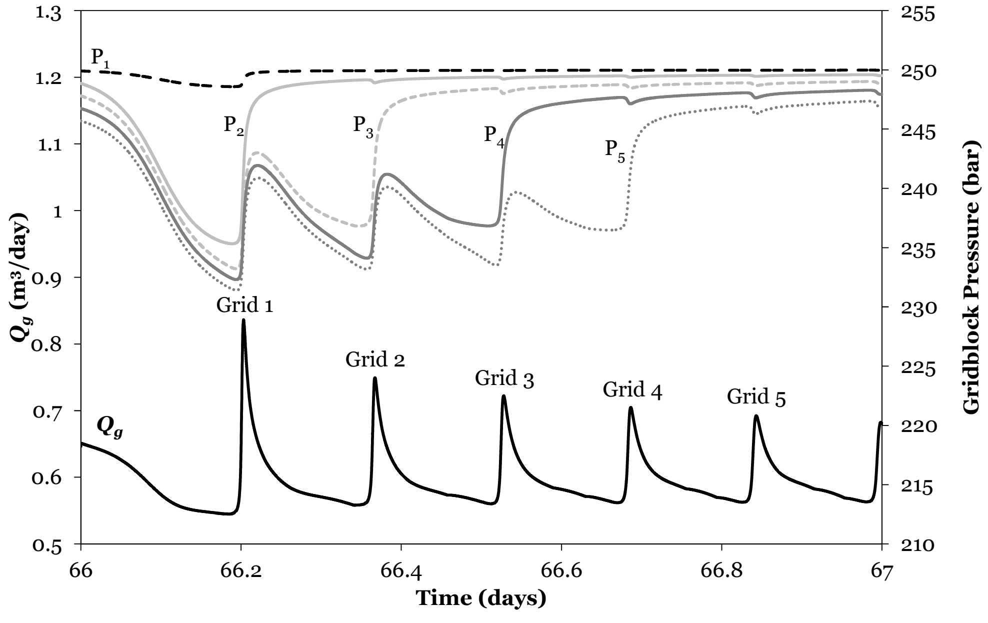

(b)

Fig. 7: Magnification of the first 5 spikes in Fig. 6 (1D displacement with 100 gridblocks). The moment at which the n^{th} spike in Q_g occurs is the moment at which S_w in the n^{th} gridblock drops below $S_w^* = 0.316$ along a shock from the initial condition S_w (*I*) = 0.7.

It is important to note that although the well gridblock is located *upstream* of all the other gridblocks and hence the fluctuations in its pressure are small and not noticed in Fig. 7b, once those small pressure differences are multiplied by the large total mobility in the well gridblock, the product produces noticeable fluctuations in the gas-injection rate.

Fig. 6 also illustrates that fluctuations get smaller as the foam front advances. This is mainly attributed to gas compressibility and the fact that the pressure difference between the wellbore and well gridblock gets smaller as the time proceeds (P_1 is influenced less by the gridblocks faraway).

We observe in Fig. 7a that there is a shock in S_w (and also in S_o and S_g, not shown in Fig. 7a) from the initial condition to a state at which $S_w \leq S_w^*$ and foam is weakened substantially[*]. **Fig. 8a** illustrates how the water-saturation profile looks like for different numbers of gridblocks. For all grid resolutions, the shock front is two gridblocks wide, because of numerical dispersion, and has lower mobility than the foam bank behind it (Fig. 8b); in reality, its width should approach zero. In this case, foam has not broken completely behind the shock and there is some control on gas mobility behind the shock[†]. As the foam front advances, a more significant contribution of the mobility reduction comes from the foam bank and the artifact at the shock front becomes less important.

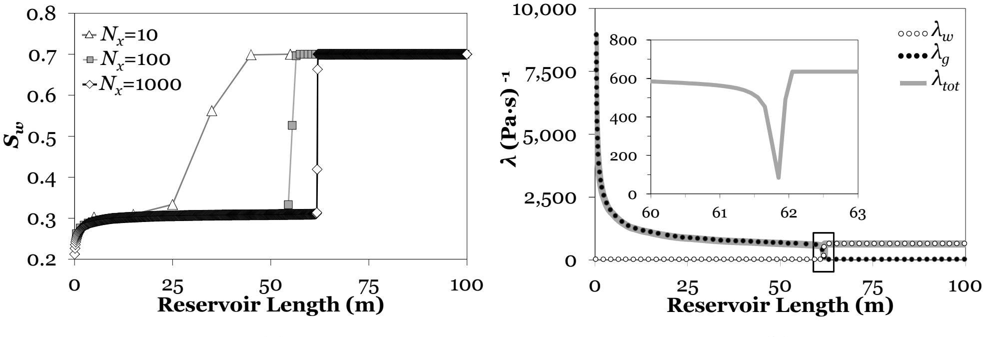

(a) (b)

Fig. 8: Results from 1D simulations with t_s = 66 days at 74 days. The total amount of surfactant solution injected is 1.9 PV and total amount of gas injected is 0.27 PV for the simulation with 1000 gridblocks. The injection well is located on the left and the production well is positioned on the right side. (a) Water-saturation profile for different numbers of gridblocks (N_x). (b) Mobilities at 74 days for N_x = 1000. The inset shows λ_{tot} of the *artificial* low-mobility bank at the shock front (2 gridblocks wide) that is an artifact of numerical dispersion. In these simulations, there is enough surfactant present in the reservoir, such that the foam strength is not affected by surfactant concentration (i.e., $C_s > C_s^*$ everywhere).

---

[*] Here, enough surfactant is injected and foam strength is not influenced by shortage of surfactant.

[†] This SAG process builds a low mobility foam bank in contradiction to the cases examined in Chapter 3.

The profile of Q_g in **Fig. 9** reflects the mobilities shown in Fig. 8b. Gas injection rises abruptly as the shock front is produced from the reservoir at 79.573 days. From the magnitude of the sudden rise in injection rate at about 79.573 days, one might estimate that 16% of the total resistance to flow across the medium was from the shock front, i.e., an artifact of numerical dispersion. Once the shock front disappears, injection rate rises gently as the foam bank slowly dries out and mobility rises throughout the medium.

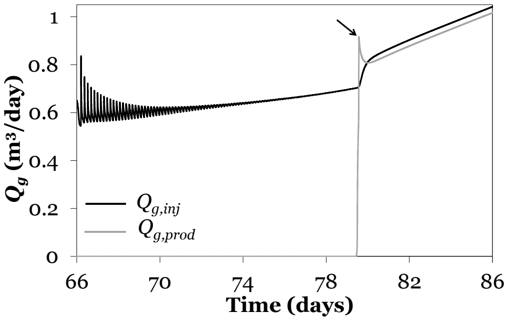

Fig. 9: Gas injection-/production-rate profiles versus time in a 1D displacement with 100 gridblocks with t_s = 66 days. This figure is similar to Fig. 6 except that it extends until 86 days and it also includes the gas production- rate profile. The arrow points to the moment at which the shock leaves the reservoir.

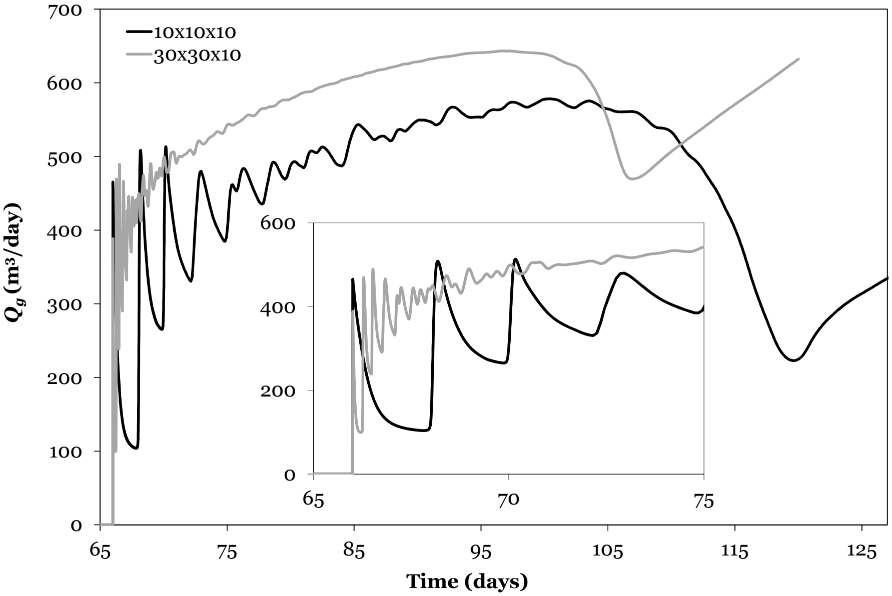

Fig. 10: Effect of spatial discretization on the fluctuations in the gas-injection profile in a 3D displacement shown in Fig. 5. Finer grids lower the amplitude of the spikes and shrink the fluctuation interval to a region very close to the switching time at t_s = 66 days. In the refined case, each gridblock is 9 times smaller than the original gridblock.

In 3D, the number of spikes is related to the number of gridblocks around the wellbore; the number of spikes grows with grid refinement (**Fig. 10**). The duration of the time interval in which the fluctuations occur is mainly dependent on the gridblock size if Δt is small enough. The smaller is the gridblock size, the shorter is the time interval of fluctuations. This is because the water content of a smaller gridblock is smaller and the water-saturation drop occurs faster accordingly. In a real reservoir, there is no spatial discretization: foam coalescence occurs within a narrow traveling wave at the shock front (Ashoori et. al. 2011b).

If Q_g is prescribed, fluctuations occur in the P_{wf}^{inj} profile to accommodate the prescribed Q_g.

5.3.2. Effect of Switching Time on Oil Recovery

The cumulative oil production can be significantly affected by the total amount of surfactant *solution* ($Q_{surf,cum}$) injected into the reservoir, which is controlled by varying the switching time t_s (**Fig. 11**). At the switching time, the surfactant injection cycle is terminated and the gas injection cycle begins. Fig. 11 illustrates the cumulative oil produced ($Q_{o,cum}$) and cumulative gas injected ($Q_{g,cum,inj}$) versus switching time for different scenarios. At each switching time, an independent simulation is performed and $Q_{o,cum}$ and $Q_{g,cum,inj}$ values are recorded at the end of the simulation. Thus, each point on the curves represents a single, independent simulation at the corresponding switching time (t_s). One needs to be careful when interpreting the results in Fig. 11: the curves are *not* plotted versus *time* but are plotted with respect to t_s.

We investigate the effect of t_s (or $Q_{surf,cum}$) on the cumulative oil production in *three* scenarios. The difference between the scenarios is after t_s; i.e., in the gas injection cycle. These scenarios differ in the active injection-well constraint and the duration of the gas-injection cycle (t_{gas}).

In Scenario 1, we prescribe Q_g. In addition, we inject gas for a fixed period of time after t_s; i.e., t_{gas} is identical for all the switching times and t_{end} varies ($t_{end} = t_{gas} + t_s$).

In Scenario 2, the injection well operates at a constant prescribed bottomhole pressure. Similar to Scenario 1; t_{gas} is identical for all the switching times and t_{end} varies ($t_{end} = t_{gas} + t_s$).

Scenario 3 is similar to Scenario 2, except that t_{end} is fixed and t_{gas} varies; i.e., $t_{gas} = t_{end} - t_s$.

The injection well is operating at a constant prescribed P_{wf} prior to t_s. Since $S_g = 0$ prior to t_s, there is no foam to obstruct the flow into the reservoir, hence, $Q_{surf,cum}$ varies linearly with t_s[*].

---

[*] $Q_{surf,cum}$ (kg) = 428,985 t_s (days). The total amount of the injected surfactant is equal to $Q_{surf,cum}$ times the surfactant concentration in the injected surfactant solution (i.e., 2.4E-3; see §4.4).

5.3.2.1. Scenario 1—Prescribed Gas-injection Rate, Fixed Gas-Injection Interval

As mentioned earlier, the gas-injection rate is prescribed in this scenario and there is no explicit bottomhole pressure constraint. We prescribe a fluctuation-free gas-injection-rate profile identical to the profile in the *foam-free case* (t_s = 0) similar to the one shown in Fig. 4. Due to the presence of foam, we observe some mild oscillation in P_{wf} of the injection well. These oscillations are mild because the prescribed gas-injection-rate profile itself is obtained at a constant prescribed bottomhole pressure ($P_{wf,max}^{inj}$). We set t_{gas} = 250 days; the gas-injection-rate profile and the cumulative gas injected ($Q_{g,cum,inj}$) are independent of the switching time in this scenario. In other words, the duration of surfactant injection has no effect on the prescribed gas-injection rate. Therefore, foam formation and coalescence do not alter the gas-injection rate in this scenario. As a result, the behavior of the cumulative oil production ($Q_{o,cum}$) of Scenario 1 in Fig. 11a merely reflects the *foam performance* in recovering oil from the reservoir as a function of the cumulative surfactant injected into the reservoir since foam does not influence the gas-injection rate. We emphasize that each point in Fig. 11 represents a single, independent simulation and that curves are plotted with respect to the switching time.

Looking at the $Q_{o,cum}$ curve of Scenario 1 in Fig. 11a, we distinguish 5 zones on the curve separated by 4 specific switching times. We refer to these switching times as *moments* T_1, T_2, T_3, and T_4. In this scenario T_1 = 5 days, T_2 = 44 days, T_3 = 52 days, and T_4 = 66 days. These moments are indicated by black markers on the curves corresponding to Scenario 1 in Fig. 11.

In this scenario, the first moment (T_1) represents the switching time below which no low-mobility foam bank forms during the displacement to improve sweep efficiency over gas flood. The second moment (T_2) corresponds to the switching time at which the foam front is at verge of reaching the production well at the end of the simulation. Moment T_3 represents the switching time above which foam front gradually starts to reach and sweep the gridblocks on the two far sides of the reservoir sharing the production well. The fourth moment (T_4) is the switching time at which foam fills the entire reservoir at the end of the simulation. We emphasize again that the gas-injection rate in this scenario is not affected by foam (Fig. 11b).

In *zone 1* with $t_s < T_1$, the relatively flat trend of $Q_{o,cum}$ in Fig. 11a is due to the absence of a low-mobility foam bank in the reservoir. As a result, foam is unable to efficiently reduce the gas mobility to improve sweep efficiency over gas flood. We have illustrated the gradual formation of the low-mobility foam bank in **Fig. 12** as a function of the switching time. In this figure, foam exists only inside the region confined by the black border. We call the part of the border separating the foam side from the no-foam side as the *foam/no-foam* boundary.

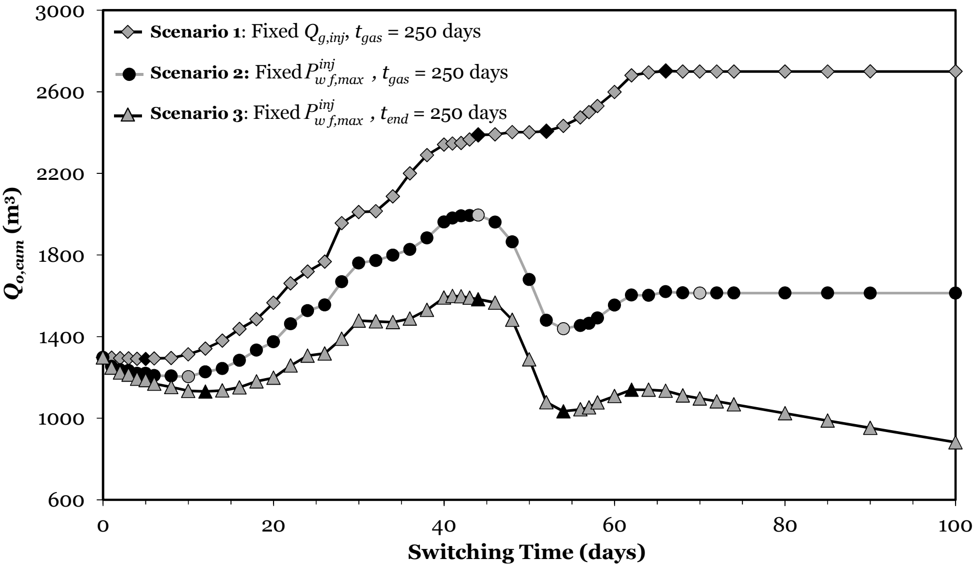

(a)

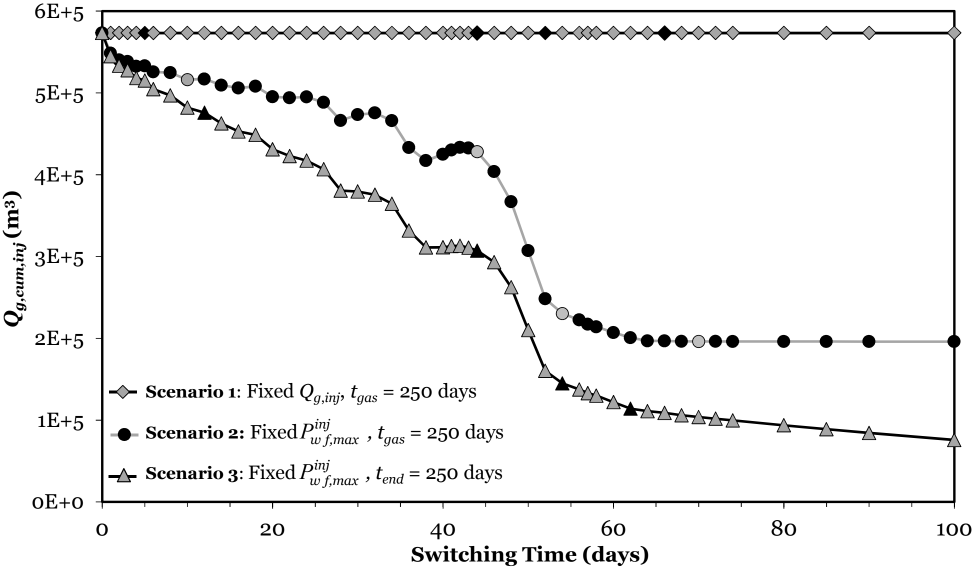

(b)

Fig. 11: (a) Cumulative oil produced ($Q_{o,cum}$) and (b) cumulative gas injected ($Q_{g,cum,inj}$) versus switching time for different scenarios. At each switching time, a simulation is performed and $Q_{o,cum}$ and $Q_{g,cum,inj}$ values are recorded at the end of the simulation. Thus, each point corresponds to a single, independent simulation at the corresponding switching time. Note that 1PV is equal to 6E4 m³.

In *zone 1*, for $t_s < T_1$ (e.g., $t_s = 3$ days), there is no significant difference in gas mobility on the two sides of the foam/no-foam boundary. For $t_s = T_1$, two low-mobility gridblocks are visible in Fig. 12; nevertheless, a complete bank has not yet formed. For $t_s > T_1$ (e.g., $t_s = 8$ days), there is a visible contrast in gas mobility on the two sides of the foam/no-foam boundary (shades of blue on one side, shades of pink on the other side) and a complete low-mobility foam bank is clearly visible in shades of blue on the foam side of the foam/no-foam boundary. The gas mobility in the low-mobility foam bank is, on average, 0.8 times less than that on the no-foam side of the boundary. Even though foam forms in the displacements with $t_s \leq T_1$; however, foam is not successful in controlling the gas mobility and improving sweep efficiency in the absence of a low-mobility bank. As a result, injecting surfactant into the reservoir for $t_s \leq T_1$ leads to no improvement in $Q_{o,cum}$ over gas flood.

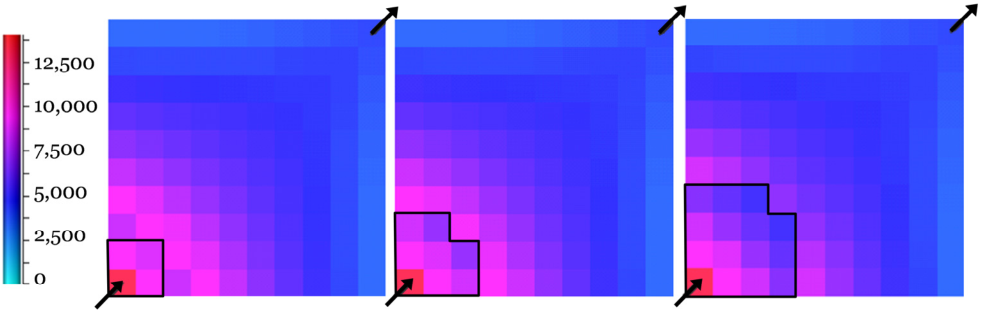

t_s = 3 days $t_s = T_1$ = 5 days t_s = 8 days

Fig. 12: Gas mobility at the top reservoir layer at the end of the simulation for different switching times in Scenario 1. The middle figure corresponds to T_1. Black border confines the region in which $C_s > C_s^*$ and foam exists only inside this region.

In *zone 2* with $T_1 < t_s < T_2$, a low-mobility foam bank is formed in the reservoir and foam is able to improve sweep efficiency over gas flood. For the simulation with $t_s = T_2$, the foam front is at the verge of reaching the production well at the end of the simulation period but has not yet reached it. If the switching time is shorter than T_2, foam does not reach the production well at the end of the simulation. Otherwise, the surfactant concentration (C_s) exceeds C_s^* (see Fig. 3c) in the lowest gridblock with the production well before the end of the simulation.

In *zone 3* with $T_2 < t_s < T_3$, increase in oil recovery is insignificant with increasing the switching time and $Q_{o,cum}$ is nearly independent of t_s. This is caused by the fact that in this zone, foam mostly forms in the rest of the gridblocks containing the production well in which there is not much oil left to sweep; therefore, $Q_{o,cum}$ is nearly independent of t_s in this interval.

In *zone 4* with $T_3 < t_s < T_4$, with switching times longer than T_3, $Q_{o,cum}$ increases with increasing switching time until reaching T_4. If the switching time is longer than T_3, the foam front reaches and sweeps the gridblocks on the two far sides of the reservoir sharing the production well. These gridblocks are not swept if the switching time is shorter than T_3 and oil saturation at these gridblocks is high (above 0.3). In this zone, foam gradually fills out those gridblocks with increasing t_s. At the switching time corresponding to T_4, foam covers the entire reservoir at the end of the simulation (i.e., $C_s \geq C_s^*$ in all the gridblocks; see Fig. 3c).

In *zone 5* with $t_s > T_4$, the gas mobility-reduction factor component corresponding to C_s (F_s) has reached its maximum of one at C_s^* (see Fig. 3c) in all the gridblocks, and increasing C_s beyond C_s^* by injecting more surfactant does not increase F_s above one. Therefore, there is no benefit in increasing the switching time beyond T_4 since it does not alter the foam strength anywhere. Thus, $Q_{o,cum}$ becomes independent of t_s after T_4 and injecting more surfactant by increasing t_s is no longer beneficial and results in significant loss of surfactant.

In Scenario 1, if $t_s > T_1$, a low-mobility foam bank forms and injecting surfactant into the reservoir leads to improved $Q_{o,cum}$ over gas flood (i.e., $Q_{o,cum}$ at $t_s = 0$ day). Therefore, one must avoid $t_s < T_1$. On the other hand, if foam covers the entire reservoir during the simulation (i.e., for $t_s > T_4$), no additional oil recovery is obtained by increasing t_s. Thus, it is only beneficial to choose $T_1 < t_s < T_4$. For $T_1 < t_s < T_4$, increasing the switching time results in higher oil recovery; economics would identify the switching time resulting in the most profitable process.

5.3.2.2. Scenario 2—Fixed Bottomhole Pressure, Fixed Gas-Injection Interval

The difference between Scenarios 1 and 2 is the active injection-well constraint. In Scenario 1, the gas-injection rate was prescribed, but there was no constraint on $P_{wf,max}^{inj}$ after the switching time. Whereas in this scenario, $P_{wf,max}^{inj}$ is prescribed and fixed and gas-injection rate is regulated to conform with the active $P_{wf,max}^{inj}$ constraint. In both scenarios, the gas-injection interval is fixed and equal to 250 days.

The difference in the active constraint of the injection well between Scenarios 1 and 2 affects the cumulative gas injected into the reservoir in this scenario. Since the production well is also operating at a constant prescribed bottomhole pressure ($P_{wf,min}^{prod}$), the overall pressure drop between the wells is fixed in this scenario (ΔP = $P_{wf,max}^{inj} - P_{wf,min}^{prod}$). Therefore, according to Darcy's law, the gas-injection rate must be regulated in accordance with the changes in the overall gas mobility due to the presence of foam. Thus, the gas-injection rate must decline as long as gas mobility declines in the reservoir; especially in the gridblocks containing the two wells (see §5.3.1.1), impairing the gas-injection rate. This is directly reflected in the value of the cumulative gas injected ($Q_{g,cum,inj}$) at the end of the simulation. The overall trend of $Q_{g,cum,inj}$ versus the switching time is declining because of the active constraint on $P_{wf,max}^{inj}$: Gas mobility is lowered to a larger extent at longer switching times since more surfactant is injected into the reservoir and foam can penetrate more deeply into the reservoir. As a result, the longer the switching time is, the smaller is $Q_{g,cum,inj}$ because less gas is injected into the reservoir. This decline may or may not influence oil recovery in the ways discussed below.

We remind that the trend of $Q_{o,cum}$ in Scenario 1 was merely reflecting the effect of *foam performance* in recovering oil, since Q_g was not influenced by t_s (or foam) in Scenario 1. Although t_{gas} is identical in both scenarios, the total gas-injection volumes are not: $Q_{g,cum,inj}$ in this scenario is influenced by the presence of foam and it varies with the switching time. Therefore, the difference between the overall trend of $Q_{o,cum}$ in Scenarios 1 and 2 in Fig. 11a is attributed to the difference in the active constraints of the injection well in these scenarios leading to the declining trend of $Q_{g,cum,inj}$ in Scenario 2 (Fig. 11b).

The trend of the $Q_{o,cum}$ curves in Scenario 2 reveals an interesting phenomenon caused by the competition between *foam performance* and declining $Q_{g,cum,inj}$. Similar to Scenario 1, we distinguish 5 zones in the $Q_{o,cum}$ curve, separated by moments T_1, T_2, T_3, and T_4. These moments are indicated by gray markers on the curves corresponding to Scenario 2 in Fig. 11. The origin of these moments is similar to the moments described in Scenario 1; however, the changes in the trend of $Q_{o,cum}$ are more significant in this scenario compared to Scenario 1. In this scenario, T_1 = 10 days, T_2 = 44 days, T_3 = 54 days, and T_4 = 70 days.

We repeat the definitions of T_1, T_2, T_3, and T_4 from Scenario 1 in §5.3.2.1 here. The first moment (T_1) represents the switching time below which no low-mobility foam bank forms in the reservoir to improve sweep efficiency over gas flood. The second moment (T_2) corresponds to the switching time at which the foam front is at the verge of reaching the production well at the end of the simulation. Moment T_3 represents the switching time above which foam front gradually starts to reach and sweep the gridblocks on the two far sides of the reservoir sharing the production well. The fourth moment (T_4) is the switching time at which foam fills the entire reservoir at the end of the simulation.

In *zone 1* with $t_s < T_1$, the moderate decline of $Q_{o,cum}$ reflects the fact that at these switching times, the low-mobility foam bank has not yet formed in the reservoir to improve sweep efficiency over gas flood. As a result, it is not reasonable to have switching times shorter than T_1. However, there is enough foam near the injection well to impair the gas injectivity. As a result, $Q_{o,cum}$ declines as $Q_{g,cum,inj}$ declines until the low-mobility foam bank forms shortly after T_1 to improve sweep efficiency despite the declining $Q_{g,cum,inj}$.

In *zone 2* with $T_1 < t_s < T_2$, $Q_{o,cum}$ increases with increasing the switching time with a trend similar to that observed in Scenario 1; despite the fact that the cumulative gas injected is declining in this scenario as t_s increases. This shows that *foam performance* overcomes the declining $Q_{g,cum,inj}$ in this zone. Further increase in t_s allows injecting more surfactant into the reservoir leading to a further advance of the foam front in the reservoir and improved sweep efficiency in the reservoir, despite the declining trend of $Q_{g,cum,inj}$.

In *zone 3* with $T_2 < t_s < T_3$, however, we observe the only substantial difference between the behavior of $Q_{o,cum}$ in Scenarios 1 and 2. We observe a rapid decline in $Q_{o,cum}$ for $t_s > T_2$. Foam breaks through to the production well for the switching time slightly longer than T_2, as observed in Scenario 1. In addition, maximum $Q_{o,cum}$ is achieved at the simulation with $t_s = T_2$ at which 0.3 PV of surfactant solution is injected into the reservoir prior to t_s. For switching times longer than T_2, a continuous foam path connects the wells, causing a significant drop in the overall gas mobility. As a result, $Q_{o,cum}$ drops significantly as well and gas productivity is impaired once the foam front reaches the production well. Thus, drop in *gas productivity* that consequently leads to the decline in $Q_{o,cum}$ is the dominant mechanism in zone 3.

In *zone 4* with $T_3 < t_s < T_4$, *foam performance* dominates once again and the decline in $Q_{g,cum,inj}$ is moderate. $Q_{o,cum}$ starts to rise again in zone 4 with increasing the switching time because foam can sweep the gridblocks on the two far sides of the reservoir sharing the production well. As mentioned in Scenario 1, these regions are not swept by foam in simulations with switching times shorter than T_3; hence, the oil saturation in these regions is high and increasing the switching time improves the sweep of these regions leading to an increase in $Q_{o,cum}$.

In *zone 5* with $t_s > T_4$, *foam performance* is the dominant mechanism as in zone 4. In the simulations with $t_s > T_4$, foam covers the entire reservoir in the simulation period. In addition, foam strength remains unchanged and independent of surfactant concentration in zone 5 (see Scenario 1 for more detail). Thus, average gas mobility and overall pressure drop in Darcy's law become constant, dictating a fixed cumulative gas-injection rate in zone 5 (Fig. 11b). As a result, $Q_{o,cum}$ remains unchanged in zone 5 and becomes independent of the amount of injected surfactant represented by the switching time; as also observed in Scenario 1 in this zone. Therefore, it is not beneficial to choose the switching times in this zone as it results in significant surfactant loss and no increase in $Q_{o,cum}$.

It is important to note that injecting surfactant into the reservoir does not necessarily lead to improved $Q_{o,cum}$ over a gas flood (i.e., $Q_{o,cum}$ at $t_s = 0$ day). In this scenario, the switching time must be longer than 16 days in order to observe an improvement in oil recovery over gas flood and one must certainly avoid $t_s < 16$ days. Besides, increasing the switching time in this scenario does not necessarily lead to higher $Q_{o,cum}$: it leads to a lower oil recovery in zones 1 and 3, and it results in no improvement in zone 5. Improved oil recovery by increasing the switching time is only observed in zones 2 and 4. $Q_{o,cum}$ has its maximum at the border of zones 2 and 3 and it corresponds to the switching time at which the foam front is at the verge of reaching the production well at the end of the simulation. If the foam front reaches the production well during the simulation, oil recovery is damaged significantly and is lower than the maximum $Q_{o,cum}$. Therefore, if one can destroy foam in the production well, more oil will be produced at the maximum $Q_{o,cum}$ (see the last paragraph in §5.3.2.4).

5.3.2.3. Scenario 3—Fixed Bottomhole Pressure, Fixed End Time

In this scenario, the injection well operates at a constant prescribed bottomhole pressure ($P^{inj}_{wf,max}$) after t_s similar to Scenario 2, and gas injectivity is reduced by increasing the switching time and accordingly increasing $Q_{surf,cum}$ (Fig. 11b). The difference between Scenarios 2 and 3 is that the end time (t_{end}) is fixed in this case. Therefore, the gas-injection interval (t_{gas}) shrinks as the switching time increases; i.e., $t_{gas} = t_{end} - t_s$. Consequently, the cumulative gas injected and cumulative oil produced are always lower than those observed in Scenario 2. Similar to Scenario 2, moments T_1, T_2, T_3, and T_4 exist in this scenario and they are indicated by black markers on the Scenario 3 curves in Fig. 11 (T_1 = 12 days; T_2 = 44 days; T_3 = 54 days; T_4 = 62 days). The behaviors observed in this scenario are explained by the same mechanisms described in Scenario 2, except for what happens in zone 5. For the simulations with switching times longer than T_4, foam covers the entire reservoir in the simulation period. However, contrary to Scenario 2, where $Q_{o,cum}$ was independent of t_s in zone 5, $Q_{o,cum}$ declines with increasing the switching time in this scenario. This is due to the fixed end-time constraint in this scenario; the period of gas injection is shortened as the switching time increases. Thus, less gas is injected into the reservoir by increasing the switching time, resulting in a declining trend in $Q_{o,cum}$ as well.

Injecting surfactant into the reservoir results in an improvement in oil recovery over gas flood (i.e., $Q_{o,cum}$ at t_s = 0 day), only if 24 days < t_s < 50 days, and one must certainly avoid choosing switching times outside this interval. Otherwise, $Q_{o,cum}$ is less than that for gas flood. The maximum $Q_{o,cum}$ is located inside this interval at the border of zones 2 and 3. It corresponds to the switching time at which the foam front is at the verge of reaching the production well at the end of the simulation. As a result, if foam formation in the production well can be delayed, more oil will be produced at the maximum $Q_{o,cum}$ (see the last paragraph in §5.3.2.4).

5.3.2.4. Concluding Remarks and Recommendations on Scenarios 1 to 3

- All the scenarios share the same $Q_{g,cum,inj}$ and the same $Q_{o,cum}$ at t_s = 0. This point corresponds to the foam-free case with a constant prescribed bottomhole pressure ($P_{wf,max}^{inj}$) without any surfactant injection prior to the gas-injection cycle. The injection profile of the foam-free case is prescribed as the gas-injection profile in Scenario 1. In all the three scenarios, the production well operates at a constant prescribed bottomhole pressure.

- The injection well is operating at a prescribed gas-injection rate (Scenario 1):
    - If the switching time is longer than T_1, injecting surfactant into the reservoir leads to improved $Q_{o,cum}$ over gas flood (i.e., $Q_{o,cum}$ at t_s = 0 day). Thus, one must avoid switching times shorter than T_1.
    - Increasing the switching time beyond T_1 improves $Q_{o,cum}$, until foam sweeps the entire reservoir at T_4.
    - If foam covers the entire reservoir during the simulation (i.e., for $t_s > T_4$), no additional oil recovery is obtained by increasing the switching time. Therefore, it is only beneficial to choose $T_1 < t_s < T_4$.
    - For $T_1 < t_s < T_4$, increasing the switching time results in higher oil recovery; economics would identify the switching time resulting in the most profitable process.
- The injection well is operating at a constant prescribed bottomhole pressure (Scenarios 2, 3):
    - Injecting surfactant into the reservoir does not necessarily lead to improved $Q_{o,cum}$ over a gas flood. With a fixed gas-injection interval, no improvement is obtained for t_s < 18 days. With a fixed end time, the situation is worse: improvement is achieved only at intermediate switching times (i.e., 24 days < t_s < 50 days). Therefore, one must avoid switching times that lead to $Q_{o,cum}$ lower than gas flood.
    - Injecting less gas (smaller $Q_{g,cum,inj}$) as a result of increasing the switching time does not necessarily result in lower cumulative oil production.
    - If the foam front reaches the production well during the process, the whole process is inferior to the situation described above. Further increase in t_s not only results in lower $Q_{o,cum}$ but also leads to wastes of surfactant.

In all the scenarios, the switching time ($t_{s,opt}$) at which the maximum cumulative oil is produced, is the switching time at which the foam front is at the verge of reaching the production well at the end of the simulation period but has not yet reached it. Therefore, if foam can be destroyed only in the proximity of the production well, more oil will be produced at the maximum $Q_{o,cum}$. One possible way of destroying foam in that zone, is by reducing the surfactant concentration well below C_s^*. This can be done by injecting sufficient amount of water in the production well, such that water would not flow beyond that zone and only lowers C_s in the desired region. It is also possible to use foam breaking agents instead of water, but it certainly increases the costs.

5.4. Optimal Control Theory

Optimal control theory, which has its roots in the classic calculus of variation, is a mathematical optimization method for finding *optimal* control policies. “The objective of optimal control theory is to determine a control policy that will cause a process to satisfy the physical constraints and at the same time minimize (or maximize) some performance criterion” (Kirk 2004). Our objective is maximizing the cumulative oil production by foam EOR within the simulation period.

5.4.1. A Literature Review

Optimal control theory was developed for optimally controlling the trajectories of satellites and rockets during the 1950s and 1960s (Jansen 2011). Optimal control theory has been applied in various disciplines since then for optimization of dynamic systems.

In petroleum engineering, it has three major applications: history matching, EOR optimization, and waterflood optimization. This theory was first applied to history matching problems in the 1970s by Chavent et al. (1973), Chen et al. (1974), and Dougherty and Khairkhah (1975) for single-phase flow. This application and its further developments are discussed in the book by Oliver et al. (2008). In the 1980s, Ramirez and his coworkers applied it for optimization of EOR processes: surfactant flooding, micellar/polymer flooding, carbon dioxide miscible flooding, and later to steamflooding in the 1990s. Application of optimal control theory to waterflood optimization was initiated by Asheim (1987, 1988). Jansen (2011) has recently reviewed the history and developments of the adjoint-based optimization of multi-phase flow in porous media. These methods were not applied in industry until the introduction of the concept of *smart well* technology into waterflooding (Brouwer 2004; Brouwer and Jansen 2004; Sarma et al. 2005).

Ramirez and his coworkers are the pioneers in the application of optimal control theory to EOR processes. They first discussed the theory and computational strategies in Ramirez et al. (1984). Fathi and Ramirez (1984) then applied it for designing an optimal surfactant flooding injection policy for maximizing oil recovery while minimizing the chemical cost in 1D. They allowed for surfactant adsorption to the rock and partitioning of surfactant between the phases in their model in addition to the convective and dispersive mechanisms of mass transfer. They defined two types of hypothetical interfacial-tension behavior (i.e., between water and oil) and they considered water viscosity as a function of surfactant concentration. They applied the steepest-descent method to search for the optimum. They found a unique optimum for the amount of surfactant needed to maximize the oil recovery while minimizing the surfactant cost for each type of the interfacial-tension function used independent of the initial guess of the injection policy. A non-unique solution implies having several local optima.

Ramirez (1987) also employed optimal control theory to 1D and 2D (i.e., 2D areal section) optimization of the micellar/polymer EOR processes. They applied both the steepest-descent and modified conjugate-gradient method as an optimization routine. The less-efficient steepest-descent method always worked satisfactorily. However, the rapid convergence of the conjugate-gradient algorithm near the optimum was undermined by requiring a good initial guess (starting point for the control variable) to ensure solution stability. They reported that the optimal injection policy was a function of the initial guess, but the optimum performance was very similar in some instances.

Ramirez (1987) and Mehos and Ramirez (1989) also applied optimal control theory to 2D (i.e., 2D areal section) optimization of carbon dioxide EOR processes. They considered a three-component (i.e., H_2O, Oil, and CO_2), two-phase, miscible system in a homogeneous reservoir. They investigated three different injection strategies (i.e., slug[*], simultaneous, and WAG), neglecting gravity and capillary effects. Water and CO_2 injection rates and producer's bottomhole pressure as a function of time were chosen as the control variables. As they reported earlier for polymer/micellar floods, their optimal injection strategy was affected by the initial guess of the control variables. In the three cases investigated (slug, simultaneous, and WAG), they reported that the optimal total injected volume of CO_2 was unique between all the three cases, but the optimum injection strategy was not. In all these optimal control policies, they found similar cumulative oil recoveries.

Liu et al. (1993) and Liu and Ramirez (1994) applied this theory to 2D and 3D steamflood optimization, respectively.

Various studies are focusing on waterflood optimization. It was first applied by Asheim (1987, 1988) and then followed by Vironovsky (1991), Zakirov et al. (1996), Sudaryanto (1998), and Sudaryanto and Yortsos (2000, 2001). It was later used by Brouwer (2004), Brouwer and Jansen (2004), Sarma et al. (2005, 2008), Zandvliet et al. (2007), Kraaijevanger et al. (2007), and van Essen et al. (2010).

---

[*] A single CO_2 slug followed by water injection.

5.4.2. Complications

Optimal control theory provides a tool to find optimal control strategies for maximizing oil production. However, applying the theory may involve certain complications as discussed below. A certain method may work well for simple examples; however, it might result in suboptimal solution in more complex systems (Brouwer 2004).

Fathi and Ramirez (1984) had difficulty in solving the adjoint PDEs backward in time, in surfactant flooding optimization. The adjoint equation had non-smooth coefficients caused by the physical nature of the original PDE, making it difficult to find a stable numerical adjoint scheme. They associated this problem with the discontinuity in the adjoint equation coefficients caused by two shocks (the first shock was a Buckley-Leverett shock and the second shock was at the surfactant front). They modified the adjoint formulation to deal with this problem. They tried various numerical schemes to solve the *continuous* adjoint equation (i.e., the system equations, adjoint equations, and objective function are discretized as the last step); however, none of them resulted in a stable solution. They discovered that using smooth approximations of the non-smooth coefficients results in a stable scheme. Later, Fathi and Ramirez (1987) applied optimal control theory to micellar/polymer flooding with both continuous and *discrete* formulations (i.e., the equations are discretized from the beginning). They encountered serious problems in the application of optimal control theory arising from the complexity of the immiscible flow equations. They further proposed that numerical dispersion can be used to replace the physical dispersion, if physical dispersion is represented by the numerical dispersion. This can both simplify the problem and remove some of the computational problems they encountered with surfactant flooding optimization.

Application of this theory to 2D steamflood optimization by Liu et al. (1993) revealed that finding a stable adjoint solution could be a significant mathematical problem. This problem needs special attention for complex EOR processes. Liu and Ramirez (1994) extended the analysis of steamflood optimization described above to 3D and they found that a too large time-step size (Δt) can cause non-smooth optimal control strategies. They claimed that refinement of Δt should smooth the control strategies.

Sudaryanto (1998) applied a finite-difference formulation for simulating the forward and adjoint equations in miscible EOR and faced problems in finding the optimum switching time (terminating water injection at one injector and starting it in another injector) for a displacement with variable mobility. The gradient of the objective function was equal to zero at a switching time *other than* the one that was maximizing the objective function. However, the gradient of the objective function must equate to zero at the *internal*[*] optimum (maximum here). He stated that this problem is caused by round-off errors in solving large system of state and adjoint equations. The numerical errors build up over hundreds of time steps and they may become significant, affecting the solutions. They were able to solve this problem by applying smaller Δt to avoid instability problems in the adjoint equation.

Regarding the time-step size, the adjoint may not necessarily find correct gradients with the same time-step sizes with which the forward simulation can find the correct solution. It is sometimes necessary to reduce Δt in the forward simulation when it is ultimately used for optimization with the adjoint routine. Liu and Ramirez (1994) indicated that although Δt is controlled in the forward simulation to limit the changes in states to the maximum allowed changes, the changes in the *adjoint* states may not necessarily match the changes in the states. They suggested that a different Δt control might be required for the adjoint run. They used a smaller, constant Δt for the adjoint equation.

We did not encounter the complications stated above; however, we faced other issues. The main issue was the magnitude of the *relative tolerance* for the adjoint linear solver. The default value in the simulator for this term (1E-7) was too large for our problem. We required to use much smaller values (i.e., 1E-12 in the simpler cases and 2.25E-16 for the most complex case) to obtain accurate adjoint gradients. The default value of the relative tolerance in our problem led to wrong adjoint gradients in some instances (see **Fig. 20**). We have discussed this in the last paragraph of §5.7.3.

In addition, we encountered non-smooth adjoint gradients with various fluctuations in this chapter. We attributed them to the nature of the nonlinear foam model (Fig. 3) applied. This model produces abrupt changes in gas mobility as a result of changes in water saturation, oil saturation, and surfactant concentration. We did not observe these symptoms with the linear foam model (Fig. 3) that did not introduce abrupt changes in gas mobility. This behavior of the nonlinear foam model resulted in major differences between the local and global trends of the objective function and made it impossible for the gradient-based optimization routine (steepest-ascent) to find the optimum. This issue is discussed in detail in §5.9.

Gradient-based methods only provide local information about the objective function in the neighborhood of the current value of the control vector (**u**). Therefore, if the objective function has multiple local optima (distinguished by having the optimum dependent on the

---

[*] By internal we mean that if the switching time is limited to a certain interval, then a necessary condition for optimality of a point inside that interval is that the gradient at that point is zero.

initial guess of **u**), it is highly probable to find a local optimum instead of a global optimum. In order to avoid this, it is advised to try a wide range of different choices of **u** as the starting guess (Dynamo/MoReS Online User Documentation 2010). However in either case, this method does not ensure finding the global optimum.

5.5. Objective Function

The objective function here is defined as the cumulative oil production at the end of the simulation (*T*):

$$\mathcal{J} = \int_0^T Q_o(t)\,\mathrm{d}t, \tag{1}$$

where Q_o is the surface volume rate of the oil phase. It should be noted that when performing life-cycle optimization, the achieved optimal control strategy may strongly differ based on the choice of $\mathcal{J}$. For instance, the optimal control strategy obtained when optimizing the cumulative oil production may be very different from the strategy obtained when optimizing the net present value.

Our aim is finding the optimum duration of the surfactant slugs in a SAG foam process for which $\mathcal{J}$ is maximized. This duration is represented by the optimum switching time ($t_{s,opt}$).

5.6. System Equation

Any dynamic system is controlled by the inputs to the system. Any variation in the inputs leads to variation in the states of the system; hence, the states are functions of the inputs. The dynamic system of our interest is a producing reservoir and its wells, described by a set of coupled algebraic and differential equations. The discrete dynamic system equations in Eq. 2 are obtained after discretizing in space and time. The equations which are internally solved by the simulator during time-stepping are a combination of reservoir equations and well equations. The reservoir equations are formulated per gridblock and consist of a flow equation (or mass-balance equation) for each component, and a volume balance equation per gridblock. The well equations consist of constraint equations, rate (or mass) balance equations and pressure-drop equations (Dynamo/MoReS Online User Documentation 2010). All these equations are combined into

$$\mathbf{g}_k(\mathbf{x}_{k-1}, \mathbf{x}_k, \mathbf{u}_k) = \mathbf{0} \qquad (k = 1, \ldots., N), \tag{2}$$

where k is the time-step index and N is the number of time steps. At every time step k, the inputs or the control vector ($\mathbf{u}_k$) contains the well control for all wells (one or more of the dynamic variables mentioned in §5.2), and the state vector ($\mathbf{x}_k$) essentially contains the saturations, pressures, and compositions of *all* reservoir gridblocks and well discretization nodes. $\mathbf{x}_k$ and $\mathbf{u}_k$ are column vectors and we denote their dimensions by m and n, respectively. $\mathbf{g}_k$ is also a column vector of dimension m. During the *forward* run (i.e., normal simulation run), $\mathbf{x}_k$ is successively calculated by solving Eq. 2, starting with the initial condition, i.e., $\mathbf{x}_0$ at t_0. In each transition from t_{k-1} to t_k, $\mathbf{u}_k$ must be specified. In the derivations below, we follow the approach of Kraaijevanger et al. (2007).

It is convenient to combine all the control vectors at different time steps in one *super* control vector $\mathbf{u}$ and all the state vectors at different time steps in one *super* state vector $\mathbf{x}$ in the form of

$$\mathbf{x}=\begin{pmatrix}\mathbf{x}_1\\ \mathbf{x}_2\\ \vdots\\ \mathbf{x}_N\end{pmatrix},\quad \mathbf{u}=\begin{pmatrix}\mathbf{u}_1\\ \mathbf{u}_2\\ \vdots\\ \mathbf{u}_N\end{pmatrix},\tag{3}$$

where $\mathbf{x}$ and $\mathbf{u}$ are column vectors with $\dim(\mathbf{x}) = N\times m$ and $\dim(\mathbf{u}) = N\times n$. We rewrite Eq. 2 in the form of the *super* function $\mathbf{g}$ defined by

$$\mathbf{g}(\mathbf{x},\mathbf{u})=\mathbf{0},\qquad \text{where}\qquad \mathbf{g}(\mathbf{x},\mathbf{u})=\begin{pmatrix}\mathbf{g}_1(\mathbf{x}_0,\mathbf{x}_1,\mathbf{u}_1)\\ \mathbf{g}_2(\mathbf{x}_1,\mathbf{x}_2,\mathbf{u}_2)\\ \vdots\\ \mathbf{g}_N(\mathbf{x}_{N\text{-}1},\mathbf{x}_N,\mathbf{u}_N)\end{pmatrix},\tag{4}$$

where $\mathbf{g}$ is a column vector and $\dim(\mathbf{g}) = \dim(\mathbf{x}) = N\times m$.

5.7. Gradient Calculation

All the following formulations are based on the assumption that $\mathbf{x}$ is a function of $\mathbf{u}$, i.e.,

$$\mathbf{x}=\mathbf{x}(\mathbf{u}).\tag{5}$$

A small variation in $\mathbf{u}$ causes a small variation in $\mathbf{x}$, or

$$\mathbf{g}_\mathbf{x}d\mathbf{x}+\mathbf{g}_\mathbf{u}d\mathbf{u}=\mathbf{0}\quad\text{where}\quad \mathbf{g}_\mathbf{x}={}^{\partial\mathbf{g}}\!/_{\partial\mathbf{x}}\quad\text{and}\quad \mathbf{g}_\mathbf{u}={}^{\partial\mathbf{g}}\!/_{\partial\mathbf{u}},\tag{6}$$

where $\mathbf{g}_\mathbf{x}$ and $\mathbf{g}_\mathbf{u}$ are the Jacobian matrices with respect to $\mathbf{x}$ and $\mathbf{u}$, respectively. $\mathbf{g}_\mathbf{x}$ is a block bi-diagonal matrix with $\dim(\mathbf{x})$ rows and $\dim(\mathbf{x})$ columns and each of its block elements has m rows and m columns (see **Fig. 13** and Eqs. 14 and 15 for more details). $\mathbf{g}_\mathbf{u}$ is a block-diagonal matrix with $\dim(\mathbf{x})$ rows and $\dim(\mathbf{u})$ columns and each of its block elements has m rows and n columns (Fig. 13).

We want to obtain the total derivative of the *scalar* objective function $\mathcal{J}$ with respect to **u**:

$$\frac{\mathrm{d}\mathcal{J}(\mathbf{x}(\mathbf{u}),\mathbf{u})}{\mathrm{d}\mathbf{u}} = \mathcal{J}_{\mathbf{u}} + \mathcal{J}_{\mathbf{x}} \frac{\mathrm{d}\mathbf{x}}{\mathrm{d}\mathbf{u}} \quad \text{where} \quad \mathcal{J}_{\mathbf{u}} = {}^{\partial \mathcal{J}}\!/_{\partial \mathbf{u}} \text{ and } \mathcal{J}_{\mathbf{u}} = {}^{\partial \mathcal{J}}\!/_{\partial \mathbf{x}}, \tag{7}$$

where $\mathcal{J}_{\mathbf{x}}$ and $\mathcal{J}_{\mathbf{u}}$ are the Jacobian matrices of $\mathcal{J}$ with respect to **x** and **u**. $\mathcal{J}_{\mathbf{x}}$ and $\mathcal{J}_{\mathbf{u}}$ are row vectors of dimension dim(**x**) and dim(**u**), respectively. Here d**x**/d**u** is the Jacobian matrix containing the *partial* derivatives of **x** with respect to **u**, and is called the *sensitivity* matrix **S**. Matrix **S** has dim(**x**) rows and dim(**u**) columns with its block elements defined by

$$\mathbf{S}_{k,l} = \frac{\partial \mathbf{x}_k}{\partial \mathbf{u}_l} \qquad (k,l = 1,2,\ldots,N).$$

Each block element of **S** has *m* rows and *n* columns. Since $\mathbf{x}_k$ does not depend on $\mathbf{u}_k$ with $l > k$, we have $\mathbf{S}_{k,l} = 0$ for all *k, l* with $l > k$. Therefore, matrix **S** is a block lower triangular matrix.

Assuming that $\mathbf{g}_{\mathbf{x}}$ is invertible, the sensitivity matrix is derived from Eq. 6:

$$\frac{\mathrm{d}\mathbf{x}}{\mathrm{d}\mathbf{u}} = -\,\mathbf{g}_{\mathbf{x}}^{-1}\mathbf{g}_{\mathbf{u}}. \tag{8}$$

Thus, the total derivative $\mathrm{d}\mathcal{J}/\mathrm{d}\mathbf{u}$ in Eq. 7 is written as:

$$\frac{\mathrm{d}\mathcal{J}}{\mathrm{d}\mathbf{u}} = \mathcal{J}_{\mathbf{u}} - \mathcal{J}_{\mathbf{x}}\mathbf{g}_{\mathbf{x}}^{-1}\mathbf{g}_{\mathbf{u}}. \tag{9}$$

Note that $\mathrm{d}\mathcal{J}/\mathrm{d}\mathbf{u}$ is a row vector with the same dimension as **u**; i.e., dim($\mathrm{d}\mathcal{J}/\mathrm{d}\mathbf{u}$) = dim(**u**). The gradient $\mathrm{d}\mathcal{J}/\mathrm{d}\mathbf{u}$ is used to construct a new, improved control vector that leads to a higher value of $\mathcal{J}$. It is important to note that $\mathrm{d}\mathcal{J}/\mathrm{d}\mathbf{u}$ reflects the behavior of $\mathcal{J}$ only in the neighborhood of **u**.

There are different ways for the calculation of the total derivative $\mathrm{d}\mathcal{J}/\mathrm{d}\mathbf{u}$. It can be calculated numerically (perturbation method), or analytically (forward method and adjoint method). In the forward method and the adjoint method, all the partial derivatives on the right side of Eq. 9 are calculated analytically from the discrete dynamic system equations in Eq. 2 and (the discrete version of) the objective function in Eq. 1. These analytical derivatives must be available in the source code.

5.7.1. The Perturbation Method

The perturbation method is a numerical gradient-calculation method. As mentioned earlier (§5.7), dim($\mathrm{d}\mathcal{J}/\mathrm{d}\mathbf{u}$) = dim(**u**), and each element of the total derivative vector $\mathrm{d}\mathcal{J}/\mathrm{d}\mathbf{u}^{i}$ is provided by a single *forward* perturbation run (i.e., the normal simulation run). In each run, one of the elements of the control vector $\mathbf{u}^i$ is slightly perturbed by $\Delta\mathbf{u}^i$ (while keeping the other elements fixed), leading to the calculation of $\mathcal{J}^i$. The term $\mathrm{d}\mathcal{J}/\mathrm{d}\mathbf{u}^i$ is then calculated by the finite-difference method:

$$\frac{\mathrm{d}\mathcal{J}}{\mathrm{d}\mathbf{u}^i}=\frac{\mathcal{J}^i-\mathcal{J}}{\Delta\mathbf{u}^i}, \tag{10}$$

where $\mathcal{J}$ is obtained from the forward run with the original guess of $\mathbf{u}$. This method is very easy to implement, but it has a severe drawback that makes it inefficient if dim($\mathbf{u}$) is large, because the number of perturbation runs is *equal* to dim($\mathbf{u}$).

In addition, finding the appropriate choice of $\Delta\mathbf{u}^i$ is nontrivial (Nocedal and Wright 1999). This method is not accurate if $\Delta\mathbf{u}^i$ is too large or too small. The perturbation must be *sufficiently* small to minimize the effects of nonlinearity, but too small perturbations may also lead to inaccurate gradients due to numerical round-off errors.

5.7.2. The Forward Method

The forward method computes the gradient $\mathrm{d}\mathcal{J}/\mathrm{d}\mathbf{u}$ analytically, as all the partial derivatives on the right side of Eq. 9 are also calculated analytically. This method is a logical step towards the adjoint method (gradient-calculation method in the simulator); hence, it is discussed here.

The difference between the forward and the adjoint method is in the way they handle the computation of the term $\mathcal{J}_\mathbf{x}\mathbf{g}_\mathbf{x}^{-1}\mathbf{g}_\mathbf{u}$ in Eq. 9 (Fig. 13). In the forward method, the term $-\mathbf{g}_\mathbf{x}^{-1}\mathbf{g}_\mathbf{u}$, i.e., the sensitivity matrix $\mathbf{S}$ is first evaluated by *solving* the *system* of linear equations

$$\mathbf{g}_\mathbf{x}\mathbf{S}=-\mathbf{g}_\mathbf{u}, \tag{11}$$

and then $\mathbf{S}$ is multiplied by $\mathcal{J}_x$ to give the total derivative in Eq. 9.

This method suffers from the same scaling of computational effort with dim($\mathbf{u}$) as the perturbation method. This can be seen from Eq. 11, in which the *number of columns* in matrix $\mathbf{g}_\mathbf{u}$ on the right-side of this equation is equal to dim($\mathbf{u}$); hence, this method is computationally very expensive for large control vectors. However, it is more robust than the perturbation method in the sense that the forward method computes the exact derivative of $\mathrm{d}\mathcal{J}/\mathrm{d}\mathbf{u}$; however, the perturbation method approximates this term and there is always a question about the proper choice of the perturbation size to arrive at an accurate derivative (Kraaijevanger 2007).

It is important to emphasize that the major part of the computational effort in this method corresponds to the calculation of the sensitivity matrix from Eq. 11. The number of equations to be solved in Eq. 11 for calculating **S** is dim(**x**)×dim(**u**), which is a function of dim(**u**).

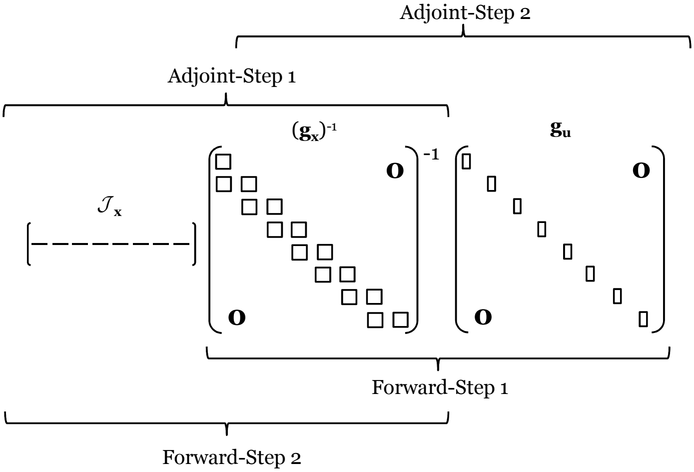

Fig. 13: Computation steps in the adjoint and forward methods. $\mathcal{J}_x$ is a row vector, $\mathbf{g_x}$ is a block bi-diagonal matrix, and $\mathbf{g_u}$ is a block-diagonal matrix. The term *block* matrix means that the matrix has been partitioned into smaller matrices called blocks or block elements. $\mathbf{g_x}$ and $\mathbf{g_u}$ have N block elements in each block row and N block elements in each block column. Each block element of $\mathbf{g_x}$ is a square matrix with a dimension of $m\times m$. Each block element of $\mathcal{J}_\mathbf{x}$ is a row vector of dimension m, and each block element of $\mathbf{g_u}$ is an $m\times n$ matrix [usually $n < m$].

5.7.3. The Adjoint Method[*]

Gradients in the simulator are calculated by the adjoint method. The adjoint method is also based on the analytical calculation of the gradient. This method is an efficient way of computing the $\mathcal{J}_\mathrm{x}\mathbf{g}_\mathrm{x}^{-1}\mathbf{g}_\mathrm{u}$ term in Eq. 9. The drawback of the forward method is that it first computes the $\mathbf{g}_\mathrm{x}^{-1}\mathbf{g}_\mathrm{u}$ term (by computing **S** from Eq. 11) which is *dependent* on dim(**u**) and hence very computationally demanding. The magic of the adjoint method is that, instead, the $\mathcal{J}_\mathrm{x}\mathbf{g}_\mathrm{x}^{-1}$ term is calculated first (by computing $\boldsymbol{\lambda}$ from Eq. 13) which is *independent* of dim(**u**) (Fig. 13). This seemingly minor difference makes the adjoint method extremely efficient for large control vectors in the way discussed below.

---

[*] In this work, a self-contained elementary derivation of the adjoint method is presented that follows Rodrigues (2006) and Kraaijevanger et al. (2007). This derivation is different from but equivalent to the well-known derivation based on the Lagrange formalism. Jansen (2010) reviews three different ways to derive and interpret the adjoint equations.

In the adjoint method, the factor d**x**/d**u** in Eq. 7 is eliminated using Eq. 8, leading to Eq. 12.

$$\frac{\mathrm{d}\mathcal{J}}{\mathrm{d}\mathbf{u}} = \mathcal{J}_{\mathbf{u}} - \boldsymbol{\lambda}\mathbf{g}_{\mathbf{u}} \qquad \text{where} \qquad \boldsymbol{\lambda} = \mathcal{J}_{\mathbf{x}}\mathbf{g}_{\mathbf{x}}^{-1}. \tag{12}$$

Then, the term **λ** (or the so-called *adjoint vector*); which is a row vector with dim(**x**) columns and *independent* of dim(**u**), is computed from the following system of equations or the so-called *adjoint equation*

$$\boldsymbol{\lambda}\mathbf{g}_{\mathbf{x}} = \mathcal{J}_{\mathbf{x}} \qquad \text{or equivalently} \qquad \mathbf{g}_{\mathbf{x}}^{T}\boldsymbol{\lambda}^{T} = \mathcal{J}_{\mathbf{x}}^{T}. \tag{13}$$

It is more convenient to use the transposed form in Eq. 13. The coefficient matrix of this equation (i.e., $\mathbf{g}_{\mathbf{x}}^{T}$) is just the transpose of the coefficient matrix in Eq. 11. The computation of the latter Eq. 13 is more efficient than Eq. 11, because the right-side of this equation ($\mathcal{J}_{\mathbf{x}}^{T}$ or the gradient of $\mathcal{J}$ with respect to **x**) is *independent* of dim(**u**). In other words, the total number of equations to be solved for computing **λ** from Eq. 13 is equal to dim(**x**), whereas the total number of dim(**x**)×dim(**u**) equations needs to be solved for computing **S** from Eq. 11. Therefore, computing **λ** is clearly less expensive than computing **S** [unless dim(**u**) = 1].

The matrix $\mathbf{g}_{\mathbf{x}}$ is a block bi-diagonal matrix

$$\mathbf{g}_{\mathbf{x}} = \begin{pmatrix} \mathbf{A}_1 & & & & \mathbf{O} \\ \mathbf{B}_2 & \mathbf{A}_2 & & & \\ & \ddots & \ddots & & \\ & & \ddots & \ddots & \\ \mathbf{O} & & & \mathbf{B}_N & \mathbf{A}_N \end{pmatrix}, \quad \mathbf{g}_{\mathbf{x}}^{T} = \begin{pmatrix} \mathbf{A}_1^{T} & \mathbf{B}_2^{T} & & & \mathbf{O} \\ & \mathbf{A}_2^{T} & \mathbf{B}_3^{T} & & \\ & & \ddots & \ddots & \\ & & & \ddots & \mathbf{B}_N^{T} \\ \mathbf{O} & & & & \mathbf{A}_N^{T} \end{pmatrix}, \tag{14}$$

where

$$\mathbf{A}_k = \frac{\partial \mathbf{g}_k}{\partial \mathbf{x}_k}, \quad \mathbf{B}_k = \frac{\partial \mathbf{g}_k}{\partial \mathbf{x}_{k-1}}, \tag{15}$$

where $\mathbf{A}_k$ and $\mathbf{B}_k$ are square matrices with *m* rows and *m* columns. Thus, Eq. 13 is written as

$$\boldsymbol{\lambda}_k\mathbf{A}_k + \boldsymbol{\lambda}_{k+1}\mathbf{B}_{k+1} = \frac{\partial \mathcal{J}}{\partial \mathbf{x}_k} \qquad (k = 1, 2, \ldots, N-1), \tag{16}$$

$$\boldsymbol{\lambda}_N\mathbf{A}_N = \frac{\partial \mathcal{J}}{\partial \mathbf{x}_N}, \tag{17}$$

where *k* is the time-step index and $\boldsymbol{\lambda}_k$ is a row vector of dimension *m*[*].

---

[*] The adjoint variables $\boldsymbol{\lambda}_k$ coincide with the Lagrange multipliers if the optimality condition is satisfied (i.e., d$\mathcal{J}$/d**u** = 0). [See Kraaijevanger et al. (2007) and Brouwer (2004) for more details.]

After the *forward* run, the linear system of adjoint equations is solved *backward* in time. During the backward run, all adjoint equations must be constructed first based on the computed super state vector **x** during the forward run[*]. The reason that the adjoint equation is solved backward in time is clearly visible from Eq. 17. The only solvable equation in the above system of equations is Eq. 17 at the last time step, having only one unknown vector $\boldsymbol{\lambda}_N$. As soon as this equation is solved for $\boldsymbol{\lambda}_N$, the rest of the equations in Eq. 16 with lower k are successively solved *backward* to construct the complete adjoint vector $\boldsymbol{\lambda}$. Once $\boldsymbol{\lambda}$ is calculated, $\boldsymbol{\lambda}$ is multiplied by $\mathbf{g_u}$ to provide the total derivative $d\mathcal{J}/d\mathbf{u}$ from Eq. 12. A very small example of constructing the adjoint equation is given in Appendix E.

The linear system of adjoint Eqs. 16 and 17 is solved by an iterative method. In iterative methods, one starts with a system of equations $\mathbf{Ax}=\mathbf{b}$ (with **x** as an unknown vector). Then, a start value $\mathbf{x}_0$ is chosen and the residual $\mathbf{r}_0 = \mathbf{b} - \mathbf{Ax}_0$ is computed. Then, $\mathbf{x}_0$ is improved by adding a correction vector $\mathbf{c}_0$ to get a new estimate $\mathbf{x}_1 = \mathbf{x}_0 + \mathbf{c}_0$. The new residual $\mathbf{r}_1$ is usually smaller than $\mathbf{r}_0$. This process is repeated until a certain norm of the residual is sufficiently small (van Kan et al. 2005). In the simulator, the convergence criterion is that the norm of the residual has become smaller than the *relative tolerance*[†] for solving the adjoint linear system, times the norm of the initial residual. If convergence is not reached after the maximum number of iterations, a warning is given but the backward run is not stopped. Having a few of these warnings does not necessarily mean that the gradients are inaccurate. On the other hand, the absence of this warning does not guarantee accurate gradients either. As a result, it is necessary to try a number of non-default values[‡] for the relative tolerance and investigate their effect on the convergence behavior and gradient accuracy (Dynamo/MoReS Online User Documentation 2010).

5.7.3.1. Validation of the Adjoint Gradients

If the gradient changes sign at points not corresponding to an internal optimum, this demonstrates that the gradient is not correctly calculated. It might also happen that despite the correct sign of the gradient, its magnitude is not right. Both of these imply that the calculated gradient is wrong and hence cannot be trusted.

---

[*] The adjoint method requires storing all the state and control vectors at every time step during the forward run.

[†] The keyword used in the simulator for the relative tolerance is ADJLINDATA.REL_TOLERANCE.

[‡] In the simulator, the default value of the relative tolerance depends on the simulation mode (i.e., fractured, non-fractured and thermal, and non-fractured and non-thermal). The highest value that is 1E-7 belongs to the non-fractured and non-thermal category that our problem also belongs to it. However, this value is too large for our problem and using the default value leads to wrong gradients in some instances.

The accuracy of the computed gradients by the adjoint method needs to be validated against a reference solution. The best choice is validating the adjoint gradients against an analytical gradient obtained from the original partial differential equation, if available. However, analytical gradients are usually only available for simple systems, whereas our system is a complex one.

We validate the gradients calculated with the adjoint method by comparing them to the gradients obtained with the perturbation method, discussed in §5.7.1. There are few papers in the petroleum engineering community that have also used the perturbation method for validating the gradients obtained with the adjoint method (applied to history matching). Wu et al. (1999) found the differences smaller than 1%. Wu and Datta-Gupta (2001) found similar differences. However, in Brouwer (2004) the agreements between the two varied from case to case. He observed a growing inconsistency between the two at early times but a good agreement at late times (i.e., a growing inconsistency in *backward time*).

5.7.4. Time Gradient

In this chapter, the goal is finding the switching time ($t_{s,opt}$) that maximizes the cumulative oil production ($\mathcal{J}$). Therefore, the relevant gradient type here is the time gradient and the corresponding control variable is the switching time (t_s). Here, we first describe how the time gradient ($\mathrm{d}\mathcal{J}/\mathrm{d}t_k$) is calculated, and then we focus on computing the time gradient at the switching time ($\mathrm{d}\mathcal{J}/\mathrm{d}t_s$), which requires special attention.

5.7.4.1. Computing the Time Gradient

The time gradient at the time point t_k (i.e., $\mathrm{d}\mathcal{J}/\mathrm{d}t_k$) represents the amount of change in the objective function when t_k slightly varies, but other times do not (**Fig. 14**). In other words, all the times except t_k (i.e., t_0, t_1, …, t_{k-1}, t_{k+1}, …, t_{N-1}, t_N) *are kept fixed* for the computation of the time gradient at each time step *k*.

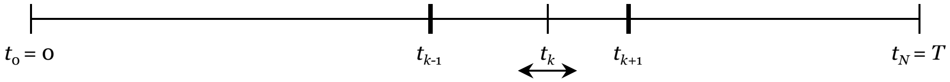

Fig. 14: Schematic for calculation of the time gradient $\mathrm{d}\mathcal{J}/\mathrm{d}t_k$ in the simulator. All the times except t_k (i.e., t_0, t_1, …, t_{k-1}, t_{k+1}, …, t_{N-1}, t_N) are kept fixed in the computation of the time gradient at each time step *k*.

Fig. 15 schematically shows how the plot of $\mathrm{d}\mathcal{J}/\mathrm{d}t$ versus time should *ideally* look for our problem with the switching time. *Large* values of $\mathrm{d}\mathcal{J}/\mathrm{d}t$ are *only* expected at the end time (T) and those times at which a change occurs in control settings like constraint type, constraint value, injection composition, etc. The value of $\mathrm{d}\mathcal{J}/\mathrm{d}t$ at T immediately reflects the effect of changing the length of the simulation[*]. Since the injection composition changes from 100% surfactant solution to 100% gas at t_s, this is considered as a change in the control settings. The sign of the gradient at t_s indicates the effect of prolonging or shortening the surfactant injection period on $\mathcal{J}$. If it is positive, prolonging the surfactant injection cycle leads to an increased $\mathcal{J}$. Conversely, if it is negative, it is *not* beneficial to extend the surfactant injection cycle and it should be shortened.

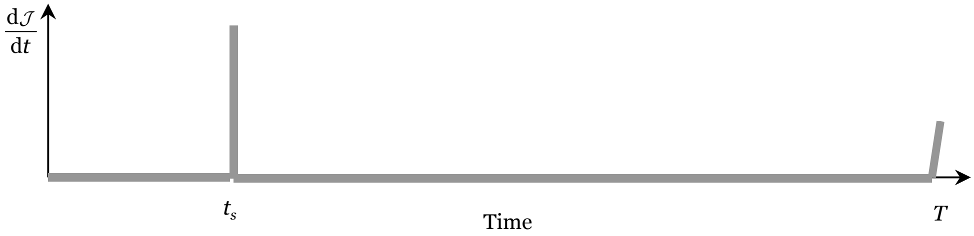

Fig. 15: Schematic of the ideal time-gradient plot in the simulator in our problem.

Apart from the large gradients at t_s and T, further spikes are not generally expected[†]. The value of $d\mathcal{J}/dt$ at the *intermediate*[‡] times should be small as they only represent the effect on $\mathcal{J}$ when one changes the time grid, so they represent the time discretization error. In other words, *small* gradient values at intermediate times indicate that the simulated value of $\mathcal{J}$ is only slightly dependent on the chosen time-step sizes. If one observes relatively large gradients at the first few time steps[§], that often corresponds to time-discretization effects (Dynamo/MoReS Online User Documentation 2010).

Considering the gradient type as the time gradient and the switching time as the control variable, the discrete dynamic system equations ($\mathbf{g}_k$) are represented *in terms of time* as a function of t_{k-1} and t_k as follows:

$$\mathbf{g}_k(\mathbf{x}_{k-1}, \mathbf{x}_k, t_{k-1}, t_k) = \mathbf{0} \qquad (k = 1, ..., N). \tag{18}$$

---

[*] Having the cumulative oil production as our objective function, the positive sign indicates that it is beneficial to produce longer.

[†] Spikes are sometimes caused due to the physical behavior of the forward run discussed in §5.3.1. The behavior of the time gradient in this case is discussed in more detail at the end of §5.7.4.3.

[‡] Times other than T and times at which control settings change. In our case, it corresponds to $0 < t < t_s$ and $t_s < t < T$.

[§] The first few time steps in the simulator are not fixed by default. The time step starts from a specified Δt^{start} and automatically grows by a certain factor (i.e., 2 in this chapter) until reaching the Δt^{max} after which it stays fixed and equal to the Δt^{max}.

We can rewrite Eq. 12 for the time gradient of the objective function as follows:

$$\left(\frac{\mathrm{d}\mathcal{J}}{\mathrm{d}t_1},\cdots\cdots,\frac{\mathrm{d}\mathcal{J}}{\mathrm{d}t_N}\right)=\left(\frac{\partial\mathcal{J}}{\partial t_1},\cdots\cdots,\frac{\partial\mathcal{J}}{\partial t_N}\right)-\left(\lambda_1,\cdots\cdots,\lambda_N\right)\begin{pmatrix} \frac{\partial\mathbf{g}_1}{\partial t_1} & & & \mathbf{O} \\ \frac{\partial\mathbf{g}_2}{\partial t_1} & \frac{\partial\mathbf{g}_2}{\partial t_2} & & \\ & \ddots & \ddots & \\ \mathbf{O} & & \frac{\partial\mathbf{g}_N}{\partial t_{N-1}} & \frac{\partial\mathbf{g}_N}{\partial t_N} \end{pmatrix}. \tag{19}$$

Since $\mathbf{g}_k$ is a function of both t_k and t_{k-1}, the Jacobian matrix $\mathbf{g}_\mathbf{u}$ is a block *bi*-diagonal matrix, as opposed to the block-diagonal matrix $\mathbf{g}_\mathbf{u}$ in Fig. 13 for control variables *other than time*. We can rearrange Eq. 19 as:

$$\begin{aligned} &\frac{\mathrm{d}\mathcal{J}}{\mathrm{d}t_k}=\frac{\partial\mathcal{J}}{\partial t_k}-\lambda_k\frac{\partial\mathbf{g}_k}{\partial t_k}-\lambda_{k+1}\frac{\partial\mathbf{g}_{k+1}}{\partial t_k} \qquad && k=1,2,\ldots,N-1, \\ &\frac{\mathrm{d}\mathcal{J}}{\mathrm{d}t_N}=\frac{\partial\mathcal{J}}{\partial t_N}-\lambda_N\frac{\partial\mathbf{g}_N}{\partial t_N} && k=N. \end{aligned} \tag{20}$$

We can *directly* compute the $\mathrm{d}\mathcal{J}/\mathrm{d}t_k$ element of the total derivative vector from Eq. 20. Note that all partial derivatives on the right side of Eq. 20 are calculated analytically from Eq.18.

In order to have a better understanding of the procedure for calculating the gradient at t_s, it is necessary to become familiar with the original time grid, i.e., the time grid in the absence of t_s.

5.7.4.2. Original Time Grid

In the simulator, two variables control the time-step size in the absence of convergence problems: the start time-step size (Δt^{start}) and the maximum time-step size (Δt^{max}). The time-step size starts from a specified Δt^{start} and automatically grows by a certain factor (i.e., 2 in this chapter) until reaching the Δt^{max} after which it stays fixed and equal to the Δt^{max}. At times when control settings change (in our case, at t_s), and at the end of the simulation, the time step must land exactly on the specified time. Therefore, the time step might be smaller than Δt^{max} in the last time step before the switching time and in the last time step. If we assume that there is no switching time, the time grid that is generated according to the above is called the *original time* grid. A sample of the original time grid is shown in **Fig. 16**.

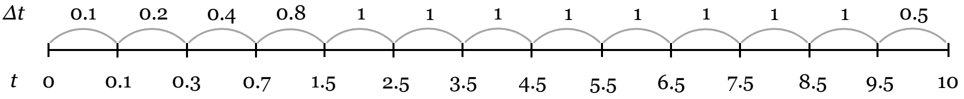

Fig. 16: *Original time grid* in the absence of the switching time. Here, Δt^{start} = 0.1 day, Δt^{max} = 1 day, and T = 10 days. Note that the steps are not equisized.

5.7.4.3. Computing the Time Gradient at the Switching Time

The switching time (t_s) is the time at which surfactant solution injection is terminated and gas injection begins. Prior to t_s, there is no foam in the reservoir due to the absence of gas, and no oil is displaced in the reservoir[*]. However, once gas injection begins, foam formation and coalescence are initiated in the reservoir, introducing a substantial change in the process (see §5.3.1 for more detail). In addition, gas is capable of displacing oil[†] leading to oil production. The cumulative oil production is significantly affected by the total amount of the injected surfactant ($Q_{surf,cum}$) into the reservoir. Therefore, a slight change in t_s and accordingly in $Q_{surf,cum}$ may result in a considerable change in $\mathcal{J}$ (see §5.3.2 for more detail; in §5.3.2, $\mathcal{J}$ is denoted by $Q_{o,cum}$). The optimization routine searches for the optimum based on the sign and magnitude of $\mathrm{d}\mathcal{J}/\mathrm{d}t_s$. As a result, the accuracy of $\mathrm{d}\mathcal{J}/\mathrm{d}t_s$ is of crucial importance for computing the correct optimum switching time ($t_{s,opt}$). A positive sign of $\mathrm{d}\mathcal{J}/\mathrm{d}t_s$ means that increasing t_s (i.e., prolonging the surfactant injection cycle) leads to an increased $\mathcal{J}$ and vice versa.

Neglecting time discretization errors, one might hope that $\mathrm{d}\mathcal{J}/\mathrm{d}t_s \approx \mathrm{d}\mathcal{J}/\mathrm{d}t_k|_{t_k=t_s}$; but unfortunately, $\mathrm{d}\mathcal{J}/\mathrm{d}t_s$ is not always equal to $\mathrm{d}\mathcal{J}/\mathrm{d}t$ at t_s. What one should take for $\mathrm{d}\mathcal{J}/\mathrm{d}t_s$ depends on the *time-step strategy* in the forward run. Based on the selected time-step strategy, the original time grid (§5.7.4.2) is altered, affecting the value of $\mathrm{d}\mathcal{J}/\mathrm{d}t_s$. The general expression for $\mathrm{d}\mathcal{J}/\mathrm{d}t_s$ is

$$\frac{\mathrm{d}\mathcal{J}}{\mathrm{d}t_s}=\sum_{k=1}^{N}\left(\frac{\mathrm{d}\mathcal{J}}{\mathrm{d}t_k}\times\frac{\mathrm{d}t_k}{\mathrm{d}t_s}\right). \tag{21}$$

The term $\mathrm{d}t_k/\mathrm{d}t_s$ is nonzero anywhere that the original time grid (see Fig. 16) is disturbed after inserting t_s into it, in other words, at those times that are not present in the original time grid after inserting t_s. In **Figs. 17 and 18** with t_s = 4.7 days, the time points in bold are the disturbed points not present in the original grid. We elaborate more on this issue below.

Having t_j corresponding to t_s, Eq. 21 retrieves $\mathrm{d}\mathcal{J}/\mathrm{d}t_s = \mathrm{d}\mathcal{J}/\mathrm{d}t_j$ only if $\mathrm{d}t_j/\mathrm{d}t_s = 1$ and $\mathrm{d}t_k/\mathrm{d}t_s = 0$ (for $k \neq j$). This is the case in Fig. 17 with t_s = 4.7 days where the step-size strategy is chosen such that $\Delta t_k + \Delta t_{k+1} = \Delta t^{max} = 1$ and the original time grid is disturbed the least (i.e., the time point at t_s = 4.7 days is the only point added to the original time grid in Fig. 16). To maintain this condition, the time points in the original time grid right before and after t_s (i.e., 4.5 and 5.5 days in Fig. 16) must stay fixed and only t_s varies between these two time points.

---

[*] The initial oil saturation $S_o(I)$ in the reservoir is taken equal to the residual oil saturation to waterflood (S_{orw}). Thus, water is unable to displace oil prior to t_s.

[†] The residual oil saturation to gas flood (S_{org}) is lower than S_{orw} and gas is capable of displacing oil.

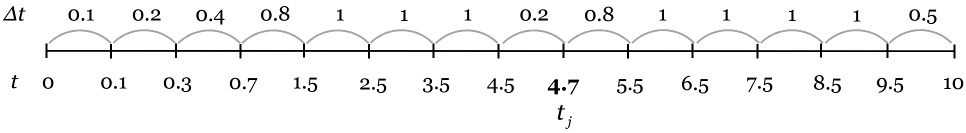

$$\frac{\mathrm{d}\mathcal{J}}{\mathrm{d}t_s}=\frac{\mathrm{d}\mathcal{J}}{\mathrm{d}t_j} \qquad \text{where} \qquad \frac{\mathrm{d}t_j}{\mathrm{d}t_s}=1 \quad \text{and} \quad \frac{\mathrm{d}t_k}{\mathrm{d}t_s}=0 \quad \text{for} \quad j<k<N.$$

Fig. 17: Simple example for calculating d$\mathcal{J}$/dt_s where $t_s = 4.7$ days. The time point in bold is not present in the original time grid in Fig. 16.The step-size strategy is chosen such that $\Delta t_k + \Delta t_{k+1} = \Delta t^{max} = 1$. Note that the steps are not equisized.

Fig. 18 shows another example with $t_s = 4.7$ days. In this step-size strategy one starts again with Δt^{start} right after the switching time, and doubles the step size each time step until reaching Δt^{max} once again. Here, if the summation of the intermediate gradients (i.e., $t_s < t < T$) is large compared to the gradients at t_s and T, it can be *generally* concluded that the time-discretization error is too large. In that case, a different step-size strategy should be considered. On the other hand, large intermediate gradients might be sometimes caused due to the physical behavior of the forward run as seen in §5.3.1 that will be discussed below.

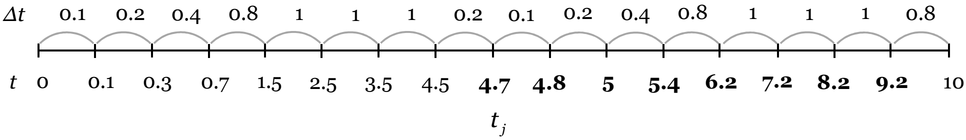

$$\frac{\mathrm{d}\mathcal{J}}{\mathrm{d}t_s}=\sum_{k=j}^{N-1}\frac{\mathrm{d}\mathcal{J}}{\mathrm{d}t_k} \qquad \text{where} \qquad \frac{\mathrm{d}t_k}{\mathrm{d}t_s}=1 \quad \text{for} \quad j\le k<N.$$

Fig. 18: Simple example for calculating d$\mathcal{J}$/dt_s where $t_s = 4.7$ days. The time points in bold are not present in the original time grid in Fig. 16. The term dt_j/dt_s is nonzero and equal to unity at these points. The time-step strategy is to start from $\Delta t^{start} = 0.1$ day and double it until reaching $\Delta t^{max} = 1$ day. Note that the steps are not equisized.

In our problem with the switching time, the time-step sizes *in the vicinity of* t_s must be refined compared to the rest of the time grid. This causes a more accurate simulation in the *hectic* period right after the switch (see §5.3.1 and Figs. 5 and 6). As mentioned in §5.3.1, the start of gas injection at t_s introduces a substantial change in the process due to initiation of foam formation and coalescence in the reservoir. Therefore, a finer time grid is required during that time period to capture the sudden changes more accurately. For instance, the following time-step strategy was used to generate Fig. 7. We took Δt of 1E-4 day in the vicinity of the switching time. For $0 \le t \le (t_s - 0.5)$, we set Δt^{start} = 1E-6 day and Δt^{max} = 1E-2 day. For $(t_s - 0.5) < t \le (t_s + 10)$, we defined $\Delta t^{start} = \Delta t^{max}$ = 1E-4 day, and for $(t_s + 10) < t \le T$, we applied Δt^{start} = 1E-4 day and Δt^{max} = 1E-3 day.

Large nonzero gradients are sometimes observed at times *after* t_s when there is no change in the control settings. If they are not resulting from an inappropriate step-size strategy, they might correspond to the physical nature of the displacement as discussed in detail in §5.3.1. This can be verified by checking the injection/production profiles (rates, pressures). If there are hectic regions in the profiles as well (even after sufficient refinement of Δt and Δx), they would most probably correspond to the real physics of the problem. In our problem, if the injection well operates at a constant prescribed bottomhole pressure, such a hectic region occurs in the gas-injection rate profile right after the switching time (see Figs. 5 and 6). Fig. 7a clearly illustrates the sequence that S_w drops below S_w^* in the gridblocks in a 1D displacement resulting in a significant drop in foam strength of those gridblocks (see Fig. 3a). As soon as S_w drops below S_w^* in a gridblock, an escape path is provided for the injected gas to escape to the next gridblock. This behavior is repeated until S_w drops below S_w^* in the last gridblock. This effect consequently influences the gas-injection-rate profile as illustrated in Fig. 7. **Fig. 19** illustrates that if dropping below S_w^* in a certain gridblock produces a spike in the Q_g profile, this behavior is also reflected in the time-gradient plot in the form of a spike at the same moment that saturation has dropped below S_w^* in that gridblock. However, our analysis in §5.9.1 reveals that these spikes are not influencing the accuracy of the adjoint gradients at t_s.

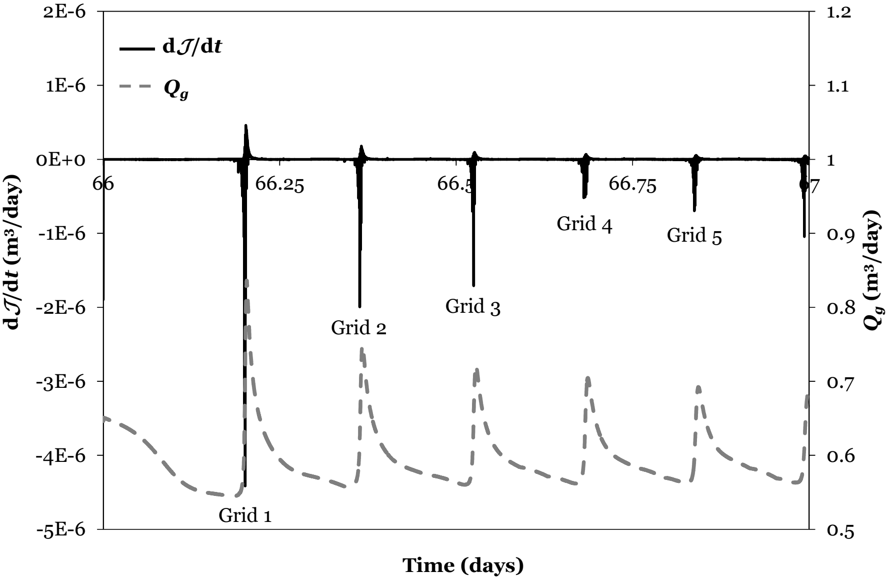

Fig. 19: Magnification of the first 5 spikes in Fig. 6. Fig. 7 showed that the moment at which the n^{th} spike in the gas-injection rate occurs corresponds to the moment at which water saturation in the n^{th} gridblock drops below $S_w^* = 0.316$. In this figure, we observe that the spikes in the time-gradient plot also occur at the same moments. For clarity, we have denoted the gridblock number corresponding to each spike beneath the spike in the time-gradient curve.

5.8. Optimization Routines

There are various optimization routines for finding the optimum. These routines perform various iterations and in each iteration, a search direction is computed. Based on that, the step length (how far to move along that direction) is evaluated (Nocedal and Wright 1999). These routines improve the control variable(s) (e.g., t_s). The steepest-descent method is a gradient-based optimization routine and is the first and the most well-known one; it goes back to Gauss (Nocedal and Wright 1999). We investigate the applicability of the steepest-ascent method in finding the optimum switching time between the surfactant and gas slug.

5.9. Optimization in the Simulator*

We investigate the capability of a gradient-based optimization routine applied to foam EOR processes. Our objective is maximizing the cumulative oil production by optimizing the switching time.

The majority of optimization problems involves a large number of control variables; thus, constructing the response surface of $\mathcal{J}$ is a very cumbersome task, if not impossible. Therefore, looking for the optimum is more like searching in the dark in these cases. Specifically for foam EOR processes involving sharp changes in gas mobility, the behavior of $\mathcal{J}$ with respect to the changes in the control settings can be very irregular. One might find a local optimum in these cases far from the global one, in the absence of proper knowledge about the behavior of the objective function with respect to the changes in the control settings. Having a better understanding of the behavior assists in having a better initial guess for the control settings and ruling out the local optimums.

We picked a simple case with only one control variable (i.e., the switching time) for this investigation. Having only one control variable, the global trend of the objective function $\mathcal{J}$ can be easily constructed with a reasonable number of perturbation runs. Once the global trend of $\mathcal{J}$ is available, the global optimum switching time ($t_{s,opt}$) can be easily identified. This way, we have a solid reference case against which to evaluate the performance of the optimization routine. In addition, we investigated the behavior of $\mathcal{J}$ with respect to the switching time in §5.3 in 3D simulations and related $t_{s,opt}$ to the physics of the process.

---

* The forward model used is according to §5.2 with the same parameters used in the simulations in §5.3 summarized in Tables B-2 and B-3. The simulator uses the procedure described in §5.7.4.1 during the backward run for computing the time gradients $\mathrm{d}\mathcal{J}/\mathrm{d}t$ by the adjoint method. The time gradient at the switching time $\mathrm{d}\mathcal{J}/\mathrm{d}t_s$ is computed by the user based on the applied time-step strategy in the forward run according to the procedure explained in §5.7.4.3.

Regarding the time-step strategy, we applied slightly different time-step sizes for 1D and 3D simulations; 1D simulations required smaller Δt due to having smaller Δx compared to 3D simulations to avoid convergence problems (see **Table 1**).

Table 1: Time-step strategy for 1D and 3D simulations in §5.9.

Time Interval	1D		3D	
	Δt^{start} (day)	Δt^{max} (day)	Δt^{start} (day)	Δt^{max} (day)
$0 \leq t \leq (t_s - 0.5)$	1E-6	1E-2	1E-6	1E-1
$(t_s - 0.5) < t \leq (t_s + 10)$	1E-4	1E-4	5E-3	5E-3
$(t_s + 10) < t \leq T$	5E-3	5E-2	5E-3	1E-1

In order for the optimization routine to successfully find the optimum, the following conditions are desirable (but not strictly necessary):

- Having accurate adjoint gradients.
- Having a convex[*] objective function times minus one ($-\mathcal{J}$).

We investigate the validity of these two conditions in our case below.

5.9.1. Validating the Adjoint Gradients

We validated the gradients calculated with the adjoint routine in the simulator by comparing them to the numerical gradients obtained with the perturbation method applying *sufficiently small*[†] perturbation sizes. We use the central-difference scheme for this purpose. We discovered that an inappropriate choice of the *relative tolerance* for the adjoint linear solver is the main source of getting wrong gradients in our problem. (We discussed about the adjoint linear solver in the last paragraph in §5.7.3.) We found the appropriate choices of the relative tolerance for each case by a thorough validation of the adjoint gradients by comparing them to the numerical gradients. However, we do not go into the details of this examination (two similar investigations are presented in §5.9.6). We found that 1E-12 is the proper choice for our 1D simulations, but this value results in wrong gradients in our 3D simulations using the nonlinear foam model as shown in Fig. 20. We had to tighten the relative tolerance to its smallest possible value of 2.25E-16 to obtain accurate adjoint gradients in this case.

---

[*] A *convex* objective function is a function for which the epigraph, i.e., the set of all points above the graph of $\mathcal{J}$, forms a *convex* set. A *convex* set is defined as a collection of points such that a line connecting any two points of the set is entirely within the set. We deal with a maximization problem here; hence, it is desirable to have $-\mathcal{J}$ as a convex function.

[†] The perturbation must be *sufficiently small* to minimize the effects of nonlinearity and agree with the adjoint gradient. A *too-small* perturbation results in inaccurate gradients due to numerical round-off errors.

After validating the adjoint gradients, we are confident that all the adjoint gradients calculated by the simulator with the *appropriate* choice of the relative tolerance are accurate. However, we emphasize that the gradients predict only the *local* behavior of $\mathcal{J}$ in the neighborhood of the switching time to which they correspond. This issue is discussed in §5.9.5 and §5.9.6.

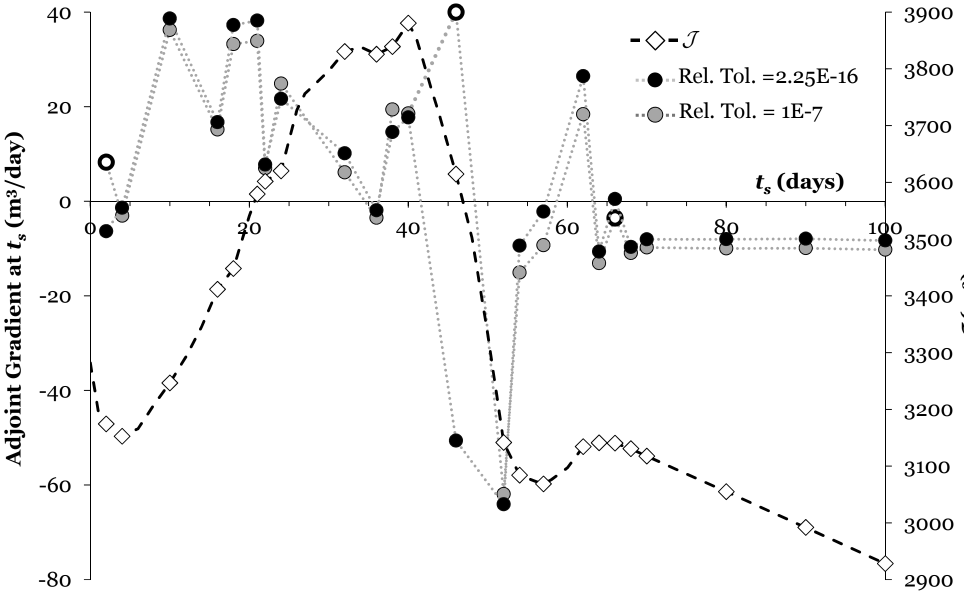

Fig. 20: Adjoint gradients are calculated incorrectly at three switching times indicated by white-filled circles with the default relative tolerance equal to 1E-7. Both the sign and magnitude of the gradient are incorrect at these three points. For instance, the trend of the objective function is decreasing around 46 days and the gradient must be negative, however, the incorrect gradient is positive. The accurate gradients are shown on the curve with the relative tolerance of 2.25E-16. These simulations use the *nonlinear* foam model in 3D. Each simulation ends after 540 days. Note that this case is *identical* to the one shown in Fig. 25. The procedure of constructing this figure is mentioned in the footnote*.

5.9.2. Convexity of the Objective Function

We see later in Figs. 22, 23, 24a, and 25, that the objective functions under study in this chapter has multiple optima and -$\mathcal{J}$ is not convex in the range of switching times shown in the figures. They have multiple minima and maxima. The objective-function curve times minus one (-$\mathcal{J}$) in Fig. 24a might appear convex; however, having a closer look at Fig. 24b reveals that -$\mathcal{J}$ is indeed a non-convex function.

---

* This figure and the similar figures below are constructed as follows. For every switching time (t_s), a backward/adjoint run is performed after a forward run. The forward run gives the cumulative oil production ($\mathcal{J}$), and the backward run provides the total gradient at t_s, i.e., d$\mathcal{J}$/dt_s. The curve corresponding to the numerical gradient is acquired by the perturbation method discussed in §5.7.1.

5.9.2.1. Local and Global Trends of the Objective Function

Fig. 21 illustrates a schematic of *global* and *local* trends of $\mathcal{J}$. From the practical point of view, by *global* we mean a trend of $\mathcal{J}$ that is obtained by coarsely sampling of the objective function, by choosing user-defined large perturbation sizes that are of the order of 1 day in the coming examples. The *local* trend of $\mathcal{J}$, however, is a close approximation of the true behavior of $\mathcal{J}$ that is obtained by choosing much smaller perturbations sizes than those used for constructing the *global* trend. In Fig. 21, the *global trend* of $\mathcal{J}$ around the two black squares appears to be increasing with increasing t_s; however, the local trend of $\mathcal{J}$ focusing on the region between the two black squares reveals details that were not noticeable on the global trend. We also note that the *local* and *global* trends of $\mathcal{J}$ are dependent on the time scale that we choose for the perturbations to construct the figures below.

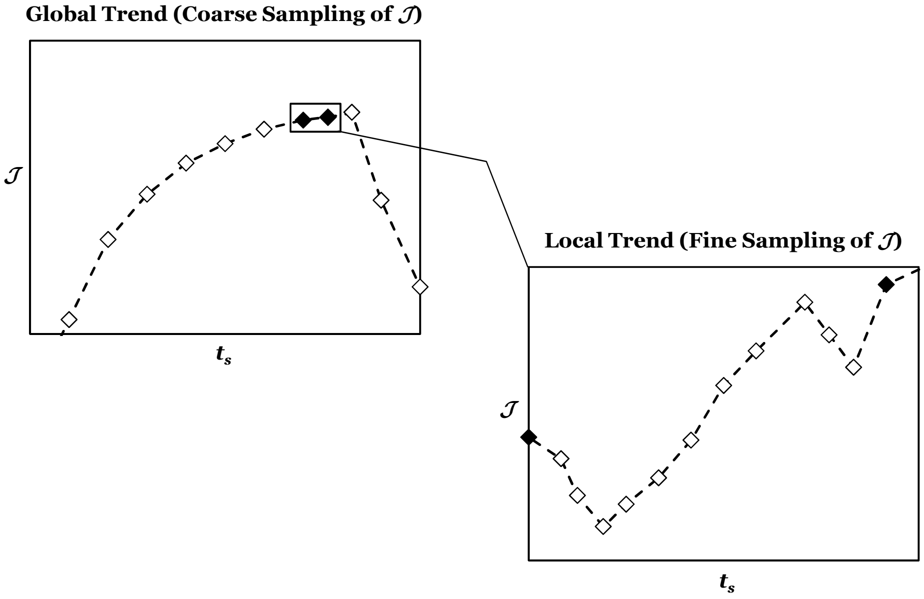

Fig. 21: Schematic of global and local trends of $\mathcal{J}$ between the two black squares. The local trend of $\mathcal{J}$ differs from the global trend of $\mathcal{J}$ and reveals details that were not noticeable on the global trend.

Objective-function curves shown in Figs. 22, 23, 24a, and 25 represent the *global* trend of $\mathcal{J}$, whereas Figs. 24b, 26, 27, and 28 illustrate the local trend. Since both the global and local trends are not the exact representation of the objective-function trend, connecting the points by lines might not be the correct representation of the behavior of $\mathcal{J}$ between the points. Therefore, these figures are better represented by scattered points. Nevertheless, we connected the points on each curve in order to make it easier for the reader to follow the trends of $\mathcal{J}$.

The numerical gradients in Figs. 22, 23, 24a, and 25 act as a tool for locating major differences between the local and global trends of $\mathcal{J}$ as the one shown in Fig. 21. When the local and global trends of $\mathcal{J}$ are analogous, the numerical gradient curve is in a close agreement with the adjoint-gradient curve both in sign and magnitude. On the other hand, if the signs of the numerical and adjoint gradient are different at a certain switching time, this indicates a behavior similar to the one in Fig. 21. Having different gradient signs may involve the entire range of switching times or only a part of it. This sign difference indicates that the numerical gradients are not accurate in that region, and that the chosen perturbation sizes for constructing the global trend of $\mathcal{J}$ were not *sufficiently small* in those regions; hence, the numerical gradients do not accurately represent the local trend of $\mathcal{J}$ and do not agree with the adjoint gradients (§5.7.1). We will show in §5.9.6 that the proper perturbation size can get as low as 1E-7 day at some switching times, in our problem.

Later in the chapter, we show that the local and global trends of $\mathcal{J}$ in the case with the *linear* foam model are analogous, whereas some major differences (as in Fig. 21) are observed between the local and global trends for the *nonlinear* foam model (see Fig. 3 for the behavior of the foam models).

In addition to the non-convexity of $\mathcal{J}$, having major differences between the local and global trends of $\mathcal{J}$ also hampers the performance of a gradient-based optimization routine. We investigate the performance of the optimization routine (steepest-ascent) in finding the optimum switching time in the following cases:

- Linear foam model in a 1D reservoir
- Linear foam model in a 3D reservoir
- Nonlinear foam model in a 1D reservoir
- Nonlinear foam model in a 3D reservoir

5.9.3. Optimization with the *Linear* Foam Model in a 1D Reservoir

A simplified linear foam model is defined for this case (Fig. 3). The foam sensitivity functions (F_w, F_o, and F_s) are linear functions of their corresponding variable (i.e., S_w, S_o, and C_s). The reason for defining this foam model is to examine the performance of the optimization routine with a foam model without abrupt changes as occur in properties in the nonlinear model. The reservoir geometry is 1D (horizontal) and the reservoir length is 100 m and the width and height of the reservoir are 1 m (see Fig. 1a). We used 100 gridblocks to model this displacement. The appropriate *relative tolerance* for the adjoint linear solver in this case leading to correct gradients is equal to 1E-12 (see the last paragraph in §5.7.3 for more information).

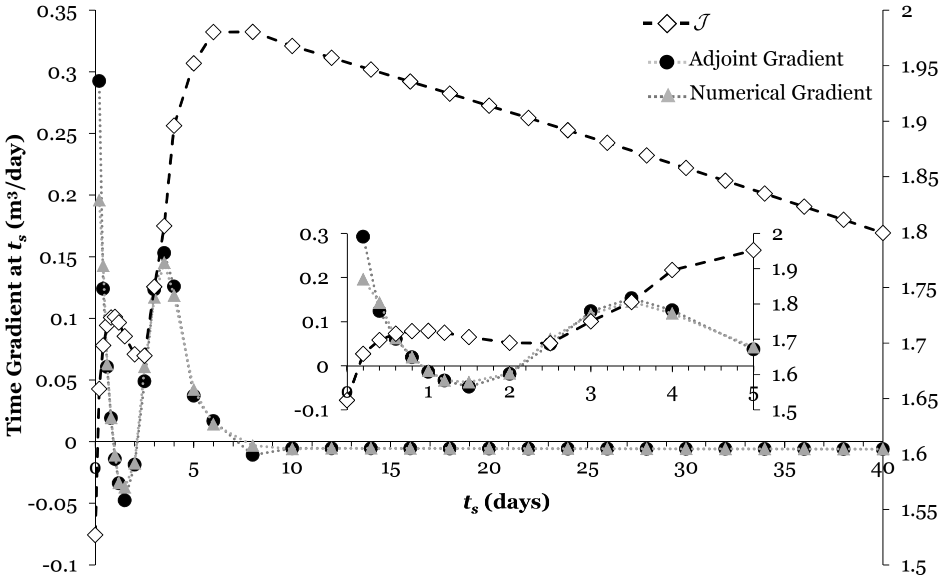

Fig. 22: The local and global trends of $\mathcal{J}$ for the *linear* foam model in a 1D reservoir (100 gridblocks or Δx = 1 m). $\mathcal{J}$ is the cumulative oil production, the total simulation time is 200 days, and the injection well operates at a constant prescribed bottomhole pressure. The plot for switching times less than 5 days is magnified in the inset. Both plots share the same axis titles. Except for the initial point at t_s = 0.2 day, the numerical (central-difference) and analytical (adjoint) gradients are in good agreement. There is no adjoint gradient at t_s = 0 day, because we start gas injection from the beginning and there is no switch.

Gradients always point to the direction of the maximum growth of $\mathcal{J}$. They must be positive in the ascending part of $\mathcal{J}$ and negative in the descending part. The gradient must equate to zero at the optima; hence there must be a sign change at the locations of the optima. The global trend of $\mathcal{J}$ in this case is shown in **Fig. 22**. $\mathcal{J}$ has a global maximum at t_s = 8 days, a local maximum at t_s = 1 day, and a global minimum at t_s = 2.5 days (the last two are magnified in the inset of Fig. 22). We observe that the sign of the adjoint gradients is consistent with the global trend of $\mathcal{J}$. Also, the adjoint-gradient sign changes at all three optima. Except for the initial point at t_s = 0.2 day, there is a good agreement between the numerical and analytical gradients. This indicates that the local and global trends of $\mathcal{J}$ are analogous and that the chosen perturbation sizes for constructing the global trend of $\mathcal{J}$ are sufficiently small in this case (varying from 0.2 day at the beginning to 2 days after t_s = 8 days). Optimizing t_s in this process by the steepest-ascent method also leads to the same $t_{s,opt}$ at 8 days. Since there are more than one maximum point here, we may need to try different choices of initial guess for t_s. In general, if different values of the initial guess result in different $t_{s,opt}$, it implies that -$\mathcal{J}$ is not convex (as is the case here) and has several local optima. Therefore, it is important to try different initial guesses for t_s to reduce the risk of finding a local optimum.

5.9.4. Optimization with the *Linear* Foam Model in a 3D Reservoir

We extend the 1D case discussed above to a 3D reservoir (involving gravity) as shown in Fig. 1b. The foam model is the linear foam model as in §5.9.3 shown in Fig. 3.

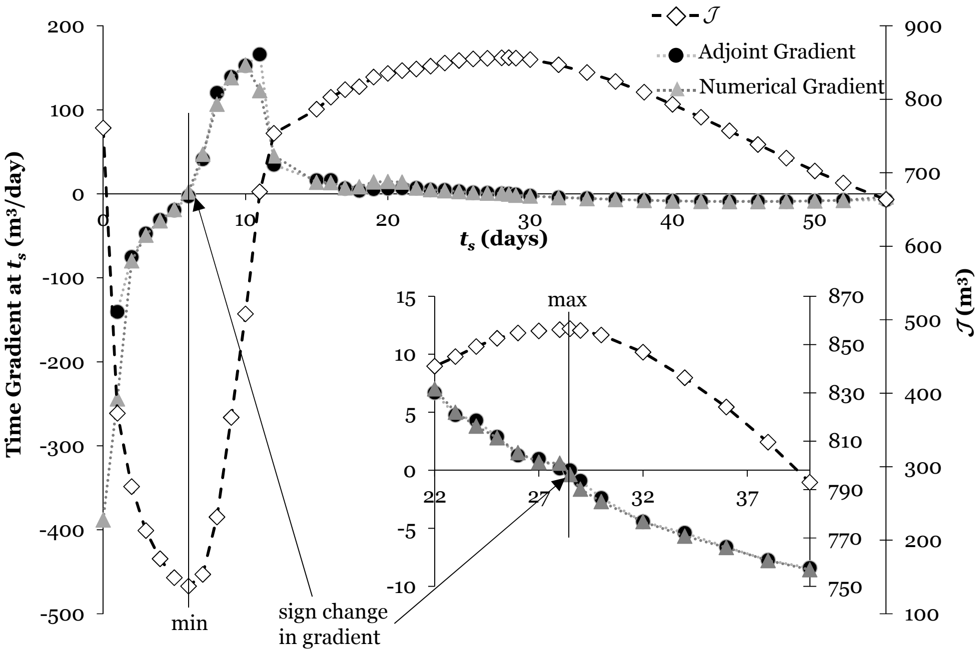

Fig. 23: Local and global trends of 𝒥 for the *linear* foam model in a 3D reservoir. 𝒥 is the cumulative oil production, the total simulation time is 200 days, and the injection well operates at a constant prescribed bottomhole pressure. Except for the initial point at t_s = 1 day, the numerical (central-difference) and analytical (adjoint) gradients are in good agreement. The middle part of the plot around the maximum is magnified in the inset. Both plots share the same axis titles. There is no adjoint gradient at t_s = 0 day, because we start gas injection from the beginning and there is no switch.

The appropriate *relative tolerance* for the adjoint linear solver in this case leading to correct gradients is equal to 1E-12. The global trend of 𝒥 in this case is shown in **Fig. 23**. 𝒥 has a global minimum at t_s = 6 days and a global maximum at t_s = 28.5 days (magnified in the inset of Fig. 23). Similar to the 1D case above, the sign of the adjoint gradients is consistent with the global trend of 𝒥. Also, the adjoint-gradient sign changes at both global optima. Except for the initial point at t_s = 1 day, there is a good agreement between the numerical and analytical gradients. This illustrates that the local and global trends of 𝒥 are analogous and that the chosen perturbation sizes for constructing the global trend of 𝒥 in Fig. 23 are sufficiently small in this case (1 day before the global maximum and 2 days after it). Optimizing the switching time in this process by the steepest-ascent method also leads to the same optimum switching time at 28.5 days.

Figs. 22 and 23 clearly show that the global and local trends of $\mathcal{J}$ are analogous for the linear foam model. The steepest-ascent method can successfully find the optimum switching times in both cases. We replace the *linear* foam model with the *nonlinear* foam model in the following sections (§5.9.5 and §5.9.6), while keeping the rest of the model unchanged.

5.9.5. Optimization with the *Nonlinear* Foam Model in a 1D Reservoir

The nonlinear foam model is shown in Fig. 3. According to this model, gas mobility changes abruptly with small changes in water saturation and/or surfactant concentration, in agreement with laboratory data. The 1D reservoir is horizontal as shown in Fig. 1a. The appropriate *relative tolerance* for the adjoint linear solver in this case leading to correct gradients is equal to 1E-12.

The only difference between this case and the case in §5.9.3 is the foam model. **Fig. 24** illustrates that replacing the linear foam model with the nonlinear foam model introduces fluctuations and jumps in the adjoint gradient (for $t_s < 10$ days) that were not present with the linear foam model in Fig. 22. The numerical-gradient curve is a representative of the global trend of $\mathcal{J}$ and it varies smoothly. However, it differs (both in sign and magnitude) from the adjoint-gradient at certain switching times. This difference originates from the fact that the local and global trends of $\mathcal{J}$ are not analogous as in Fig. 21. As a result, the numerical gradient does not represent the local trend of $\mathcal{J}$ in that range.

Fig. 24a illustrates the global trend of $\mathcal{J}$ in which the global maximum is at $t_{s,opt} = 8.25$ days. As already mentioned, the numerical gradients are inaccurate for $t_s < 10$ days, indicating that the global and local trends are not analogous in this region. This also shows that the perturbation size in this interval is not *sufficiently small* to match the adjoint gradients, as discussed in §5.9.2.1. For instance, we observe a *negative* adjoint gradient and a *positive* numerical gradient at $t_s = 7$ days. The global trend of $\mathcal{J}$ appears to be monotonically increasing before $t_{s,opt}$, and a negative gradient is not consistent with this trend. A closer look at this interval in Fig. 24b (by running more simulations in this interval) reveals that the global and local trends of $\mathcal{J}$ are not analogous and there are two local minima and one local maximum in this interval. The magnitude of the numerical and adjoint gradients differ around $t_{s,opt}$ shown in Fig. 24c, because perturbation sizes in this interval are not sufficiently small.

With regards to the performance of the optimization routine in this case, the global and local trends of $\mathcal{J}$ are analogous for $t_s > 10$ days. Therefore, if one approaches the optimum with an initial guess greater than 10 days, the steepest-ascent method can get very close to the optimum. It can even find the global optimum if there are no local optima after $t_{s,opt}$. However, if the initial guess of t_s is less than $t_{s,opt}$, for which the global and local trends of $\mathcal{J}$ are not analogous (Fig. 24b), the correct adjoint gradients may not accurately reflect the *global* trend of $\mathcal{J}$ that is of our interest in finding $t_{s,opt}$. Therefore, a gradient-based optimization routine might encounter serious problems.

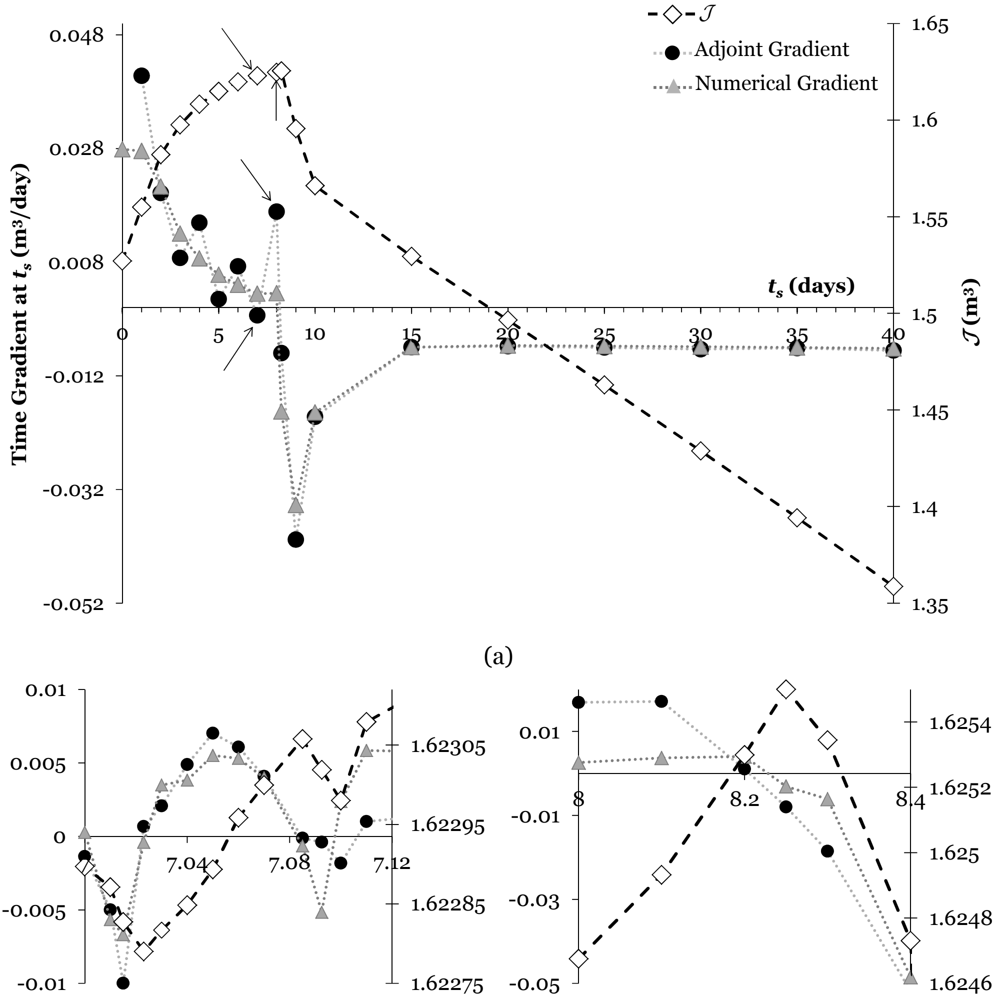

(a)

(b)

(c)

Fig. 24: (a) Global trend of $\mathcal{J}$ for the *nonlinear* foam model in a 1D reservoir (100 gridblocks; Δx = 1 m). $\mathcal{J}$ is the cumulative oil production, the total simulation time is 200 days, and the injection well operates at a constant prescribed bottomhole pressure. (b) Magnification of the switching time interval from 7 to 7.12 days. Point 7 days is indicated by arrows in Fig. 24a. (c) Magnifying the region around the global maximum at t_s = 8.25 days. Point 8 days is indicated by arrows in Fig. 24a. The adjoint gradient changes sign at this point. Figs. 24b and 24c share the same axis titles as in Fig. 24a; we removed them to avoid clutter. There is no adjoint gradient at t_s = 0 day, because we start gas injection from the beginning and there is no switch.

To clarify, if the initial guess is at t_s = 7.015 days (3^{rd} point from left in Fig. 24b), the negative sign of the adjoint gradient suggests that reducing t_s results in a higher value of $\mathcal{J}$, which leads towards a local optimum away from the global one. As a result, the optimization routine may fail with the initial guess in the region with different local and global trends. The strategy of using different values for the initial guess (discussed at the end of §5.4.2) does not always work if there are major differences as in Fig. 21 between the local and global trends of $\mathcal{J}$, as observed here and in §5.9.6.

5.9.6. Optimization with the *Nonlinear* Foam Model in a 3D Reservoir

In §5.9.5, we investigated the performance of the optimization routine with a nonlinear foam model in 1D. We now extend it to 3D simulations in the presence of gravity (see Fig. 1b for the reservoir geometry). We note that the adjoint linear solver was giving *wrong* gradients at some points with a *relative tolerance* of 1E-12 used in §5.9.3, §5.9.4, and §5.9.5. We had to tighten the tolerance to its lowest value of 2.25E-16 to obtain accurate gradients.

As we mentioned earlier in §5.9, understanding the physics behind the process is very helpful. In the absence of proper knowledge about the behavior of the objective function with respect to the changes in the control settings, one might find the local optimum instead of the global one. Therefore, having a better understanding of the behavior, assists in having a better initial guess for the control settings and reducing the chance of ending up in a local optimum. For this reason, we investigated the effect of the switching time on oil recovery in detail in §5.3.2 for 3D simulations in three scenarios. The scenarios studied in §5.3.2 varied in the active constraint of the injection well and the end-time constraint. Therefore, their optimum switching times were not the same. However, the procedure for finding the optimum in all the scenarios is the same. Thus, we confine ourselves to illustrate our findings in only one case. In the case under study, the simulation ends after 540 days (i.e., t_{end} = 540 days). Therefore, the gas-injection interval is dependent on the switching time (i.e., $t_{gas} = t_{end} - t_s$). The injection well operates at a constant prescribed bottomhole pressure.

For this case, we discovered that $t_{s,opt}$ is the switching time at which the foam front is just short of the production well but has not yet reached it at the end of the simulation. If the switching time grows slightly above $t_{s,opt}$, the foam front breaks through to the production well during the simulation, leading to a cumulative oil production smaller than its value at $t_{s,opt}$. We can identify the presence of foam in the production well by monitoring the surfactant concentration (C_s) in the gridblocks containing the well. Exceeding C_s^* (see Fig.3) in any of the well gridblocks is an indication that foam front has reached the production well. Therefore, if $C_s \geq C_s^*$ in the well gridblocks at the optimum found by the optimization routine, that optimum is clearly off from the global one (i.e., $t_s > t_{s,opt}$) and is rejected. Conversely, if the foam front is far from the well at the optimum, it is a clear indication that we are still not at the global optimum and we have to increase the switching time (i.e., $t_s < t_{s,opt}$).

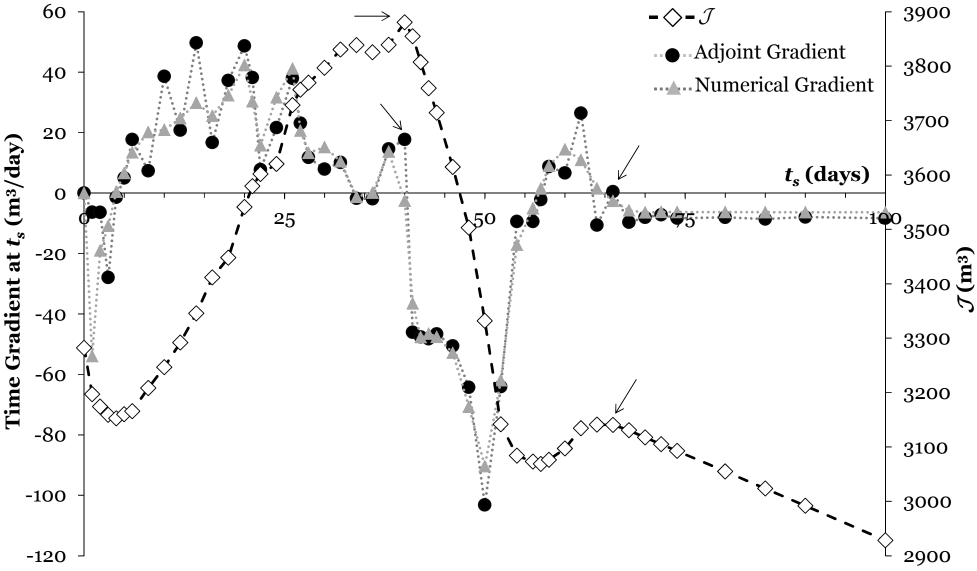

Fig. 25: Global trend of $\mathcal{J}$ for the *nonlinear* foam model in a 3D reservoir. $\mathcal{J}$ is the cumulative oil production, the total simulation time is 540 days, and the injection well operates at a constant prescribed bottomhole pressure. The sign of the adjoint and numerical gradients (central-difference) are different at 40 days and 66 days. The adjoint gradient and $\mathcal{J}$ at these two points are indicated by arrows. There is no adjoint gradient at t_s = 0 day, because we start gas injection from the beginning and there is no switch.

We observed in §5.9.4 that in the 3D reservoir with the linear foam model, the gradient-based optimization routine was able to successfully find the optimum switching time, because the local and global trends of the objective function were analogous. However, **Fig. 25** illustrates differences between both the sign and the magnitude of the numerical and adjoint gradients at certain switching times. These differences are more pronounced in the 3D reservoir, compared to the 1D reservoir with the nonlinear foam model discussed in §5.9.5. On the global trend, we observe a difference in *sign* of the two gradients *near all the optima*; i.e., at 5, 40, 57, and 66 days. Having major differences between the global and local trends of $\mathcal{J}$ in the neighborhood of the optima seriously challenges the optimization-routine's performance. These trends are analogous only after the last local optima at 66 days. We investigate the local trend for two of these points: the apparent global maximum at $t_{s,opt}$ = 40 days and the local maximum at t_s = 66 days, indicated by arrows in Fig. 25.

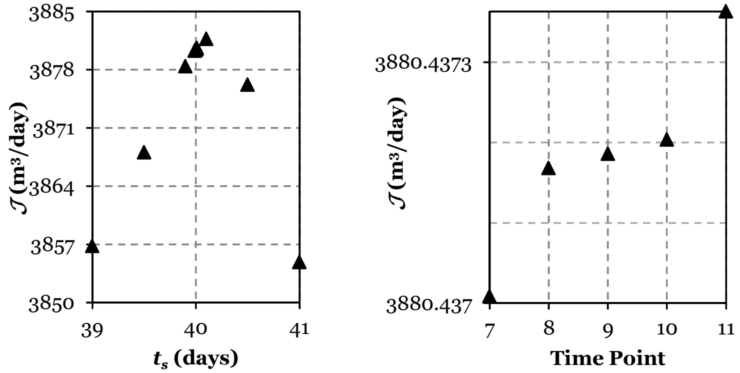

Time Point	Switching Time
1	39
2	39.5
3	39.9
4	39.99
5	39.999
6	39.9999
7	39.99999
8	39.999999
9	40
10	40.000001
11	40.00001
12	40.0001
13	40.001
14	40.01
15	40.1
16	40.5
17	41

(a) (b) (c)

Fig. 26: Trend of $\mathcal{J}$ around t_s = 40 days. (a) $\mathcal{J}$ versus the switching time. There are 17 switching times (column 2 of table c) in this figure. However, since the middle points are very closely spaced, their trend is not visible in this figure. The correct $t_{s,opt}$ is at 40.1 days and not at 40 days. (b) $\mathcal{J}$ versus *time points* (column 1 of table c) in the vicinity of 40 days (i.e., time point 9). (c) Table of switching times and time points used to construct Figs. 26a and 26b.

Fig. 26 shows the behavior of $\mathcal{J}$ very close to t_s = 40 days. Right after this point, the global trend appears to be decreasing, but the adjoint gradient is positive (Fig. 25). However, the local trend around 40 days in Fig. 26a reveals that $t_{s,opt}$ is at 40.1 days and not at 40 days. Further, the increasing trend of $\mathcal{J}$ just after t_s = 40 days (Fig. 26b) is consistent with the positive sign of the adjoint gradient at this point (see Fig. 25). In addition, Fig. 25 shows that the numerical gradient is inaccurate at this point; hence, the perturbation size used is not sufficiently small.

Table 2 shows the effect of the perturbation size (Δt_s) on the accuracy of the numerical gradients around t_s = 40 days. The numerical gradient at t_s = 40 days in Fig. 25 is calculated by the central-difference scheme, and Δt_s right before and after 40 days are 2 and 1 days, respectively. According to Table 2 at t_s = 40 days, Δt_s = 1 day results in 105% error in the numerical gradient and the smallest error is obtained with Δt_s = 1E-5 day. Therefore, an improper choice of Δt_s causes the difference between the analytical (adjoint) and numerical gradients at t_s = 40 days. Table 2 also reveals that at Δt_s = 1E-6 day, the error has started to grow. Thus, Δt_s is *too small* causing inaccurate gradients.

Table 2[*]: Finding the suitable perturbation size at t_s = 40 days.

Δt_s (day)	Adjoint $\mathrm{d}\mathcal{J}/\mathrm{d}t_s$ (m^3/day)	Central $\Delta\mathcal{J}/\Delta t_s$ (m^3/day)	Error (%)
1	17.729	-0.963	-105
5E-1		8.107	-54
1E-1		16.289	-8
1E-2		17.329	-2.3
1E-3		17.851	0.7
1E-4		17.703	-0.1
1E-5		17.729	-1E-3
1E-6		17.728	-1E-2

Table 3: Finding the suitable perturbation size at t_s = 66 days.

Δt_s (day)	Adjoint $\mathrm{d}\mathcal{J}/\mathrm{d}t_s$ (m^3/day)	Central $\Delta\mathcal{J}/\Delta t_s$ (m^3/day)	Error (%)
1	0.457	-2.57	-662
1E-3		1.332	191
1E-4		1.035	126
1E-5		0.795	74
1E-6		0.43	-4.3
1E-7		0.457	4.5E-3
1E-8		0.455	-0.4

We now investigate the cause of the difference observed at the local maximum at t_s = 66 days. At this point, the global trend appears to be decreasing after 66 days but the adjoint gradient is positive as seen in Fig. 25. However, the local trend of $\mathcal{J}$ shown in **Fig. 27** is increasing; contradicting the global trend.

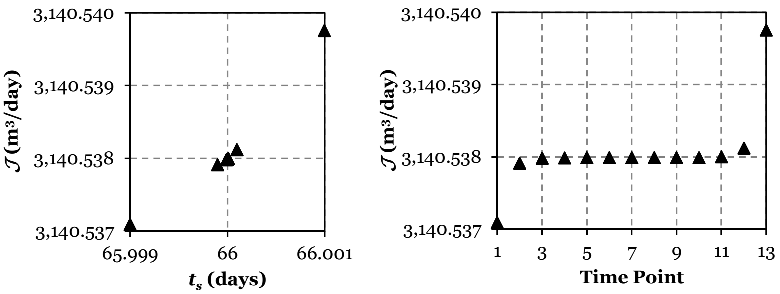

Time Point	Switching Time
1	65.999
2	65.9999
3	65.99999
4	65.999999
5	65.99999999
6	65.999999999
7	66
8	66.000000001
9	66.00000001
10	66.000001
11	66.00001
12	66.0001
13	66.001

(a) (b) (c)

Fig. 27: Trend of $\mathcal{J}$ around t_s = 66 days. (a) $\mathcal{J}$ versus switching time. There are 13 switching times (column 2 of table c) in this figure. However, since the middle points are very closely spaced, their trend is not visible in this figure. (b) $\mathcal{J}$ versus time points (column 1 of table c). Table of switching times and time points used to construct Figs. 27a and 27b.

---

[*] The time-step strategy that we used is similar to the strategy shown in Fig. 14, in which $\mathrm{d}\mathcal{J}/\mathrm{d}t_s = \mathrm{d}\mathcal{J}/\mathrm{d}t_j$. In this strategy, the step-size strategy is chosen such that the original time grid is disturbed the least (i.e., the time point t_s is the only point added to the original time grid). In order to maintain this condition, the time points in the original time grid right before and after t_s (i.e., 39.995 and 40.005 days) stay fixed and only t_s varies between these two time points.

Fig. 28 illustrates the local trend around this point in a wider range. Moreover, **Table 3** clearly shows that the choice of the perturbation size (i.e., 1 day) was not right around this point, causing a very large error in the numerical gradient. Thus, both the differences between the global and local trends of $\mathcal{J}$ and the improper perturbation size are causing the difference between the two gradients at this point. At t_s = 66 days, the lowest error is obtained with Δt_s = 1E-7 day, and Δt_s = 1E-8 day is considered to be *too small.*

Tables 2 and 3 imply that an appropriate choice of perturbation size (Δt_s) is case dependent. Δt_s with the lowest error for t_s = 66 days is 100 times *smaller* than that for t_s = 40 days.

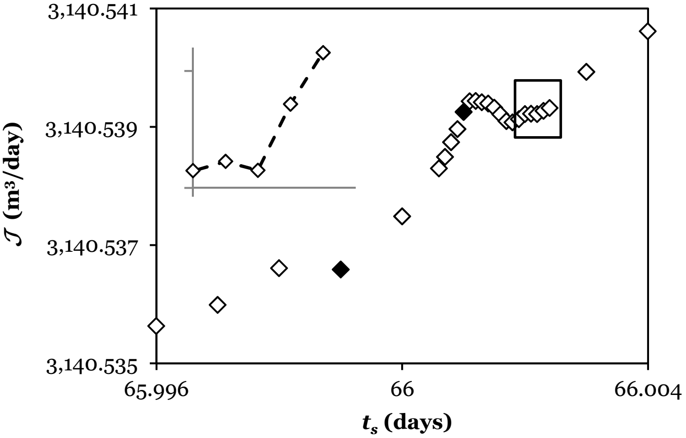

Fig. 28: The local trend of $\mathcal{J}$ around t_s = 66 days, different from the global descending trend after 66 days. This figure shows the local trend in a wider range than the one in Fig. 27a. The left and right limits in Fig. 27a are indicated by filled symbols here.

5.9.7. Cause of the Differences Between Local and Global Trends of $\mathcal{J}$

Comparing Figs. 22 and 24 for the 1D reservoir on one side, and comparing Figs. 23 and 25 for the 3D reservoir on the other side, reveal that all the symptoms (major differences between the global and local trends of the objective function and fluctuations in the adjoint gradient) are introduced once the linear foam model is replaced with the nonlinear foam model. We conjecture that in most simulation models, the fluctuations on the local trend of $\mathcal{J}$ and the fluctuations in its gradient are small, so that they remain unnoticed. In our case with the nonlinear foam model, where small perturbations in the switching time are noticed in terms of wild fluctuations, the symptoms are much more pronounced, to an extent that can reverse the sign of the gradient and the adjoint gradients cannot be trusted any more. Therefore, the adjoint method gives correct gradients, but it should be realized that these correct gradients may not accurately reflect the *global* trend of $\mathcal{J}$ that is of our interest in finding $t_{s,opt}$.

Another indication that relates the symptoms to the nonlinear foam model is that once foam covers the entire reservoir during the simulation time (i.e., for $t_s \geq 10$ days in Fig. 24 in 1D and for $t_s \geq 70$ days in Fig. 25 in 3D), all the symptoms disappear and the local and global trends become analogous. This is due to the fact that foam dynamics becomes inactive after a certain moment within the simulation period, because the reservoir reaches and *maintains* favorable conditions for foam survival (i.e., $S_w > S_w^*$, $S_o < S_o^*$, and $C_s > C_s^*$) after a certain time (within the simulation period)[*]. Therefore, foam formation and coalescence stop after this moment; hence, there is no abrupt change in gas mobility afterwards. To elaborate, for *shorter* switching times (i.e., for $t_s < 10$ days in 1D and for $t_s < 70$ days in 3D), foam continuously forms throughout the entire simulation period, introducing abrupt changes in gas mobility throughout the entire simulation. However, for *longer* switching times, foam covers the entire reservoir *within* the simulation period. As a result, the simulation is entirely free from abrupt changes in gas mobility after the moment that foam covers the entire reservoir and foam dynamics become inactive.

Appendix F shows that these symptoms are not caused by the non-differentiabilities in the foam tables.

Overall, we conjecture that the abrupt changes in gas mobility caused by the nonlinear foam model are the main suspect for causing the symptoms. However, verifying that as the main source of fluctuations on the local trend and finding a remedy for relaxing them requires further comprehensive investigation.

5.9.8. Recommendations

In the cases studied in this chapter with the nonlinear foam model, we concluded that due to the existence of major differences between the local and global trends of $\mathcal{J}$, the *correct* adjoint gradients may not accurately reflect the *global* trend of $\mathcal{J}$ that is of our interest in finding the optimum switching time. For the majority of the switching times in the nonlinear foam model, the global and local trends were not analogous. Therefore, although the adjoint gradients were accurate, but they were unable to represent our user-defined, scale-dependent global trend. On the other hand, the user-defined perturbation sizes for constructing the numerical gradients were sufficiently small in our case and the resulting numerical gradients provided an acceptable representation of the global trend of $\mathcal{J}$. Therefore, those numerical gradients can be trusted in our problem in searching for the optimum switching time. As a result, for the

---

[*] We also note that foam does not collapse after this moment within the time scale of our simulations.

cases with the nonlinear foam model studied in this chapter, the numerical gradients are preferred over the adjoint gradient* to be used in the steepest-ascent method for finding the optimum switching time.

This sort of challenges that we encountered with the nonlinear foam model in foam EOR processes can be also present in other applications. Having abrupt changes in properties may cause similar symptoms challenging gradients-based optimization routines in these applications. Therefore, a thorough understanding of the process in such applications is necessary to be able to find a proper optimization routine for the process. Obviously, if these symptoms are also observed in those applications, gradient-based optimization routines might not be suitable and other options must be considered for optimizing these processes.

In higher dimensions (having more than one control variable), however, a gradient-based optimization routine *might be* able to escape from a valley (local minimum) or a peak (local maximum) on the local trend of $\mathcal{J}$. In multi dimensions, the problematic zone could be a narrow valley or peak with steep sides (along which you cannot easily escape), but maybe almost flat in the other direction such that with a small perturbation you may move out to another region. In multi-dimensional space, there may be many more directions in which the objective function is hardly increasing. We tend to think about local optima as isolated mountain peaks, but quite likely they are more like *mountain ridges*.

5.10. Summary, Conclusions, and Recommendations

Our objective in this chapter was maximizing the cumulative oil production within the simulation period by finding the optimum switching time ($t_{s,opt}$) between the surfactant and gas injection cycles. We also investigated the capability of a gradient-based optimization routine applied to foam EOR processes. This work is a first attempt to apply optimal control theory to foam EOR processes.

Applying the nonlinear foam model introduced fluctuations in the gas-injection rate (Q_g) at early times. These fluctuations are caused by drastic changes in gas mobility as a result of foam formation and coalescence in the gridblocks adjacent to the well. We found that there is a relationship between the spikes in Q_g and the water-saturation drop in specific gridblocks. We showed in 1D simulations that the moment at which the n^{th} spike in Q_g occurs corresponds to the moment at which water saturation in the n^{th} gridblock drops below $S_w^* = 0.316$. We illustrated that if dropping below S_w^* in a certain gridblock produces a spike in the Q_g profile,

---

* Provided that the right scale for perturbation sizes is used.

this behavior is also reflected in the time-gradient plot in the form of a spike at the same moment that saturation has dropped below S_w^* in that gridblock. Nevertheless, our analysis revealed that these spikes are not influencing the accuracy of the adjoint gradients at the switching time. In other words, the spikes in the adjoint gradients reflect an accurate solution of the process once space is discretized.

We investigated the behavior of our objective function (cumulative oil production) with respect to one control variable, the switching time (t_s), in a SAG process in three scenarios:

- The injection well is operating at a prescribed gas-injection rate (Scenario 1):
    - If $t_s > T_1$, injecting surfactant into the reservoir leads to improved $Q_{o,cum}$ over gas flood (i.e., $Q_{o,cum}$ at $t_s = 0$ day). Thus, one must avoid switching times shorter than T_1.
    - Increasing t_s beyond T_1 improves $Q_{o,cum}$, until foam sweeps the entire reservoir at T_4.
    - If foam covers the entire reservoir during the simulation (i.e., for $t_s > T_4$), no additional oil recovery is obtained by increasing t_s. Thus, it is only beneficial to choose $T_1 < t_s < T_4$.
    - For $T_1 < t_s < T_4$, increasing the switching time results in higher oil recovery; economics would identify the switching time resulting in the most profitable process.
- The injection well is operating at a constant prescribed bottomhole pressure (Scenarios 2, 3):
    - Injecting surfactant into the reservoir does not necessarily lead to improved $Q_{o,cum}$ over a gas flood. With fixed t_{gas}, no improvement is obtained for $t_s < 18$ days. With fixed t_{end}, the situation is worse: improvement is achieved only at 24 days $< t_s <$ 50 days. Therefore, one must avoid switching times that lead to $Q_{o,cum}$ lower than gas flood.
    - Injecting less gas as a result of increasing t_s does not necessarily result in lower $Q_{o,cum}$.
    - If the foam front reaches the production well during the process, the whole process is inferior to the situation described above. Further increase in t_s not only results in lower $Q_{o,cum}$ but also leads to wastes of surfactant.

In all the scenarios, the switching time ($t_{s,opt}$) at which the maximum cumulative oil is produced, is the one at which the foam front is at the verge of reaching the production well at the end of the simulation period but has not yet reached it. Therefore, if foam can be destroyed only in the proximity of the production well, more oil will be produced at the maximum $Q_{o,cum}$. One possible way of destroying foam in that zone, is by reducing the surfactant concentration well below C_s^*. This can be done by injecting sufficient amount of water in the production well, such that water would not flow beyond that zone and only lowers C_s in the desired region. It is also possible to use foam breaking agents instead of water, but it certainly increases the costs.

We examined the capability of a gradient-based optimization routine to find the switching time that maximizes the cumulative oil production in four cases varying in the simulation mode (i.e., 1D or 3D) and the foam model (i.e., linear or nonlinear). We showed that an inappropriate choice of the *relative tolerance* for the adjoint linear solver is the source of getting wrong gradients in our problem. We gained the following insights from the analysis:

Linear foam model (1D and 3D):

- The local and global trends of $\mathcal{J}$ are analogous.
- The chosen perturbation sizes for constructing the numerical gradients are sufficiently small for accurate determination of the gradient of $\mathcal{J}$, and they match the adjoint gradients.
- The gradient-based optimization routine is capable of finding the optimum switching time.

Nonlinear foam model (1D and 3D):

- Replacing the linear foam model with the nonlinear foam model introduced major differences between the local and global trends of $\mathcal{J}$ and fluctuations in the adjoint gradient in both 1D and 3D simulations at some switching times. The local and global trends are analogous and the adjoint gradient is free from fluctuations only at switching times for which foam covers the entire reservoir within the simulation period. In those cases, the gas mobility-reduction factor remains relatively unchanged (without any abrupt changes) once C_s exceeds C_s^* in all the reservoir gridblocks, until the end of the simulation. We note that these symptoms were not present for the linear foam model in both 1D and 3D simulations.
- The symptoms observed in the 1D case worsened in the 3D simulations.
- The chosen perturbations (i.e., 1 day) for constructing the global trend of $\mathcal{J}$ in the fluctuating zones were not sufficiently small (to match the adjoint gradients) except for large switching times, for which the local and global trends of $\mathcal{J}$ were analogous. Nevertheless, the user-defined numerical gradients gave an acceptable representation of the global trend of $\mathcal{J}$.
- An appropriate choice of the perturbation size is case dependent. The perturbation size with the lowest error for one switching time can be several orders of magnitude smaller/larger than that for another switching time.
- In 1D, gradient-based optimization is not suitable for finding the optimum switching time, unless the initial guess is larger than $t_{s,opt}$.

- In 3D, there were major differences between the global and local trends of $\mathcal{J}$ in the neighborhood of the optima that would seriously challenge the optimization-routine's performance. As a result, gradient-based optimization is not suitable for finding the optimum switching time in this case.

- We conjecture that in most simulation models, the fluctuations on the local trend of $\mathcal{J}$ and the fluctuations in its gradient are small, so that they remain unnoticed. In our case with the nonlinear foam model, where small perturbations in the switching time are noticed in terms of wild fluctuations, the symptoms are much more pronounced, to an extent that can reverse the sign of the gradient and the gradients cannot be trusted any more. Therefore, the adjoint method gives correct gradients, but it should be realized that these gradients may not accurately reflect the global trend of the objective function that is of our interest.

- With the nonlinear foam model, even though the numerical gradients differed from the accurate adjoint gradients for the chosen perturbation sizes; however, they gave an acceptable representation of the global trend of $\mathcal{J}$. As a result, in the case studied in this work, the numerical gradients are preferred over the adjoint gradient to be used in the steepest-ascent method for finding the optimum switching time with the nonlinear foam model.

- We conjecture that the abrupt changes in gas mobility caused by the nonlinear foam model are the main suspect for causing the symptoms. However, verifying that as the main source of fluctuations on the local trend of $\mathcal{J}$ and finding a remedy for relaxing them requires further comprehensive investigation.

- This sort of challenges that we encountered with the nonlinear foam model in foam EOR processes can be also present in other applications. Having abrupt changes in properties may cause similar symptoms challenging gradients-based optimization routines in these applications. Therefore, a thorough understanding of the process in such applications is necessary to be able to find a proper optimization routine for the process. Obviously, if these symptoms are also observed in those applications, gradient-based optimization routines might not be suitable and other options must be considered for optimizing these processes.

- All these complexities and challenges are yet for the case in which only one control variable is involved. In higher dimensions (having more than one control variable), however, a gradient-based optimization routine *might be* able to escape from local optima. Having a different objective function such as net present value makes the physical analysis harder and more complex.

Chapter 6

Conclusions and Recommendations

6.1. Method of Characteristics

We extend the method of characteristics (MOC) to foam flow with oil. We examine the effects of foam quality, initial oil saturation, foam sensitivity to high oil saturation (S_o) and low water saturation (S_w), and relative-permeability models on oil displacements with foam in one dimension (1D) using the MOC. The effect of low S_w and high S_o on foam must be well understood and represented accurately to avoid spurious decisions leading to failure based on unrealistic foam models and parameter values. Foam models that represent foam collapse at the limiting capillary pressure as a function of S_w should ensure that they do not imply finite foam strength at connate water saturation (S_{wr}). Incorporating foam collapse at S_{wr} results in the failure of a gas-injection cycle of a SAG process in cases examined in Chapter 3, regardless of the reservoir initial condition and foam sensitivity to S_w and S_o, for the relative-permeability models we examined. The failure to represent this mechanism properly in models (having finite foam strength at S_{wr}) may lead to misleading prediction of success in surfactant-alternating-gas (SAG) foam processes. However, Chapter 5 presents a foam model where foam collapses at S_{wr} and yet successful mobility control at the foam bank is predicted. This topic deserves fuller study.

Based on this study, it is not recommended to start foam EOR at early stages of the reservoir life for a foam formulation that is sensitive to high S_o. If foam is destroyed by oil at the initial condition (regardless of whether foam is sensitive to S_w), the displacement is nearly as inefficient as if no foam were present at all for both injection schemes (i.e., pure gas injection and foam flood, i.e., coinjection of water and gas). Failing to do so causes the foam EOR process to fail.

Foam collapse at S_{wr} is not so crucial to modeling foam-injection processes. If foam collapse at S_{wr} is incorporated into the linear-relative-permeability model, foam flood is always preferred over waterflood and is considered successful for the initial oil saturation smaller than the critical oil saturation. A foam flood is successful for any initial condition if foam is only weakened (not killed) by low S_w and not affected by S_o.

6.2. Validating the 1D Simulations Against the MOC Solutions

All hydrocarbon reservoirs are in 3D. However, there is no analytical solution for a real 3D displacement (with gravity) to evaluate the correctness and accuracy of the numerical simulations. The MOC provides exact solutions for benchmarking the accuracy and numerical artifacts of numerical simulators. Therefore, it is essential to evaluate the performance of the numerical simulator in 1D with the available analytical solutions from the MOC, prior to performing simulations in higher dimensions (i.e., 2D and 3D). This analysis elucidates many important aspects.

In finding an accurate numerical solution that matches the MOC solution, some displacements are more sensitive to the choice of Δt and Δx than others. If a part of the solution (e.g., rarefaction wave, constant-state region) is in the proximity of the boundary at which drastic changes in gas mobility occur, the simulator may exhibit oscillations across the boundary with an improper choice of Δt and Δx and fail to find the correct solution. In some cases, we were unable to obtain a correct numerical solution with the choices of Δt and Δx examined.

An inappropriate choice of Δt and Δx leads to erroneous results that might be hard to identify in 3D in the absence of the MOC solution. One needs to look for symptoms to identify them and find the proper choices of Δt and Δx by performing sensitivity analysis on these parameters. This procedure gives some assurance (if not perfect assurance) in the absence of the MOC solution. With the insight that we gained through the validation of the simulator's performance against the MOC solution, we concluded to apply simpler physics for the foam model in the 3D simulations to ensure finding the correct solution.

6.3. Simulation and Optimization of Foam EOR Processes

6.3.1. Simulation

Applying the nonlinear foam model introduced fluctuations in the gas-injection rate (Q_g) at early times. These fluctuations are caused by drastic changes in gas mobility as a result of foam formation and coalescence in the gridblocks adjacent to the well. We found that there is a relationship between the spikes in Q_g and the water-saturation drop in specific gridblocks. These gridblocks include the gridblocks adjacent to the injection well in 3D, and the entire set of gridblocks in 1D. We showed for the 1D simulations that the moment at which the n^{th} spike in Q_g occurs corresponds to the moment at which water saturation in the n^{th} gridblock drops below $S_w^* = 0.316$. We illustrated that if dropping below S_w^* in a certain gridblock produces a spike in the Q_g profile, this behavior is also reflected in the time-gradient plot in the form of a spike at the same moment that saturation has dropped below S_w^* in that gridblock. Nevertheless, our analysis revealed that these spikes are not influencing the accuracy of the adjoint gradients at the switching time. In other words, the spikes in the adjoint gradients reflect an accurate solution of the process once space is discretized.

We investigated the effect of the switching time (t_s) on oil recovery for 3D simulations of a SAG process in three scenarios. The scenarios varied in the active constraint of the injection well and the end-time constraint. We distinguished five zones in all these scenarios, separated by the following switching times: T_1, T_2, T_3, and T_4. For switching times shorter than T_1, a low-mobility foam bank does not form in the reservoir to efficiently reduce the gas mobility and improve sweep efficiency over gas flood. The low-mobility foam bank forms for $t_s > T_1$. At a simulation with a switching time equal to T_2, the maximum cumulative oil production ($Q_{o,cum}$) was obtained. At this switching time, the foam front was at the verge of reaching the production well at the end of the simulation, but has not yet reached it. Once foam breaks through at the end of the simulation with the switching time longer than T_2, $Q_{o,cum}$ declines dramatically. As a result, the cumulative oil production is impaired once foam appears in the production well for switching times longer than T_2. This decline ends once the switching time becomes longer than T_3. For the simulations with $t_s > T_3$, foam gradually sweeps the gridblocks at the two far sides of the reservoir sharing the production well. However, for $t_s > T_4$, foam sweeps the entire reservoir during the simulation. For the simulations with these switching times, the cumulative oil production either stays the same (with fixed gas-injection interval) or declines (with fixed end time) after T_4.

For the injection well operating at a prescribed gas-injection rate, one must avoid switching times shorter than T_1. Increasing the switching time beyond T_1 improves $Q_{o,cum}$, until foam sweeps the entire reservoir at T_4. If foam covers the entire reservoir during the simulation (i.e., for $t_s > T_4$), no additional oil recovery is obtained by increasing the switching time. Therefore, it is only beneficial to choose $T_1 < t_s < T_4$. In this interval, increasing t_s results in higher oil recovery; economics would identify the switching time resulting in the most profitable process.

For the injection well operating at a constant prescribed bottomhole pressure, injecting surfactant into the reservoir does not necessarily lead to improved $Q_{o,cum}$ over a gas flood. With a fixed gas-injection interval, no improvement is obtained for switching times shorter than a certain value. With a fixed end time, the situation is worse: improvement is achieved only at intermediate switching times. Therefore, one must avoid switching times that lead to $Q_{o,cum}$ lower than gas flood. Increasing the switching time does not necessarily lead to higher $Q_{o,cum}$. Injecting less gas (smaller $Q_{g,cum,inj}$) as a result of increasing t_s does not necessarily result in lower cumulative oil production.

In all the scenarios, the switching time ($t_{s,opt}$) at which the maximum cumulative oil is produced, is the switching time at which the foam front is at the verge of reaching the production well at the end of the simulation period but has not yet reached it. Therefore, if foam can be destroyed only in the proximity of the production well, more oil will be produced at the maximum $Q_{o,cum}$. One possible way of destroying foam in that zone, is by reducing the surfactant concentration well below C_s^*. This can be done by injecting sufficient amount of water in the production well, such that water would not flow beyond that zone and only lowers C_s in the desired region. It is also possible to use foam breaking agents instead of water, but it certainly increases the costs.

6.3.2. Optimization

We aimed at maximizing the cumulative oil production by finding the optimum switching time ($t_{s,opt}$) between the surfactant and gas injection cycles. We examined the capability of a gradient-based optimization routine in finding $t_{s,opt}$ in four cases varying in the simulation mode (i.e., 1D or 3D) and the foam model (i.e., linear or nonlinear). We showed that an inappropriate choice of the *relative tolerance* for the adjoint linear solver is the source of getting wrong gradients in our problem and a very tight relative tolerance is required for the simulator to obtain accurate gradients in 3D for the nonlinear foam model.

For the *linear* foam model in both 1D and 3D simulations, the local and global trends of $\mathcal{J}$ were analogous and the gradient-based optimization routine was capable of finding $t_{s,opt}$.

In both our 1D and 3D simulations, replacing the linear foam model with the nonlinear foam model introduced major differences between the local and global trends of $\mathcal{J}$ and fluctuations in the adjoint gradient at some switching times. The local and global trends are analogous and the adjoint gradient is free from fluctuations only at switching times for which foam covers the entire reservoir within the simulation period. In those cases, once foam forms in the entire reservoir, the gas mobility-reduction factor remains relatively unchanged (without any abrupt changes) until the end of the simulation. We emphasize that these symptoms were not present for the linear foam model in both 1D and 3D simulations.

For the *nonlinear* foam model in 1D simulations, the gradient-based optimization routine was not suitable for finding $t_{s,opt}$, unless the initial guess was larger than $t_{s,opt}$.

For the *nonlinear* foam model in 3D simulations, there were major differences between the local and global trends of $\mathcal{J}$ in the neighborhood of the optima. This seriously challenged the performance of the gradient-based optimization routine and made it inappropriate for finding $t_{s,opt}$.

We conjecture that in most simulation models, the fluctuations on the local trend of $\mathcal{J}$ and the fluctuations in its gradient are small, so that they remain unnoticed. In our case with the nonlinear foam model, where small perturbations in the switching time are noticed in terms of wild fluctuations, the symptoms are much more pronounced, to an extent that can reverse the sign of the gradient and the gradients cannot be trusted any more. Therefore, the adjoint method gives correct gradients, but it should be realized that these gradients may not accurately reflect the global trend of the objective function that is of our interest. Even though the numerical gradients differed from the accurate adjoint gradients for the chosen perturbation sizes; however, the numerical gradients gave an acceptable representation of the global trend of $\mathcal{J}$. As a result, in the case studied in this work, the numerical gradients are preferred over the adjoint gradient to be used in the steepest-ascent method for finding the optimum switching time with the nonlinear foam model.

This sort of challenges that we encountered with the nonlinear foam model in foam EOR processes can be also present in other applications. Having abrupt changes in properties may cause similar symptoms challenging gradients-based optimization routines in these applications. Therefore, a thorough understanding of the process in such applications is necessary to be able to find a proper optimization routine for the process. Obviously, if these symptoms are also observed in those applications, gradient-based optimization routines might not be suitable and other options must be considered for optimizing these processes.

All these complexities and challenges are yet for the case in which only one control variable is involved. In higher dimensions (having more than one control variable), however, a gradient-based optimization routine *might be* able to escape from local optima. Having a different objective function such as net present value makes the physical analysis harder and more complex.

Nomenclature

1D = one-dimensional

3D = three-dimensional

cp = centipoise, unit of dynamic fluid viscosity (1 cp = 10^{-3} Pa·s)

C_s = surfactant concentration

C_s^* = critical surfactant concentration for foam stability

CMC = critical micelle concentration

dim = dimension

dim(S_α) = number of saturation points used to represent the function F_α (for plugging tables)

$\mathrm{d}\mathcal{J}/\mathrm{d}t_s$ = total derivative of the objective function with respect to time at the switching time

$\mathrm{d}S_\alpha$ = saturation increment of phase α

epdry = regulates the slope of the k_{rg} curve near *fmdry* in Eqs. C-1 and C-2

epdry′ = controls k_{rg} dependence on S_w in Eq. C-3

epoil = controls k_{rg} dependence on S_o in Eq. C-4

epoil′ = regulates the slope of the k_{rg} curve near *fmoil* in Eq. C-5

EOR = enhanced oil recovery

$\boldsymbol{f}$ = vector of fractional flows (f_w, f_o)

f_α = fractional-flow function of phase α (volume fraction)

$f_{\alpha\beta}$ = $(\partial f_\alpha/\partial S_\beta)_{S_\alpha}$

f_{mr} = mobility-reduction factor

FAWAG = foam assisted water alternating gas

floil = lower oil saturation (volume fraction) for the effect of oil on foam in Eq. C-4

fmdry = critical water saturation (volume fraction) for foam stability in Eqs. C-1 to C-3

fmmob = reference mobility-reduction factor

fmoil = critical oil saturation (volume fraction) for foam stability in Eqs. C-4 and C-5

fudry = the upper water saturation above which F_w^k is no longer affected by S_w

F_α = function describing the effect of S_α or C_s on lamellae stability

$\mathbf{g}$ = nonlinear vector-valued function

h = time-step size, the same as Δt

I = initial condition

IJ = constant-state region
J = injection condition
$\mathcal{J}$ = objective function
$\mathbf{J}$ = Jacobian matrix
k = absolute permeability of the porous medium in Chapter 2
k = counter (time step) in Chapter 5
$k_{r\alpha}$ = relative permeability of phase α
$k_{r\alpha}^{o}$ = end-point relative permeability of phase α
k_{rg}^{f} = gas relative permeability in the presence of foam
k_{rg}^{nf} = gas relative permeability in the absence of foam
kg = kilograms
L = length of the reservoir
mD = millidarcies, unit of absolute rock permeability (1 mD $\cong 10^{-12}$ m^2)
MOC = method of characteristics
MoReS = Modular Reservoir Simulator, Shell in-house reservoir simulator
ODE = ordinary-differential equation
ppm = part per million
P = pressure
P_{wf} = well bottomhole pressure
P_c^* = limiting capillary pressure for gas-water system
P_{ref} = reference pressure in the reservoir
PDE = partial-differential equation
PVI = pore volume injected
$Q_{surf,cum}$ = total amount of surfactant solution injected into the reservoir
$\boldsymbol{r}$ = eigenvector of Eq. 6 in Chapter 2
R = rarefaction wave
RF = oil-recovery factor at the end of simulation (oil in excess of residual saturation)
$RF_{1\mathrm{PVI}}$ = RF after injecting one pore volume of the injected fluid
RF_{sim} = RF at $t_{end,\mathrm{MOC}}$ computed by the numerical simulator
$\boldsymbol{s}$ = vector of saturations (S_w, S_o)
S = shock wave
$\mathbf{S}$ = sensitivity matrix
S_α = saturation of phase α (volume fraction)
S_α^* = critical saturation of phase α (i.e., water or oil) (volume fraction)
$S_{\alpha r}$ = residual saturation of phase α (volume fraction)
SAG = surfactant alternating gas

t = time
$t_{D,final}$ = dimensionless time required to produce all movable oil in the reservoir
$t_{end,\mathrm{MOC}}$ = time in years to produce all movable oil in the reservoir computed by the MOC
t_s = switching time; time at which the fluid composition at the injection well changes
TRC = passive-tracer concentration array in the simulator
$\mathbf{u}$ = vector of control variables (column vector)
v_{shock} = velocity across the shock
V_{res} = reservoir volume
wt. = weight
WAG = water alternating gas
x = position; x coordinate
$\mathbf{x}$ = vector of state variables (column vector)
y = y coordinate
z = z coordinate

Greek

φ = porosity
η = arc length
λ = mobility
$\boldsymbol{\lambda}$ = adjoint vector
μ = viscosity
σ = characteristic speed
ξ = self-similarity variable; eigenvalues of Eq. 6 in Chapter 2.

Math Signs and Operators

$|\;|$ = absolute value
$\approx$ = almost equal to
$\surd$ = square root
d = differential
∂ = partial differential
π = pi (math constant = 3.1416)
Δ = delta (difference operator)

Subscripts

cum = cumulative
d = downstream of the shock

D = dimensionless
g = gas phase
gb = gridblock
inj = injected
I = initial condition
J = injection condition
max = maximum
min = minimum
o = oil phase
opt = optimum
res = reservoir
s = switch in t_s/surfactant in C_s
$surf.\ inj.$ = surfactant solution injected
tot = total
u = upstream of the shock
w = water phase
x = x coordinate
y = y coordinate
z = z coordinate
α = water/oil/gas phase
β = water/oil/gas phase

Superscripts

$*$ = critical
d = downstream of the shock
f = in the presence of foam
$full$ = full-strength foam
inj = injection well
k = killed
max = maximum
min = minimum
nf = in the absence of foam
$prod$ = production well
u = upstream of the shock
w = weakened

Bibliography

Aarra, M.G., Skauge, A., Søgnesand, S., and Stenhaug, M. 1996. A Foam Pilot Test Aimed at Reducing Gas Inflow in a Production Well at the Oseberg Field. *Petroleum Geosciences* **2** (2): 125-132.

Ahmadloo, F., Asghari, K., and Yadali Jamaloei, B. 2009. Experimental and Theoretical Studies of Three Phase Relative Permeability. Paper SPE 124538 presented at the SPE Annual Technical Conference and Exhibition, New Orleans, Louisiana, 4-7 October. DOI: 10.2118/124538-MS.

Alvarez, J.M. 1998. Foam-Flow Behavior in Porous Media: Effects of Flow Regime and Porous-Medium Heterogeneity. PhD dissertation, University of Texas at Austin, Austin, Texas.

Alvarez, J.M., Rivas, H.J., and Rossen, W.R. 2001. Unified Model for Steady-State Foam Behavior at High and Low Foam Qualities. *SPE J.* **6** (3): 325-333. SPE-74141-PA. DOI: 10.2118/74141-PA.

Apaydin, O.G., Kovscek, A.R. 2000. Transient Foam Flow in Homogeneous Porous Media: Surfactant Concentration and Capillary End Effects. Paper SPE 59286 presented at the SPE/DOE Improved Oil Recovery Symposium, Tulsa, Oklahoma, 3-5 April 2000. DOI: 10.2118/59286-MS.

Aronson, A.S., Bergeron, V., Fagan, M.E., and Radke, C.J. 1994. The Influence of Disjoining Pressure on Foam Stability and Flow in Porous Media. *Colloids Surfaces A: Physicochem Eng. Aspects* **83** (2): 109-120. DOI: 10.1016/0927-7757(94)80094-4.

Asheim, H. 1987. Optimal Control of Water Drive. Unsolicited. SPE-15978-MS.

Asheim, H. 1988. Maximization of Water Sweep Efficiency by Controlling Production and Injection Rates. Paper SPE 18365 presented at the SPE European Petroleum Conference, London, 16-19 October.

Ashoori, E., van der Heijden, T.L.M., and Rossen, W.R. 2010. Fractional-Flow Theory of Foam Displacements With Oil. *SPE J.* **15** (2): 260-273. SPE-121579-PA. DOI: 10.2118/121579-PA.

Ashoori, E., Marchesin, D., and Rossen, W.R. 2011a. Dynamic Foam Behavior in the Entrance Region of a Porous Medium. *Colloids Surfaces A: Physicochem Eng. Aspects* **377** (1-3): 217-227.

Ashoori, E., Marchesin, D., and Rossen, W.R. 2011b. Roles of Transient and Local Equilibrium Foam Behavior in Porous Media: Traveling Wave. *Colloids Surfaces A: Physicochem Eng. Aspects* **377** (1-3): 228-242.

Azevedo, A.V. and Marchesin, D. 1995. Multiple Viscous Solutions for Systems of Conservation Laws. *Transactions of the American Mathematical Society* **347** (8): 3061-3077. DOI: 10.2307/2154771.

Azevedo, A.V., de Souza, A.J., Furtado, F., Marchesin, D., and Plohr, D. 2010. The Solution by the Wave Curve Method of Three-Phase Flow in Virgin Reservoirs. *Transport in Porous Media* **83** (1): 99-125.

Aziz, K. and Settari, T. 1979. *Petroleum Reservoir Simulation*. London: Applied Science Publishers.

Baker, L.E. 1988. Three-Phase Relative Permeability Correlations. Paper SPE 17369 presented at the SPE Enhanced Oil Recovery Symposium, Tulsa, Oklahoma, 16-21 April. DOI: 10.2118/17369-MS.

Baker, L.E. 1993. Three-Phase Relative Permeability of Water-Wet, Intermediate-Wet, and Oil-Wet Sandstone. *Proc.* Presented at the Seventh European Improved Oil Recovery Symposium, Moscow, Oct 26-28. Proceedings **2:** 391-397.

Bell, J., Trangenstein, J., and Shubin, G. 1986. Conservation Laws of Mixed Type Describing Three-Phase Flow in Porous Media. SIAM J Appl Math **46**: 1000–1017.

Bernard, G.G. and Holm, L.W. 1964. Effect of Foam on Permeability of Porous Media to Gas. *SPE J.* **4** (3): 267-274. SPE-983-PA. DOI: 10.2118/983-PA.

Bernard, G.G. and Jacobs, W.L. 1965. Effect of Foam on Trapped Gas Saturation and on Permeability of Porous Media to Water. *SPE J.* **5** (4): 295-300. SPE-1204-PA. DOI: 10.2118/1204-PA.

Bernard, G.G., Holm, L.W., and Harvey, C.P. 1980. Use of Surfactant to Reduce CO2 Mobility in Oil Displacement. *SPE J.* **20** (4): 281-292. SPE-8370-PA. DOI: 10.2118/8370-PA.

Bertin, H.J., Quintard, M.Y., and Castanier, L.M. 1998. Development of a Bubble-Population Correlation for Foam-Flow Modeling in Porous Media. *SPE J.* **3** (4): 356-362. SPE-52596.

Blaker, T., Aarra, M.G., Skauge, A., Rasmussen, L., Celius, H.K., Martinsen, H.A., and Vassenden, F. 2002. Foam for Gas Mobility Control in the Snorre Field: The FAWAG Project. *SPE Res Eval & Eng* **5** (4): 317-323. SPE-78824-PA. DOI: 10.2118/78824-PA.

Blunt, M.J. 2000. An Empirical Model for Three-Phase Relative Permeability. *SPE J.* **5** (4): 435-445. SPE-67950-PA. DOI: 10.2118/67950-PA.

Bond, D.C. and Holbrook, C.C. 1958. Gas Drive Oil Recovery Process. U.S. Patent No. 2,866,507.

BP Statistical Review of World Energy. 2010. Available at: www.bp.com/statisticalreview.

Brouwer, D.R. 2004. Dynamic Water Flood Optimization with Smart Wells Using Optimal Control Theory. PhD dissertation, Delft University of Technology, Delft, The Netherlands.

Brouwer, D.R. and Jansen, J.-D. 2004. Dynamic Optimization of Water Flooding with Smart Wells Using Optimal Control Theory. *SPE J.* **9** (4): 391-402. SPE-78278-PA. DOI: 10.2118/78278-PA.

Buckley, S.E. and Leverett, M.C. 1942. Mechanism of Fluid Displacement in Sands. SPE-942107-G. *Trans.,* AIME, **146:** 107-116.

Chad, J., Matsalla, P., and Novosad, J.J. 1988. Foam Forming Surfactants in Pembina/Ostracod ‘G’ Pool. Paper presented at the 39th Annual technical meeting of the petroleum society of CIM, Calgary, June 12-16.

Chalbaud, C.A., Moreno, R.A., and Alvarez, J.M. 2002. Simulating Foam Process for a Venezuelan Pilot Test. Paper SPE 77699 presented at the SPE Annual Technical Conference and Exhibition, San Antonio, Texas, 29 September-2 October. DOI: 10.2118/77699-MS.

Chavent, C., Dupuy, M., and Lemonnier, P. 1973. History Matching by Use of Optimal Control Theory. Paper SPE 4627 presented at the SPE-AIME Annual Fall Meeting, Las Vegas, Nevada, 30 September - 3 October.

Chen, H.L., Ke, M.J., Chuang, T.K., and Flumerfelt, R.W. 1990. Experimental Studies of Capillary Pressure Effects of Foams in Porous Media. Paper SPE 20069 presented at the SPE California Regional Meeting, Ventura, California, April 4-6. DOI: 10.2118/20069-MS.

Chen, Q., Gerritsen, M.G., and Kovscek, A.R. 2010. Modeling Foam Displacement with Local Equilibrium Approximation: Theory and Experiment Verification. *SPE J.* **15** (1): 171-183. SPE-116735.

Chen, M., Yortsos, Y.C., and Rossen, W.R. 2005. Insights on Foam Generation in Porous Media from Pore-Network Studies. *Colloids Surfaces A: Physicochem Eng. Aspects* **256** (2-3): 181-189.

Chen, Q., Gerritsen, M.G., and Kovscek, A.R. 2010. Modeling Foam Displacement with the Local-Equilibrium Approximation: Theory and Experimental Verification. *SPE J.* **15** (1): 171-183. SPE-116735-PA. DOI: 10.2118/116735-PA.

Chen, W.H., Gavalas, G.R., Seinfeld, J.H., and Wasserman. 1974. A New Algorithm for Automatic History Matching. *SPE J.* **14** (6): 593-608. SPE-4545-PA. DOI: 10.2118/4545-PA.

Chen, Y., Oliver, D.S., and Zhang, D. 2009. Efficient Ensemble-Based Closed-Loop Production Optimization. *SPE J.* **14** (4): 634-645. SPE-112873-PA. DOI: 10.2118/112873-PA.

Cheng, L., Reme, A.B., Shan, D., Coombe, D.A., and Rossen, W.R. 2000. Simulating Foam Processes at High and Low Foam Qualities. Paper SPE 59287 presented at the SPE/DOE Improved Oil Recovery Symposium, Tulsa, Oklahoma, 3-5 April. DOI: 10.2118/59287-MS.

Cheng, L. 2002. Modeling and Simulation Studies of Foam Processes in Improved Oil Recovery and Acid-Diversions. PhD dissertation, University of Texas at Austin, Austin, USA.

Chou, S.I. 1990. Percolation Theory of Foam in Porous Media. Paper SPE 20239 presented at the SPE/DOE Enhanced Oil Recovery Symposium, Tulsa, Oklahoma, 22-25 April.

Chou, S.I. 1991. Conditions for Generating Foam in Porous Media. Paper SPE 22628 presented at the SPE Annual Technical Conference and Exhibition, Dallas, Texas, 6-9 October. DOI: 10.2118/22628-MS.

Chou, S.I., Jasek, D.E., and Goodgame, J.A. 1992. CO2 Foam Field Trial at North Ward-Estes. Paper SPE 24643 presented at the SPE Annual Technical Conference and Exhibition, Washington, D.C, 4-7 October. DOI: 10.2118/24643-MS.

Courant, R. and Friedrichs, K.O. 1948. *Supersonic Flow and Shock Waves*. New York: Interscience Publishers.

Courant, R., Friedrichs, K., and Lewy, H. 1967. On the Partial Difference Equations of Mathematical Physics. *IBM Journal*: 215–234, English translation of the 1928 German original.

Dafermos, C.M. ed. 2005. *Hyperbolic Conservation Laws in Continuum Physics*, second edition, Vol. 325. New York: A Series of Comprehensive Studies in Mathematics, Springer.

Delshad, M. and Pope, G.A. 1989. Comparison of the Three-Phase Oil Relative Permeability Models. *Transport in Porous Media* **4** (1): 59-83. DOI: 10.1007/BF00134742.

de Souza, A. 1992. Stability of Singular Fundamental Solutions Under Perturbations for Flow in Porous Media. *Mat Aplic Comput* **11** (2): 73–115.

Dong, Y. and Rossen, W.R. 2007. Insights from Fractional-Flow Theory for Models for Foam IOR. Paper A20 presented at the 14th European Symposium on Improved Oil Recovery, Cairo, 22-24 April.

Dougherty, E. L. and Khairkhah, D. A. 1975. History Matching of Gas Simulation Models Using Optimal Control Theory. Paper SPE 5371 presented at the SPE-AIME Annual California Regional Fall Meeting, Venture, California, 2-4 April.

Dynamo/MoReS Online User Documentation. 2010. Rijswijk, The Netherlands: Shell International Exploration & Production, restricted.

Eson, R.L. and Cooke, R.W. 1989. A Comprehensive Analysis of Steam Foam Diverters and Application Methods. Paper SPE 18785 presented at the SPE California Regional Meeting, Bakersfield, California, April 5-7. DOI: 10.2118/18785-MS.

Falls, A.H., Hirasaki, G.J., Patzek, T.W., Gauglitz, D.A., Miller, D.D., and Ratulowski, T. 1988. Development of a Mechanistic Foam Simulator: The Population Balance and Generation by Snap-Off. *SPE Res Eng* **3** (3): 884-892. SPE-14961-PA. DOI: 10.2118/14961-PA.

Falls, A.H. and Schulte, W.M. 1992a. Theory of Three-Component, Three-Phase Displacement in Porous Media. *SPE Res Eng* **7** (3): 377-384. SPE-19387-PA. DOI: 10.2118/19387-PA.

Falls, A.H. and Schulte, W.M. 1992b. Features of Three-Component, Three-Phase Displacement in Porous Media. *SPE Res Eng* **7** (4): 426-432. SPE-19678-PA. DOI: 10.2118/19678-PA.

Fathi, Z. and Ramirez, W.F. 1984. Optimal Injection Policies for Enhanced Oil Recovery: Part 2-Surfactant Flooding. *SPE J.* **24** (3): 333-341. SPE-12814-PA. DOI: 10.2118/12814-PA.

Fathi, Z. and Ramirez, W. F. 1987. Optimization of an Enhanced Oil Recovery Process with Boundary Controls - A Large-Scale Non-Linear Maximization. *Automatica* **23**(3): 301-310.

Flaaten, A.K., Nguyen, Q.P., Pope, G.A., and Zhang, J. 2009. A Systematic Laboratory Approach to Low-Cost, High-Performance Chemical Flooding. *SPE J.* **12** (5): 713-723. SPE-113469-PA.

Flaaten, A.K., Nguyen, Q.P., Zhang, J., and Mohammadi, H. 2010. Alkaline/Surfactant/Polymer Chemical Flooding Without the Need for Soft Water. *SPE J.* **15** (1): 184-196. SPE-116754-PA.

Fried, A. N. 1961. The Foam Drive Process for Increasing the Recovery of Oil. Bureau of Mines Report of Investigation 5866.

Friedmann, F., Chen, W.H., and Gauglitz, P.A. 1991. Experimental and Simulation Study of High-Temperature Foam Displacement in Porous Media. *SPE Res Eng* **6** (1): 37-45. SPE-17357-PA.

Gdanski, R.D. 1993. Experience and Research Show Best Designs for Foam-Diverted Acidizing. *Oil & Gas Journal* **91** (36): 85-89.

Guzmán, R.E. 1995. Mathematics of Three-Phase Flow. PhD dissertation, Stanford University, Stanford, California.

Hanssen, J.E., Holt, T., and Surguchev, L.M. 1994. Foam Processes: An Assessment of Their Potential in North Sea Reservoirs Based on a Critical Evaluation of Current Field Experience. Paper SPE 27768 presented at the SPE/DOE Improved Oil Recovery Symposium, Tulsa, Oklahoma, 17-20 April. DOI: 10.2118/27768-MS.

Hatziavramidis, D.T., Alameddine, B.R., Weinstein, H.G., Djabbarah, N.F., and Revay, J.M. 1995. A Mechanistic Foam Model for Simulation of Steamfoam Field Applications. Paper SPE 30728 presented at the SPE Annual Technical Conference and Exhibition, Dallas, Texas, 22-25 October.

Heiba, A.A., Davis, H.T., and Scriven, L.E. 1984. Statistical Network Theory of Three-Phase Relative Permeabilities. Paper SPE 12690 presented at the SPE/DOE Enhanced Oil Recovery Symposium, Tulsa, Oklahoma, 15-18 April. DOI: 10.2118/12690-MS.

Helfferich, F.G. 1981. Theory of Multicomponent, Multiphase Displacement in Porous Media. *SPE J.* **21** (1): 51-62. SPE-8372-PA. DOI: 10.2118/8372-PA.

Helfferich, F.G. and Klein, G. 1970. *Multicomponent Chromatography: Theory of Interference*. New York: Marcel Dekker.

Helset, H.M., Nordtvedt, J.E., Skjaeveland, S.M., and Virnovsky, G.A. 1998. Three-Phase Relative Permeabilities from Displacement Experiments with Full Account for Capillary Pressure. *SPE J.* **1** (2): 92-98. SPE-36684-PA. DOI: 10.2118/36684-PA.

Hill, A.D. and Rossen, W.R. 1994. Fluid Placement and Diversion in Matrix Acidising. Paper SPE 27982 presented at the University of Tulsa Centennial Petroleum Engineering Symposium, Tulsa, Oklahoma, 29-31 August. DOI: 10.2118/27982-MS.

Hirasaki, G.J. 1989. The Steam-Foam Process. *J Pet Technol* **41** (5): 449-456. SPE-19505-PA.

Hirasaki, G.J., Jackson, R.E., Jin, M., Lawson, J.B., Londergan, J., Meinardus, H., Miller, C.A. et al. 2000. Field Demonstration of the Surfactant/Foam Process for Remediation of a Heterogeneous Aquifer Contaminated with DNAPL. In *NAPL Removal: Surfactants, Foams, and Microemulsions*, ed. S. Fiorenza, C.A. Miller, C.L. Oubre, and C.H. Ward, Part 1, 3-163. AATDF monograph series, Boca Raton, Florida, USA: Lewis Publishers, CRC Press.

Hoefner, M.L., Evans, E.M., Buckles, J.J., and Jones, T.A. 1995. CO2 Foam: Results From Four Developmental Field Trials. *SPE Res Eng* **10** (4): 273-281. SPE-27787-PA. DOI: 10.2118/27787-PA.

Holm, L.W. 1970. Foam Injection Test in the Siggins Field, Illinois. *J Pet Technol* **22** (12): 1499-1506. SPE-2750-PA. DOI: 10.2118/2750-PA.

Huh, D.G. and Handy, L.L. 1989. Comparison of Steady and Unsteady-State Flow of Gas and Foaming Solution in Porous Media. *SPE Res Eng* **4** (1): 77-84. SPE-15078-PA. DOI: 10.2118/15078-PA.

Isaacson, E.L., Marchesin, D., Plohr, B.J., and Temple, J.B. 1992. Multiphase Flow Models with Singular Riemann Problems. *Mat. Aplic. Comp.* **11** (2): 147-166.

Islam, M.R. and Farouq Ali, S.M. 1990. Numerical Simulation of Foam Flow in Porous Media. *J Can Pet Technol* **29** (4). DOI: 10.2118/90-04-03.

Jansen, J.-D. 2010. Systems Theory for Reservoir Management. Lecture notes for the course AES1490 taught at TU Delft.

Jansen, J.-D. 2011. Adjoint-Based Optimization of Multi-Phase Flow Through Porous Media - A Review. *Comput Fluids.* **46** (1): 40-51. DOI: 10.1016/j.compfluid.2010.09.039.

Jiménez, A.I. and Radke, C.J. 1989. Dynamic Stability of Foam Lamellae Flowing Through a Periodically Constricted Pore. In *Oil-Field Chemistry; Enhanced Recovery and Production Stimulation*, ed. J. Borchardt and T.F. Yen. **396**: 460-479. Washington, DC: ACS Symposium Series, American Chemical Society.

Jonas, T.M., Chou, S.I., and Vasicek, S.L. 1990. Evaluation of a CO2 Foam Field Trial: Rangely Weber Sand Unit. Paper SPE 20468 presented at the SPE Annual Technical Conference and Exhibition, New Orleans, Louisiana, 23-26 September. DOI: 10.2118/20468-MS.

Juanes, R. and Patzek, T.W. 2004a. Analytical Solution to the Riemann Problem of Three-Phase Flow in Porous Media. *Transport in Porous Media* **55** (1): 47-70.

Juanes, R. and Patzek, T.W. 2004b. Three-Phase Displacement Theory: An Improved Description of Relative Permeabilities. *SPE J.* **9** (3): 302-313. SPE-88973-PA. DOI: 10.2118/88973-PA.

Kam, S.I. 2008. Improved Mechanistic Foam Simulation with Foam Catastrophe Theory. *Colloids Surfaces A: Physicochem Eng. Aspects* **318** (1-3): 62-77. DOI: 10.1016/j.colsurfa.2007.12.017.

Kam, S.I., Nguyen, Q.P., Li, Q., and Rossen, W.R. 2007. Dynamic Simulations with an Improved Model for Foam Generation. *SPE J.* **12** (1): 35-48. SPE-90938-PA. DOI: 10.2118/90938-PA.

Kamal, M. and Marsden, S.S. 1973. Displacement of a Micellar Slug by Foam in Unconsolidated Porous Media. Paper SPE 4584 presented at the 48th Annual Fall Meeting of the Society of Petroleum Engineers of AIME, Las Vegas, Nevada, 30 September-3 October. DOI: 10.2118/4584-MS.

Kharabaf, H. and Yortsos, Y.C. 1998. Pore Network Model for Foam Formation and Propagation in Porous Media. *SPE J.* **3** (1): 42-53. SPE-36663-PA. DOI: 10.2118/36663-PA.

Khatib, Z.I., Hirasaki, G.J., and Falls, A.H. 1988. Effects of Capillary Pressure on Coalescence and Phase Mobilities in Foams Flowing Through Porous Media. *SPE Res Eng* **3** (3): 919-926. SPE-15442-PA.

Kibodeaux, K.R. and Rossen, W.R. 1997. Coreflood Study of Surfactant-Alternating-Gas Foam Processes: Implications for Field Design. Paper SPE 38318 presented at the SPE Western Regional Meeting, Long Beach, California, USA, 25-27 June. DOI: 10.2118/38318-MS.

Kirk, D.E. 2004. *Optimal Control Theory-An Introduction*. Mineola, New York: Dover Publications.

Koczo, K., Lobo, L.A., and Wasan, D.T. 1992. Effect of Oil on Foam Stability: Aqueous Foams Stabilized by Emulsions. *Journal of Colloid and Interface Science* **150** (2): 492-506.

Kovscek, A.R., Patzek, T.W., and Radke, C.J. 1995. A Mechanistic Population Balance Model for Transient and Steady-State Foam Flow in Boise Sandstone. *Chemical Engineering Science* **50** (23): 3783-3799. DOI: 10.1016/0009-2509(95)00199-9.

Kovscek, A.R., Patzek, T.W., and Radke, C.J. 1997. Mechanistic Foam Flow Simulation in Heterogeneous and Multidimensional Porous Media. *SPE J.* **2** (4): 511-526. SPE-39102-PA. DOI: 10.2118/39102-PA.

Kraaijevanger, J.F.B.M., Egberts, P.J.P., Valstar, J.R., and Buurman, H.W. 2007. Optimal Waterflood Design Using the Adjoint Method. Paper SPE 105764 presented at the SPE Reservoir Simulation Symposium, Houston, Texas, 6-28 February. DOI: 10.2118/105764-MS.

Krause, R.E., Lane, R.H., Kuehne, D.L., and Bain, G.F. 1992. Foam Treatment of Producing Wells to Increase Oil Production at Prudhoe Bay. Paper SPE 24191 presented at the SPE/DOE Enhanced Oil Recovery Symposium, Tulsa, Oklahoma, April 22-24. DOI: 10.2118/24191-MS.

Kuehne, D.L., Ehman, D.I., Emanuel, A.S., and Magnani, C.F. 1990. Design and Evaluation of a Nitrogen-Foam Field Trial. *J Pet Technol* **42** (4): 504-512. SPE-17381-PA. DOI: 10.2118/17381-PA.

Lake, L.W. 1989. *Enhanced Oil Recovery*. Englewood Cliffs, New Jersey: Prentice Hall.

Law, D.H.-S., Yang, Z.-M., and Stone, T.W. 1992. Effect of the Presence of Oil on Foam Performance: A Field Simulation Study. *SPE Res Eng* **7** (2): 228-236. SPE-18421-PA. DOI: 10.2118/18421-PA.

Lawson, J.B. and Reisberg, J. 1980. Alternate Slugs of Gas and Dilute Surfactant for Mobility Control During Chemical Flooding. Paper SPE 8839 presented at the SPE/DOE Enhanced Oil Recovery Symposium, Tulsa, Oklahoma. DOI: 10.2118/8839-MS.

Lax, P.D. 1957. Hyperbolic Systems of Conservation Laws II. *Comm. Pure Appl. Math.* **10** (4): 537-566.

Lax, P.D. 1973. Hyperbolic Systems of Conservation Laws and the Mathematical Theory of Shock Waves, Regional Conference Series Lectures in Applied Mathematics, **11**. Society for Industrial and Applied Mathematics. Philadelphia, Pennsylvania.

Liu, P.C. and Besserer, G.J. 1988. Application of Foam Injection in Triassic Pool, Canada: Laboratory and Field Test Results. Paper SPE 18080 presented at the Annual Technical Conference and Exhibition, Houston, Texas, 2-5 Oct. DOI: 10.2118/18080-MS.

Li, R.F., Yan, W., Liu, S., Hirasaki, G.J., and Miller, C.A. 2008. Foam Mobility Control for Surfactant EOR. Paper SPE 113910 presented at the SPE/DOE Symposium on Improved Oil Recovery, Tulsa, Oklahoma, 19-23 April. DOI: 10.2118/113910-MS.

Liu, T.P. 1974. The Riemann Problem for General 2×2 Conservation Laws. *TransAmerMath Soc* **199**: 89–112.

Liu, W., Ramirez, W.F., and Qi, Y.F. 1993. Optimal Control of Steamflooding. *SPE Advanced Technology Series* **1** (2): 73-82. SPE-21619-PA. DOI: 10.2118/21619-PA.

Liu, W. and Ramirez, W.F. 1994. Optimal Control of Three-Dimensional Steamflooding Processes. *Journal of Petroleum Science and Engineering* **11** (2): 137-154.

Mamun, C.K., Rong, J.G., Kam, S.I., Liljestrand, H.M., and Rossen, W.R. 2002. Extending Foam Technology from Improved Oil Recovery to Environmental Remediation. Paper SPE 77557 presented at the SPE Annual Technical Conference and Exhibition, San Antonio, Texas, 29 September-2 October. DOI: 10.2118/77557-MS.

Manlowe, D.J. and Radke, C.K. 1990. A Pore-Level Investigation of Foam/Oil Interactions in Porous Media. *SPE Res Eng* **5** (4): 495-502. SPE-18069-PA. DOI: 10.2118/18069-PA.

Mannhardt, K. and Svorstøl, I. 1999. Effect of Oil Saturation on Foam Propagation in Snorre Reservoir Core. *J. Pet. Sci. Eng.* **23** (3): 189-200. DOI: 10.1016/S0920-4105(99)00016-9.

Marchesin, D. and Medeiros, H.B. 1989. A Note on the Stability of Eigenvalue Degeneracy in Nonlinear Conservation Laws of Multiphase Flow. *Contemporary Mathematics* **100:** 215-224.

Marchesin, D. and Plohr, B.J. 2001. Wave Structure in WAG Recovery. *SPE J.* **6** (2): 209-219. SPE-71314-PA. DOI: 10.2118/71314-PA.

Marfoe, C.H., Kazemi, H., and Ramirez, W.F. 1987. Numerical Simulation of Foam Flow in Porous Media. Paper SPE 16709 presented at the SPE Annual Technical Conference and Exhibition, Dallas, Texas, 27-30 September. DOI: 10.2118/16709-MS.

Marsden Jr., S.S., Eerligh, J.J.P., Albrecht, R.A., and David, A. 1967. Use of Foam in Petroleum Operations. Paper 12224 presented at the 7th World Petroleum Congress, Mexico City, Mexico, 2-9 April.

Martinsen, H.A. and Vassenden, F. 1999. Foam-Assisted Water Alternating Gas (FAWAG) Process on Snorre. Paper 015 presented at the 10th European Symposium on Improved Oil Recovery, Brighton, UK, 18-20 August.

Masalmeh, S.K. and Wei, L. 2010. Impact of Relative Permeability Hysteresis, IFT Dependent and Three Phase Models on the Performance of Gas Based EOR Processes. Paper SPE 138203 presented at the Abu Dhabi International Petroleum Exhibition and Conference, Abu Dhabi, UAE, 1-4 November.

Mayberry, D.J., Afsharpoor, A., and Kam, S.I. 2008. The Use of Fractional Flow Theory for Foam Displacement in Presence of Oil. *SPE Res Eval & Eng* **11** (4): 707-718. SPE-100964-PA.

Mehos, G.J. and W.F. Ramirez. 1989. Use of Optimal Control Theory to Optimize Carbone Dioxide Miscible-Flooding Enhanced Oil Recovery. *J. Pet. Sci. Eng.* **2** (4): 247-260.

Moritis, G. 2000. EOR Weathers Low Oil Prices. *Oil and gas Journal* **98** (12): 39-44.

Namdar Zanganeh, M., Kam, S.I., LaForce, T.C., and Rossen, W.R. 2009. The Method of Characteristics Applied to Oil Displacement by Foam. Paper SPE 121580 presented at the EUROPEC/EAGE Annual Conference and Exhibition, Amsterdam, 8-11 June. DOI: 10.2118/121580-MS.

Namdar Zanganeh, M., Kam, S.I., LaForce, T.C., and Rossen, W.R. 2011. The Method of Characteristics Applied to Oil Displacement by Foam. *SPE J.* **16** (1): 8-23. SPE-121580-PA. DOI: 10.2118/121580-PA.

Nguyen, Q.P., Alexandrov, A.V., Zitha, P.L., and Currie, P.K. 2000. Experimental and Modeling Studies on Foam in Porous Media: A Review. Paper SPE 58799 presented at the SPE International Symposium on Formation Damage Control, Lafayette, Louisiana, 23-24 February.

Nikolov, A.D., Wasan, D.T., Huang, D.W., and Edwards, D.A. 1986. The Effect of Oil on Foam Stability: Mechanisms and Implications for Oil Displacement by Foam in Porous Media. Paper SPE 15443 presented at the SPE Annual Technical Conference and Exhibition, New Orleans, 5-8 October.

Nocedal, J. and Wright, S.J. 1999. *Numerical Optimization*. New York: Springer Verlag.

Oliver, D.S., Reynolds, A.C., and Liu N. 2008. *Inverse Theory for Petroleum Reservoir Characterization and History Matching*. Cambridge: Cambridge University Press.

Orr Jr., F.M. 2005. *Theory of Gas Injection Processes*. Copenhagen, Denmark: Tie-Line Publications.

Patzek, T.W. 1988. Description of Foam Flow in Porous Media by the Population Balance Method. *Surfactant Based Mobility Control Progress in Miscible Flood Enhanced Oil Recovery*, ed. D.H. Smith. **373**: 326-341. Washington, DC: ACS Symposium Series, American Chemical Society.

Peaceman, D.W. 1983. Interpretation of Well-Block Pressures in Numerical Reservoir Simulation with Non-Square Grid Blocks and Anisotropic Permeability. *SPE J.* **23** (3): 531-543. SPE-10528-PA.

Pejic, D. and Maini, B.B. 2003. Three-Phase Relative Permeability of Petroleum Reservoirs. Paper SPE 81021 presented at the SPE Latin American and Caribbean Petroleum Engineering Conference, Port-of-Spain, Trinidad and Tobago, 27-30 April. DOI: 10.2118/81021-MS.

Pope, G.A. 1980. The Application of Fractional Flow Theory to Enhanced Oil Recovery. *SPE J.* **20** (3): 191-205. SPE-7660-PA. DOI: 10.2118/7660-PA.

Ramirez, W.F. 1987. *Application of Optimal Control Theory to Enhanced Oil Recovery,* Vol. 21. Amsterdam: Development in Petroleum Science, Elsevier.

Ramirez, W.F., Fathi, Z., and Cagnol J.L. 1984. Optimal Injection Policies for Enhanced Oil Recovery: Part 1-Theory and Computational Strategies. *SPE J.* **24** (3): 328-332. SPE-11285-PA.

Raza, S.H. and Marsden Jr., S.S. 1965. The Flow of Foam: I. Rheology and Streaming Potential. Paper SPE 1205 presented at the Fall Meeting of the Society of Petroleum Engineers of AIME, Denver, Colorado, 3-6 October. DOI: 10.2118/1205-MS.

Reisberg, J. 1972. U. S. Patent No. 3,653,440.

Renkema, W.J. and Rossen, W.R. 2007. Success of SAG Foam Processes in Heterogeneous Reservoirs. Paper SPE 110408 presented at the at the SPE Annual Technical Conference and Exhibition, Anaheim, California, USA, 11-14 November. DOI: 10.2118/110408-MS.

Rhee, H.-K., Aris, R., and Amundson, N.R. 1971. Multicomponent Adsorption in Continuous Countercurrent Exchangers. *Philosophical Transactions of the Royal Society of London. Series A, Mathematical and Physical Sciences* **269** (1194): 187-215.

Rhee, H.-K., Rutherford, A., and Amundson, N.R. 2001. *First-Order Partial Differential Equations: Volume 2, Theory and Application of Hyperbolic Systems of Quasilinear Equations*. Mineola, New York: Dover Publications.

Riemann, B. 1860. Ueber die Fortpflanzung ebener Luftwellen von endlicher Schwingungsweite. *Abhandlungen der Königlichen Gesellschaft der Wissenschaften zu Göttingen* **8:** 43-65.

Rodrigues, J.R.P. 2006. Calculating Derivatives for Automatic History Matching. *Computational Geosciences.* **10** (1): 119-136. DOI: 10.1007/s10596-005-9013-3.

Rodrigues, J.R.P. 2010. Buoyancy Driven Three-Phase Flow in Porous Media. PhD dissertation, Instituto Nacional de Matemática Pura e Aplicada, IMPA, Brazil.

Rosman, A. and Kam, S.I. 2009. Modeling Foam-Diversion Process Using Three-Phase Fractional Flow Analysis in a Layered System. *Energy Sources Part A: Recovery, Utilization, and Environmental Effects* **31**: 1-20.

Rossen, W.R. 1992. Rheology of Foam in Porous Media at the 'Limiting Capillary Pressure'. *Revue de l'Institut Français du Pétrole* **47** (1): 68-80. Rossen, W.R. 1996. Foams in Enhanced Oil Recovery. In *Foams: Theory, Measurements and Applications*, ed. R.K. Prud'Homme and S. Khan. New York: Marcel Dekker.

Rossen, W.R. 1996. Foams in Enhanced Oil Recovery. Foams: Theory, Measurement, and Applications, ed. R.K. Prud'Homme and S. Khan. New York: Marcel Dekker.

Rossen, W.R. 2003. A Critical Review of Roof Snap-Off as a Mechanism of Steady-State Foam Generation in Homogeneous Porous Media. *Colloids Surfaces A: Physicochem Eng. Aspects* **225** (1-3): 1-24.

Rossen, W.R. and Gauglitz, P.A. 1990. Percolation Theory of Creation and Mobilization of Foams in Porous Media. *AIchE J.* **36** (1176).

Rossen, W.R., Shi, J., and Zeilinger, S.C. 1994. Percolation Modeling of Foam Generation in Porous Media. *AIchE J.* **40** (6).

Rossen, W.R. and Zhou, Z.H. 1995. Modeling Foam Mobility in Porous Media. *SPE Advanced Technology Series* **3** (1): 146-153. SPE-22627-PA. DOI: 10.2118/22627-PA.

Rossen, W.R., Zeilinger, S.C., Shi, J.-X., and Lim, M.T. 1999. Simplified Mechanistic Simulation of Foam Processes in Porous Media. *SPE J.* **4** (3): 279-287. SPE-57678-PA. DOI: 10.2118/57678-PA.

Rossen, W.R. and Bruining, J. 2007. Foam Displacements with Multiple Steady States. *SPE J.* **12** (1): 5-18. SPE-89397-PA. DOI: 10.2118/89397-PA.

Rossen, W.R., Johns, R.T., Kibodeaux, K.R., Lai, H.V., and Moradi Tehrani, N. 2008. Fractional-Flow Theory Applied to Non-Newtonian IOR Processes. Paper presented at 11th European Conference on Mathematics of Oil Recovery, Bergen, Norway, 8-11 September.

Rossen, W.R., van Duijn, C.J., Nguyen, Q.P., Shen, C., and Vikingstad, A.K. 2010. Injection Strategies to Overcome Gravity Segregation in Simultaneous Gas and Water Injection into Homogeneous Reservoirs. *SPE J.* **15** (1): 76-90. SPE-99794-PA. DOI: 10.2118/99794-PA.

Sahni, A., Guzman, R., and Blunt, M. 1996. Theoretical Analysis of Three Phase Flow Experiments in Porous Media. Paper SPE 36664 presented at the SPE Annual Technical Conference and Exhibition, Denver, Colorado, 6-9 October. DOI: 10.2118/36664-MS.

Salimi, H. and Bruining, J. 2011. Upscaling in Partially Fractured Oil Reservoirs Using Homogenization. *SPE J.* SPE-125559-PA.

Sarma, P., Aziz, K., and Durlofsky, L.J. 2005. Implementation of Adjoint Solution for Optimal Control of Smart Wells. Paper SPE 92864 presented at the SPE Reservoir Simulation Symposium, Houston, Texas, 31 January-2 February. DOI: 10.2118/92864-MS.

Sarma, P., Chen, W.H., Durlofsky, L.J., and Aziz, K. 2008. Production Optimization with Adjoint Models Under Nonlinear Control-State Path Inequality Constraints. *SPE Res Eval & Eng* **11** (2): 326-339. SPE-99959-PA. DOI: 10.2118/99959-PA.

Schecter, S., Marchesin, D., and Plohr, B.J. 1996. Structurally Stable Riemann Solutions. *Journal of Differential Equations* **126** (2): 303-354. DOI: 10.1006/jdeq.1996.0053.

Schramm, L.L. and Novosad, J.J. 1992. The Destabilization of Foams for Improved Oil Recovery by Crude Oils: Effect of the Nature of the Oil. *J. Pet. Sci. Eng.* **7** (1-2): 77-90.

Schramm, L.L. ed. 1994. *Foams: Fundamentals and Applications in the Petroleum Industry*. Advances in Chemistry Series **3** (242). Washington, DC: American Chemical Society.

Shan, D. 2001. Simulation Study of Gravity Override for Foam Processes. MSc. Thesis, University of Texas at Austin, Austin, Texas.

Shan, D. and Rossen, W.R. 2004. Optimal Injection Strategies for Foam IOR. *SPE J.* **9** (2): 132-150. SPE-88811-PA. DOI: 10.2118/88811-PA.

Shrivastava, V.K., Belgrave, J.D.M., Singhal, A.K., and Coombe, D.A. 1999. Numerical Simulation of Foam Flooding for Sweep Improvement. *J Can Pet Technol* **38** (13): 45-53.

Smoller, J. 1983. *Shock Waves and Reaction-Diffusion Equations*. New York: Springer Verlag.

STARS™ User Guide. 1998, 2007, 2009. Calgary, Alberta: Computer Modeling Group (CMG).

Stevens, J.E., Harpole, K.J., Zornes, D.R., and Martin, F.D. 1992. CO2 Foam Field Verification Pilot Test at EVGSAU: Phase II - Foam Injection Design and Operating Plan. Paper SPE 24642 presented at the SPE Annual Technical Conference and Exhibition, Washington, D.C., Oct. 4-7.

Stevens, J.E. and Martin, F.D. 1995. CO2 Foam Field Verification Pilot Test at EVGSAU: Phase IIIB-Project Operations and Performance Review. *SPE Res Eng* **10** (4): 266-272. SPE-27786-PA.

Stone, H.L. 1970. Probability Model for Estimating Three-Phase Relative Permeability. *J Pet Technol* **22** (2): 214-218. SPE-2116-PA. DOI: 10.2118/2116-PA.

Stone, H.L. 1973. Estimation of Three-Phase Relative Permeability and Residual Oil Data. *J Can Pet Technol* **12** (4): 53-61. DOI: 10.2118/73-04-06.

Stosur, G.J., Hite, J.R., Carnahan, N.F., and Miller K. 2003. The Alphabet Soup of IOR, EOR and AOR: Effective Communication Requires a Definition of Terms. Paper SPE 84908 presented at the SPE International Improved Oil Recovery Conference in Asia Pacific, Kuala Lumpur, Malaysia, 20-21 October. DOI: 10.2118/84908-MS.

Sudaryanto, B. 1998. Optimization of Displacement Efficiency of Oil Recovery in Porous Media Using Optimal Control Theory. PhD dissertation, University of Southern California, LA, California.

Sudaryanto, B. and Yortsos, Y.C. 2000. Optimization of Fluid Front Dynamics in Porous Media Using Rate Control. *Phys Fluids* **12**(7): 1656-70.

Sudaryanto, B. and Yortsos, Y.C. 2001. Optimization of Displacements in Porous Media Using Rate Control. Paper SPE 71509 presented at the SPE Annual Technical Conference and Exhibition, New Orleans, Louisiana, 30 September-3 October. DOI: 10.2118/71509-MS.

Surguchev, L.M., Coombe, D.A., Hanssen, J.E., and Svorstøl, I. 1995. Simulation of WAG and Gas Injection with Potential Sweep Improvement by Application of Foam. *Proc.,* Eighth European Symposium on Improved Oil Recovery, Vienna, Austria, 15-17 May, **1:** 318-330.

Svorstøl, I., Vassenden, F., and Mannhardt, K. 1996. Laboratory Studies for Design of a Foam Pilot in the Snorre Field. Paper SPE 35400 presented at the SPE/DOE Improved Oil Recovery Symposium, Tulsa, Oklahoma, 21-24 April. DOI: 10.2118/35400-MS.

Svorstøl, I., Blaker, T., Tham, M.J., and Hjellen, A. 1997. A Production Well Foam Pilot in the North Sea Snorre Field - Application of Foam to Control Premature Gas Breakthrough. Paper presented at 9th European symposium on Improved Oil Recovery, The Hague, The Netherlands, 20-22 October.

Turta, A.T. and Singhal, A.K. 1998. Field Foam Applications in Enhanced Oil Recovery: Screening and Design Aspects. Paper SPE 48895 presented at the SPE International Oil and Gas Conference and Exhibition, Beijing, China, 2-6 November. DOI: 10.2118/48895-MS.

Van Doren, J., Douma, S., Wassing, B., Kraaijevanger, H., and de Zwart, B.-R. 2011. Adjoint-Based Optimization of Polymer Flooding. Paper SPE 144024 presented at the SPE Enhanced Oil Recovery Conference, Kuala Lumpur, Malaysia, 19-21 July. DOI: 10.2118/144024-MS.

van Essen, G.M., Jansen, J.-D., Brouwer, D.R., Douma, S.G., Zandvliet, M.J., Rollett, K.I., and Harris, D.P. 2010. Optimization of Smart Wells in the St. Joseph Field. *SPE Res Eval & Eng* **13** (4): 588-595. SPE-123563-PA. DOI: 10.2118/123563-PA.

van Kan, J., Segal, A., and Vermolen, F. 2005. *Numerical Methods in Scientific Computing*. Delft, The Netherlands: VSSD.

Vassenden, F. and Holt, T. 2000. Experimental Foundation for Relative Permeability Modeling of Foam. *SPE Res Eval & Eng* **3** (2): 179-185. SPE-62506-PA. DOI: 10.2118/62506-PA.

Vassenden, F., Holt, T., Ghaderi, A., and Solheim, A. 1999. Foam Propagation on Semi-Reservoir Scale. *SPE Res Eval & Eng* **2** (5): 436-441. SPE-58047-PA. DOI: 10.2118/58047-PA.

Vikingstad, A.K. 2006. Static and Dynamic Studies of Foam and Foam-Oil Interactions. PhD dissertation, University of Bergen, Norway.

Vironovsky, G.A. 1991. Waterflooding Strategy Design Using Optimal Control Theory. 6th European IOR Symposium, Stavanger, 21-23 May.

Wang, D., Cheng, J., Yang, Z., Li, Q., Wu, W., and Yu, H. 2001. Successful Field Test of the First Ultra-Low Interfacial Tension Foam Flood. Paper SPE 72174 presented at the SPE Asia Pacific Improved Oil Recovery Conference, Kuala Lumpur, Malaysia, 6-9 October. DOI: 10.2118/72147-MS.

Wassmuth, F.R., Green, K.A., and Randall, L. 2001. Details of In-Situ Foam Propagation Exposed with Magnetic Resonance Imaging. *SPE Res Eval & Eng* **4** (2): 135-149. SPE-71300-PA. DOI: 10.2118/71300-PA.

Wu, Z., Reynolds, A.C., and Oliver, D.S. 1999. Conditioning Geostatistical Models to Two-Phase Production Data. *SPE J.* **4** (2): 142-155. SPE-56855-PA. DOI: 10.2118/56855-PA.

Wu, Z. and Datta-Gupta, A. 2001. Rapid History Matching Using a Generalized Travel Time Inversion Method. Paper SPE 66352 presented at the SPE Reservoir Simulation Symposium, Houston, Texas, 11-14 February. DOI: 10.2118/66352-MS.

Xu, Q. and Rossen, W.R. 2004. Experimental Study of Gas Injection in Surfactant-Alternating-Gas Foam Process. *SPE Res Eval & Eng* **7** (6): 438-448. SPE-84183-PA. DOI: 10.2118/84183-PA.

Yang, D., Zhang, Q., and Gua, Y. 2003. Integrated Optimization and Control of the Production-Injection Operation Systems for Hydrocarbon Reservoirs. *J. Pet. Sci. Eng.* **37** (1-2): 69-81.

Yin, G., Reid, R.B., and Svec, Y. 2009. Oil Recovery and Surfactant Adsorption During CO2-Foam Flooding. Paper OTC 19787 presented at the Offshore Technology Conference, Houston, Texas, 4-7 May. DOI: 10.4043/19787-MS.

Yuen, B., Siu, A., Shenawi, S., Bukhamseen, N., Lyngra, S., and Al-Turki, A. 2008. A New Three-Phase Oil Relative Permeability Simulation Model Tuned by Experimental Data. Paper IPTC 12227 presented at the International Petroleum Technology Conference, Kuala Lumpur, Malaysia, 3-5 December. DOI: 10.2523/12227-MS.

Zakirov, I.S., Aanonsen, S.I., Zakirov, E.S., and Palatnik, B.M. 1996. Optimization of Reservoir Performance by Automatic Allocation of Well Rates. Paper presented at the 5th European conference on the mathematics of oil recovery (ECMOR V), Leoben, Austria.

Zandvliet, M.J., Bosgra, O.H., Van den Hof, P.M.J., Jansen, J.-D., and Kraaijevanger, J.F.B.M. 2007. Bang-Bang Control and Singular Arcs in Reservoir Flooding. *J. Pet. Sci. Eng.* **58**: 186-200. DOI: 10.1016/j.petrol.2006.12.008.

Zeilinger, S.C. 1996. A Modeling and Experimental Study of Foam in Acid Diversion and Enhanced Oil Recovery. PhD dissertation, University of Texas at Austin, Austin, Texas.

Zhang, Y., Yue, X., Dong, J., and Liu, Y. 2000. New and Effective Foam Flooding to Recover Oil in Heterogeneous Reservoirs. Paper SPE 59367 presented at the SPE/DOE Improved Oil Recovery Symposium, Tulsa, Oklahoma, 3-5 April. DOI: 10.2118/59367-MS.

Zhou, Z.H. and Rossen, W.R. 1994. Applying Fractional-Flow Theory to Foams for Diversion in Matrix Acidization. *SPE Prod & Fac* **9** (1): 29-35. SPE-24660-PA. DOI: 10.2118/24660-PA.

Zhou, Z.H. and Rossen, W.R. 1995. Applying Fractional-Flow Theory to Foam Processes at the “Limiting Capillary Pressure”. *SPE Advanced Technology Series* **3** (1): 154-162. SPE-24180-PA. DOI: 10.2118/24180-PA.

Zitha, P.L.J., Du, D.-X., Uijttenhout, M.G.H., and Nguyen, Q.P. 2006. Numerical Analysis of a New Stochastic Bubble Population Foam Model. Paper presented at the SPE/DOE Symposium on Improved Oil Recovery, Tulsa, Oklahoma, 22-26 April. DOI: 10.2118/99747-MS.

Appendix A

The MOC Displacement Routes

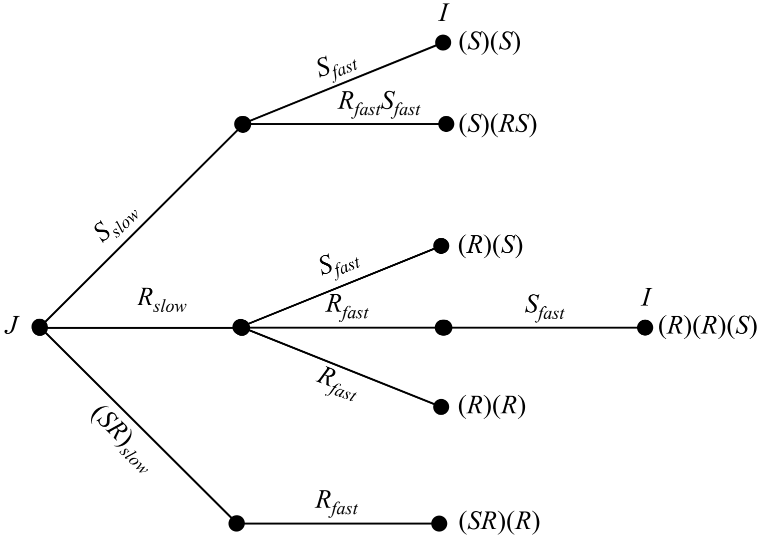

Fig. A-1: Schematic tree of possible displacement routes encountered in Chapter 3. Solid black circles are the constant states, and each wave group is confined between two of them. (S), (R), (RS), and (SR) refer to shock, rarefaction, rarefaction/shock, and shock/rarefaction wave groups, respectively. Subscripts *slow* and *fast* represent the wave family to which they belong.

Table A-1: Wave groups observed in the displacement routes of Chapter 3; $S_g(I)=0$.

Oil Effect	Water Effect	Injection Condition	Initial Condition	Displacement Route
Weaken[*]	**No Effect**	Gas/SAG	$S_o(I) < a_1$	$(S)(S)$
			$S_o(I) > a_1$	$(SR)(R)$
		Foam Flood	$S_o(I) < a_1$	$(S)(S)$
			$S_o(I) > a_1$	$(SR)(R)$
	Weaken	Gas/SAG	$S_o(I) < a_2$	$(RS)(S)$
			$a_2 < S_o(I) < a_3$	$(S)(RS)$
			$S_o(I) > a_3$	$(SR)(R)$
		Foam Flood	$S_o(I) < a_3$	$(S)(S)$
			$S_o(I) > a_3$	$(SR)(R)$
	Kill	Gas/SAG	$S_o(I) < a_4$	$(R)(R)(S)$
			$S_o(I) > a_4$	$(R)(R)$
		Foam Flood	$S_o(I) < a_4$	$(S)(S)$
			$S_o(I) > a_4$	$(SR)(R)$
No Effect	**Weaken**	Gas/SAG	*Any I*	$(R)(S)$
		Foam Flood		
Kill[**]	**No Effect**	Gas/SAG	$S_o(I) < b_1$	$(S)(S)$
			$S_o(I) > b_1$	$(SR)(R)$
		Foam Flood	$S_o(I) < b_1$	$(S)(S)$
			$S_o(I) > b_1$	$(SR)(R)$
	Weaken	Gas/SAG	$S_o(I) < b_2$	$(S)(RS)$
			$S_o(I) > b_2$	$(SR)(R)$
		Foam Flood	$S_o(I) < b_2$	$(S)(S)$
			$S_o(I) > b_2$	$(SR)(R)$
	Kill	Gas/SAG	$S_o(I) < b_1$	$(R)(R)(S)$
			$S_o(I) > b_1$	$(R)(R)$
		Foam Flood	$S_o(I) < b_1$	$(S)(S)$
			$S_o(I) > b_1$	$(SR)(R)$
No Effect	**Kill**[***]	Gas/SAG	$S_w(I) > c$	$(R)(R)(S)$
			$S_w(I) < c$	$(R)(R)$
		Foam Flood	$S_w(I) > c$	$(R)(S)$
			$S_w(I) < c$	$(R)(R)$

Foam flood means $f_w(J) = \frac{1}{3}$.

[*] If oil weakens foam and water effect varies, the solution type changes at the following points: $a_1 = 0.5574$, $a_2 = 0.2864$, $a_3 = 0.6840$, and $a_4 = 0.6706$.

[**] If oil kills foam and water effect varies, the point at which the solution type changes (i.e., b_1, b_2) is very close to S_o^*, e.g., $b_1 = 0.1936$ and $b_2 = 0.2064$.

[***] If water kills foam and oil has no effect, the point at which the solution type changes (i.e., c) is close to S_w^*, i.e., $c = 0.3255$.

Appendix B

Model Parameters

Table B-1: Model parameters in Chapters 2, 3, and 4. For each phase α, Eq. 1 in Chapter 3 gives the relative permeability in the absence of foam.

<table>
<tr><td>S_{wr}</td><td>S_{or}</td><td>S_{gr}</td><td>μ_w (cp)</td><td>μ_o (cp)</td><td>μ_g (cp)</td></tr>
<tr><td>0.1</td><td>0.1</td><td>0</td><td>1</td><td>5</td><td>0.02</td></tr>
<tr><td colspan="2">k^o_{rw}</td><td colspan="2">k^o_{ro}</td><td colspan="2">k^o_{rg}</td></tr>
<tr><td colspan="2">1</td><td colspan="2">1</td><td colspan="2">1</td></tr>
<tr><td rowspan="4">*fmmob*
55,000</td><td>*fmdry* (S_w^*)</td><td>*epdry*</td><td>*epdry′*</td><td colspan="2">*fudry*</td></tr>
<tr><td>0.316</td><td>1,000</td><td>2</td><td colspan="2">0.532</td></tr>
<tr><td>*fmoil* (S_o^*)</td><td>*epoil*</td><td>*epoil′*</td><td colspan="2">*floil*</td></tr>
<tr><td>0.2</td><td>2</td><td>1,000</td><td colspan="2">0.1</td></tr>
</table>

* *epoil′ is equal to* 100 *if oil weakens and water kills foam.*

Table B-2: Model parameters in Chapter 5. Relative-permeability parameters correspond to the nonlinear relative-permeability model introduced in §4.2.4. Foam parameters are related to the nonlinear foam model (water weakens foam and oil kills foam).

<table>
<tr><td>S_{wr}</td><td>S_{orw}</td><td>S_{org}</td><td>S_{gr}</td><td>μ_w (cp)</td><td>μ_o (cp)</td><td>μ_g (cp)</td></tr>
<tr><td>0.1</td><td>0.3</td><td>0</td><td>0</td><td>computed by MoReS</td><td>5</td><td>0.02</td></tr>
<tr><td>K_{rw}</td><td colspan="2">K_{row}</td><td colspan="2">K_{rog}</td><td colspan="2">K_{rg}</td></tr>
<tr><td>0.3</td><td colspan="2">0.8</td><td colspan="2">0.8</td><td colspan="2">0.94</td></tr>
<tr><td>n_w</td><td colspan="2">n_{ow}</td><td colspan="2">n_{og}</td><td colspan="2">n_g</td></tr>
<tr><td>4</td><td colspan="2">2</td><td colspan="2">3</td><td colspan="2">3</td></tr>
<tr><td rowspan="4">*fmmob*
1,000</td><td>*fmdry* (S_w^*)</td><td>*epdry*</td><td>*fmoil* (S_o^*)</td><td>*epoil*</td><td colspan="2">*floil*</td></tr>
<tr><td>0.316</td><td>1,000</td><td>0.4</td><td>1.5</td><td colspan="2">0</td></tr>
<tr><td colspan="3">*fmsurf* (C_s^*)</td><td colspan="3">*epsurf*</td></tr>
<tr><td colspan="3">1.2E-3</td><td colspan="3">100</td></tr>
</table>

Table B-3: Reservoir and well parameters for the 3D simulations in Chapter 5. Same parameters apply to 1D simulations in Chapter 5 except the length and number of gridblocks: the 1D reservoir is 100x1x1 m with 100x1x1 gridblocks (i.e., $\Delta x = \Delta y = \Delta z = 1$ m); unless otherwise is stated.

Length (m)	Width (m)	Height (m)	Depth(m)	Δx (m)	Δy (m)	Δz (m)
100	100	30	1,600	10	10	10

φ	k_x (mD)	k_y (mD)	k_z (mD)
0.2	100	100	10

$C_{s,inj} = 2C_s^*$	P_{ref} (bar)	$P_{wf,max}^{inj}$ (bar)	$P_{wf,min}^{prod}$ (bar)
2.4E-3*	165	250	145

* 2.4 kg surfactant in 1000 kg surfactant solution.

Appendix C

Foam Models

C.1. Introduction

This appendix introduces the functions we used to incorporate foam sensitivity to water saturation (S_w), oil saturation (S_o), and surfactant concentration (C_s). We assume that foam could be weakened or killed as a result of low S_w or high S_o, and its strength is dependent on C_s below a critical concentration. We denote the functions representing foam sensitivity to S_w, S_o, and C_s by F_w, F_o, and F_s, respectively. In case of foam sensitivity to S_w and S_o, if foam is weakened, we add superscript w (e.g., F_w^w , F_o^w) and if it is killed, we add superscript k (e.g., F_w^k , F_o^k).

We applied only two of the built-in functions of STARS™ (i.e., F_w^w in Eq. C-1 from the 1998 version and F_o^k from the 2007 version). Some of these functions (e.g., F_o^k in Eq. C-4 and F_s in Eq. C-7) are not differentiable at certain points. Non-differentiable foam-sensitivity functions result in non-differentiable fractional-flow functions at those points, leading to problems in solving PDEs. This problem exists for both the MOC solution procedure and numerical simulators, but it is serious for the MOC solution. Therefore, we did not apply the F_s function provided by STARS™ and we introduced a new differentiable correlation instead. We also stated the condition for which F_o^k is differentiable.

New correlations are introduced for the sensitivity types to S_w and S_o (i.e., F_w^k and F_o^w) that are not available in STARS™. Although we have adopted some of the empirical correlations from this simulator, we have not, however, used this simulator in any of our simulations.

Each of the functions F_w^w , F_o^k , F_w^k , F_o^w , and their combinations [(F_w^w , F_o^k); (F_w^w , F_o^w); (F_w^k , F_o^k); (F_w^k , F_o^w)] are used in Chapters 3 and 4. Nevertheless, the combination of F_w^w (Eq. C-2) and F_o^k is the only choice used in Chapter 5. Therefore, the foam-parameter values mentioned in this appendix correspond to those used in Chapters 3 and 4, unless otherwise is stated. Table B-1 summarizes the foam-parameter values applied in Chapters 3 and 4, whereas Table B-2 gives the parameter values used in Chapter 5.

C.2. Effect of *fmmob*

fmmob corresponds to the normalized resistance to flow of a foam of minimum-size bubbles, *in the absence of factors increasing bubble size* (Surguchev et al. 1995). Cheng et al. (2000) fitted the oil-free core-flood data of Alvarez (1998) for foam without oil in Berea core at room temperature [also in Alvarez et al. (2001)] to Eq. C-1. They found a match with *fmdry* equal to 0.316 and *fmmob* approximately equal to 55,000. In Chapters 3 and 4 we use this value of *fmmob* for the 1D analytical and numerical simulations. In Chapter 5, we set *fmmob* = 1,000 to minimize the effect of abrupt changes in the gas mobility, to ensure finding the correct solution in the forward run with a reasonable time-step and gridblock size in 3D simulations. In addition, if a foam represented by a high value of *fmmob* such as 55,000 were to form near an injection well, it would cause a significant drop in the injection rate in an injection well operating at a constant prescribed bottomhole pressure. In the case of injecting at a fixed rate, the presence of a very low mobility foam near an injection well leads to an extremely high bottomhole pressure that can even lead to fracturing the formation around the wellbore.

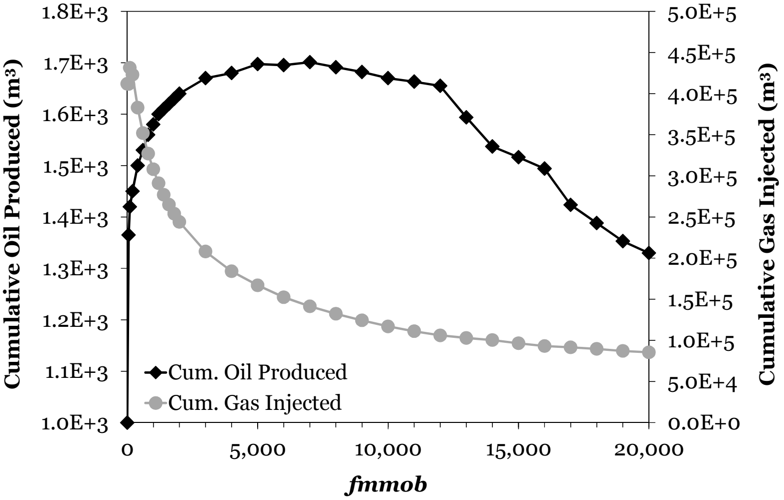

Fig. C-1: Effect of *fmmob* on oil recovery and cumulative gas injected in Scenario 3 in Chapter 5 (§5.3.2.3) at the optimum switching time equal to 44 days. Values in the figure are after 250 days of simulation. Gas is injected only after the switching time. The injection well operates at a constant prescribed bottomhole pressure. The larger is *fmmob*, the stronger the foam is. Stronger foam hampers gas injection and subsequently oil production drops for *fmmob* above a certain value (7,000 here).

Moreover, a higher value of *fmmob* and therefore a stronger foam does not necessarily correspond to higher oil production. In our simulations in Chapter 5 at which the injection well operates at a constant prescribed bottomhole pressure, a larger value of *fmmob* (larger than 100) causes reduced gas injection because of limits on the bottomhole pressure. We find an optimum value for *fmmob* that leads to the highest oil production, above which oil production declines due to the formation of too-strong foam. For the choice of parameters used in Chapter 5 where water weakens foam and oil kills foam, the optimum value of *fmmob* is approximately 7,000 (**Fig. C-1**). Since in this chapter we assume that $S_{oI} = S_{orw}$, gas is the only displacing fluid unless S_o goes above S_{orw}.

C.3. Effect of Low Water Saturation on Foam

C.3.1. Foam is Weakened at Low Water Saturations

We use the STARS™ (1998 version) function [see Cheng et al. (2000)] for this purpose (see **Fig. C-2a**):

$$F_w^w = 0.5 + \frac{\arctan\left[epdry(S_w - fmdry)\right]}{\pi} \qquad S_{wr} \le S_w \le (1 - S_{or}), \tag{C-1}$$

where *fmdry* corresponds to S_w^* and *epdry* regulates the slope of the k_{rg}-function curve near *fmdry*. The larger is the *epdry*, the more abrupt the transition is between strong foam and foam collapse.

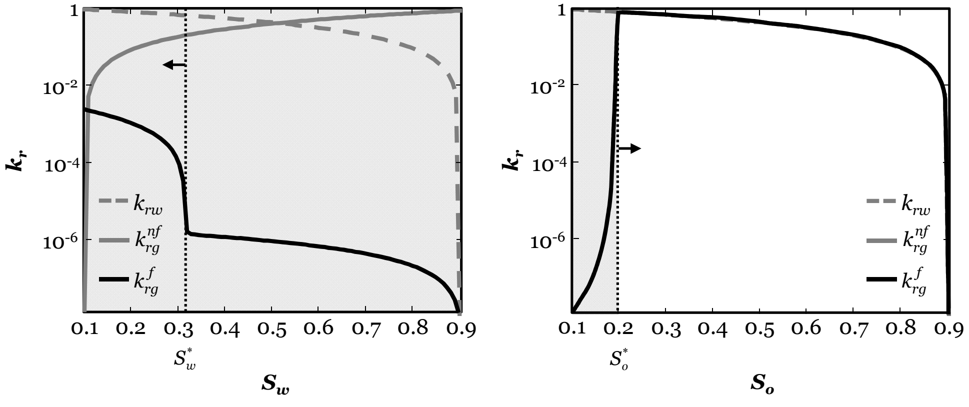

Fig. C-2: Effect of foam on gas relative permeability. Note the logarithmic scale of the vertical axes. The gray-filled region represents the region with foam. The curves in the absence of foam are according to the linear relative-permeability model in Chapter 3 and the parameters are based on Table B-1. (a) Foam is weakened at low water saturations (i.e., $S_w \le S_w^*$) according to Eq. C-1 and oil has no effect. Note that foam strength does not approach zero at $S_w = S_{wr}$ as it should. (b) Foam is killed at high oil saturations (i.e., $S_o \ge S_o^*$) according to Eq. C-3 and water has no effect.

As mentioned earlier, Cheng et al. (2000) fitted the oil-free core-flood data of Alvarez (1998) to Eq. C-1 and found a match with *fmdry* = 0.316. We choose the same values in our model since we could not find a data set having both the water- and oil-related parameters available in the same data set. We set *epdry* to 1,000, smaller than the value Cheng et al. (2000) selected. We used the same values for *fmdry* and *epdry* in Chapter 5.

One shortcoming of Eq. C-1 is that foam does not collapse completely at $S_w = S_{wr}$ (Fig. C-2a), despite the very high capillary pressure at $S_w = S_{wr}$; for our parameter choices in Table B-1, k_{rg} is reduced by a factor of 82 at S_{wr} in the absence of any oil effect. One way to deal with that is by making F_w^w a function of capillary pressure, choosing another function, or choosing parameter values that set F_w^w to zero at $S_w = S_{wr}$. A subtle change in Eq. C-1 makes foam strength approach zero at S_{wr}:

$$F_w^{w,new} = F_w^w(S_w) - F_w^w(S_{wr}) = \frac{1}{\pi}\begin{pmatrix} \arctan\left(epdry(S_w - fmdry)\right) - \\ \arctan\left(epdry(S_{wr} - fmdry)\right) \end{pmatrix} \quad S_{wr} \le S_w \le (1 - S_{or}). \tag{C-2}$$

This change hardly affects F_w^w except near S_{wr}, but applying this equation significantly alters the behavior observed from Eq. C-1 for gas/SAG processes.

C.3.2. Foam is Killed at Low Water Saturations

For this purpose, we need a *continuous* function equal to zero for $S_w \le fmdry$ and gradually increasing to unity for $S_w > fmdry$. This function must also be *differentiable* at $S_w = fmdry$. Manipulating Eq. C-1 for this purpose (by introducing a new function that is equal to zero at $S_{wr} \le S_w \le fmdry$ and equal to Eq. C-1 for $S_w > fmdry$) results in a function that is discontinuous and not differentiable at $S_w = fmdry$. Therefore, we introduced a function that is differentiable at $S_w = fmdry$; this is similar to Eq. C-4 for foam sensitivity to oil saturation (see below):

$$F_w^k = \begin{cases} 0 & S_{wr} \le S_w \le fmdry \\ \left(\dfrac{S_w - fmdry}{fudry - fmdry}\right)^{epdry'} & fmdry < S_w < fudry \\ 1 & fudry \le S_w \le (1 - S_{or}) \end{cases}, \tag{C-3}$$

where *fmdry* corresponds to S_w^*, *fudry* is the upper water saturation above which F_w^k is no longer affected by S_w and F_w^k becomes equal to unity, and *epdry′* controls the k_{rg} dependence on S_w and should be larger than unity; otherwise, function F_w^k will not be differentiable at $S_w = fmdry$. This function is not differentiable at $S_w = fudry$, but our MOC results are not affected by it because the solutions always shock past this region. In order to plot the saturation paths for the MOC solution including S_w = *fudry* (Fig. 6a in Chapter 1), we plot the saturation paths from one side of the diagram until reaching the point of discontinuous derivative (i.e., *fudry*), at which we stop using the expression for F_w^k that applies on that side of the discontinuity. We switch to a new expression for F_w^k on the other side of the discontinuity and continue constructing the paths on the other side of the discontinuity. We set *fudry* equal to 0.532 and *epdry'* equal to 2 in order to have a smooth, rounded corner at *fmdry*, and we keep *fmdry* equal to 0.316.

The SAG success design criterion developed from the MOC without oil (Shan and Rossen 2004) focuses on the mobility of the foam bank behind a shock identified on the gas/water fractional-flow curve without mobile oil. Our models in Chapter 3 (with the linear relative-permeability model in Eq. 1 of Chapter 3 and parameters in Table B-1) give the following behavior for gas injection in the absence of mobile oil ($S_o = S_{or}$). For full-strength foam (*fmmob* = 55,000; $F_w = 1$), the fractional-flow curve $f_w(S_w)$ has a corner at $S_w = 0.1$ and rises steeply for $S_w > 0.1$. Therefore, with no mobile oil present, the fractional-flow solution for gas injection in a SAG process (Zhou and Rossen 1995; Dong and Rossen 2007) gives a shock from $S_w = (1 - S_{wr})$ to $S_w = 0.1$, with full-strength (low-mobility) foam behind the shock. If Eq. C-1 applies instead, for gas injection in a SAG process there is a shock from $S_w = (1 - S_{wr})$ to $S_w = 0.1$, with gas mobility reduced by a factor of 82 in the gas bank. If Eq. C-2 applies, there is a shock to $S_w = 0.1454$, with gas mobility reduced by a factor of 22.6; total mobility is more than twice that of water alone at residual oil saturation. This case would not be considered really satisfactory for a SAG process (Shan and Rossen 2004), but it is significantly better than a gas flood without foam. If Eq. C-3 applies, there is a shock from $S_w = (1 - S_{wr})$ to a point of tangency at S_w just above 0.316, with nearly complete foam collapse throughout the gas bank. (Gas mobility is reduced by only 1% at the point of tangency.) Although there is a point of tangency rather than a corner in the $f_w(S_w)$ curve, Eq. C-3 is essentially like cases described by Zhou and Rossen (1995) and Dong and Rossen (2007), with a shock to nearly complete foam collapse behind the gas front. Thus, none of our examples in Chapter 3 include both foam collapse at S_{wr} and a low-mobility foam bank predicted without mobile oil. Among several foam models we tested, none satisfied this second criterion with the linear relative-permeability model (Eq. 1 in Chapter 3). The nonlinear relative-permeability model used (Eq. 2 in Chapter 3), which does not produce elliptic regions, does not satisfy this second criterion. However, Chapter 5 presents a foam model where foam collapses at S_{wr} (Eq. C-2) and yet successful mobility control at the foam bank is predicted (Fig. 8 in Chapter 5). In this case, there is a shock from the initial condition [$S_w(I) = 0.7$] to a foam bank with a mobility just slightly less than that of the water ahead of it (in time). This topic deserves fuller study.

C.4. Effect of High Oil Saturation on Foam

It is generally accepted that foam is destabilized by oil. However, foam strength is influenced by the compositions of oil, surfactant and aqueous phase (Li et al. 2008). The most widely known mechanism of foam destruction by oil is that foam films rupture, as oil droplets enter and spread at the air/water interface of the foam films (Koczo et al. 1992). The foam/oil interactions and the effect of oil on foam stability and the mechanisms involved are widely investigated in Nikolov et al. (1986), Manlowe (1990), Schramm and Novosad (1992), Koczo (1992), and Vikingstad (2006).

Here, we only incorporate the effect of oil saturation on foam strength, based on the following experiments. Law et al. (1992) presented the results of 1D foam-generation experiments inside a sandpack in the presence of oil. For $S_o \geq 0.25$, foam collapsed and pressure gradient was the same as when there was no foam. They also stated that determining S_o^* is very difficult and dependent on the surfactant. For a certain surfactant, results indicated a range of 0.15 to 0.25 for S_o^*. Hatziavramidis et al. (1995) used a value of 0.3 for S_o^*, determined experimentally, for their simulations. Svorstøl et al. (1996) found that S_o affects foam performance in their experiments at Snorre reservoir conditions. Svorstøl et al. (1996) and Mannhardt and Svorstøl (1999) have shown that apparent foam viscosity is strongly reduced at high S_o at Snorre reservoir conditions. However, foam was still present for $S_o > S_o^*$ in their experiments. They reported apparent foam viscosities of the order of 1,000 cp for $0.08 < S_o < 0.13$, 200 cp at $S_o = 0.19$ and 60 cp at $S_o = 0.42$. Mannhardt and Svorstøl (1999) also found that apparent foam viscosity decreased steeply for S_o between 0.13 and 0.15. Above S_o^*, strong foams with apparent viscosities of about 200 cp were still formed with the same surfactant, compared to the apparent gas viscosity in the absence of surfactant of 0.5 to 0.7 cp. Considering these observations, we set $S_o^* = 0.2$ in our models in Chapters 3 and 4. In Chapter 5, we set S_o^* equal to 0.4.

C.4.1. Foam is Killed at High Oil Saturations

We use the STARS™ function (2007 version) for this purpose (see Fig. C-2b):

$$F_o^k = \begin{cases} 1 & S_o < floil \\ \left(\dfrac{fmoil - S_o}{fmoil - floil}\right)^{epoil} & floil \leq S_o < fmoil \\ 0 & fmoil \leq S_o \leq (1 - S_{wr}) \end{cases} , \qquad \text{(C-4)}$$

where *fmoil* corresponds to S_o^*, *floil* is the lower oil saturation at which oil affects foam, and *epoil* controls the k_{rg} dependence on S_o. F_o^k is differentiable at $S_o = fmoil$ only if *epoil* is larger than unity. We set *epoil* equal to 2 and *floil* equal to S_{or}. In Chapter 5, we set *epoil* equal to 1.5 and *floil* equal to zero.

C.4.2. Foam is Weakened at High Oil Saturations

We used a function similar to F_w^w (Eq. C-1) for defining the weakening effect of oil:

$$F_o^{w,\text{old}} = 0.5 + \frac{\arctan\left(epoil' \times \left(fmoil - S_o\right)\right)}{\pi} \qquad S_{or} \le S_o \le (1 - S_{wr}), \qquad \text{(C-5)}$$

where *fmoil* corresponds to S_o^* and *epoil′* regulates the slope of the k_{rg} curve near *fmoil.*

C.4.2.1. Enhancement

Eq. C-5 has a shortcoming that F_o does not equate to zero in the absence of any oil. This shortcoming is fixed in the following equation, in which F_o (S_o = 0) = 1:

$$F_o^{w,\text{new}} = F_o^{w,\text{old}} + \left(1 - F_o^{w,\text{old}}(S_o = 0)\right) \qquad 0 \le S_o \le (1 - S_{wr}). \qquad \text{(C-6)}$$

C.5. Effect of Low Surfactant Concentration on Foam

Surfactants serve as foaming agents for foam generation. Various experimental studies (Svorstøl et al. 1996; Vassenden and Holt 1998; Mannhardt and Svorstøl 1999; Apaydin and Kovscek 2000) revealed that foam strength was reduced only at relatively low surfactant concentrations (C_s) (**Fig. C-3**).

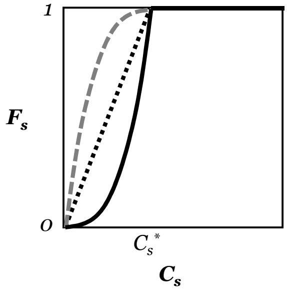

Fig. C-3: Schematic of the foam sensitivity to surfactant concentration: foam strength is affected for $C_s < C_s^*$. The black-dotted line correspond to *epsurf* = 1. The black-solid curve represents *epsurf* > 1 and the light-gray dashed curve is for *epsurf* < 1.

The effect of C_s on foam strength is represented in STARS™ (2007 version) by the following function:

$$F_s = \begin{cases} \left(\dfrac{C_s}{C_s^*}\right)^{epsurf} & C_s \le C_s^* \\ 1 & C_s > C_s^* \end{cases}, \tag{C-7}$$

where C_s^* is the critical surfactant concentration above which foam is at its full strength in the absence of any other factors influencing foam strength (Fig. C-3). However, this function is not differentiable at C_s^*. Instead, we use another function that is smooth (i.e., continuous and differentiable) at every C_s:

$$F_s = \left(\tanh\left(a\left(aC_s\right)^b\right)\right)^c, \tag{C-8}$$

where *a*, *b*, and *c* are the parameters regulating the F_s curve. In our simulations, we took C_s^* half the injected concentration; i.e., C_s^*=0.0012 and *epsurf* = 100. By adjusting the above parameters (see Table C-1) we can get very good matches with Eq. C-7 as shown in **Fig. C-4**:

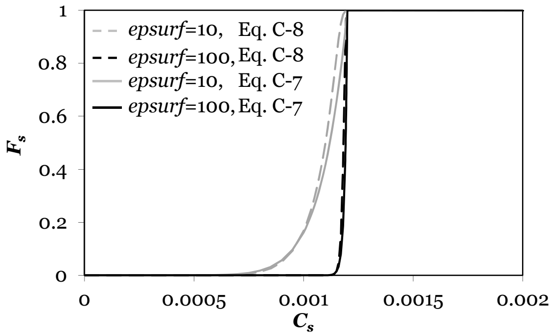

Fig. C-4: Comparing Eqs. C-7 and C-8 with the regulating parameters in Table C-1 for C_s^* = 0.0012.

Table C-1: Regulating parameters in Eq. C-8 for matching Eq. C-7 with C_s^* = 0.0012 or 0.12 wt.%.

	a	*b*	*c*
epsurf = 10	750	50	0.23
epsurf = 100	800	130	1

As mentioned earlier, we took C_s^* half the injected concentration ($C_{s,inj}$). In reality, foam strengthens more than linearly with C_s (*epsurf* < 1 in Fig. C-3). However, if one implements the corresponding physical relationship into the simulator, the surfactant front spreads out due to numerical dispersion. Therefore, foam forms in the regions that surfactant would not have reached in the absence of numerical dispersion. To reduce this effect and move the foam bank back to nearly where it should be, we pick C_s^* = ½ $C_{s,inj}$ and we choose a high value of *epsurf* (100 in our case) to make foam suddenly form at C_s^* (Fig. C-4). The strategy of setting $C_s^* = ½\ C_{s,inj}$ was first mentioned in Rossen et al. (1999) and explored in depth in Cheng (2002). We have illustrated and discussed the effect of this choice (i.e., *epsurf* = 100) in reducing the effect of numerical dispersion in §4.4.3. If one uses *epsurf* = 1, then C_s^* must be taken equal to $C_{s,inj}$ or a physically measured concentration at which full-strength foam is attained. Using $C_s^* = ½\ C_{s,inj}$ and *epsurf* = 1 results in foam bank acceleration by dispersion.

C.6. Complications in Implementing Foam Models in a Ternary Diagram[*]

In the absence of foam, all the saturation paths are straight lines (see Fig. 1a in Chapter 3) and there is no inflection point along them, using the linear relative-permeability model in Eq. 1 in Chapter 3. In this case, the only umbilic point is along the S_{wr} line. The solution here is of type (*R*)(*R*); that is, both waves are rarefaction waves.

By incorporating only *fmmob* in Eq. 3 in Chapter 3, the ideal case of full-strength foam occurs, where k_{rg}^{nf} is reduced 55,001-fold everywhere (see Fig. 2a). The single umbilic point is on the S_{or} line, and there is no inflection point along the saturation paths on the ternary diagram. Because of the presence of strong foam and hence reversal of the direction of the arrows along the path from *J* to *I* compared to what we see in the no-foam case in Fig. 1a, the only possible solution for the injection schemes appearing in this work is of type (*S*)(*S*): That is, both waves are shock waves. Note the small segment of fast path close to the injection point in the inset of Fig. 2a. Such a small segment also exists in Fig. 3 and **Fig. C-5a**.

If foam is killed at low water saturations (i.e., $S_w \leq S_w^*$) and oil has no effect, two distinct zones appear on each side of the $S_w = S_w^*$ line (see Fig. 6a). The zone with $S_w \leq S_w^*$ is exactly similar to the same zone in the no-foam case in Fig. 1a. As S_w exceeds S_w^*, paths shift abruptly from the no-foam to full-strength-foam pattern. Moreover, inflection points emerge in this case, but only along the fast paths. The inflection locus is a straight line at $S_w = S_w^* = fmdry$. There are three umbilic points in this case, one along each residual-saturation line.

Implementing the weakening effect of water on foam according to Eq. C-1 (oil has no effect) again divides the ternary diagram into two zones at $S_w = S_w^*$ (see Fig. 6b). However, the zone at $S_w \leq S_w^*$ no longer resembles the same zone in Fig. 1a because the umbilic point along the S_{wr} line is gone. As in the preceding paragraph, inflection points appear only along the fast paths, but the inflection locus is no longer a straight line. The only umbilic point in this case is along $S_o = S_{or}$ and the only possible solution is of type (*R*)(*S*).

---

[*] All the figures that we refer to in this section belong to Chapter 3.

On the other hand, if foam is affected only by high oil saturations [i.e., killed (Fig. 3a) or weakened (Fig. 3b) at $S_o \geq S_o^*$], and not affected by low water saturations, inflection points occur only along the slow paths. The inflection locus is a straight line at $S_o = S_o^*$. Note the abrupt turns in Fig. 3a along the slow paths at S_o^* because of the sharp change in foam strength across the foam/no-foam boundary at S_o^*. In this case and all the cases following, there is one umbilic point along every residual-saturation line.

In cases where foam strength is affected by both high oil and low water saturations, the ternary diagram becomes more complicated because of the occurrence of several inflection points along the saturation paths. Inflection points would occur on both fast and slow paths passing through the foam/no-foam boundary or on those located in the regions where foam exists. In all these cases, there is at least one inflection point along the slow paths passing through the line at $S_o = S_o^*$ at or around S_o^*. There might be multiple inflection points along the slow paths in some cases (e.g., Figs. 5 and 6). No inflection point emerges along the slow path, if $S_o < S_o^*$ along the entire path. However, there is always a single inflection point along the fast paths passing through $S_w = S_w^*$ located in the region with foam present.

Fig. C-5 shows a challenging case in which our fine-grid numerical simulator did not find the solution. This figure shows the result of the numerical simulation for the gas-injection cycle of a SAG process. The correct displacement route consists of two shocks with *IJ* along the S_{wr} line at (0.1, 0.1957, 0.7043). The reason for the failure of the numerical simulation appears to be that point *IJ* is very close to S_o^* and a very small perturbation may cause the solution to fall to the right of the foam/no-foam boundary, where k_{rg} changes drastically. Thus, the numerical solution had numerous oscillations across this boundary (Figs. C-4a and C-4b), and it was unable to find *IJ*. We have discussed the cause of these oscillations in §4.5.1. In this case, we used the analytical procedure to find *IJ* (Fig. C-5a). In principle, it should be possible to overcome these oscillations by sufficiently reducing the time-step and gridblock size; however, it would be computationally very expensive. (We could not find a solution free from oscillations even with Δt = 1E-6 day and Δx = 0.01 m in a 100 m long reservoir.) In Fig. C-5, the value of *fmmob* is equal to 55,000. This results in a very sharp transition in gas mobility over the foam/no-foam boundary leading to the situation where the numerical simulation does not find the correct solution. However, the numerical simulator finds the correct solution for the smaller values of *fmmob* in ranges lower than 1,000 (a much weaker foam), leading to a smoother transition in gas mobility over the foam/no-foam boundary.

These complexities make the task of finding the displacement route more difficult. We used the numerical simulator in a number of cases to find the approximate trajectory of the routes before applying the analytical criteria to confirm the solution.

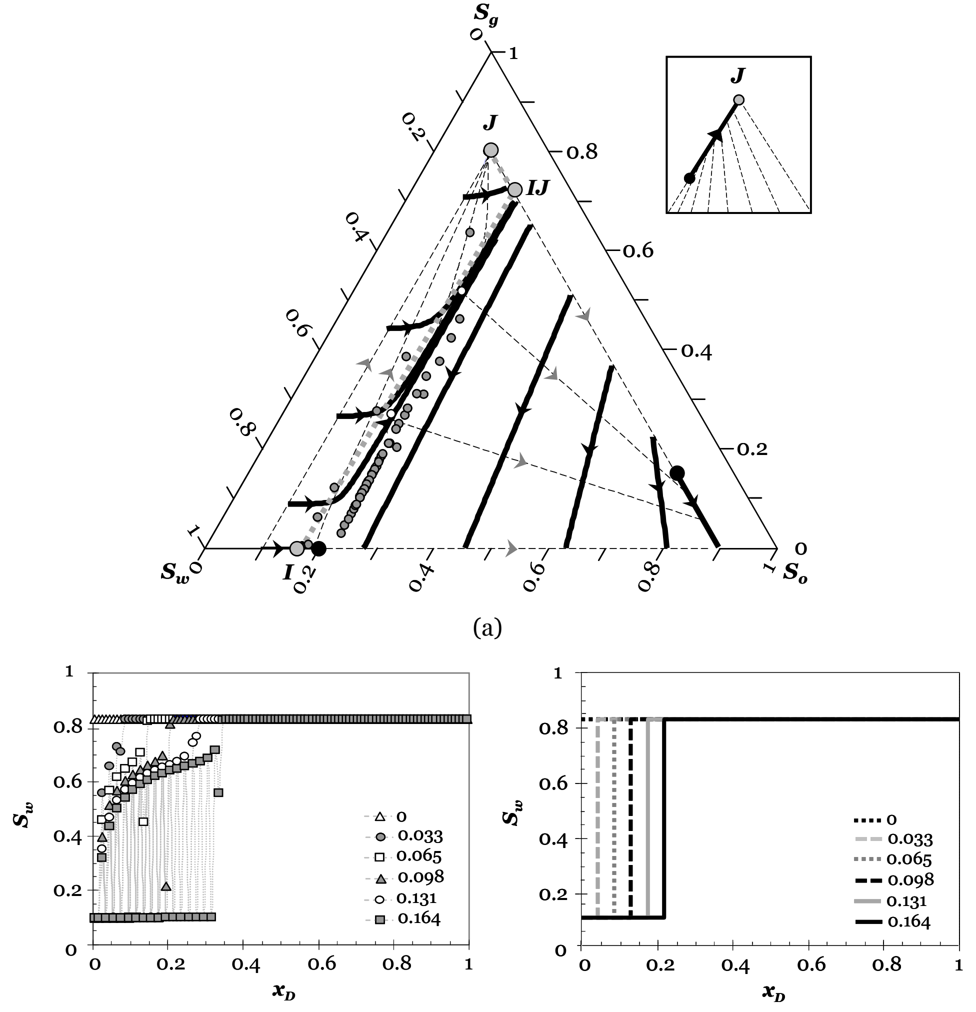

(a)

(b)

(c)

Fig. C-5: Numerical simulations do not always find the correct solution, and, in this example, they are in substantial error. Here, foam is killed at $S_o(I) \geq S_o^*$ ($S_o^* = 0.2$) and water has no effect. The displacement route found analytically for gas-injection cycle of SAG with *I* at (0.83, 0.17, 0) consists of two shocks with *IJ* along the S_{wr} line at (0.1, 0.1957, 0.7043). However, the numerical solution cannot find the correct solution. (a) Saturations (based on the numerical solution) across the reservoir at different values of t_D plotted on the ternary diagram depicted by small, dark-gray circles. Note the oscillations across the foam/no-foam boundary at $S_o = S_o^*$. The MOC solution is shown by the thick gray, dotted lines connecting points *J*, *IJ,* and *I*. (b) Water-saturation profile at various values of t_D, obtained numerically. Water saturation is alternating wildly from one gridblock to the next. Note that saturations in individual gridblocks do not fluctuate versus t_D (not shown here). (c) Water-saturation profile at various values of t_D according to the MOC solution.

Appendix D

Numerical Dispersion

The numerical dispersion coefficient is derived for two-phase immiscible equations in one dimension neglecting capillary pressure. A similar concept applies for three-phase equations.

$$\varphi \frac{\partial S_w}{\partial t} + u \frac{\partial f_w}{\partial x} = 0, \tag{D-1}$$

where S_w is water saturation, f_w is water fractional-flow function, φ is porosity, t is time, x is the x-coordinate, and u is the total velocity. We discretize Eq. D-1 *upwind* in space and we use a *backward* Euler time approximation (implicit).

$$\varphi \frac{S_{w,i}^{n+1} - S_{w,i}^{n}}{\Delta t} + u \frac{f_{w,i}^{n+1} - f_{w,i-1}^{n+1}}{\Delta x} = 0. \tag{D-2}$$

Taylor's expansion:

$$S_{w,i}^{n} = S_{w,i}^{n+1} - \Delta t \frac{\partial S_w}{\partial t} + \frac{\Delta t^2}{2} \frac{\partial^2 S_w}{\partial t^2} + O(\Delta t^3), \quad \Delta t = t^{n+1} - t^{n}, \tag{D-3}$$

$$f_{w,i-1}^{n+1} = f_{w,i}^{n+1} - \Delta x \frac{\partial f_w}{\partial x} + \frac{\Delta x^2}{2} \frac{\partial^2 f_w}{\partial x^2} + O(\Delta x^3), \quad \Delta x = x_i - x_{i-1}. \tag{D-4}$$

The discretized terms in Eq. D-2 are substituted with Eq. D-3 and Eq. D-4:

$$\varphi \left(\frac{\partial S_w}{\partial t} - \frac{\Delta t}{2} \frac{\partial^2 S_w}{\partial t^2} + O(\Delta t^2) \right) + u \left(\frac{\partial f_w}{\partial x} - \frac{\Delta x}{2} \frac{\partial^2 f_w}{\partial x^2} + O(\Delta x^2) \right) = 0, \quad \frac{\partial f_w}{\partial x} = \frac{\mathrm{d} f_w}{\mathrm{d} S_w} \frac{\partial S_w}{\partial x},$$

or

$$\varphi \frac{\partial S_w}{\partial t} + u \frac{\partial f_w}{\partial x} = \varphi \frac{\Delta t}{2} \frac{\partial^2 S_w}{\partial t^2} + u \frac{\Delta x}{2} \frac{\partial^2 f_w}{\partial x^2} + \ldots = \varphi \frac{\Delta t}{2} \frac{\partial^2 S_w}{\partial t^2} + u \frac{\Delta x}{2} \frac{\partial}{\partial x} \left(\frac{\mathrm{d} f_w}{\mathrm{d} S_w} \frac{\partial S_w}{\partial x} \right) + \ldots . \tag{D-5}$$

We derive the following auxiliary expressions by differentiating Eq. D-1 with respect to time (Eq. D-6) and space (Eq. D-7):

$$\frac{\partial^2 S_w}{\partial t^2}=-\frac{u}{\varphi}\frac{\partial}{\partial t}\left(\frac{\partial f_w}{\partial x}\right)=-\frac{u}{\varphi}\frac{\partial}{\partial t}\left(\frac{\mathrm{d}f_w}{\mathrm{d}S_w}\frac{\partial S_w}{\partial x}\right)=-\frac{u}{\varphi}\frac{\partial}{\partial x}\left(\frac{\mathrm{d}f_w}{\mathrm{d}S_w}\frac{\partial S_w}{\partial t}\right), \tag{D-6}$$

$$\begin{aligned}\frac{\partial}{\partial x}\left(\frac{\partial S_w}{\partial t}\right)&=-\frac{u}{\varphi}\frac{\partial}{\partial x}\left(\frac{\partial f_w}{\partial x}\right)=-\frac{u}{\varphi}\frac{\partial}{\partial x}\left(\frac{\mathrm{d}f_w}{\mathrm{d}S_w}\frac{\partial S_w}{\partial x}\right)=-\frac{u}{\varphi}\left[\frac{\mathrm{d}f_w}{\mathrm{d}S_w}\frac{\partial^2 S_w}{\partial x^2}+\frac{\partial S_w}{\partial x}\frac{\partial}{\partial x}\left(\frac{\mathrm{d}f_w}{\mathrm{d}S_w}\right)\right]=\\&=-\frac{u}{\varphi}\left[\frac{\mathrm{d}f_w}{\mathrm{d}S_w}\frac{\partial^2 S_w}{\partial x^2}+\frac{\mathrm{d}^2 f_w}{\mathrm{d}S_w^2}\left(\frac{\partial S_w}{\partial x}\right)^2\right].\end{aligned} \tag{D-7}$$

We substitute Eq. D-6 in Eq. D-5:

$$\varphi\frac{\partial S_w}{\partial t}+u\frac{\partial f_w}{\partial x}=\varphi\frac{\Delta t}{2}\left[-\frac{u}{\varphi}\frac{\partial}{\partial x}\left(\frac{\mathrm{d}f_w}{\mathrm{d}S_w}\frac{\partial S_w}{\partial t}\right)\right]+u\frac{\Delta x}{2}\frac{\partial}{\partial x}\left(\frac{\mathrm{d}f_w}{\mathrm{d}S_w}\frac{\partial S_w}{\partial x}\right)+\dots .$$

Applying chain rule:

$$\begin{aligned}\varphi\frac{\partial S_w}{\partial t}+u\frac{\partial f_w}{\partial x}&=\varphi\frac{\Delta t}{2}\left\{-\frac{u}{\varphi}\left[\frac{\partial S_w}{\partial t}\frac{\partial}{\partial x}\left(\frac{\mathrm{d}f_w}{\mathrm{d}S_w}\right)+\frac{\mathrm{d}f_w}{\mathrm{d}S_w}\frac{\partial}{\partial x}\left(\frac{\partial S_w}{\partial t}\right)\right]\right\}+\\&+u\frac{\Delta x}{2}\left[\frac{\partial S_w}{\partial x}\frac{\partial}{\partial x}\left(\frac{\mathrm{d}f_w}{\mathrm{d}S_w}\right)+\frac{\mathrm{d}f_w}{\mathrm{d}S_w}\frac{\partial}{\partial x}\left(\frac{\partial S_w}{\partial x}\right)\right]+\dots .\end{aligned} \tag{D-8}$$

We substitute Eq. D-7 in Eq. D-8:

$$\begin{aligned}\varphi\frac{\partial S_w}{\partial t}+u\frac{\partial f_w}{\partial x}&=\varphi\frac{\Delta t}{2}\left\{-\frac{u}{\varphi}\left[\frac{\partial S_w}{\partial t}\frac{\mathrm{d}^2 f_w}{\mathrm{d}S_w^2}\frac{\partial S_w}{\partial x}-\frac{u}{\varphi}\frac{\mathrm{d}f_w}{\mathrm{d}S_w}\left(\frac{\mathrm{d}f_w}{\mathrm{d}S_w}\frac{\partial^2 S_w}{\partial x^2}+\frac{\mathrm{d}^2 f_w}{\mathrm{d}S_w^2}\left(\frac{\partial S_w}{\partial x}\right)^2\right)\right]\right\}+\\&+u\frac{\Delta x}{2}\left[\frac{\partial S_w}{\partial x}\frac{\partial}{\partial x}\left(\frac{\mathrm{d}f_w}{\mathrm{d}S_w}\right)+\frac{\mathrm{d}f_w}{\mathrm{d}S_w}\frac{\partial^2 S_w}{\partial x^2}\right]+\dots .\end{aligned} \tag{D-9}$$

After some manipulations and rearranging Eq. D-9 in terms of $\partial^2 S_w/\partial x^2$ we finally get:

$$\begin{aligned}\varphi\frac{\partial S_w}{\partial t}+u\frac{\partial f_w}{\partial x}&=\frac{u}{2}\frac{\mathrm{d}f_w}{\mathrm{d}S_w}\left(\frac{u\Delta t}{\varphi}\frac{\mathrm{d}f_w}{\mathrm{d}S_w}+\Delta x\right)\frac{\partial^2 S_w}{\partial x^2}+\\&+\frac{u}{2}\frac{\mathrm{d}^2 f_w}{\mathrm{d}S_w^2}\left(\frac{\partial S_w}{\partial x}\right)^2\left[\frac{u\Delta t}{\varphi}\left(\frac{\mathrm{d}f_w}{\mathrm{d}S_w}+1\right)+\Delta x\right]+\dots .\end{aligned} \tag{D-10}$$

The expression preceding $\partial^2 S_w/\partial x^2$ term in Eq. D-10 is called the *numerical dispersion coefficient*.

Appendix E

Simple Example of Adjoint Equation

We construct the adjoint equation in Eq. 13 in Chapter 5 here for a very small example. We consider a 1D reservoir including 3 gridblocks with a *single-phase*, isothermal flow for only *one* time step. There is an injection well operating at a constant prescribed rate (i.e., Q_{inj}) and a production well operating at a constant prescribed bottomhole pressure (i.e., $P_{wf,min}^{prod}$). These wells are located at the opposite sides of the reservoir. Therefore, we have:

- $N = 1$ (number of time steps)
- $N_{\mathrm{gb}} = 3$ (number of gridblocks)
- $\dim(\mathbf{u}_1) = \dim(\mathbf{u}) = 2$ (i.e., Q_{inj} and $P_{wf,min}^{prod}$)
- $\dim(\mathbf{x}_1) = \dim(\mathbf{x}) = 3$ [i.e., phase pressures in each gridblock (p^1, p^2, p^3); we ignored the state variables corresponding to well discretization nodes to avoid further complexity.]
- $\dim(\mathbf{g}_1) = \dim(\mathbf{x}_1) = 3$ [i.e., 3 pressure equations in each gridblock (g_1^1, g_1^2, g_1^3); we ignored the well equations to avoid further complexity.]

Therefore, we have

$$\mathbf{x} = \mathbf{x}_1 = \begin{pmatrix} p^1 \\ p^2 \\ p^3 \end{pmatrix}, \qquad \mathbf{u} = \mathbf{u}_1 = \begin{pmatrix} Q_{inj} \\ P_{wf,min}^{prod} \end{pmatrix}, \qquad \mathbf{g} = \mathbf{g}_1 = \begin{pmatrix} g_1^1 \\ g_1^2 \\ g_1^3 \end{pmatrix},$$

where in g_k^j, k and j are the time-step and gridblock index, respectively. We aim at constructing the adjoint equation:

$$\mathbf{g}_{\mathbf{x}}^T \boldsymbol{\lambda}^T = \mathcal{J}_{\mathbf{x}}^T. \tag{E-1}$$

Having only one time step, $\mathbf{g}_{\mathbf{x}}^{T}$ is a block matrix with only one block $\mathbf{A}_1^T$ (see Eqs. 14 and 15 in Chapter 5), and this element has a dimension of dim($\mathbf{x}_1$)×dim($\mathbf{x}_1$):

$$\mathbf{g}_{\mathbf{x}} = \mathbf{A}_1 = \begin{pmatrix} \dfrac{\partial g_1^1}{\partial p^1} & \dfrac{\partial g_1^1}{\partial p^2} & \dfrac{\partial g_1^1}{\partial p^3} \\ \dfrac{\partial g_1^2}{\partial p^1} & \dfrac{\partial g_1^2}{\partial p^2} & \dfrac{\partial g_1^2}{\partial p^3} \\ \dfrac{\partial g_1^3}{\partial p^1} & \dfrac{\partial g_1^3}{\partial p^2} & \dfrac{\partial g_1^3}{\partial p^3} \end{pmatrix}, \qquad \mathbf{g}_{\mathbf{x}}^{T} = \mathbf{A}_1^{T} = \begin{pmatrix} \dfrac{\partial g_1^1}{\partial p^1} & \dfrac{\partial g_1^2}{\partial p^1} & \dfrac{\partial g_1^3}{\partial p^1} \\ \dfrac{\partial g_1^1}{\partial p^2} & \dfrac{\partial g_1^2}{\partial p^2} & \dfrac{\partial g_1^3}{\partial p^2} \\ \dfrac{\partial g_1^1}{\partial p^3} & \dfrac{\partial g_1^2}{\partial p^3} & \dfrac{\partial g_1^3}{\partial p^3} \end{pmatrix}.$$

The adjoint vector $\boldsymbol{\lambda}^T$ and $\mathcal{J}_{\mathbf{x}}^{T}$ are column vectors with dim($\mathbf{x}$). Therefore, Eq. E-1 reads:

$$\begin{pmatrix} \dfrac{\partial g_1^1}{\partial p^1} & \dfrac{\partial g_1^2}{\partial p^1} & \dfrac{\partial g_1^3}{\partial p^1} \\ \dfrac{\partial g_1^1}{\partial p^2} & \dfrac{\partial g_1^2}{\partial p^2} & \dfrac{\partial g_1^3}{\partial p^2} \\ \dfrac{\partial g_1^1}{\partial p^3} & \dfrac{\partial g_1^2}{\partial p^3} & \dfrac{\partial g_1^3}{\partial p^3} \end{pmatrix} \begin{pmatrix} \lambda_1^1 \\ \lambda_1^2 \\ \lambda_1^3 \end{pmatrix} = \begin{pmatrix} \dfrac{\partial \mathcal{J}}{\partial p^1} \\ \dfrac{\partial \mathcal{J}}{\partial p^2} \\ \dfrac{\partial \mathcal{J}}{\partial p^3} \end{pmatrix} \Rightarrow \begin{cases} \dfrac{\partial g_1^1}{\partial p^1}\lambda_1^1 + \dfrac{\partial g_1^2}{\partial p^1}\lambda_1^2 + \dfrac{\partial g_1^3}{\partial p^1}\lambda_1^3 = \dfrac{\partial \mathcal{J}}{\partial p^1} \\ \dfrac{\partial g_1^1}{\partial p^2}\lambda_1^1 + \dfrac{\partial g_1^2}{\partial p^2}\lambda_1^2 + \dfrac{\partial g_1^3}{\partial p^2}\lambda_1^3 = \dfrac{\partial \mathcal{J}}{\partial p^2} \\ \dfrac{\partial g_1^1}{\partial p^3}\lambda_1^1 + \dfrac{\partial g_1^2}{\partial p^3}\lambda_1^2 + \dfrac{\partial g_1^3}{\partial p^3}\lambda_1^3 = \dfrac{\partial \mathcal{J}}{\partial p^3} \end{cases}. \tag{E-2}$$

where in λ_k^j, k and j are the time-step and gridblock index, respectively. Eq. E-2 has 3 unknowns (i.e., $\lambda_1^1, \lambda_1^2, \lambda_1^3$) that are solved from the above system of equations. It is important to note that $\mathbf{A}_1$ is known and is constructed after the convergence of the Newton-Raphson iterations during the forward run and $\mathcal{J}_{\mathbf{x}}$ is computed based on the state vector computed in the forward run. Eq. E-2 corresponds only to one time step ($k = N = 1$). It is similar to Eq. 17 in Chapter 5.

Appendix F

Are Local Fluctuations in the Objective Function Caused by Foam Tables?

Another important issue to discuss is the source of fluctuations (peaks and valleys) on the local trend of $\mathcal{J}$ that are not noticed on the global trend in Chapter 5. At first, they might be attributed to the discontinuities of the plugging table interpolation (see §4.3.2) used instead of analytical expressions to represent the foam model. Tables introduce non-differentiabilities (i.e., discontinuities in the derivatives of gas mobility with respect to S_w, S_o, and C_s) that might lead to the fluctuations on the local trend of $\mathcal{J}$. In order to examine this idea, the source code of the simulator was adapted and the plugging table was replaced with the analytical expression for the foam model and its exact analytical derivatives. The resulting source code is implicit and applies the exact derivatives. However, similar fluctuations are still evident as shown in **Fig. F-1**. Therefore, the local fluctuations are not caused by foam tables.

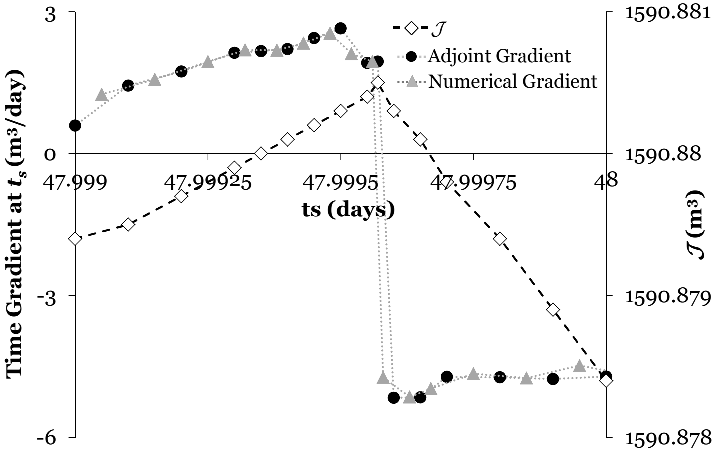

Fig. F-1: A peak on the local trend of $\mathcal{J}$ and a possible discontinuity in the time gradient still exist after implementing the exact foam functions in the source code of the simulator.

Summary

Chemical enhanced oil recovery (EOR) is relatively expensive due to the high cost of the injected chemicals such as surfactants. Excessive use of these chemicals leads to processes that are not economically feasible. Therefore, optimizing the volume of these injected chemicals is of extreme importance. We intend to maximize the long-term cumulative oil production ($Q_{o,cum}$) through optimizing the volume of the injected surfactant (represented by the switching time between surfactant and gas slugs) in a surfactant-alternating-gas (SAG) process in a 3D reservoir using a commercial simulator. Evaluating the correctness and accuracy of the numerical simulator is an essential step towards achieving reliable results. However, since no analytical solution exists for a real 3D displacement (with gravity), the performance of the simulator in 1D is evaluated against the exact analytical solutions provided by the method of characteristics (MOC).

The MOC has proved useful in highlighting key mechanisms and strategies for improving foam performance. We extended the MOC to foam flow with oil and examined the effects of foam quality, initial oil saturation $S_o(I)$, and foam sensitivity to high oil saturation (S_o) and low water saturation (S_w) on oil recovery in 1D. In the cases examined, our analysis revealed the following insights. Regardless of whether foam is sensitive to S_w, if foam is destroyed by oil at the initial condition, the displacement is nearly as inefficient as if no foam were present at all. In real foams, foam bubbles collapse at the residual water saturation (S_{wr}) because of high capillary pressure. The failure to represent this mechanism properly in models leads to misleading prediction of success in SAG foam processes. Incorporating foam collapse at S_{wr} results in the failure of a gas-injection cycle of a SAG process, regardless of the reservoir initial condition and foam sensitivity to S_w and S_o, for the relative-permeability models we examined. A foam flood is successful for any initial condition if foam is only weakened (not killed) by low S_w and not affected by S_o. Based on this study, it is not recommended to start foam EOR at early stages of the reservoir life for a foam formulation that is sensitive to high oil saturation, because high $S_o(I)$ causes the foam EOR process to fail. Thus, the effect of low S_w and high S_o on foam must be well understood and represented accurately to avoid spurious decisions leading to failure based on unrealistic foam models and parameter values.

The MOC solutions developed earlier are utilized to evaluate the performance of the simulator in 1D. In finding an accurate numerical solution that matches the MOC solution, some displacements were found to be more sensitive to the choice of time-step (Δt) and gridblock size (Δx) than others. For instance, if a part of the solution (e.g., rarefaction wave, constant-state region) is in the proximity of the foam/no-foam boundary at which drastic changes in gas mobility occur, the simulator may exhibit oscillations across the boundary with an improper choice of Δt and Δx and fail to find to the correct solution. Moreover, an inappropriate choice of Δt and Δx leads to erroneous results that might be hard to identify in 3D in the absence of the MOC solutions. One needs to look for symptoms, such as gridblocks with unexpected high/low saturation/pressure, to identify artifacts and find a proper choice of Δt and Δx by performing sensitivity analysis on these parameters. Insights achieved from this analysis led to applying simpler physics for the foam model in the 3D simulations to ensure finding the correct solution.

The effect of the switching time (t_s) between surfactant and gas slugs on $Q_{o,cum}$ was examined for 3D simulations of a SAG process in scenarios varying in the active constraint on the injection well and the end-time constraint. For all the scenarios, the highest oil recovery was obtained at a value of t_s for which the foam front was on the verge of breaking through to the production well, but has not yet broken through, at the end of the simulation. Moreover, the cumulative oil production was impaired once foam appeared in the production well. Therefore, if foam can be destroyed in the proximity of the production well, the optimal oil recovery increases. On the other hand, for an injection well operating at a constant prescribed bottomhole pressure, injecting surfactant into the reservoir did not necessarily lead to improved $Q_{o,cum}$ over a gas flood. Further, increasing t_s did not result in higher $Q_{o,cum}$ under certain conditions. In addition, injecting less gas as a result of increasing t_s did not lower $Q_{o,cum}$ in many occasions.

An investigation was conducted on the capability of a gradient-based optimization routine applied to foam EOR processes. We concluded that an inappropriate choice of the *relative tolerance* for the adjoint linear solver is the source of getting wrong gradients in our problem, and a very tight relative tolerance was required for the simulator to obtain accurate gradients in certain problems. We applied two types of foam models in this investigation: a *linear* model introducing gradual changes in gas mobility and a *nonlinear* model leading to abrupt changes in gas mobility. For the *linear* foam model (both in 1D and 3D simulations), the local and global trends of the objective function ($Q_{o,cum}$) were analogous and the optimization routine was capable of finding the optimum switching time ($t_{s,opt}$). However, replacing the linear foam model with the nonlinear foam model introduced inconsistencies between the local and global trends of the objective function and fluctuations in the adjoint gradient, in both 1D and 3D simulations. For the nonlinear foam model, the local and global trends were analogous and the adjoint gradient was free of fluctuations only at switching times for which the entire reservoir was swept by foam within the simulation period. For the 1D-*nonlinear* foam model, the gradient-based optimization routine was not suitable for finding $t_{s,opt}$, unless the initial guess is larger than $t_{s,opt}$. For the 3D-*nonlinear* foam model, there were major differences between the local and global trends of $\mathcal{J}$ in the neighborhood of the optima that would seriously challenge the performance of the optimization routine. As a result, a gradient-based optimization routine was not suitable for finding $t_{s,opt}$.

Overall, it is shown that accurate representation of the physics of the process in the simulation model and also careful examination of the mechanisms controlling the displacement process elucidate many valuable aspects of the foam EOR processes. Their inaccurate representation in simulations or neglecting them may result in a prediction of success for a process that will be unsuccessful in a real reservoir. Moreover, formation of foam may introduce abrupt changes in gas mobility that might challenge the performance of the simulator and also the gradient-based optimization routines.

Samenvatting

Chemisch-verbeterde oliewinning ("enhanced oil recovery"; EOR) kost relatief veel geld vanwege de hoge kosten van de geïnjecteerde chemicaliën zoals oppervlakteactieve stoffen. Overmatig gebruik van deze chemische stoffen leidt tot processen die niet economisch haalbaar zijn. Het is daarom van belang om het volume van deze chemische stoffen te optimaliseren. Ons doel is de cumulatieve olieproductie over een langere termijn ($Q_{o,cum}$), berekend m.b.v. een commerciële driedimensionale (3D)-reservoir simulator, te maximaliseren. Dit doen we door de schakeltijden in een proces van alternerende injectie van van oppervlakteactieve stoffen en gas (het z.g. "surfactant-altenating-gas" (SAG) proces) te optimaliseren. Er is echter geen analytische oplossing die de juistheid en nauwkeurigheid van een 3D numerieke verplaatsing (met de zwaartekracht) kan evalueren. De methode van karakteristieken ("method of characteristics"; MOC) geeft exacte oplossingen in 1D waarmee de juistheid en numerieke artefacten van numerieke simulatoren kunnen worden getoetst. Het is essentieel om eerst de prestaties van de numerieke simulator in 1D te evalueren voordat de simulaties in meerdere dimensies worden uitgevoerd.

De MOC heeft zijn nut bewezen in het benadrukken van de belangrijkste mechanismen en strategieën voor het verbeteren van de prestatie van schuim. We hebben de MOC uitgebreid met stromingseffecten van schuim in combinatie met olie, en daarbij gekeken naar de effecten op oliewinning in 1D simulaties. Daarbij is gekeken naar de kwaliteit van het schuim, de initiële olieverzadiging $S_o(I)$, de gevoeligheid van het schuim voor hoge olieverzadiging (S_o) en lage waterverzadiging (S_w). De analyse van de onderzochte gevallen resulteerde in de volgende inzichten. Als het schuim wordt afgebroken door olie bij de initiële condities, dan is de verplaatsing bijna net zo inefficiënt als in het geval dat er geen schuim aanwezig is; dit is onafhankelijk van de gevoeligheid van het schuim voor de watersaturatie. In echt schuim bezwijken schuimbellen bij een residuele waterverzadiging (S_{wr}) vanwege de hoge capillaire druk. Deze processen zijn niet goed weer te geven in het model, hetgeen leidt tot misleidende voorspellingen van het succes van het SAG proces met schuim. Uitbreiding van het model met het bezwijkmechanisme van schuimbellen bij residuele watersaturatie resulteert in het mislukken van een gas-injectie cyclus van een SAG proces, ongeacht de begincondities van het reservoir en de gevoeligheid van het schuim voor water- en oliesaturaties van de onderzochte relatieve permeabiliteitmodellen. Het produceren van olie door middel van SAG is succesvol onder alle condities als het schuim alleen wordt verzwakt maar niet wordt vernietigd. Het is echter niet succesvol bij lage watersaturaties en voor het geval dat het niet wordt beïnvloed door de oliesaturatie. Op basis van deze studie kan worden is het niet aan te bevelen om schuim EOR te beginnen in een vroeg stadium van de olieproductie, met een schuimformulering die gevoelig is voor hoge oliesaturatie, omdat een hoge $S_o(I)$ ervoor zorgt dat het schuim EOR-proces mislukt. Daarom moet het effect van lage watersaturatie en hoge oliesaturatie op schuim goed worden begrepen en nauwkeurig worden weergegven om verkeerde beslissingen te vermijden die een verhoging van de olieproductie tegengaan.

De uitgebreide MOC oplossing zijn toegepast voor het evalueren van de prestaties van de simulator. In het bepalen van een numerieke oplossing die overeenkomt met het resultaat van de MOC zijn sommige verplaatsingen gevoeliger voor de keuze van Δt en Δx. Oscillaties in de oplossing kunnen optreden bij incorrecte keuzes van Δt en Δx als een deel van de oplossing zich bevindt in de nabijheid is van de schuim/geen-schuim grens waar drastische veranderingen in de mobiliteit van het gas optreden. Bovendien leiden een incorrecte keuze van Δt en Δx tot onjuiste resultaten die misschien moeilijk te identificeren zijn in 3D simulaties bij gebrek aan MOC oplossingen. Men moet op zoek naar symptomen, zoals roosterpunten met een onverwacht hoge of lage saturatie of druk, om numerieke artefacten te identificeren en de juiste keuze van Δt en Δx te maken. Inzichten uit deze analyse hebben geleid tot het toepassen van een simplificaties in het model van het schuim in de 3D-simulaties om te verzekeren dat de oplossing convergeert naar de juiste oplossing.

Het effect van de schakeltijd (t_s) tussen het injecteren van oppervlakte-actieve stof en gas op $Q_{o,cum}$ is bekeken voor 3D-simulaties van een SAG proces in scenario's met verschillend controlestrategiën voor de injectie put en de eindtijd. De hoogste oliewinning in alle simulaties werd verkregen met een waarde van t_s waarbij het schuimfront op het punt staat door te breken bij de productieput aan het einde van de simulatie. De cumulatieve olieproductie vermindert zodra schuim geproduceerd wordt. Zodoende vermeerdert de optimale olie productie als het schuim bezwijkt in de nabijheid van de productieput. Aan de andere kant leidt het injecteren van een oppervlakteactieve stof in een injectieput opererend bij constante bodemdruk niet noodzakelijkerwijs tot een verhoging van $Q_{o,cum}$ in vergelijking met het injecteren van gas. Ook het verhogen van de schakeltijd leidt niet noodzakelijkerwijs tot een hogere $Q_{o,cum}$. Verder leidt het verminderen van de geïnjecteerde hoeveelheid gas, door het verhogen van de schakeltijd, niet noodzakelijkerwijs tot een lagere $Q_{o,cum}$.

De mogelijkheden van de gradiënt-gebaseerde optimaliseringmethode in de simulator zijn onderzocht voor schuim EOR processen. We laten zien dat een verkeerde keuze van de relatieve toleranties van de geadjugeerde lineaire oplosroutine (de “adjoint linear solver”) leidt tot verkeerde gradiënten in ons probleem en dat zeer strenge relatieve toleranties vereist zijn voor het verkrijgen van nauwkeurige gradiënten in 3D simulaties voor een niet-lineair schuim model. De lokale en globale richtingen van de doelfunctie vallen samen in het lineaire schuim model (1D en 3D) en de optimalisatieroutine is in staat om de optimale schakeltijd te bepalen. Het vervangen van het lineaire model door het niet-lineaire model introduceert inconsistenties tussen de lokale en globale richtingen van de doelfunctie en leidt tot schommelingen in de geadjugeerde gradiënt. De lokale en globale richtingen vallen alleen samen zonder schommelingen in de geadjugeerde gradiënt voor schakeltijden waarin het schuim het gehele reservoir bestrijkt gedurende de simulatieperiode.

De gradiënt-gebaseerde optimaliseringsmethode is niet geschikt voor het vinden van de optimale schakeltijd in het 1D nietlineaire schuim model, tenzij de beginschatting groter is dan de optimale schakeltijd. Inconsistenties in de nabijheid van de optima in het 3D nietlineaire model zijn een grote uitdaging voor de optimaliseringmethode. Daardoor is de gradiënt-gebaseerde optimalisatie niet geschikt voor het vinden van de optimale schakeltijd.

Samenvattend, het is aangetoond dat een nauwkeurige weergave van de fysica in het simulatie model in combinatie met een gedetailleerde analyse van de mechanismes die het verplaatsingproces bepalen vele waardevolle aspecten van schuim EOR processen verduidelijken. Onzorgvuldige of afwezige weegave in simulaties kan leiden tot een voorspelling waarbij toepassing van schuim EOR zal leiden tot een hogere olieproductie terwijl dat in een werkelijk reservoir niet zal gebeuren. Bovendien kan de vorming van schuim leiden tot abrupte veranderingen in de mobiliteit van het gas die de prestatie van de simulator en gradiënt-gebaseerde optimaliseringsmethodes nadelig kunnen beïnvloeden.

Acknowledgments

I would like to express my gratitude to my supervisors Bill Rossen and Jan Dirk Jansen for their continuous support in my Ph.D. They have been always there to listen and give advice. I also appreciate their careful review of the thesis and their valuable remarks. I am very thankful to Bill Rossen for encouraging me to carefully analyze the physics of the process that significantly added to the quality of the thesis.

I am sincerely grateful to Dan Marchesin and Hans Kraaijevanger for numerous useful discussions and carefully reading and giving insightful comments on this thesis, despite their limited time. I also thank Hans for his great support with MoReS. My special thanks go to Hans Bruining for our fruitful discussions. I am also very thankful to the rest of the examination committee members Arnold Heemink and Pacelli Zitha for participating in my Ph.D. defense and for carefully reviewing my work.

I gratefully acknowledge Shell for using their reservoir simulator MoReS and for providing me with access to their facilities in Rijswijk. I am thankful to Lingli Wei, Tsuyoshi Matsuura, Willem Schulte, Cor van Kruijsdijk, Toon Weisenborn, Jorn van Doren, Justina Przybysz, Mohand Talanana, Alexey Andrianov, Gerard Joosten, Paul van den Hoek at Shell for useful discussions and support. I am also very thankful to Pim Buurman for his valuable help with MoReS.

I would like to show my appreciation to Anke, Marlijn, Ralf, Hannie, Margot, Lydia, and Marijk for their various forms of support regarding administrative and bureaucracy affairs during my Ph.D. study.

I am very grateful to Patrick for translating the summary to Dutch and to Christiaan for editing it.

I am also very thankful to my dearest friends Elaheh, Ghazaleh, Marjan, Nasrin, Simin, Somayeh, and Zahra for believing in me and their continuous support. I am grateful to Gosia, Mariya, and Wiktoria for all the pleasant times that we spent together in Delft and Sibiu.

My most heartfelt appreciation goes to my beloved Hamidreza for his true love, understanding, endless support, encouragement and having confidence in me, for listening to my complaints and frustrations, and for inspiring, amazing, and helping me get through my Ph.D. study. I am also thankful to him for carefully reviewing my thesis. I can never thank him enough for all that.

Last, but not least, I most want to thank my wonderful parents for their unconditional love and life-long support to pursue my interest, for believing in me, and for helping me at any time all these years. I am greatly indebted to my parents for absolute support. They deserve far more credit than I can ever give them. My special and loving gratitude is due to my sweet sister and to my brothers for their loving support. Without them, this doctoral degree would not have been possible.

About the Author

Maryam Namdar Zanganeh was born on 30 September 1980 in Tehran, Iran. She obtained her high school diploma in mathematics and physics in 1998 from Toloo high school, Tehran. She received her B.Sc. degree in Chemical Engineering in 2002 from Amir-Kabir University of Technology, Tehran. In July 2005, Maryam obtained her M.Sc. degree (with Cum Laude) in Petroleum Engineering from Delft University of Technology (TU Delft). From August 2007, she was appointed as a Ph.D. student of reservoir engineering in the Department of Geotechnology at the TU Delft. Her research was focused on simulation and optimization of foam EOR processes and the results are presented in this thesis.